THE UNIVERSITY *of* EDINBURGH

Investigation of the Bacterial Mechanosensitive Ion Channel of Large Conductance within Bacterial Membrane Mimetics in Response to Simple Antimicrobial Molecules.

Sophie Ayscough

Doctor of Philosophy
The University of Edinburgh
November 2020

Abstract

This thesis describes the use of neutron and X-ray scattering and reflectivity to characterize the structure of the Mechanosensitive Ion Channel of Large Conductance, MscL, within bilayer constructs.

MscL is known to gate with increased surface tension in the lipid bilayer. In bacteria, mechanosensitive ion channels such as MscL protect cells against osmotic shock. The channel has also been shown to gate in the presence of amphiphilic molecules. By investigating the response of MscL to two different amphiphilic antimicrobials in three different bacterial membrane mimetics, we explore whether gating of the channels triggered by interaction with these molecules can play a role in their antimicrobial behaviour.

Cell-free expression of MscL directly into 3:1 POPC:POPG liposomes was optimised to produce proteoliposomes, that are the basis of the membrane mimetics used in this study. Small angle scattering provided evidence that single MscL channels were successfully expressed into liposomes. The response of the proteoliposomes to the antimicrobial peptide pexiganan and the naturally occurring antimicrobial surfactant, lyso-PC was investigated. We have shown through scattering experiments that we can observe a conformational change in MscL in the presence of lyso-PC and pexiganan that could be a signature of MscL gating.

Reflectivity measurements require a planar membrane of about 10 cm^2 and we have developed a novel membrane mimetic, in which a POPC:POPG bilayer is suspended beneath a cationic surfactant monolayer. Our neutron reflectivity experiments show that a high quality bilayer can be formed and that there is a water layer between the surfactant monolayer and the lipid bilayer. This water gap means that the suspended bilayer can fluctuate and there is sufficient space to allow for membrane proteins inserted into the suspended bilayer to protrude

out from the bilayer.

We have also developed an experimental system in which the POPC:POPG:MscL bilayer is tethered to a gold layer, which sits on top of a thin permalloy film coated onto a silicon block. The silicon block acts as a neutron window, and the permalloy layer means that we can exploit the two spin states of the neutron to measure polarised reflectivity from the tethered bilayer system, allowing two data sets, with slightly different structural sensitivities, to be measured simultaneously .

Using our planar membrane mimetics, we were able to investigate changes in the membrane and the MscL on addition of pexiganan. We observed a decrease in the distance that the proteins protrude out from the membrane from 50-60 Å to 30 Å, which we suggest is evidence that the channel has gated in response to the interaction of pexiganan with the membrane mimetic. In addition to further insight into the gating mechanism of the MscL this highlights the potential benefit of further investigating the channel as an antimicrobial target.

Declaration

I declare that this thesis was composed by myself, that the work contained herein is my own except where explicitly stated otherwise in the text, and that this work has not been submitted for any other degree or professional qualification except as specified.

(*Sophie Ayscough, November 2020*)

Acknowledgements

First and foremost I would like to thank my supervisor, Dr. Simon Titmuss for his continuous support and encouragement during this project, and for showing me how to be enthusiastic about science even in the bleak moments. I would also like to thank my supervisor Dr. Max Skoda for looking out for me and always being on-hand to provide sound advice and interesting discussions.

This work would not have been possible without funding from the SOFI centre fro doctoral training (EP/L015536/1) and ISIS Neutron and Muon Source facility development studentship (STFC). It would also not have been possible without access to neutron and X-ray facilities through beamtimes at ISIS neutron and muon source (Oxford, UK), Institut Laue-Langevin (Grenoble) and Diamond Light Source (Oxford, UK). I am thankful to Dr James Doutch for support and discussion on small angle scattering analysis, and also to Dr Andrew Caruana, Dr Christy Kinane, Dr Luke Clifton and Dr Gavin Stenning at ISIS, for the invaluable support they have provided while using facilities at ISIS. I am also thankful to Dr Yuri Gerelli and Dr Thomas Saerbeck at Institut Laue-Langevin (Grenoble) for instrument support and training. Similarly I'm thankful to Dr Andrew McCluskey for the data reduction and fitting discussions on my IO7 beamtime at Diamond Light Source, as well as to Dr Jonathan Rawle in aiding the set-up and running of the experiment.

I would like to thank my Cohort of the SOFI CDT with whom I've collected many great memories alongside this project. Particular shout out to David Crosby who I've discussed science with over many a coffee. I am also grateful to the other friends I've made during my time at Edinburgh. Cheers to Katherine, Emily, Eoin, Iain and Amy who continued to keep me smiling through video calls, trips outside and even the occasional baked goods delivery during the writing of this thesis.

Thank you to my parents who always fuelled my love of science and encouraged me to do anything I set my mind to. Finally my gratitude to Sky Brewer, who knew living with me during writing of this thesis would be tough and then had to suffer it under a lock-down. Thank you for always providing fun and distraction when it's been needed and for sticking with me through it all.

Contents

List of Figures

List of Tables

Chapter 1

Lay Summary

Antimicrobial resistance is a threat to the prevention and treatment of a wide-range of infections. Antimicrobial resistance occurs when the bacteria, fungi, parasites or viruses change over time and can no longer be killed or inactivated by the current medications and treatments available. These antimicrobial resistant microorganisms are often referred to as 'Superbugs'. Antimicrobial peptides (AMPs) are an innate part of plant and animal immune systems. AMPs are thought to be less specific than many antibiotics, in that they are effective at killing a wider range of pathogens and they show reduced antibiotic resistance. All AMPs catalogued so far have both water-loving and water-hating parts in their structure which promote self-assembly in solution. AMPs are thought to kill bacteria by disrupting their membranes. In this thesis I investigate the AMP pexiganan, a synthetically developed peptide, which has performed promisingly in clinical trials. The current popular model of AMP action, as investigated by *in-vitro* studies, is that the peptides assemble to form a pore (a hole) in the bacterial membrane, through this pore the contents of cell leak out resulting in bacterial death. This has only been observed in oversimplified models in which the membrane mimetic is assembled in the presence of pexiganan.

The main constituents of membranes of living cells are lipids. Lipids have a hydrophobic (water-hating) part and a hydrophilic (water-loving part) that enable them to self-assemble into large-scale structures. In cell membranes they self-assemble into two-layers (a bilayer) with the hydrophobic part protected on the inside and the hydrophilic parts exposed to the outside. Biological membranes also contain proteins, complex structures composed of amino acids that are

responsible for many of the processes that enable cell survival.

I investigated the hypothesis that AMPs and other molecules could insert in the membrane and change the curvature and in doing so induce stress or tension. Bacterial membranes include native valves (gated pores) that enable the bacteria to respond to increased membrane tension (induced by osmotic stress). It is conceivable that these safety valves also serve as an Achilles heel that increases antimicrobial activity of AMPs. Explicitly that AMP interaction induces a change in membrane curvature that induces a tension that triggers gating of the pores. These pores are called mechanosensitive ion channels.

Studying membrane proteins is difficult, bacterial membranes are too complex to analyse proteins directly in bacteria. Obtaining sufficient quantities and delivering them into membrane mimetics is also challenging. This thesis addressed this in a number of ways. The protein was produced by cell free protein expression in the presence of an artificial membrane, of a spherical shape and a single phospholipid bilayer (a liposome). This meant that the protein was expressed and inserted directly into liposomes that were used to assemble other membrane mimetics.

The liposomes containing the protein, the Mechanosensitive Ion Channel of Large Conductance (MscL), were analysed using small angle scattering. Small angle scattering analysis is achieved by analysing the scattering behaviour of X-ray or neutrons after travelling through a sample and recording the scattering at small angles. It can give shape and size information of particles between 1-100 nm in size. The models fitted to the collected scattering from the protein containing liposomes, confirmed that we had expressed the MscL successfully into the liposomes.

Neutron reflectivity is well suited to analysing 2-D models for bacterial membranes at molecular length scales. Although low-resolution compared to crystallography, it does have sufficient resolution to detect thinning of membranes, in response to an increase in the lipid area per molecule (i.e. a tension). Furthermore there is sufficient contrast between proteins/lipids/peptides to be able to probe complex systems. Neutron reflectivity measures the intensity of the reflected beam compared to that of the initial beam, this intensity is dependent on the variation of scattering length density (synonymous to refractive index for light) of the material perpendicular to the interface enabling structure determination of layered systems, such as membranes.

The 2-D model membranes investigated in this thesis were assembled from liposomes. Two generic approaches were followed:

(a) Tethered bilayer Membranes were tethered to a gold surface with lipid-tethers containing a long spacer molecule, to ensure a large gap between the solid gold substrate and the bilayer. Tethered bilayers are a well established membrane mimetic approach and lend themselves well to optimisation through interfacial techniques.

(b) Suspended bilayer The constraint of the solid-support in (a) could restrict the curvature and membrane tension of the lipid bilayer. Our alternative planar lipid membrane mimic, developed in this thesis, suspends a lipid bilayer underneath a surfactant monolayer at the air-water interface.

With both of these approaches there was a need to be able to appropriately constrain the fitting of the neutron reflectivity profiles, which was achieved by using a range of complementary techniques.

By analysing the bacterial MscL protein in multiple membrane mimetics, I was able to investigate the impact of the antimicrobial peptide pexiganan on the protein and surrounding lipid membrane. My results determined that in all constructs, on insertion of pexiganan into the lipid membrane, the MscL protein underwent a large conformational change consistent with opening its pore. Permanent gating of this large pore in a bacterium's membrane would cause leakage of the cell contents and result in bacterial death. This project has provided evidence that the MscL protein could be an Achilles heel of bacteria and opens the door to further research into MscL as an antimicrobial target. The development of new 2-D model membranes in this project can also be used to investigate other membrane protein and antimicrobial peptides.

Chapter 2

Theory Chapter

2.1 Bacterial Membranes

Bacterial cell envelopes are critical to the survival of the bacteria. They maintain cell structure, function and control influx and efflux of vital ions and nutrients, as well as playing a role in the free energy cycle of the cell.[14]

All bacteria have a phospholipid-based bilayer membrane underneath a mesh of peptidoglycan. Lipids are amphiphilic molecules with hydrophobic tails and a hydrophilic head group giving them the propensity to self assemble into 3D structures. The driving force of this self-assembly is to decrease the hydrophobic interactions of the non-polar tails with the water-based surrounding medium; ultimately the hydrophobic interaction is an entropic penalty that can be traced to the tetrahedral disposition of electron density in a water molecule.[178] In bacterial membranes, the molecular geometry of the lipids involved mean that they self-assemble into locally planar bilayer structures that are the basis of a permeable (to water) barrier that is the cell membrane. Lipids coexist in multiple phases (disordered fluid and gel)within in a lipid bilayer. In the fluid phase, which is considered to be most representative of a lipid cell membrane, the acyl chains are conformationally disordered.

The most noticeable distinction between gram-positive and gram-negative bacteria, is that in the former the outer lipid membrane is replaced by a peptidoglycan layer that is thicker (30 nm) than the thin 2–7 nm layer that sits between the inner and outer membranes of a gram-negative bacterium. Examples of gram

negative bacteria include *Escherichia coli* and *Pseudomonas aeruginosa*.

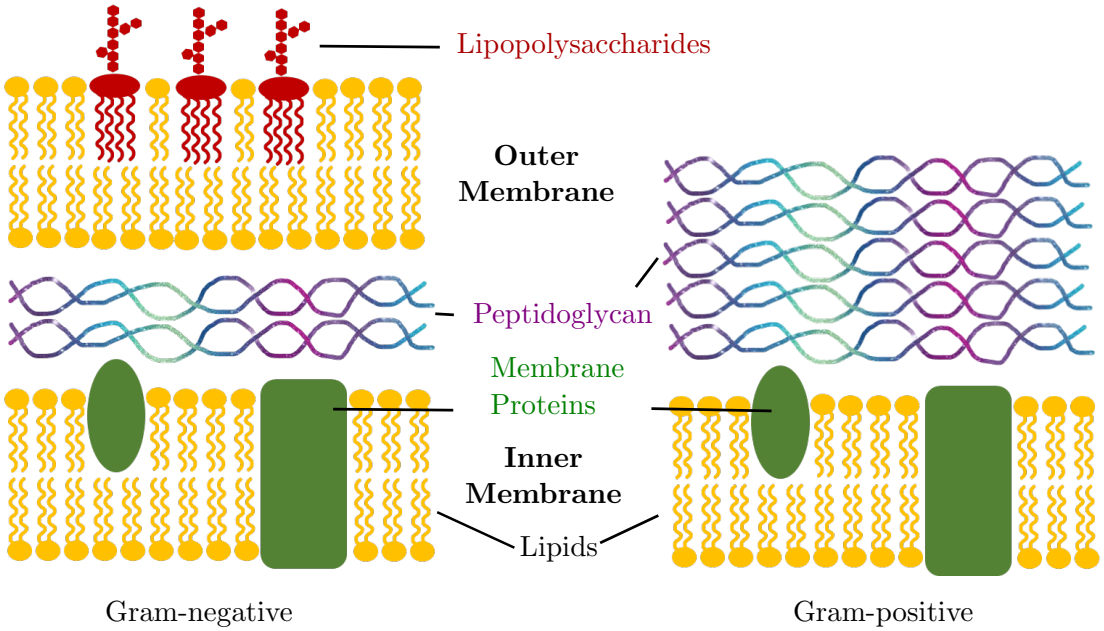

Figure 2.1 *Gram–negative and Gram–positive Bacterial Membrane Diagrams.*

Figure 2.1 shows the structure of a gram negative and gram-positive cell envelopes. The diagram on the left of the gram-negative cell envelope, indicates the two bilayer membranes separated by a thin peptidoglycan mesh. The diagram on the right depicts the gram-positive cell envelope with the much thicker peptidoglycan mesh or cell wall. Peptidoglycan is a polysaccharide chain with peptide crosslinks, the covalently bound mesh network is the largest macromolecule found in nature. The rigidity of the peptidoglycan layer determines the cell shape and also acts as a flexible surface to support the bilayer membranes.[24] Given that that bending rigidity scales with thickness, the gram-postive peptidoglycan layer will be stiffer than the layer in gram-negative cell envelopes.

The inner membrane, often referred to as the cytoplasmic membrane, is a bilayer composed mostly of phosphatidylethanolamine (PE) and phosphatidylglycerol (PG) lipids and membrane proteins. Specifically in *E. coli* the lipid composition is roughly 75% PE and 25% PG. The inner membrane incorporates many proteins essential for cell functionality and survival.

The fluid mosaic model of membrane structure was proposed in 1972 by Singer and Nicholson, which described a layer comprising mostly of lipids and some transmembrane proteins.[207] This remained the standard description until Engelman suggested that membranes were more mosaic than fluid with high

disorder, membrane patches and a high proportion of the membrane composed of protein.[59] This model is supported by Lillemeir who proposed that membranes can have large protein free regions and protein rich regions and also supported by Goodsell who proposed that bacterial membranes are composed of $\sim$ 50% membrane protein and are very crowded.[55, 72, 130]

2.2 Mechanosensitive Ion Channels: Bacterial Safety Valves

Cells can respond to a variety of mechanical stimuli. The cell membrane is subject to external mechanical forces, to which it must respond to ensure cell survival. Mechanosensitive (MS) ion channels convert mechanical stimuli such as in-plane expansion or membrane tension into biophysical, biochemical or electrical signals.[66]

The most extensively studied MS channels are MscL (The Mechnosensitive Ion Channel of Large Conductance) and MscS (The Mechanosensitive Ion Channel of Small Conductance) both found in prokaryotes.[129, 219] MscL and MscS act as emergency release valves for bacteria when subject to osmotic stress. In the absence of a means to release this pressure, the cells would lyse. MscL and MscS act as emergency release valves by responding to the change in tension in the membrane, and in response opening pores allowing cytoplasmic solution to be jettisoned from the cell, reducing the pressure. *E. coli* mutants with no MscS or MscL channel proteins die when they are transferred from a medium of high osmolarity to a low osmolarity.[26, 129]

MscL and MscS channels were initially characterised with patch clamp experiments, sequenced and the crystal structures determined.[13, 31, 120, 219] Both MscL and MscS have large conductances and pore sizes in comparison to eukaryotic MS channels. The two channels belong to distinctly different families of proteins. Many variations of MscS channels exist in bacteria, fungi and plants and some plants even encode multiple variations of MscS channels within their genome.[87] MscL on the other hand is highly conserved in bacteria and plants.[156] The threshold on the membrane tension required for gating of MscS channels is lower, at about 6 mN m^{-1}, than the threshold for MscL channels at 12 mN m^{-1}.[166, 215, 216] The lower threshold of MscS protein channels,

and its greater variation in pore size has solidified it's role as a non-emergency release valve, enabling it to control the pressure of the bacteria without large loss of solutes.[129] MscL protein channels are viewed as providing a response of last resort to larger changes in osmolarity and only gate at pressures just below pressures that would compromise cell integrity.[28]

2.3 The Mechanosensitive Ion Channel of Large Conductance

The Mechanosensitive Ion Channel of Large Conductance (MscL) is crucial to the survival of bacteria as it provides protection against osmotic shock.[144] The crystal structure of the MscL homolog from *Mycobacterium tuberculosis* was determined in 1998.[31] Knowledge of the crystal structure aided research groups to make further studies into the function and behaviour of the mechanosensitve ion channel.[142, 176] In response to osmotic shock, MscL opens up a central water-filled hole in the membrane of 30 Å diameter.[143, 175] Changes in membrane potential and insertion of amphiphilic molecules into the membrane also cause the channel to open.[143, 155, 175]

The MscL protein is a homopentamer. Each monomer consists of two transmembrane helices; TM1 lines the pore whilst TM2 interacts with the lipid bilayer and is connected to a coiled helical bundle with a c-terminus, as shown in Figure 2.2. The TM1 helix is connected to the n-terminal helix through a glycine hinge. During gating of the channel, the channel undergoes large in-plane expansion as depicted in Figure 2.2. Fluorescence Resonance Energy Transfer (FRET) measurements revealed the pore size to be 28 Å in diameter, [47] in close agreement with electrophysiological experiments (30 Å).[49]

During the expansion of the MscL pore the TM1 helix tilts in response to membrane tension. Experiments with a range of MscL constructs and deletions have shown the n-terminal helix to be crucial in induced gating of the MscL-channel by coupling the channel to the membrane. The n-terminus is well-conserved in nature and molecular dynamics simulations have shown the channel to be significantly less sensitive when the n-terminus is deleted.[15] The c-terminus is at the end of the protrusion from the membrane-spanning part of the channel, which the crystal structure suggests extends 35 Å into the cytoplasm.[31]

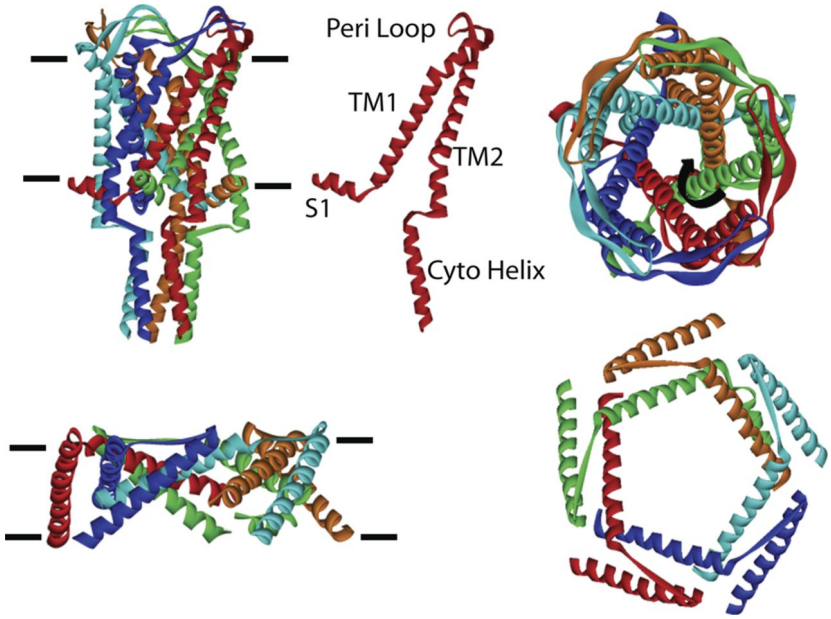

Figure 2.2 *Models of the MscL channel. Top panel depicts the crystal structure for MscL, as observed across the plane of the membrane, with approximate locations of the membrane depicted as horizontal lines (left) or from the periplasmic side of the membrane (right). A single subunit is shown in the centre. The bottom panels show the model for the open structure ignoring the c-terminal domain. Note the tilting of the domains within the membrane and the thinning of the membrane itself. Figure reproduced with permission from [25].*

2.4 Antimicrobials

2.4.1 Antimicrobial Resistance

In 2014 the World Health Organisation, WHO, released a statement that "without urgent, coordinated action, the world is headed for a post-antibiotic era, in which infections and minor injuries which have been treatable for decades can once again kill".[170] Society has increasingly become aware of the dangers of antibiotic resistance with 'Superbugs', bacteria resistant to common antibiotics, becoming more prevalent in hospitals.[186] Antibiotic resistance is a naturally occurring genetic process that plays a role in bacterial survival, however, it is becoming an issue due to overuse and misuse of antibiotics.[163] Uncontrolled increases in resistance could result in an increase in deaths from simple bacterial infections. Commonly used antibiotics target specific biological pathways and therefore are only effective against a small range of pathogens.

2.4.2 Antimicrobial Peptides

Antimicrobial peptides (AMPs) are an innate part of plant and animal immune systems for fighting off bacterial infection. AMPs are short peptides generally 12-50 amino acid residues in length, produced by plants and animals for defense against bacteria. With increasing concern over antibiotic resistance, research is growing into AMPs as a way to augment treatment by traditional antibiotics. There is some expectation that the lower specificity of AMPs compared to traditional antibiotics could reduce the ability of bacteria to become resistant to AMP based treatments.[177] It is important to note that bacteria have been shown to become resistant to certain AMPs, however increasing our understanding of their mechanism could result in development and identification of drugs with low resistance rates.[114]

The predominantly anionic lipid bilayer bacterial membrane is thought to be the target of the cationic AMPs.[98] The role of charge in the interaction confers selectivity towards bacteria rather than eukaryotic membranes, which contain a lower fraction of anionic lipids.

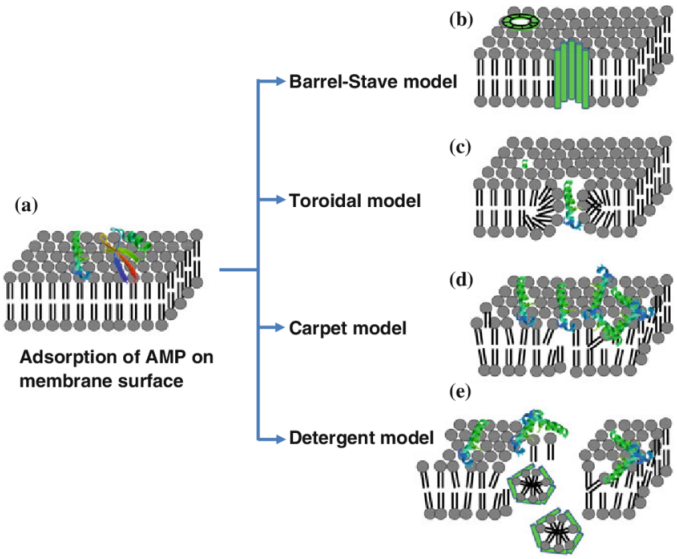

Figure 2.3 *Models of membrane permeabilization by antimicrobial peptides. Image reproduced with permission from [74].*

Research into AMPs has focused on peptide discovery and characterisation of the mechanism by which peptides target and destabilise membranes. The current dogma focusses on the way in which AMPs permeabilise the membrane by pore formation. Popular models are the toroidal pore model,[136] the barrel stave model[88] and the carpet model,[61] the last of which describes destabilisation

of the membrane without the need for pore formation. Part of the drive of this thesis is to provide structural evidence that peptides do not need to form their own pores to cause membrane leakage, but could activate the innate membrane protein pores.

2.4.3 Pexiganan

Pexiganan is a synthetic derivative of the naturally occurring peptide Manganin 2, extracted from the skin of the African clawed frog.[247][35] Pexiganan was submitted for clinical trials at a treatment for foot ulcers, but was denied approval in 1999 after phase III trials revealed that it was only as effective as the current treatment. Pexiganan is still being considered in other antimicrobial drug formulations.[71] Given the relative clinical success of pexiganan compared to other antimicrobial peptides, it has been widely used as an archetype for short-chained cationic AMPs.[73]

Pexiganan is a single chain peptide of 22 amino acid residues and forms an amphipathic helix on interaction with membranes. The 2-D structure of pexiganan is shown in Figure 2.4.

NMR, Raman and fluorescence analysis of pexiganan action suggest the toroidal pore model.[241][146][92] However, in these studies the toroidal pore is only observed at high membrane coverage of the peptide. The pexiganan concentration within the membrane needs to be high, roughly 1-5 mol% for the peptide to self assemble into a toroidal pore conformation. At 10 mol%, pexiganan creates a hexagonal phase in the lipid bilayer.[81] The naphthalene procedure, the method of preparation of the lipid membranes used to assess toroidal pore formation by ^{31}P NMR, involved preparing a solution of lipid and pexiganan to the desired mol% in chloroform, methanol and napthalene and drying on glass slides and sealing for 1-2 days before measurement. The preparation procedure is not analogous to pexiganan interaction with bacterial membranes and allows a significant time period in which the pexiganan can self-assemble into complex architectures. The potency of the peptide, with a minimum inhibitory concentration of 1.6 µM also suggests that cell death would occur before toroidal pore formation.[64] The minimum inhibitory concentration of pexiganan is not clearly defined as it is dependent on cell density, salt concentration and media composition.[114] However, by working with 1.6 µM pexiganan concentrations, our work is more comparable to *in-vivo* studies.[64, 114]

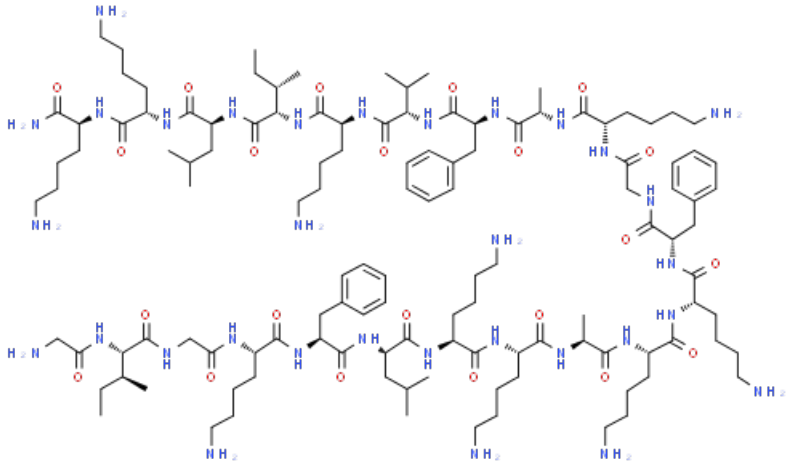

Figure 2.4 *Chemical structure of the antimicrobial peptide pexiganan (MS1-78).[34]*

Membrane thinning has been suggested to play a critical role in the mechanism of AMP behaviour for similar helical peptides.[135] Atomic force microscopy measurements by Mecke et al. provided evidence that pexiganan causes thinning of supported 1,2–dimyristoyl-sn-glycero-3-phosphocholine, DMPC, bilayers of 11 Å (±2 Å).[150] L. McKinley showed that insertion of pexiganan into a POPC:POPG monolayer increases the area per lipid from 58 $Å^2$ to 77 $Å^2$.[149] It is possible that this membrane thinning effect which is observed at concentrations closer to the minimum inhibitory concentration of pexiganan, could result in a increase in membrane permeability of the membrane resulting in cell death.

Depolarisation of the cytoplasmic membrane potential has been proposed as a general mechanism for antimicrobial behaviour of AMPs. The increased permeability that accompanies an increase in the AMP allows for an increase in the non-selective transport of ions across the membrane, decreasing the cell membrane potential. Since the membrane potential plays a role in the free energy cycle of the bacterial cells, dissipation will not be favourable for the survival of the bacterium.[60, 224]

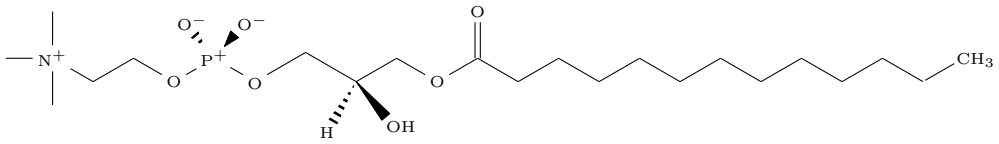

Figure 2.5 *Chemical structure of 16:0 lysophosphatidylcholine (16:0 lyso-PC).*

It is important to note that all of the bacterial membrane models used to date to study the mechanism of pexiganan antimicrobial behaviour have comprised only of lipids.

2.4.4 Antimicrobial Surfactants

As well as investigating antimicrobial peptides, the interaction of an antimicrobial surfactant, specifically lyso-PC with bacterial membranes was also investigated. Using soap and water to remove pathogens from your hands is a well known practice, perhaps even more so in the current period of the 2019-2020 coronavirus pandemic.[180, 229] Whilst it is common public knowledge that the surfactants in the soap remove pathogens from your skin, cleaning it, it is less well known that surfactants kill pathogens. They are thought to act by destabilising the lipid membranes found in bacteria and some viruses. The research into how different surfactants permeabilise and destabilise phospholipid membranes is ongoing.[8, 33] Designing surfactants and surfactant formulations with high bacteriocidal activity that do not irritate skin is a considerable challenge.[1, 84, 118]

LysoPhosphatidylcholines (lyso-PC) are single tailed lipids found in nature. For single-chained lipids such as lyso-PC, the effective head group area is larger the ratio of the volume of the tail, to its length, so in the framework of the Israelachvili packing parameter [108] it can be viewed as a cone-shaped molecule (packing parameter $< \frac{1}{3}$) that will induce a positive curvature on insertion into a bilayer of double-chained lipids, each of which can be regarded as having a cylindrical molecular geometry (packing parameter ~ 1).

Lyso-PC is found in many types of milk at concentrations that results in bactericidal activity.[211] Lyso-PC has since been shown to have antimicrobial effects on a range of problematic bacteria including Methicillin-resistant *Staphylococcus aureus* (MRSA).[154, 190, 210] Feeding honeybees a low concentration of lyso-PC was shown to provide them defence against American foulbrood infection.[190] As well as displaying its own antimicrobial behaviour it has been shown to increase

the efficacy of antimicrobial peptides.[128]

2.5 Techniques

2.5.1 Model Membranes

Models of bacterial membranes play a key role in the investigation of the structure and function of membrane proteins, as well as the interaction of antibiotics with membranes.

Simple model membranes are generally composed of a mixture of phospholipids. These lipids are abbreviated by four letter acronyms with the first two letters referring to the acyl chain and the last two refer to the phospholipid headgroup. A table of the abbreviations of the lipids used in this thesis are shown in Table 2.1. The tail shorthand represents the number of carbon atoms in each tail of the lipid and the number of double bonds. For example 16:0 18:1, indicates one 16 carbon atom chain with no double bonds and one 18 carbon atom chain with a single double bond. Figure 2.6 displays the chemical structures of the lipids used in this thesis.

Table 2.1 *Lipid shorthands and abbreviations of lipids used in this thesis.*

abbreviation	full name	tail shorthand
POPC	1-palmitoyl-2-oleoyl-sn-glycero-3-phosphocholine	16:0 18:1
POPG	1-palmitoyl-2-oleoyl-sn-glycero-3-phospho-rac-1-glycerol	16:0 18:1
DSPE	1,2-distaeroyl-sn-glycero-3-phosphorylethanolamine	18:0 18:0

All lipids are amphiphiles, composed of hydrophilic head groups and hydrophobic tail regions. This allows for self-assembly of lipid molecules into large scale structures in solution, so that the hydrophobic tail regions can be separated from the aqueous environment.

2.5.1.1 Liposomes

Liposomes (also referred to as vesicles) are well-established as a model membrane system. Vesicles are self-assembled spherical bilayer structures between 10 and 1000 nm in diameter. In an aqueous environment, the polar head groups sit at

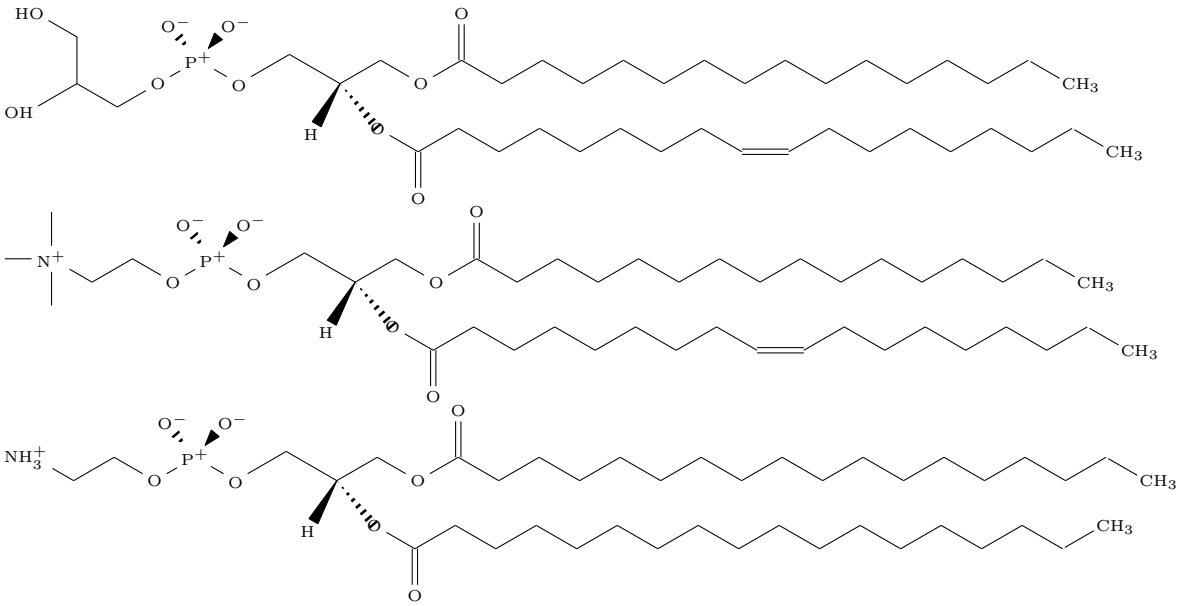

Figure 2.6 *Chemical structure of POPG and POPC and DSPE from top to bottom.*

the interface between the acyl chains and water. A bilayer is a two molecule thick layer with hydrophilic head groups either side of the bilayer, with the hydrophobic tails protected from unfavorable interactions with the surrounding solution in the middle of the bilayer. The planar bilayer closes up to form a spherical shell, a liposome, to eliminate edge effects that would otherwise result in an unfavourable interaction between hydrophobic acyl chains and water. Vesicles are widely used in research, for example to encapsulate drugs and dyes.[58] Vesicles offer a relatively straightforward approach to incorporate membrane proteins either through reconstitution or direct cell-free protein expression techniques.[2, 191] Vesicles are prepared through a number of techniques, making them an accessible platform to be used to compare drug interactions or protein stability. The caveat of using vesicles as model membranes is that the molecular packing of the lipids cannot be controlled, and the curvature of the membrane is greater than is typical for a bacterium ($R_c^{liposome}$ = 50-100 nm $R_c^{spherocylindricalbacterium}$ = 500 nm).

2.5.1.2 Monolayers and Supported Bilayers

A monolayer is a single assembled layer of lipids that can self-assemble at the air-water or oil-water interface. A monolayer represents a simple and accessible membrane mimic, but with the obvious disadvantage that it only includes a single lipid leaflet. This restricts its application, particularly where membrane-

spanning proteins are to be studied. By using a suitably designed trough, the packing of lipid molecules can be controlled. Monolayers have been used heavily in the analysis of antimicrobial peptides and interaction with membrane-associating proteins.[27, 39, 68, 233]

Monolayers cannot be used to analyse transmembrane proteins but they do however represent an appropriate model for studies in which it is at least anticipated that the interaction might principally be with a single lipid leaflet, such as carpet forming AMPs and membrane-associating proteins. [149] There is also a case to argue that they cannot give a full picture of the behaviour of antimicrobial peptides. Due to a monolayer being a single-leaflet opposed to a bilayer, the model does not allow for an accurate model of insertion behaviour.

Supported bilayers have also been extensively used in membrane biophysics research. Supported bilayers are lipid bilayers formed on a solid support, commonly silicon or quartz. Such bilayers have the advantage of providing a suitable sample for a range of interfacial science techniques including atomic force microscopy, attenuated total reflection infrared spectroscopy (ATR-IR), quartz crystal microbalance with dissipation (QCM-D) and neutron reflectivity.

Several strategies for forming supported bilayers exist and have been thoroughly reviewed.[29, 183, 197, 213] The main approaches to supported bilayer formation are the Langmuir-Blodgett technique[230] or vesicle deposition.[18] Langmuir-Blodgett (LB) deposition involves first spreading a single monolayer of lipid and compressing it to the desired phase and area per molecule using a movable barrier. The monolayer is then transferred to a solid substrate by moving a solid-substrate through the sub-phase.[21] A further monolayer can then be spread over the support using the Langmuir-Schaefer technique. Formation of suspended bilayers by liposome deposition doesn't require specialist equipment but liposome and buffer conditions need to be optimised to achieve full coverage of the interface.[132, 189] Both techniques can form close-packed bilayers that are stable for many hours, enabling analysis measurements.

When investigating trans-membrane proteins there is cause for concern that the solid support might interfere with the insertion of the molecule. Lipid membranes can also have a strong van der Waals attraction to the solid surface restricting the bilayer fluctuations and influencing lipid phase behaviour.[67]

2.5.1.3 Tethered and Floating Bilayers

To overcome this disadvantage of solid-supported bilayer having an insufficient space between the bilayer and the substrate for incorporation of membrane proteins, tethered and floating bilayer approaches have been developed. In both of these approaches there is a fluid layer (of thickness 3-30 nm between bilayer and the underlying solid-substrate.

In the case of the tethered bilayer the fluid layer is aqueous buffer, whereas in the tethered and polymer-supported case it is a polymer brush-like layer. The presence of a fluid layer between the bilayer and the solid substrate allows for the bilayer to retain dynamic properties such as lipid exchange between leaflets.[205]

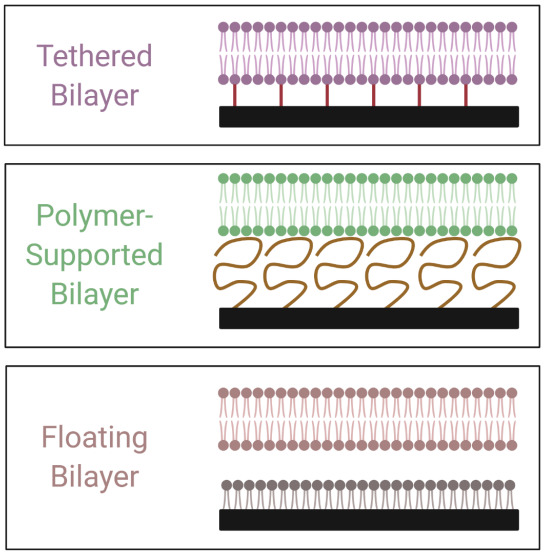

Figure 2.7 *Cartoon diagram depictions of example tethered, polymer-supported and floating bilayers. Image created with biorender.com.*

Tethered bilayers make use of a tether, a molecule covalently bound to a solid substrate at one end with the other end either inserting into the hydrophobic centre of the lipid bilayer or covalently binding to a membrane protein.[100, 111]

Protein-tethered lipid bilayers are prepared by functionalising a solid surface with linker molecules followed by His-tagged protein stabilised in detergent. The His-tag binds with the linker molecule. Then the detergent is replaced with lipids with a slow detergent to lipid exchange until a bilayer is formed around the tethered proteins.[69] This technique allows a greater control over the protein to

lipid composition of the formed bilayer. The method does require a large volume of detergent stabilised protein and of lipid so that a thorough detergent to lipid exchange can be carried out. The protein needs to be stable in both the detergent and the lipid environment to ensure it retains functionality within the membrane mimic and the presence of the tether should not hinder the protein functionality. This method is not suitable for all proteins and studies have shown that the length of the tether used can affect protein clustering.[182]

Formation of lipid-tethered bilayers relies on the tethering of a monolayer or partial layer of lipids to solid-surfaces. Initial membrane mimetics used gold surfaces due to the easy ability to form dense alkane-thiol linkages.[179] The bilayer is then formed by vesicle rupture or by incubating the surface with high concentrations of lipids. Depending on the length and density of the lipid tether, the membrane properties such as fluidity, curvature, and stability can be affected.

Polymer–supported or polymer–cushioned bilayers allow for less constrained lipid bilayers, although this comes with lower stabilty. Polymer layers are first assembled on the solid substrate before formation of the lipid bilayer, typically by vesicle rupture or Langmuir-Blodgett deposition. [223, 242] Polymer-cushions were designed as a lubricating layer between the substrate and bilayer, which should allow for sufficient exchange of lipids to allow self-healing and removal of local defects, as well as allowing for protein of large transmembrane domains to be investigated without contact with the solid substrate. The poor stability and high roughness of these systems has resulted in them being applied less than the other model systems.

The floating bilayer overcomes many of the issues with the other mimics. Such systems are formed by performing Langmuir-Blodgett deposition followed by Langmuir-Shafer deposition onto a Self-Assembled Monolayer (SAM)-functionalized solid substrate. They have been shown to form with a sufficient gap (greater than 5 Å) between the monolayer and bilayer.[101] The water gap, or the steric repulsions associated with the monolayer undulations, provides a repulsion that 'cushions' the bilayer by softening the attractive van der Waals interaction. This provides the deposited bilayer greater translational freedom closer to that of a natural biomembrane. The bilayer sits close enough to the surface to enable surface-characterisation but is floating about 30 Å from the surface. Recent literature have shown an improvement in the stability of these systems.[45]

2.5.2 Neutron and X-ray Scattering

In this PhD, extensive studies have been carried out using neutron and X-ray scattering, both small angle scattering (SAS) and reflectometry. The theory of neutron scattering parallels that of light and X-ray scattering. The size of the wavelengths determines the size of the scattering objects that can be observed.

A brief introduction into scattering theory and instrumentation will be given here, but more thorough theoretical foundations can be found in *Elementary Scattering Theory* by D.S.Sivia and *Polymers and Neutron Scattering* by J.S.Higgins and H.C.Benoit.[91, 208] A more in depth guide to instrumentation and experiment planning for biological systems has been written by Clifton *et al.*.[44] Here the theory will be framed in the context of neutron scattering, but the underlying physics is essentially the same for X-ray scattering, with the distinction being that neutrons are scattered by atomic nuclei, whereas X-rays are scattered by the electrons. It is variations in neutron scattering length density and electron density that respectively provide the inhomogeneities from which neutrons and X-rays scatter.

2.5.3 Neutron Scattering Theory

The neutron is a spin–half sub–atomic particle that exhibits wave–particle duality. The neutron wavelength is well suited to investigating the structure (and dynamics) of biological large-scale structures with resolution of 1 Å and penetration depth of up to 1000 Å.[196]

Neutrons in a collimated beam with initial wave vector $\mathbf{k}_i$ and a scattered wave vector $\mathbf{k}_s$ undergo a momentum transfer:

$$\mathbf{Q} = \mathbf{k}_s - \mathbf{k}_i. \tag{2.1}$$

Neutrons interact with materials through nuclear interactions with the atomic nuclei. The scattering associated with a sample, more specifically its coherent cross section ($\frac{d\sigma_{coh}}{d\Omega}$), has a spatial distribution associated with the distribution of

atoms in that sample,

$$\frac{d\sigma_{coh}}{d\Omega} = \sum_{i,j} b_i b_j exp[i\mathbf{Q}.(\mathbf{r}_i - \mathbf{r}_j)] \tag{2.2}$$

where Ω refers to the angle. The sum is for all pairs of atoms i,j with scattering length $b_{i,j}$ with position $\mathbf{r}_{i,j}$.

In an experiment, the differential coherent cross-section is measured as a function of the scattering angle 2θ. The magnitude of the scattering vector Q is:

$$Q = \frac{4\pi}{\lambda} \sin\theta \tag{2.3}$$

where 2θ is the angle of scattering and λ is the neutron wavelength.

The scattering length density, $\rho(z)$ is given as a function of the number of nuclei in a given density and the chemical composition of the material:

$$\rho(z) = \sum N_i(z) b_i, \tag{2.4}$$

where $N_i(z)$ is the atomic length density of the constituent atoms and b_i is their coherent scattering length.

The difference between two media can be described by the difference in scattering length densities $\Delta\rho$ in terms of the magnitude of the critical scattering vector Q_c by

$$Q_c = \sqrt{16\pi\Delta\rho}. \tag{2.5}$$

An advantage of neutron scattering comes from the large contrast in coherent scattering lengths between hydrogen and deuterium, -0.3742$\times$ 10^{-4} Å and 0.6671$\times$ 10^{-4} Å respectively. A distinct advantage over X-ray scattering, is that the scattering length varies non-monoatomically across the periodic table i.e. does not increase with atomic number. This enables smaller atoms such as hydrogen and deuterium to be identified. In order to distinguish the structure of interest from the surrounding solution two methods are used: either variation in deuteration of the surrounding water or selective deuteration of the molecule of interest. The first is commonly referred to as the contrast variation method

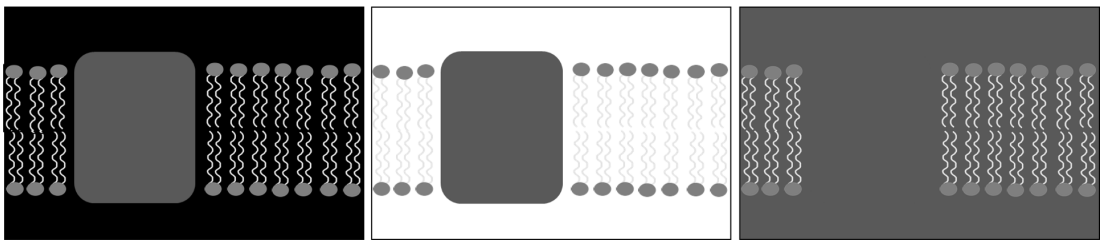

Figure 2.8 *Diagram depicting a protein containing lipid bilayer in different solution contrasts to depict the effect of contrast-matching.*

and the second as selective deuteration. The second is more costly and time-consuming however enables more distinction to be made between individual sections of the structure such as protein domains. Often the case is that both of these methods are used to enable a large number of different contrasts.

Figure 2.8 highlights the variation in scattering length density (SLD) contrasts when a protein containing bilayer is measured in multiple solution contrasts of varying H_2O and D_2O composition. In this depiction the change from light to dark depicts an increase in SLD, such that black represents the SLD of D_2O and white the SLD of H_2O, and grey the SLD intermediate H_2O/D_2O compositions

Depending on the solution contrast the sample is measured in, the different components in the structure make differently weighted compositions to the measured scattering. In H_2O solution (SLD $= -0.56 \times 10^{-6}$ Å^{-2}), the lipid tails have a similarly low SLD ($\sim -0.4 \times 10^{-6}$ Å^{-2}) and therefore contribute little to the collected scattered intensity. Whereas the protein has a higher SLD ($\sim 2.7 \times 10^{-6}$ Å^{-2}) so does contribute to the scattering in this contrast.

The percentage of H_2O and D_2O can be controlled to completely contrast-match a component in the system. By using 55% H_2O and 45% D_2O mixture, the SLD of the solution and protein can be matched ($\sim 2.7 \times 10^{-6}$ Å^{-2}), so that the protein does not contribute to the scattering in this contrast, only the lipids. In 100% D_2O (6.35×10^{-6}Å^{-2}) both the protein and lipids have a different SLD to the solution and so will have different scattering contributions to the collected scattering. By analysing multiple solution contrasts in unison the contribution of each component of the system can be ascertained and the structure extrapolated. It is important to note that some molecules with exchangeable hydrogens, such as proteins, have a different SLD depending on the D_2O composition which needs to be calculated.

2.5.4 Small Angle Scattering

The set-up of a small angle scattering experiment is relatively simple, the sample is placed in the path of the collimated beam and the scattered neutrons or X-rays are recorded on an area detector.

Small angle scattering (SAS) is when the objects are large compared to the scattering wavelengths used. Low Q probes long distances in the sample and high Q probes short distances and correlations. Size, shape and interaction of particles can be determined from SAS.

The intensity $I(\mathbf{Q})$ is the absolute scattering cross section $\frac{(\delta\Sigma\mathbf{Q})}{(\delta\Omega)}$ in units of cm^{-1}. It is the probability of a neutron (or X-ray) at wavelength λ being scattered per unit angle at that $\mathbf{Q}$.

$$I(\mathbf{R},\lambda) = I_0(\lambda)\frac{(\delta\Sigma\mathbf{Q})}{(\delta\Omega)}\Delta\Omega(\mathbf{R})tT(\lambda)\eta(\lambda) \tag{2.6}$$

where $\Delta\Omega$ is the solid angle, t = sample thickness and T = sample transmission and $\eta(\lambda)$ is the detector efficiency. Most of these terms are instrument dependent other than the absolute scattering cross section $\frac{(\delta\Sigma\mathbf{Q})}{(\delta\Omega)}$. The absolute scattering cross section is a sum of the coherent, incoherent and absorption cross sections:

$$\frac{(\delta\Sigma\mathbf{Q})}{(\delta\Omega)} = \frac{d\Sigma_{coh}}{d\Omega} + \frac{d\Sigma_{incoh}}{d\Omega} + \frac{d\Sigma_{abs}}{d\Omega}. \tag{2.7}$$

The coherent cross section, $\frac{d\Sigma_{coh}}{d\Omega}$ contains information of the distribution of particles in the sample, the incoherent cross section $\frac{d\Sigma_{incoh}}{d\Omega}$ is independent of Q and raises the background signal. The absorption cross section, $\frac{d\Sigma_{abs}}{d\Omega}$, is small and lowers the overall detected scattering.

An object/solution will exhibit both elastic and inelastic scattering interactions. For our small angle neutron scattering measurements inelastic scattering is a nuisance parameter which is limited by experimental design. Since Hydrogen has a much stronger inelastic scattering cross section than Deuterium, using a deuterated solvent (i.e. a D_2O buffer) reduces the amount of inelastic scattering and decreases the background noise.

2.5.5 Neutron Reflectivity

Specular neutron reflectivity is a special case of neutron scattering, where the angle of incidence is equal to the angle of reflection. The reflectivity measured depends on the gradient of the scattering length density profile, projected onto the axis perpendicular to the interface.[91, 208]

Reflectivity experiments are used to study layered materials. For this reason, neutron reflectivity is a powerful technique for studying model lipid bilayer-based systems. The variation in chemical composition and hence scattering length density between the polar head groups and the acyl chains, mean that it is natural to describe the bilayer in terms of multiple layers (heads-tails-heads), of thicknesses $\sim$ wavelength of neutrons, and hence significant interference effects are present in the reflectivity profiles. This means that the reflectivity profiles encode a significant amount of structural information about the bilayer (i.e. thickness, packing density). However, because we measure the reflected intensity, the data suffers from the phase problem that is common to all scattering based techniques. For this reason, although in the kinematic limit, the reflectivity can be formulated as a Fourier Transform of the gradient of the SLD profile, it is not generally possible to directly invert the measured reflectivity to a structure.

The refractive index is defined as:

$$n = 1 - \frac{\lambda \rho_i}{2\pi}, \tag{2.8}$$

where λ is the neutron wavelength and ρ_i is the scattering length density of medium i.

Figure 2.9 shows the reflectivity profiles measured in Chapter 3 measured for neutrons incident from air on D_2O, protein-matched water (PMW), H_2O interfaces. Equation 2.8 indicates that the refractive index for D_2O will be slightly less than 1 (refractive index of air) and hence one should expect a total external reflection that is analogous to the total internal reflection observed for light propagating along a fibre optic. As the difference in the refractive indices of the air and the water sub-phase narrows, a fraction of the neutrons penetrate the interface and thus for scattering vectors $Q > Q_c$ the reflectivity falls below 1. For a sharp interface the variation in reflectivity with scattering vector is given

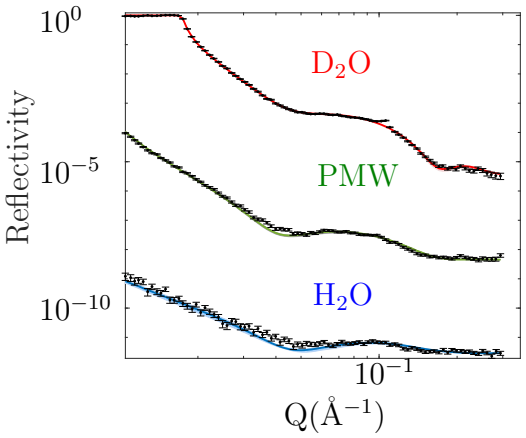

Figure 2.9 *Neutron reflectivity data measured in three solution contrasts of D_2O, protein-matched water and H_2O from a suspended bilayer construct, data analysed fully in Chapter 3.*

by the Fresnel reflectivity, which gives rise to the $R(Q) \sim Q^{-4}$ dependence,

$$R(Q) = \frac{16\pi\Delta\rho^2}{Q^4}. \tag{2.9}$$

This occurs from reflection from a single smooth planar interface. Even the air-water interface is not completely sharp, with capillary waves introducing a roughness of ~ 3 Å.[139]

A presence of an interfacial layer between the two bulk interfaces produces Kiessig fringes in the reflectivity profile. The distance between the fringes, ΔQ in the measured measured reflectivity profile gives the thickness of the film:

$$d = \frac{2\pi}{\Delta Q}. \tag{2.10}$$

In the case of multiple layers or more complex layer the Kiessig fringes are modulated. Roughness of interfacial layers also impacts the measured reflectivity profile and at high roughnesses will smear the reflectivity profile, resulting is less defined Kiessig fringes.

The interpretation of neutron scattering data is model dependent. It is not possible to directly determine the structure from the scattering due to the phase-rule. The scattering measurements therefore needs to be fitted against models of the system which requires some pre-knowledge of the system under investigation.

2.5.6 A note on X-ray Reflectivity

X-ray reflectivity is a very similar technique to neutron reflectivity and the theory is synonymous. Since X-rays interact with the electron-shell of an atom, instead of measuring the variation in SLD across an interface, X-ray reflectivity measures the difference in electron density across an interface. Given that the scattering is from the electron shell of atoms, the scattering cross-section of atoms increases with their periodicity. This means X-ray reflectivity can be used to provide an additional contrast for studying membranes at interfaces. X-ray synchotron experiments are higher flux, meaning higher resolution scattering and better statistics. X-ray experiments can be crucial to assembling the whole picture.

2.5.7 Data Analysis of Reflectivity Measurements

The reflectivity data collected in this thesis was analysed using the Matlab Rascal procedure [99], which calculates the reflectivity for trial stuctures using an approach based on Parratt's recursive formula.[174] Custom models were constructed to simulate the scattering profiles, by modelling contributions from components of the interface to a scattering length density profile normal to the surface.

Each model structure is represented by layers arranged perpendicular to the interface. Each layer has a uniform scattering length density over its thickness, and the Névot-Croce approach is used to describe the roughness between adjacent layers.[164] The SLDs are calculated from the sum of the nuclear component scattering lengths and molecular volumes, using literature confirmed values where possible.[9] The lipid bilayers were fitted by area per molecule and associated water. This approach previously described in detail by Hughes *et al.* , allowed for linking of head and tail group parameters to ensure consistent number density.[100]

The comparison between the calculated and measured reflectivity profiles is made by calculating a χ^2 value. In model fitting the model parameters are changed to minimise the χ^2 value. The model parameters are constrained by the prior probability distribution to ensure that only models describing physically and biologically realistic models are sampled in the fitting procedures. A differential evolution search strategy is used to explore the χ^2 hypersurface, reducing the

chance that the search becomes trapped in a local minimum, as can be the case with downhill methods such as the Simplex method.[134]

Once the model fit is optimised, Markov Chain Monte Carlo (MCMC) error estimation can be undertaken using RasCALs Bayesian Error estimation routines. Monte Carlo simulates a large number of fake datasets and finds the best fit parameters, the range of parameters fitted to these fake data experiments is then a reasonable approximation to the underlying error of the best fit parameters. Monte Carlo is a technique for randomly sampling a probability distribution and approximating a desired quantity. Markov Chain is a systematic method of generating a sequence of random variables where the current value is probabilistically dependent on the value of prior variables. Markov Chain Monte Carlo (MCMC) is for performing inference for probability distributions where independent samples from the distribution cannot be drawn, and is needed for high dimensionality probability distributions. In the case of creating the posterior probability distribution of our model fitting parameters, our parameters are not isolated from each other and therefore cannot be treated independently.

2.5.8 Bayesian Analysis/MCMC error estimation

Bayesian model selection compares the posterior probability distributions of two models given a dataset D. The posterior probability of a given model H, can be determined from Bayes theorem.

$$\mathbb{P}(H \mid D) = \frac{\mathbb{P}(D \mid H)\mathbb{P}(H)}{\mathbb{P}(D)} \tag{2.11}$$

where $\mathbb{P}(D \mid H)$ is the evidence of the model given the data, $\mathbb{P}(H)$ is the prior probability of the model and $\mathbb{P}(D)$ is the probability of the measured data.

The probability of the measured data is equal to the sum of the evidence of all potential models, which is potentially infinite. Since it is not possible to calculate the evidence for all possible models, the $\mathbb{P}(D)$ term is given a value of 1 and the posterior probability is determined from the evidence of the model and the prior probability of the model. Since often the prior probability of the model can not be determined, it is assumed that the prior probability of all models assessed is a uniform prior. Therefore the models are assessed primarily on the evidence of

the model given the data,

$$\mathbb{P}(H \mid D) = \mathbb{P}(D \mid H). \tag{2.12}$$

The likelihood function then takes the form

$$\mathbb{P}(D \mid H) \propto exp\left(\chi^2/2\right), \tag{2.13}$$

where χ^2 is the familiar sum of the squares of the data minus the fit over the errorbar.[209]

In Rascal, marginalised posteriors are obtained using a Delayed Rejection Adaptive Metropolis (DRAM) algorithm [80], an efficient and adaptive form of a Markov Chain Monte Carlo (MCMC) algorithm. Delayed Rejection improves the efficiency of the Monte Carlo estimators and the adaptive metropolis algorithm adapts the proposal distribution depending on the past history of the chain.[80]

The best fit parameters taken as those that maximise the marginalised posterior probability distribution functions, confidence intervals presented in this thesis are the 95% confidence intervals.

Both RasCAL and REFnx (a python based, reflectivity data fitting software) are to differing degrees rooted in a Bayesian inference framework.[100, 162] This has resulted in an increase in the statistical analysis carried out in fitting of this type of data and has the potential to greatly increase the extent to which information encoded in reflectivity data can be reliably extracted. Properly implemented, Bayesian methods allow a quantification of the significance of the parameter values that are determined.[45, 147, 148]

2.5.9 Ellipsometry

Ellipsometry measures the change in polarization of light, typically when reflected from a thin film at an interface. A polarized beam of light of known incident polarization is reflected from the sample and the polarization of the reflected beam is measured. Optical properties of the sample are then determined from the change in polarization. The reflectivity of an interface depends on the dielectric constant of the incident and reflective media. Reflectivity is expressed in real ($\Re$) and imaginary ($\Im$) parts, where the imaginary part is determined by attenuation by the media of electromagnetic waves. The polarization ellipse is characterized

by:

$$r = \Re(r) + \imath\Im(r) = \frac{r_p}{r_s}$$

Where r_p and r_s are the reflectivity of the p and s polarized light. Linearly polarised light becomes elliptically polarized on reflection from media with a complex dielectric constant.

A phase-modulated ellipsometer, such as used to make the measurements reported herein, does not measure $\Im(r)$ and $\Re(r)$ directly. Instead they measure parameters x and y:

$$x = \Re(r)\frac{2}{1 + \Re(r)^2 + \Im(r)^2},$$
$$y = \Im(r)\frac{2}{1 + \Re(r)^2 + \Im(r)^2}.$$

For p - polarized light incident at the Brewster angle (53° for air-water) both $\Re(r)$ and $x = 0$. When both $\Re(r)$ and $\Im(r)$ are small $\Re(r) = x/2$ and $\Im(r) \ = y/2$.

$$\Delta = \tan^{-1}\left(\frac{\Im(r)}{\Re(r)}\right) = \tan^{-1}\left(\frac{y}{x}\right)$$

The change in Δ at or close to the Brewster angle measures a quantity, η that is linearly proportional to the integral of the dielectric constant across an interface,

$$\eta = \int \frac{(\epsilon - \epsilon_1)(\epsilon - \epsilon_2)}{\epsilon} dz,$$

where ϵ, ϵ_1 and ϵ_2 are the dielectric constants of the surface, incident media and substrate respectively. This calculation is described as an integral due to the dielectric constant varying with height across the interface.

$$\Im(r) = \frac{\pi\sqrt{(\epsilon_1 - \epsilon_2)}}{\lambda(\epsilon_1 - \epsilon_2)}\eta$$

The dielectric constant is directly related to the refractive index as a result of the Maxwell equations.

$$\epsilon = n^2$$

Where n is the refractive index. Film thickness of a dielectric thin film can be calculated however for adsorption of layers at the liquid-air interface, simplification is not so simple.[225] Since we do not know the state of our adsorbed material i.e. whether it is a thin film (a uniform bilayer) or adsorbed vesicles

calculation of film thickness has not been estimated in this thesis. Instead the ellipsometry measurement has been used to qualitatively observe increase in material at the interface.

2.5.10 Quartz Crystal Microbalance

The Quartz Crystal Microbalance (QCM) is a technique for analysing surface phenomena at solid interfaces such a thin film formation. Several thorough articles on QCM theory and application have been written.[4, 116] QCM sensors consist of a thin quartz disc between two electrodes. The quartz is excited to oscillate at its resonance frequency by application of an alternating voltage.

QCM monitors the frequency of a freely oscillating sensor. An increase in mass at the interface results in a decrease in the frequency of oscillation. The increase in mass can be calculated from the change in frequency Δf, by the Sauerbrey equation:

$$\Delta m = -(C.\Delta f)/n, \tag{2.14}$$

where C is the mass sensitivity constant 17.7 ngHz^{-1} for a 5 MHz crystal and n= 1,3,5,7 for the overtone number. [198] The Sauerbrey equation makes several assumptions: i) that the added mass is small compared with the mass of the crystal, ii) that the mass is homogeneous with uniform density over the active area of the crystal iii) that the added mass is rigidly adsorbed.

The effective thickness, d_{eff} can then be calculated from the change in mass Δm by:

$$d_{eff} = \frac{\Delta m}{\rho_{eff}}, \tag{2.15}$$

where ρ_{eff} is the effective density.

QCM has found numerous applications in biology, electrochemistry, proteins, lipids and colloids, that often involve analysis of soft viscoelastic films. A viscoelastic film does not satisfy the assumptions underpinning the Sauerbrey

equation, dissipation, D, needs to be taken into account.[198]

$$D = \frac{E_d}{2\pi E_s}, \tag{2.16}$$

where E_d is the energy dissipated in a single cycle and E_s is the energy stored in the system.

In Quartz Crystal Microbalance with Resistance (QCM-R), the resistance of the crystal is measured by having a small resistor in the circuit and measuring the voltage. Resistance, R, can be related to dissipation, D through:

$$D = \frac{R}{2\pi f L}, \tag{2.17}$$

where f is the resonant frequency and L is the inductance. However the inductance of the system is not directly measured and if there is a residual imbalanced capacitance (such as when the crystal is overloaded) then resistance cannot be directly translated into dissipation.

A more widely used technique is Quartz Crystal Microbalance with Dissipation (QCM-D). The quartz crystal is excited to its resonance frequency for a short period. The voltage is then turned off and the frequency decay recorded as a function of time.

$$D = \frac{1}{2\pi f \tau}, \tag{2.18}$$

where τ is the decay time constant. In QCM-D both frequency and dissipation can be measured simultaneously.

When $D > 1 \times 10^{-6}$, the Sauerbrey equation is no longer valid as the layer cannot be characterised as a rigid film. Viscoelastic models exist to relate frequency and dissipation to mass and thickness of films such as the Voigt model.[199] However to use these models, density and viscosity of the assembled film need to be known. These variables are unknown in our system as they are dependent on tether density and membrane lipid packing. Therefore, analysis of the QCM data is restricted to comparisons in changes in conditions and to published literature.

QCM has been used to follow the adsorption, deformation and rupture of lipid vesicles during planar lipid bilayer formation. [69, 236][43, 109] Rupture of

liposomes onto solid substrates to from supported bilayers is well characterised and results in a characteristic pattern of change in frequency and dissipation, as demonstrated in a protocol by N. Cho *et al.* [40] See Figure 2.10 for an example of a characteristic vesicle rupture QCM study both figure and caption taken from [40].

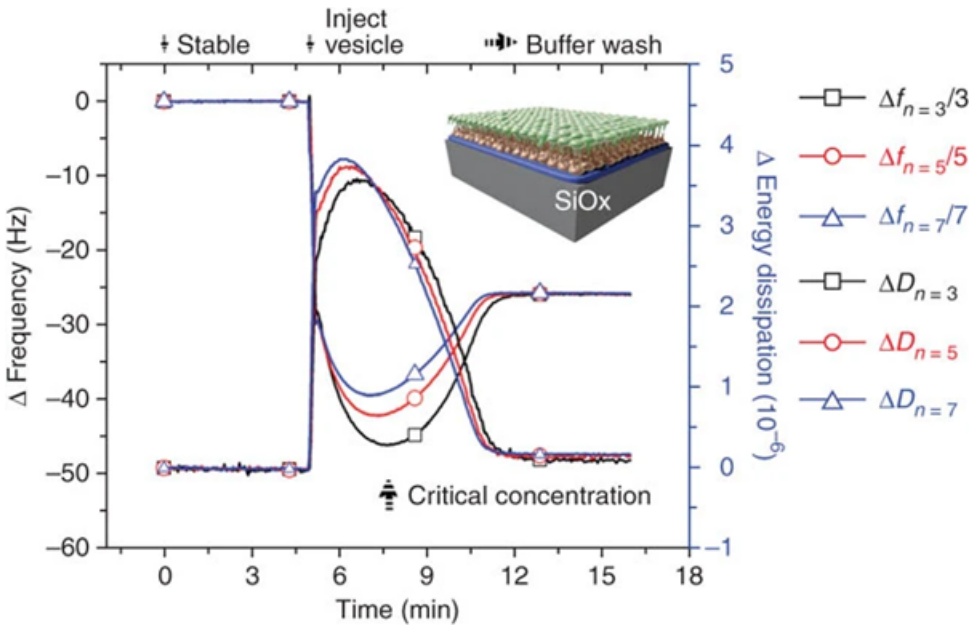

Figure 2.10 *Figure taken from [40]. After the baseline buffer measurement stabilised, POPC vesicles (*0.1 mg ml^{-1} *were injected at* 5 *min, leading to a rapid adsorption onto the substrate and a corresponding frequency decrease and dissipation increase in all overtones (n= 3, 5 and 7). As indicated by the maximum changes in the frequency and dissipation responses, the critical vesicle coverage was reached at 8 minutes. Thereafter vesicles began to rupture on the substrate, forming a supported lipid bilayer. The inset is a figure of the supported lipid bilayer on silicon oxide. Note that at the start of the measurement the change in dissipation and the change in frequency equal 0.*

The characteristic QCM-D trace of vesicle rupture on a solid substrate has an immediate decrease in frequency and increase in dissipation on injection of the liposomes. The increase in dissipation indicates an increase in elasticity in the system and it is therefore theorised that intact vesicles are initially adsorbing on the substrate. At a critical coverage of liposomes adsorbed on the solid substrate, the liposomes rupture resulting in an increase in frequency and decrease in dissipation to less than 1×10^{-6}, which indicates that a thin rigid film is now at the interface-that of a supported lipid bilayer.

Chapter 3

Cell Free Expression of MscL into Liposomes

3.1 Introduction

3.1.1 Aims

The aims of this chapter are two fold. The initial aim was to utilise cell free protein expression to produce proteoliposomes in which the distribution of MscL channels is hopefully representative of their native biological distribution in bacterial membranes. Our secondary aim is to characterise these proteoliposomes using small angle neutron scattering and determine if channel gating can be observed in response to the presence of amphiphilic antimicrobial molecules.

3.1.2 Gating of the Mechanosensitive Ion Channel of Large Conductance

The Mechanosensitive Ion Channel of Large Conductance (MscL) is a bacterial membrane protein that gates in response to an increase in membrane tension.[144] When a bacterium is subjected to a hypo-osmotic stress (internal osmotic pressure higher than external osmotic pressure), the excess tension generated in the membrane triggers the channels to open, allowing osmotic pressure to equalise.[129] MscL forms the largest pore of the bacterial mechanosensitive ion

channels which has resulted in it being well studied. Figure 3.1 shows the molecular structure of MscL based on the crystal structure 2OAR and how the conformation of the MscL channel may alter on gating based on electron paramagnetic resonance measurements and molecular dynamic simulations. [212, 218]

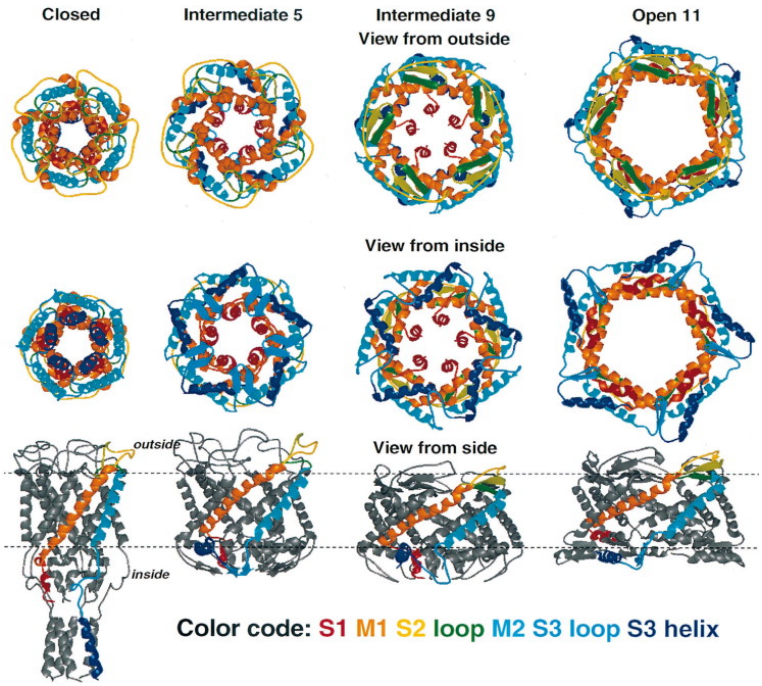

Figure 3.1 *Ribbon representation of models of EcoMscL in a closed, two intermediate, and an open conformations shown as viewed from outside the cell (top row), inside the cell (middle), and from the side (bottom). Only one subunit is coloured in the side view, so that the conformation of a single subunit can be visualized. Reproduced from Sukharev et al with permission.[217] The M1, M2 and periplasmic loop sections of the closed conformation are based on the crystal structure 2OAR whilst the N-terminus and C-terminus sections are modelled by Sukharev at al.[217]*

3.1.3 MscL Clustering

Lattice-like clustering of membrane proteins has been observed in several systems and may be a mechanism by which bacteria and other cells modulate protein function.[59] Clustering of MscL channels has been observed directly in *in–vitro* membrane mimetic systems leading to some consideration being given to the relevance to the protein channels function *in–vivo*.[75] The number of MscL channels in a single bacterium was initially thought to be low and estimated to be

around 4-100 channels from a combination of electrophysiology studies,[23, 214] however more recently a broader range of culture conditions have been tested and the number of Green Fluorescence Protein (GFP)-labelled MscL channels assessed by fluorescence microscopy to be between 300-1400 channels per cell.[19] A larger number of MscL channels are expressed when the bacteria are grown in a media of higher salt concentration suggesting osmoregulation of expression.[19]

In-vivo confocal fluorescence imaging of GFP-labelled MscL revealed an inhomogeneous distribution in bacterial membranes, with a higher percentage of protein observed at the poles of the bacterium.[167] This could be suggestive of either protein-protein or protein-lipid interactions mediating clustering. However, more recent literature has suggested that fluorescence tagging of MscL channels can lead to clustering in environments where the protein would otherwise be evenly distributed.[231]

Atomic force microscopy experiments have shown evidence of clustering with simulations and patch-clamp recordings suggesting that protein-protein interactions in clusters could alter the sensitivity of the channels, enabling clustering to have an osmoregulatory functional role in the membrane. [75] The small angle scattering analysis by the same group observes MscL clusters of up to 278 channels per 120 nm diameter DOPC lipid vesicle, they also concluded that cluster size was independent of protein to lipid ratio.[75] The size determination of their clusters was extrapolated from the small angle neutron scattering intensity as $Q \to 0$ and so was unable to give an insight into the shape of the channels or clusters.

Minimal computer models of MscL channel clustering within a fluid membrane that include a weak inter-protein interaction, have shown that channels exhibit strong cooperative gating.[75, 173] The computer models further show that the gating activity is dependent on cluster size and shape, with gating probability of a single channel being dependent on the number of protein-protein interactions. The hypothesis as to how this would be useful to a bacterium, is that clusters could prevent unnecessary gating in stressful environments by requiring a higher tension to gate clustered channels and also prevent volume overshoot, i.e. prevent too much solute loss by only gating a percentage of available channels, both of these effects could improve bacterial survival.

A possible complication when studying MscL is that it has been found to form a tetrameric state *in-vitro*, in addition to the pentameric state.[31, 65, 133, 237] The tetrameric state has not been observed *in-vivo* and as such its biological

significance is debated. It has been shown that the detergent or lipid used to stabilise MscL channels impacts its oligomeric state [54], suggesting that in lipid compositions similar to that of a bacterium the pentameric state only would be present but the presence of detergent could stabilise other oligomeric states.

The clustering of both of tetrameric and pentameric oligomeric states has been modelled as organised lattices with the results showing that clustering of individual oligomeric states and mixtures of oligomeric states are possible.[115] In the investigations presented in this thesis, expression is direct into lipid constructs, with no detergents being used. Since we are expressing the protein directly into lipid constructs in the absence of detergent, the pentameric form of MscL should be the only oligomeric state present in the resulting proteoliposomes. The extent of clustering within the proteoliposomes studied is likely to be dependent on the number of channels per liposome, our chosen lipid environment as well as the native protein-protein interactions of MscL channels.

3.1.4 Cell Free Protein Expression

Cell free protein expression (CFPE) is the expression of protein using crude cellular extracts and exogeneous resources instead of intact cells. Recent engineering and technology developments have broken the barrier to wide-spread use of CFPE, enabling higher protein yields and lowered costs.

By expressing the protein outwith a cellular environment, the environment can be more rigorously controlled to observe protein expression and assembly pathways but also to place proteins within a desired construct or to produce pure protein for drug research. CFPE also lends itself well to protein modification, be it for protein-drug complexes, selective deuteration of protein or production of tagged proteins.

In the next few years it is expected that industry will take increasing advantage of the technique for on-site biosensing and for bio-manufacture, though there are still some barriers involved in scale up of the expression. By using the cell lysate instead of living cells then all of the cells transcriptional/translational and metabolic capacity is devoted into making a single product.

For more in-depth review of the advantages and limitations of cell free protein expression and its applications I direct the reader to the following thorough

reviews:[206], [94].

It works as a useful alternative to *in-vivo* expression systems that are limited in the ability to over-express certain proteins and removes difficulties associated with proteins that are unstable to bacterial extraction. The increasing availability of commercial CFPE kits and services make using this kind of expression accessible and increasingly affordable. The main limitation of CFPE, is that it remains more expensive than *in–vivo* expression systems. By using CFPE to express our protein of interest, MscL, directly into liposomes we hope to produce MscL distributed in a similar manner as the native channels in bacteria.

3.2 Cell Free Protein Expression

3.2.1 Method

The MscL expression plasmid, a pDuet-1 WT MscL-6 His construct under T7 promoter, was kindly supplied by Paul Rohde and Boris Martinac of the Victor Chang Cardiac Research Institute, Sydney. The cell free protein expression was carried out using RTS500 Biotechrabbit Proteomaster *E. coli* HY kit following manufacturer instructions.[20] Optimisation of the expression was done with further guidance taken from Abdine *et al.*, on their optimisation of MscL expression.[2] The expression reaction solution contained 4mg of 3:1 POPC:POPG lipid per 1 ml reaction mix, as the membrane construct the protein is expressed into.

To prepare the reaction solution with the appropriate concentration of lipids for our experiments, the following experimental steps and modification to the manufacturer protocol were performed.[20] A modification was required due to the desire to have a large enough volume of lipid solution such that we could dissolve and sonicate the lipid solution to form unilamellar uniform vesicles, prior to incorporating the lipid solution with other reaction components.

First a concentrated solution (18 mg ml^{-1}) of 3:1 POPC:POPG lipids was prepared. POPC (13.5 mg) and POPG (4.5 mg) were dissolved in the minimum amount of chloroform and the chloroform removed under a stream of nitrogen to produce a dried lipid film. Then 0.976 ml of BiotechRabbit reconstitution buffer was added to the lipid film and the solution tip-sonicated for 30 minutes

at room temperature. The liposome mixture was then ready to be added to the final reaction solution (0.32 ml) of the 1 ml reaction mix.

All components of the RTS500 BiotechRabbit kit were stored at –20°C until the day of expression. The Dithiorithretol (DTT) solution, reconstitution buffer and MscL plasmid were thawed at room temperature whilst all other components of the RTS kit were thawed on ice (*E.coli* lysate, feeding mix, reaction mix). After thawing, components were reconstituted by adding in an appropriate volume of reconstitution buffer and lightly rolling the reaction vessel (no shaking) to avoid shearing of delicate biological components. After reconstitution, components were kept on ice until they were combined into the final reaction vessel. The *E.coli* lysate was reconstituted in buffer (0.2 ml) and liposome solution (0.32 ml). The reaction mix was reconstituted in buffer (0.22 ml), the amino acid mix was reconstituted in buffer (3 ml) and the methionine was reconstituted in buffer (1.8 ml). Finally the lyophilised feed mix was reconstituted with buffer (8.1 ml).

After reconstitution, all components were then combined into a reaction solution and a feeding mix was placed into the reaction vessel (supplied by BiotechRabbit).[20] Splitting the solutions into a reaction mix and feeding mix this way, allowed for a higher yield to be produced. In the reaction compartment a high concentration of critical components are present, whilst small components such as amino acids can be exchanged into the reaction compartment and waste products can diffuse out. The feeding mix was prepared by adding lyophilised feed mix (8.1 ml), amino acid solution (2.6 ml), methionine solution (0.3 ml) and DTT solution (0.3 ml). The reaction solution was prepared by adding reaction mix (0.22 ml), reconstituted *E.coli* mix (0.52 ml), amino acid solutions (0.27 ml) and methionine (30 µl). Finally a solution of the expression plasmid (10 µl, 464 µg ml^{-1}) was added to reaction mix and the reaction container was assembled and placed in a shaker incubator at 30°C for 23 hours. See Figure 3.2 for photographs of the cell free protein expression reaction chamber.

After 23 hours of incubation, the reaction mix was removed from the reaction container and centrifuged at 4 °C for 1 hour to produce pellets, the supernatant removed and the pellet resuspended in 4-(2-hydroxyethyl)-1-piperazineethanesulfonic acid (HEPES) buffer(1 ml, 20 mM, pH 7, 100 mM KCl). The proteoliposome solution was then characterised, stored at 4℃ until use and used within a week.

Figure 3.2 *Photographs of the Biotechrabbit Cell Free Protein expression reaction container. Reaction mix is injected in the central opening with red cover and the feeding solution was injected into the opening to the side with a clear opening.*

3.2.2 Gel Electrophoresis

Sodium Dodecyl Sulfate Poly Acrylamide Gel Electrophoresis (SDS-PAGE) was run on 12% acrylamide gels. Aliquots (10 µl) were taken from each protein expression and mixed with aliquots of Sigma Aldrich SDS-PAGE staining solution (10 µl) and heated at 60°C (1 hour) and cooled to room temperature before loading onto the gel. Lipids were not removed from the protein sample before analysis which may have led to some blurring of the protein bands. After the samples had run on the gels (approximately 1.5 hours), the gels were removed from the glass supports and rinsed multiple times with Milli-Q water. The gels were left to soak in Milli-Q water for 1 hour, the water was then replaced and left again for an hour to remove SDS from the gel. ThemoFisher Coomassie safe stain was then used to stain the gels by covering the gels in the solution for an hour followed by rinsing and soaking (1 hour) with Milli-Q water.[226] Photos were then taken of the gels.

3.2.3 Protein Quantification-BCA Analysis

The BCA (Bicinchroninic Acid) method of protein quantification was used following the protocol from Takeda, M. *et al.*.[222] A Thermo Fisher Scientific Pierce BCA protein assay kit was used which contained Bovine Serum Albumin (BSA) standards for the expressed protein to be quantified against.

The solubilisation buffer was prepared from Triton-X 100 (0.2%), solubilised in HEPES-KOH buffer (20 mM, pH 7.4). An aliquot (60 µl) of the proteoliposome

sample was made up to 1500 µl with solubilisation buffer, decanted into three separate tubes (500 µl). Cold acetone (1 ml) was added to each of the tubes, the tubes vortexed and incubated for 20 minutes at −20°C. The tubes were then centrifuged at room temperature (10 000×g, 10 minutes), the supernatant discarded and pellets incubated for 30 minutes at room temperature to allow any remaining acetone to evaporate. Solubilisation buffer (500 µl) was added to re-suspend the pellets and the tubes vortexed. BCA working reagent (500 µl) is added and the tubes incubated at 60 °C for 1 hour. Samples are allowed to cool for 10 minutes before measurement.

Bovine Serum Albumin (BSA) standards were prepared over a concentration range of 0.5–20 µg in the same solubilisation buffer as the proteoliposome samples to produce a calibration against which we could quantify our protein. Each standard (500 µl) was prepared in the same way as the proteoliposome samples by adding BCA working reagent (500 µl) and heating for an hour at 60°C before cooling to room temperature for 10 minutes. A spectrophotometer was then used to measure absorbance at 562 nm.

3.2.4 CFPE Characterisation

The yields from each protein expression used to produce proteoliposomes are shown in Table 3.1.

Initial protein yields were a little low, between 0.15-4 mg ml^{-1} for reactions 1-3. Further optimisation by decreasing the plasmid concentration increased the yields to between 0.53-0.74 mg ml^{-1}. MscL was expressed directly into the liposome composition desired, here we expressed the protein into POPC only liposomes, 3:1 POPC:POPG liposomes and partially deuterated d-31 POPC: d-31 POPG liposomes. The partially deuterated lipid has only one tail deuterated and the other is hydrogenous.

Comparison of a proteoliposome sample to the corresponding expression supernatant by gel electrophoresis is shown in Figure 3.3. Observation of the gels shows that definitive bands appeared when expression was successful at a molecular weight between 14.4 and 18.4 kDa according to the protein marker used. The aliquot taken directly from the reaction chamber after 22 hours of CFPE is labelled as PL on the photograph of the gel and shows a strong band at about 16 kDa, but there is evidence that the gel is overloaded and some bands are present

Table 3.1 *Expression yields of MscL into liposomes using the RTS500 expression kit for different protein expressions, note that the starred expression numbers were carried out at higher plasmid concentration before the expression system was optimised. The uncertainty on the protein concentration is* 0.02 mg ml^{-1}.

#	Lipid composition	Lipid Conc. (mg ml^{-1})	Protein Conc. (mg ml^{-1})	Protein to lipid ratio (w/w)
1*	3:1 POPC:POPG	4	0.15	0.04
2*	3:1 POPC:POPG	4	0.30	0.08
3*	POPC	4	0.40	0.10
4	3:1 POPC:POPG	4	0.69	0.17
5	3:1 POPC:POPG	4	0.72	0.18
6	3:1 d31-POPC:d31-POPG	4	0.53	0.13
7	3:1 POPC:POPG	5	0.67	0.13
8	3:1 d-31-POPC:d31-POPG	5	0.56	0.11

higher on the gel. When running the gels of reactions 1-3, the reaction solution was centrifuged and dialysed before running on the gel. This produced narrower bands around 16 kDa. The monomeric units of MscL have a molecular mass of 14.1 kDa , with the His-tag, this becomes a molecular mass of 16.7 kDa.

The results from the Gel electrophoresis and BCA analysis confirm that protein of the correct molecular weight was expressed using cell free protein expression. These measurements do not confirm the correct folding of the MscL channel which in its pentameric untagged form has a molar mass of 70 kDa. This band is not present in our gels due to the samples being run in SDS buffer which doesn't support the pentameric state.

3.2.5 CFPE Conclusions

Expression of MscL into our liposome constructs was successful and good yields were achieved to allow for analysis by scattering. We do not observe a clear increase in protein yield with increasing lipid concentration, as might have been expected from a previous study by Jacobs *et al.*[110] However the study by Jacobs *et al.* looking into the effect of lipid concentration and composition on the amount of MscL expressed by cell free protein expression compared larger

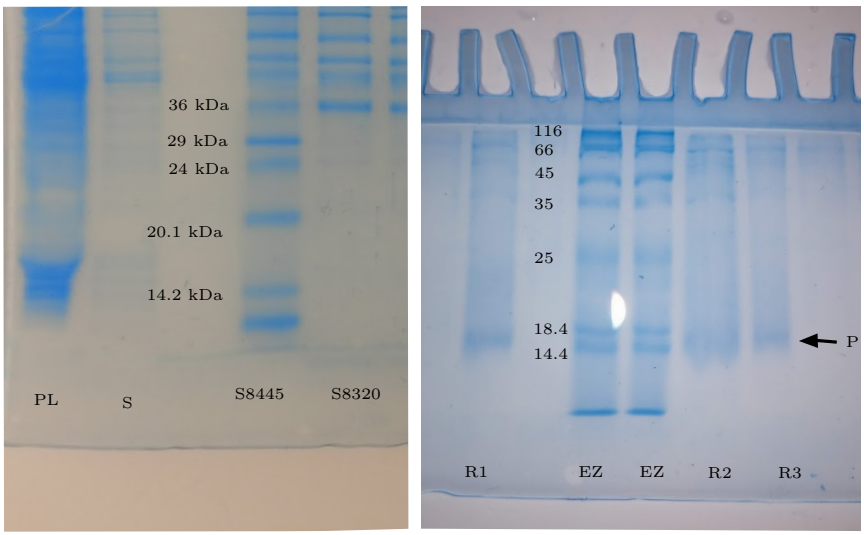

Figure 3.3 *Right: Photograph of Acrylaminde gel run with Sigma Aldrich protein markers S8445 and S8320 and aliquots of the proteoliposomes sample (PL) and supernatant (S).Right: Photograph of Acrylaminde gel run with Fisher scientific EZ marker and the aliquots of reactions 1,2 and 3 after centrifugation and dialysis. P indicates the position of the expressed protein band.*

differences in lipid concentration at the 10 mM scale for DOPC liposomes. The in-significant change in protein expression on increasing the lipid concentration from 4 mg ml^{-1}(5.26 mM) to 5 mg ml^{-1} (6.58 mM) may simply be that available membrane surface area has increased insufficiently to increase the level of protein expression to a significant extent.

Two other observations from our protein expression yields are that higher expression yields are obtained when expressing into POPC only liposomes of the same concentration and lower yields when expressing into partially deuterated lipid liposomes. Incorporation of POPG lipids into POPC bilayers decreases the area per molecule [112] which may have two effects. A decrease in area per molecule decreases the total membrane surface area available for MscL expression however this effect is likely to be negligible, since our results suggest that we are not sensitive to small changes in available membrane area when comparing liposome concentration. Another effect, is that the decrease in APM on incorporation of POPG, decreases membrane elasticity. Membrane elasticity or more specifically the area expansion modulus of a membrane has been shown in other research to reduce the number of proteins correctly folded into the membrane.[110, 137] Therefore it seems consistent with current literature that our expression yield is higher in pure POPC lipid liposomes than in 3:1 POPC:POPG liposomes. Despite the lower yield, the mixed lipid composition is closer to the

composition of bacterial membranes we are attempting to mimic and investigate so we continued the expression in 3:1 POPC:POPG liposomes.

Differences in expression yield with lipid packing does not explain the lower protein expression yield in the presence of our partially deuterated lipids. Deuteration of lipid tails slightly increases the fluidity of the lipids and therefore results in an increase in area per molecule (APM). Given that our partially deuterated lipids would only have a slightly greater fluidity any change in APM would be negligible. Along with any change in membrane expansion modulus we would not expect the difference in expression yield that we observe. It is possible that the lower expression for these two samples is part of the overall variation in expression observed. Part of the large variation we observe is due to doing our expressions on such a small scale (1 ml reaction volumes) where many of the components are measured out in small volumes, increasing measurement errors on how accurately expression sensitive components such as the plasmid solutions and energy molecules can be measured. Doing this expressions on a larger scale would decrease these measurement errors.

3.3 Analysis of Proteoliposomes

3.3.1 Small Angle Neutron Scattering

Small angle neutron scattering (SANS) experiments were carried out on SANS2D, ISIS Neutron and Muon source, Didcot over 3 days awarded beamtime: RB180511 (10.5286/ISIS.E.RB1820511) and RB1910570 (DOI:10.5286/ISIS.E.RB1910570-1). Beamtime was carried out in collaboration with instrument scientist James Doutch. All samples were measured with an 8 mm aperture with a source to sample and sample to detector distance of 12 metres and kept at 20°C using a recirculated water bath. For samples suspended in D_2O buffer or comprising deuterated lipids in H_2O, exposures of 12 mAh and 8 mAh proton beam current were used, for SANS and transmission measurements respectively. Triple the counting time was used for tail–matched water (TMW) and protein–matched water buffer (PMW) contrasts. Rectangular cross–section quartz cuvettes of 1 mm path length were used for all contrasts other than the D_2O contrast buffer for which 2 mm path length cuvettes were used. SANS cells were cleaned by soaking in Hellmanex solution (2%) for 1 hour then rinsing with Milli-Q water,

ethanol and rinsing out with Milli-Q water 20 times, cells were then dried in a 50°C oven. The outside of the cells were wiped with ethanol and Kimtech tissues shortly before measurement.

All measurement buffers were HEPES buffer (20 mM, pH 7.4/pD 7), prepared from two batches of buffer, one prepared in D_2O, the other in H_2O. Sodium Chloride (NaCl) was not used in the buffers to reduce aggregation of liposomes. Since the proteoliposome samples are stored in a H_2O based buffer, all samples were dialysed against the appropriate buffer before measurement, each 500 µl sample was dialysed in 500 ml of the desired buffer.

3.3.2 Small angle X-ray scattering

All small angle X-ray scattering was carried out at ISIS Neutron and Muon source using a Nano-inXider SAXS instrument using a copper K-α source and Pilatus 2M detector. All samples were measured in 1.5 mm diameter quartz glass capillaries. SAXS from HEPES buffer (20 mM, pH 7.4, 150 mM NaCl) was measured and subtracted from proteoliposome samples. Samples were normalised against a measurement of water in a quartz glass capillary to get an absolute scale.

3.3.3 Guinier–Porod Model

The small angle scattering from a system of particles can be characterised by a Guinier (low-Q) and Porod regions (high-Q). The Guinier region allows a radius of gyration to be determined whereas the Porod region gives a good estimate of the shape of particles or the inhomogeneity of the surface.

Table 3.2 *Table of Porod exponents and its relation to common scattering objects.*

Porod exponent, d	Nature of scattering object
4	Very smooth sphere
3	Very rough object or collapsed polymer chains
2	Gaussian polymer chain or 2-D structure(lamellae or platelets)
1	Stiff rod or thin cylinder

A Porod exponent between 3 and 4 indicates a surface fractal whilst a Porod

exponent between 2 and 3 indicates a mass fractal.

Hammouda *et al.* proposed a Guinier-Porod model to fit a mixture of arbitrary shapes or fractal structures in one model for which it is difficult to build analytical models.[83]

In an empirical Guinier–Porod model, the scattering intensity is given by two contributions:

$$\begin{aligned} I(Q) = G\exp\left(\frac{-Q^2R_g^2}{3}\right) \text{for } Q \ \leq \ Q_1 \\ I(Q) = \frac{D}{Q^4} \text{for } Q \ \geq \ Q_1, \end{aligned} \tag{3.1}$$

where Q is the scattering vector, $I(Q)$ is the scattered intensity, R_g is the radius of gyration, and G and D are the Guinier and Porod scale factors respectively. This model applies when the scattering object is spherical.

A further generalisation of this model suggested by Hammouda *et al*, accounts for non-spherical shaped objects such as rods and lamellae.[83] This is done by introducing a non-spherical shape parameter into the Guinier term based on generalised Guinier Laws for elongated objects. [70, 93, 122, 138]

The generalisation of the Guinier-Porod model is achieved using the following functional form:

$$\begin{aligned} I(Q) = \frac{G}{Q^s}\exp\left(\frac{-Q^2R_g^2}{3-s}\right) \text{for } Q \ \leq \ Q_1 \\ I(Q) = \frac{D}{Q^d} \text{ for } Q \ \geq \ Q_1, \end{aligned} \tag{3.2}$$

where Q is the scattering vector, $I(Q)$ is the scattered intensity, R_g is the radius of gyration, d is the Porod exponent and G and D are the Guinier and Porod scale factors respectively. The s-parameter enables modelling of non-spherical objects. For globular structures such as spheres $s = 0$, for 2-dimensional objects such as rods and platelets the s-parameter is defined as $s = 1$ and $s = 2$ respectively.

A general Guinier-Porod model for a 2-dimensional particle such as a rod can be

described by the following model:

$$
\begin{aligned}
I(Q) &= \frac{G_2}{Q^{s_2}} \exp\left(\frac{-Q^2 R_{g2}^2}{3-s_2}\right) \text{ for } Q \ \leq \ Q_2 \\
I(Q) &= \frac{G_1}{Q^{s_1}} \exp\left(\frac{-Q^2 R_{g1}^2}{3-s_1}\right) \text{ for } Q_2 \ \leq \ Q \ \leq \ Q_1 \\
I(Q) &= \frac{D}{Q^d} \text{ for } Q \ \geq \ Q_1.
\end{aligned}
\tag{3.3}
$$

The model consists of two Guinier regions and a Porod region where $3 - s_2$ and $3 - s_1$ are dimensionality parameters and R_{g1} and R_{g2} are the radius of gyration of the short and overall sizes of the scattering object. For the example of a cylinder of radius R and length L, $R_{g2} = (L^2/12 + R^2/2)^{\frac{1}{2}}$ and $R_{g1} = R/2^{\frac{1}{2}}$.

All fitting to Guinier-Porod models was carried out on Igor v.6.37 using the NCNS Irena SAS macro v.2.63.[105] The Irena Macro allows for multiple Guinier-Porod levels to be fitted where each level corresponds to a different scattering object and each level can correspond to multiple Guinier and Porod regions as demonstrated in Equation 3.3.[105] This is important for our system where in all measured contrasts there will be scattering from the protein and from the overall proteoliposome structure.

3.3.4 Radius of Gyration

The radius of gyration describes the distribution of mass of an object or particle, or more precisely the second moment of the distribution of the mass of the particle.

Mathematically, radius of gyration is the root mean squared distance of the subunits making up the object, from the centre of mass of the object.

For a protein:

$$
R_g^2 = \left(\sum_i m_i r_i^2 / \sum_i m_i\right)^{\frac{1}{2}}, \tag{3.4}
$$

where m_i is the mass of an atom and r_i is the distance of an atom from the centre of mass.

Using this calculation the 2OAR crystal structure of MscL yields a radius of gyration of 27.8 Å, this can be calculated from the pdb file using a number of free online resources. [31, 51, 232, 243] Separately the radii of gyration can be calculated around each directional centre of mass as $R_g^x = 18.3$ Å, $R_g^y = 16.9$ Å and $R_g^z = 12.3$ Å. Whilst MscL is a globular protein its structure is not spherical, in common with most proteins.

3.3.5 Small Angle X-ray Scattering Results

Three cell free protein reaction vessels were used to express roughly 0.5 mg of MscL into 4 mg of lipid dispersed as 4 mg ml^{-1} liposome reaction solutions. After centrifugation, dialysis, sonication and extrusion of the proteoliposomes, samples from each reaction were analysed using Small Angle X-ray Scattering. Reactions 1 and 2 expressed MscL into 3:1 POPC:POPG lipids whilst reaction 3 contained only POPC lipids. The expression yields are shown in Table 3.1.

Table 3.3 *Table of Guinier–Porod (GP) Fitting parameters to scattering from three MscL containing proteoliposomes. The Porod exponent, d of the first GP level was fixed to 3.5 due to the Porod region being too close to the background and 3.5 being a good estimate for a globular protein. The radius of gyration of the second GP level was fixed to* 1×10^6 Å *due to being outside of the detectable limit of the Xenocs instrument.*

Model parameter	Reaction 1 3:1 POPC:POPG	Reaction 2 3:1 POPC:POPG	Reaction 3 POPC
GP1			
s	0.8 ± 0.2	0.3 ± 0.2	0.7 ± 0.2
G	$9.51 \times 10^{-4} \pm 7.14 \times 10^{-4}$	0.0251 ± 0.014	0.0291 ± 0.002
R_g (Å)	50 ± 16	64 ± 3	50 ± 4
GP2			
G (10^{10})	4.79 ± 1.60	62.1 ± 4.87	155 ± 122
d	3.01 ± 0.05	3.30 ± 0.11	3.41 ± 0.11
Background (cm^{-1})	0.00108	0.00500	0.00700
χ^2	125	135	118
Reduced χ^2	0.76	0.82	0.72

The small angle X-ray measurements were fit to a two-level Guinier-Porod (GP) expression, the fits are shown in Figure 3.4. The first level corresponds to

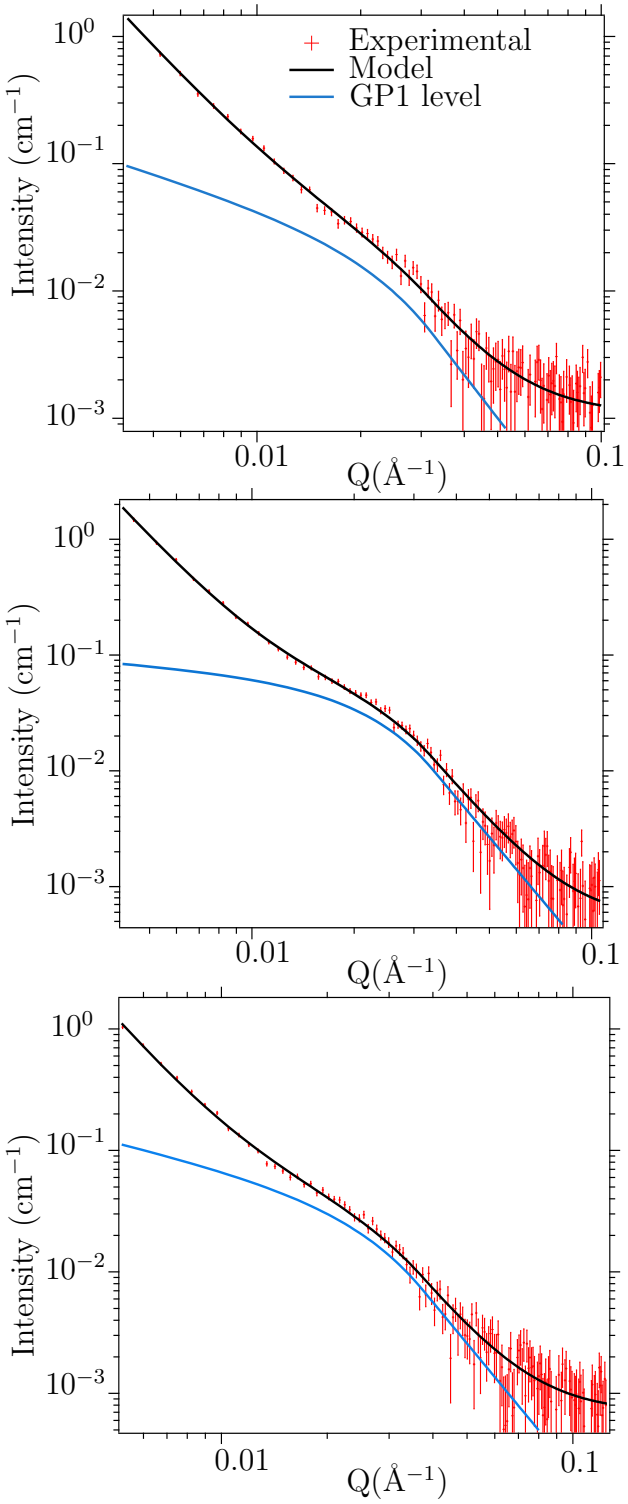

Figure 3.4 *Small angle X-ray scattering from* 4 mg ml^{-1} *MscL-proteoliposomes in* H_2O *buffer fit to a two level Guinier-Porod fits. Solid blue lines represent the first Gunier-Porod level of the model whilst the solid-black lines represent the full fitted model. SAXS measurements shown of proteoliposomes from reaction 1, 2 and 3 from top to bottom.*

the scattering from the protein, and a single Guinier and Porod region are fit within this level. The second Guinier-Porod region corresponds to the overall proteoliposome/buffer interface. Since our proteoliposomes are so large as to be outside of the detectable range of the XENOX instrument (greater than 200 nm diameter), a Guinier-region cannot be fitted, but by setting the R_g value to 1×10^6 Å then a fit to a Porod region can be made to assess the dimensionality of the scattering object.[105]

Since $s > 0$ was determined from the first GP level, we know that the protein doesn't scatter as a perfect sphere. In principle, a second Guinier region could be determined for this level, however the scattering from the proteoliposome interface dominates at low-Q meaning there was there were insufficient data points to fit such a region. This doesn't render the model incorrect, but means that we cannot calculate the smaller radius of gyration (R_{g2}).

The Porod exponent d for the second GP level is determined from the SAXS measurements to be between 3.0 and 3.4, indicating a complex globular shape consistent with a sphere with a rough surface as we might expect for a proteoliposome. The roughness can be attributed to the protrusion of MscL proteins from the membrane interface and the fractal Q-dependence of the scattering profiles suggest the proteoliposomes contain a significant portion of proteins across its surface, segmenting the lipid bilayer significantly. We do not observe a perfect smooth sphere for which d would tend to 4.

The first GP region in the model is attributed to MscL protein on the proteoliposome surface. Since we know that the radius of gyration of a single MscL channel should be 27.8 Å, the larger radii of gyration calculated here of 50 to 64 Å could suggest that the channels have clustered in the membrane. However for the SAXS analysis of reactions 1 and 2 there is a weak Bragg feature at $Q = 0.06$ Å^{-1}, suggesting that multilamellar vesicles are present which will have also affected the overall shape of the SAXS curve.[200] This is likely what has caused the overestimation of protein size.

To prevent formation of multilamellar vesicles in our SANS samples, they were dialysed into 20 mM HEPES buffer containing 0 mM NaCl salt at pH 7.4, and extrusion and sonication was performed within an hour of the start of the measurement. This contrasts with the SAXS measurements which were made over a 24 hour period from the point of loading the samples. It seems likely that the proteoliposomes were aggregating and forming multilamellar structures over this

extended measurement time. This makes the meaningful interpretation of this SAXS data difficult. It had been intended to repeat these SAXS measurements in Spring 2020, but COVID-19 meant this was not possible.

3.3.6 Small Angle Neutron Scattering Results

Small Angle Neutron Scattering (SANS) was measured from suspensions of proteoliposomes (4 mg ml^{-1}) in four solution contrasts: D_2O, Tail-Matched Water (TMW), Protein-Matched Water (PMW) and H_2O; in the latter case the proteoliposomes were formulated using partially deuterated lipids. The contrast in PMW gave insufficient contrast so scattering was low after 4 hours of measurement, therefore the data is not shown. The SANS curves are shown in Figure 3.5 plotted as Intensity$\times Q^{\ 2}$ vs Q. IQ^2 SANS curves, often referred to as Kratky plots are commonly used to observe the conformation of proteins i.e. how folded or unfolded they are.

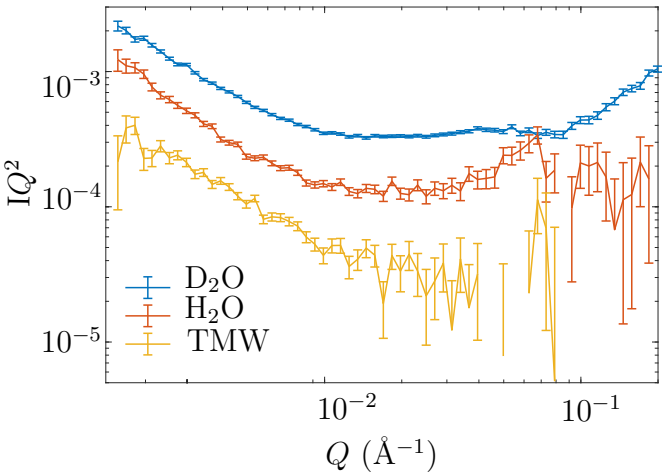

Figure 3.5 *Small angle neutron scattering measurement of* 4 mg ml^{-1} *MscL-proteoliposomes in different buffer contrasts plotted as an* IQ^2 *Kratky plot.*

Ideally to observe the conformation of a protein using SANS, the protein would be in an isolated monomeric form either outwith the membrane or membrane contrast-matched to the buffer contrast. The proteoliposome samples analysed here are more complicated as we observe scattering from the overall surface of the proteoliposomes and from protein. Since we are working with hydrogenous samples, the coherent scattering that would yield structural information is obscured by the incoherent background at high-Q ($Q > 0.1$Å^{-1}. From Figure

3.5 we can clearly see that the scattering intensity is highest in D_2O and lowest in the TMW buffer contrast. By plotting in IQ^2 the different Porod regions are clearer. The flatter region at about 0.01 $Å^{-1}$ indicates a new Guinier region, corresponding to the scattering from the MscL. In D_2O and H_2O contrasts we can see the curve dip (a decrease in IQ^2) before the background, consistent with a folded globular protein.

All of the scattering profiles were fitted to two-level Guinier-Porod (GP) models. The resulting fits to the SANS measured from proteoliposomes in each of the 3 contrasts are shown in Figure 3.6.

From the Porod exponent, d, of the second GP level (GP2) we can infer the inhomogeneity of the proteoliposome buffer interface. The fitted d values for the proteoliposome scattering in all contrasts are within a range of 3.10 to 3.25, suggesting a very rough surface. The Porod exponent for a POPC liposome has previously been reported as $d = 3.6$,[161] so we can infer that the incorporation of protein in our liposomes has increased the roughness of the surface. Given that MscL has a section of its structure that protrudes from the membrane, the increase in roughness observed is consistent with liposomes incorporating MscL.

That the scattered intensity in the Porod region of GP1 is close to the incoherent background, means that it is difficult to reliably fit d for GP1, so it has been fixed at $d = 3.5$, consistent with a globular protein.

In D_2O buffer there is a significant contrast between the buffer and both the lipid and the proteins, meaning the scattering is sensitive to both the lipid bilayer and the proteins. The small angle scattering data is shown in Figure 3.6 and the fitted parameters of the GP fit are displayed in Table 3.4. A two–level model was used, as was the case for the SAXS data. The best fit to the radius of gyration of the protein is 26 ± 3 Å, in agreement with the radius of gyration calculated from the protein crystal structure of 27.8 Å. This strongly suggests that the the GP1 scattering is from single MscL channels within the proteoliposome bilayer, rather than clusters of MscL. The s-parameter (or dimensionality parameter) is determined to be 0.96 ± 0.3. As this is close to 1, which corresponds to a rod-shape, it means that two distinct radii of gyration can be identified along orthogonal axes. A sphere of consistent density would have the same radius of gyration across all axes. Given the distribution of density for MscL depicted in Figure 3.7, this seems reasonable. However, as can be seen from Figure 3.7, the aspect ratio of this rod is $\sim 85/50 = 1.7$, which means that the two Guinier regions are too close

Table 3.4 *Results of Guinier-Porod fitting to* 4 mg ml^{-1} *MscL-proteoliposomes in D_2O, TMW and H_2O buffer shown in Figure 3.6*

.

D_2O				
Parameter	GP1		GP2	
s	0.96	± 0.3	0	
G	1.33×10^{-2}	$\pm 1.7 \times 10^{-3}$	3.92×10^{12}	$\pm 1.0 \times 10^{-11}$
R_g(Å)	26.1	± 2.6	1×10^{6}	$(fixed)$
d	3.2	± 0.3	3.14	± 0.08
Background (cm^{-1})	0.0257			
χ^2	72.1			
Normalised χ^2	1.08			
TMW				
Parameter	GP1		GP2	
s	1.01	± 1.2	0	
G	6.52×10^{-4}	$\pm 5 \times 10^{-5}$	9.87×10^{11}	$\pm 6.47 \times 10^{11}$
R_g (Å)	46	± 28	1×10^{6}	(fixed)
d	3.5	(fixed)	3.18	± 0.10
Background (cm^{-1})	0.00523			
χ^2	58.2			
Normalised χ^2	1.49			
H_2O				
Parameter	GP1		GP2	
s	0.69	± 0.9	0	
G	1.46×10^{-2}	$\pm 1.46 \times 10^{-3}$	3.40×10^{12}	$\pm 6.15 \times 10^{11}$
R_g(Å)	21	± 5	1×10^{6}	(fixed)
d	3.5	(fixed)	3.23	± 0.02
Background (cm^{-1})	0.00573			
χ^2	104			
Normalised χ^2	1.55			

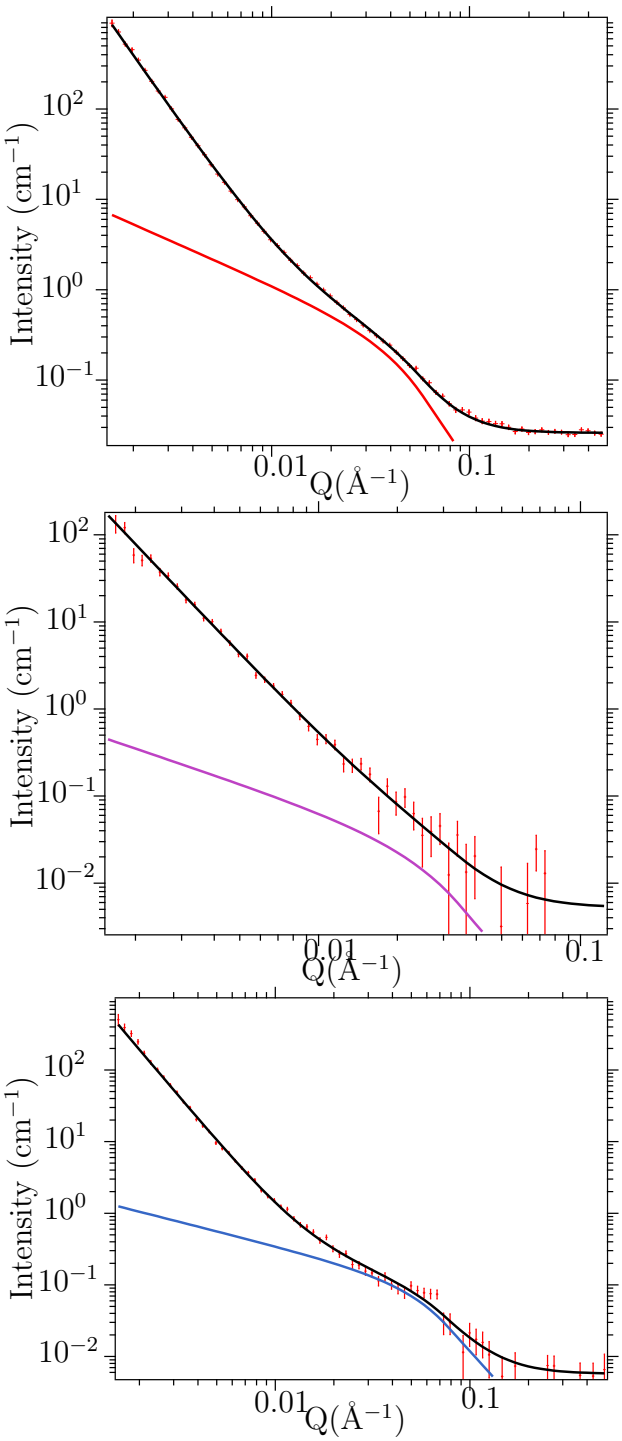

Figure 3.6 *Small angle neutron scattering measurement of* 4 mg ml^{-1} *MscL-proteoliposomes in different buffer contrasts. From top to bottom:* D_2O *buffer contrast, TMW buffer contrast and* H_2O *buffer contrast. All contrasts were fitted to two level Guinier-Porod models. The coloured solid lines represent the first Guinier-Porod level of the model whilst the solid black lines represent the combined Guinier-Porod model.*

to allow the two distinct radii of gyrations to be separately determined reliably, particularly as the scattering from the proteoliposome interface (GP2) starts to contribute to the low-Q region of GP1.

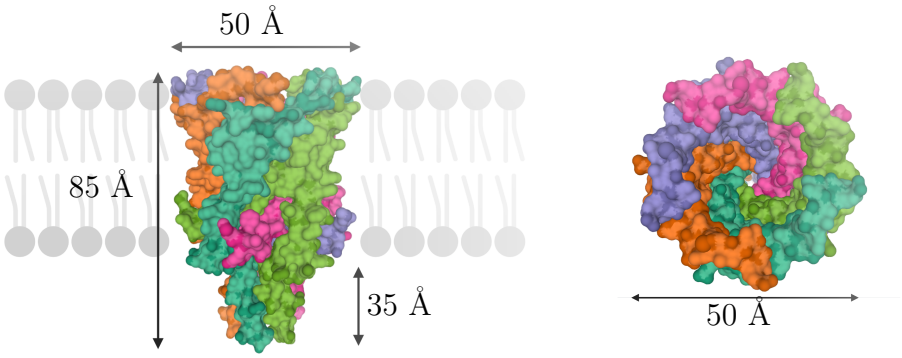

Figure 3.7 *Diagram of the closed state of the protein MscL with dimensions labelled. Dimensions taken from the crystal structure. [31] MscL molecular surface figures taken from 20AR PDB database (10.2210/pdb2OAR/pdb) [193, 203] and images created with Biorender.com.*

In Tail-Matched Water buffer (TMW) the lipid tails are contrast matched to the solution so the measured SANS is only sensitive to the lipid heads and protein, however contrast with the buffer for these components is low, resulting in a low signal-to-noise ratio. Consequently the resulting fit parameters in the two-level Guinier-Porod model have large uncertainties. All of the fitted parameters in TMW are within error of the fitted parameters to the scattering in D_2O, even though the samples were prepared from proteoliposomes from different expression reactions.

The final contrast corresponds to proteoliposomes containing d-31 lipids, suspended in H_2O buffer. In this contrast there is a large difference in SLD between the tails and the solution as well as a contrast to the lipid heads and the MscL clusters. The strong contrast between the partially deuterated lipids and the buffer solution results in strong SANS with distinct features to fit to Guinier-Porod levels. The radius of gyration in the GP1 level was fitted to 21 ± 5 Å, possibly due to the contribution from the small peak that is visible in the measured data but is not accounted for in the GP model.

In the SANS measurements of proteoliposomes at 4 mg ml^{-1} lipid concentration,

the best fit models suggest that the proteoliposomes have a rough interface, consistent with MscL protruding from the membrane. In all of the buffer contrasts measured, the models suggest that the protein is not clustered, but exists as single channels spread across the liposome surface. The best radii of gyration values agree closely with the radius of gyration calculated from the crystal structure.

SANS measurements were made from dispersions of proteoliposomes prepared at different levels of protein expression, to investigate if either the total amount of protein/proteoliposome or protein/lipid ratio had any effect on the proteoliposome. In these protein expressions 5 mg ml^{-1} of lipid was used per expression kit and so the lipid concentration is higher.

Once again the proteoliposomes were measured in three buffer contrasts: in D_2O buffer, in TMW buffer and d-31 lipids in H_2O buffer, the fitted SANS profiles are in Figure 3.8.

The Porod exponent determined for the GP2 level to the scattering measured in D_2O buffer is $d = 2.51 \pm 0.012$, which corresponds to scattering from a structure between an extended 2D layer ($d = 2$), such as bilayer or a large protein disc, and a globular stucture ($d = 3$). This may be an indication that the surface of the proteoliposome consists of extended areas of pure lipid bilayer, which would give $d = 2$ and areas of globular protein. If protein clusters are present, the lack of another Guinier region in the scattering profile suggests that they would need to be large, over 15 channel clusters. The scattering in the GP1 region is again consistent with being from isolated MscL channels within the bilayer.

The scattering from proteoliposomes in TMW buffer contrast is again low in intensity and the resultant fit parameters have a correspondingly large uncertainty. The proteoliposomes used in the measurement were from the same reaction batch measured in D_2O buffer. Inspite of this, the best fit radius of gyration is larger than can be expected for a single MscL channel.

The Guinier-Porod fit to the H_2O contrast, gives a R_g of 26.5($\pm$6) Å which has a large uncertainty due to the close presence of a peak feature, but would correspond to a single MscL protein channel. Since the s-parameter is less than one, this rules out the suggestion of large protein disks.

The repeat SANS measurement of the proteoliposome in H_2O buffer with partially deuterated lipids shows a peak at $Q = 0.04$ $Å^{-1}$. This could be due to an in-plane correlation between protein channels with a corresponding correlation length of

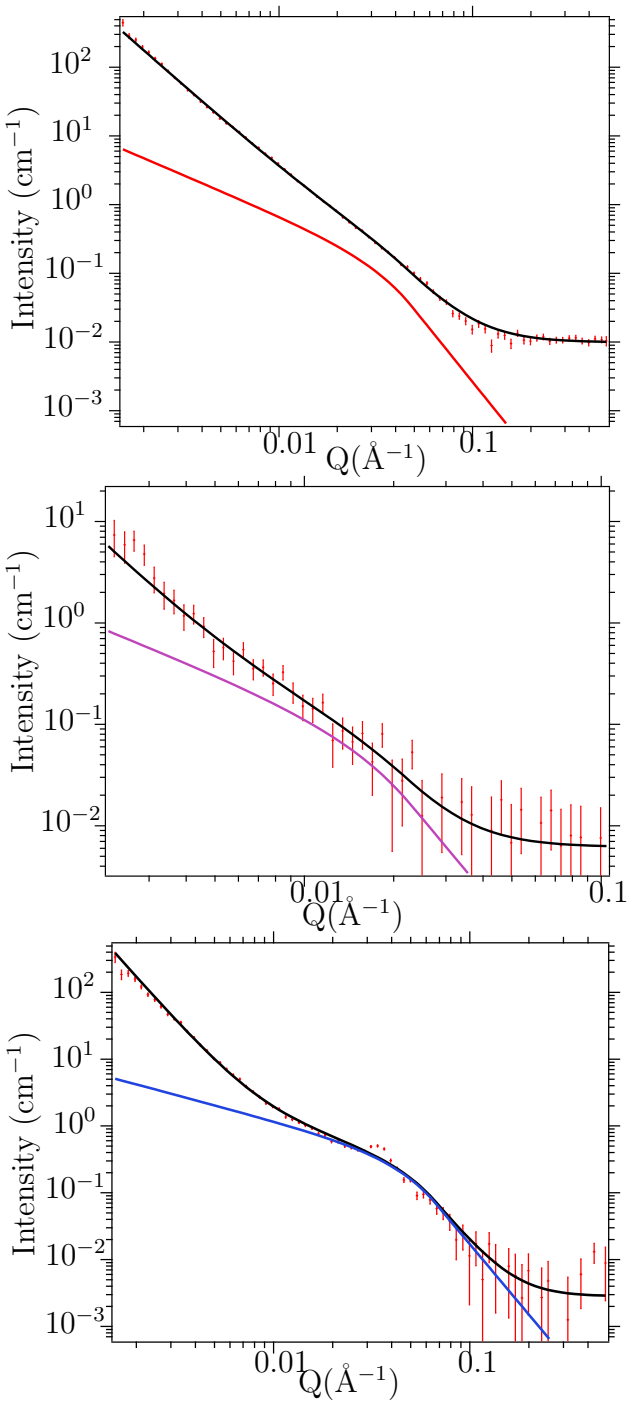

Figure 3.8 *Small angle neutron scattering measurement of* 5 mg ml^{-1} *MscL-proteoliposomes in* D_2O *buffer fit, in TMW buffer and in* H_2O *buffer all fit to two-level Guinier-Porod models. The coloured solid-lines show the first Guinier-Porod level and the black solid-lines represent the combined Guinier-Porod fit.*

Table 3.5 *Results of the two level Guinier-Porod fit to* 5 mg ml^{-1} *MscL-proteoliposomes in D_2O, TMW and H_2O buffer.*

D_2O				
Parameter	GP1		GP2	
s	1.21	± 0.03	0	
G	2.73×10^{-3}	$\pm 2.03 \times 10^{-4}$	2.22×10^{10}	$\pm 2.91 \times 10^{9}$
R_g(Å)	29	± 4	1×10^{6}	
d	3.5	(fixed)	2.51	± 0.012
χ^2	205			
Normalised χ^2	3.06			
Background (cm^{-1})	0.00906			
TMW				
Parameter	GP1		GP2	
s	1.19	± 0.45	0	
G	5.03×10^{-4}	$\pm 4.07 \times 10^{-4}$	1.75×10^{10}	$\pm 1.6 \times 10^{9}$
R_g(Å)	61.6	± 16.8	1×10^{6}	
d	3.5	(fixed)	2.95	± 1.44
Background (cm^{-1})	0.00618	(fixed)		
χ^2	25.5			
Normalised χ^2	0.75			
H_2O				
Parameter	GP1		GP2	
s	0.785	± 0.029	0	
G	3.20×10^{-2}	$\pm\ 4.06 \times 10^{3}$	4.87×10^{11}	$\pm\ 1.16 \times 10^{11}$
R_g(Å)	26.5	± 6.2	1×10^{6}	
d	3.5	(fixed)	2.98	$+/-0.03$
Background (cm^{-1})	0.002825			
χ^2	404.5			
Normalised χ^2	6.04			

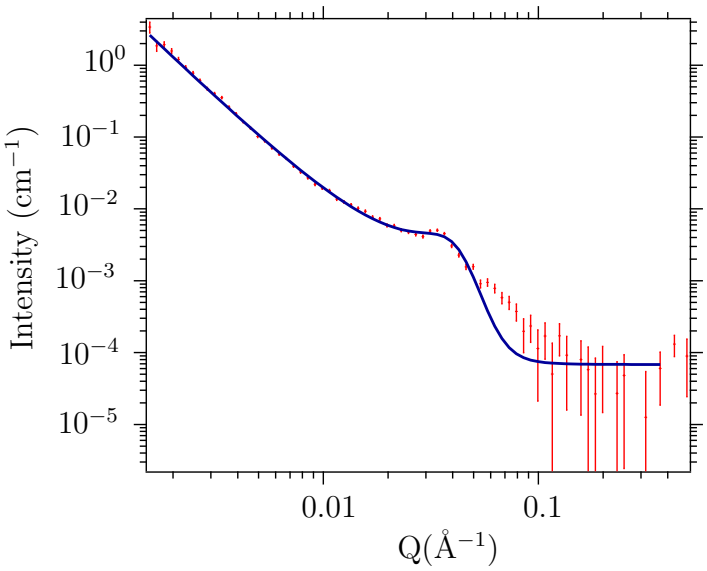

Figure 3.9 *Small angle neutron scattering measurement of* 5 mg ml^{-1} *MscL-proteoliposomes in* H_2O *buffer fit to a Lorentzian peak.*

$\zeta = 157$ Å.[135] It could also be a signature of the presence of some multi-lamellar proteoliposomes. For this contrast, the measured data was additionally fit to a Lorentzian peak model. The Lorentzian peak was fitted using the Small Angle Diffraction fitting platform available in the IGOR IRENA SAS package.[103]

Neither of the models in Figure 3.8 or Figure 3.9 fit all of the features present in the SANS curve from proteoliposomes in H_2O buffer, however between the two we can explain all of the features. The Porod exponent for the proteoliposome surface in both models are close in the range of 2.95($\pm$0.05), fixing the radius of gyration of the proteoliposomes to 1×10^6 Å. As with the D_2O contrast the Porod exponent of the level 2 fit is lower in the higher lipid concentration sample.

Table 3.6 *Results of the Lorentzian peak fitting to MscL-proteoliposomes in* H_2O *buffer.*

Fitting Parameters	Fitted Parameter Values
Porod exponent (Å)	2.91
B	1.15 E-7
Rg (Å)	1×10^6 (fixed)
Background (cm^{-1})	0.000628
Peak Prefactor	74.0
Peak Position(Å^{-1})	0.040
Peak Width (Å^{-1})	0.0153
Peak Position Spacing (Å)	159

The fitting parameters in Table 3.6 display that the Lorentzian peak has a narrow peak width suggesting scattering structures that are highly correlated. The fitted Q position of 0.039 $Å^{-1}$ correlates to a d-spacing of around 160 Å. The Q position is larger than would be expected for multi-lamellar liposomes as the thickness of 3:1 POPC:POPG bilayers is 41.7 Å, so the expected d-spacing would be about 83 Å. [158] The d-spacing of 160 Å may be a correlation between MscL channels on the surface of the liposomes. This suggests that the MscL protein is evenly distributed across the liposome surface in an ordered pattern in order to form a strong correlation peak.

In Figure 3.10 the SANS measurements from 5 mg ml^{-1} and 4 mg ml^{-1} proteoliposomes have been overlaid and plotted as IQ^2. This enables a comparison as to the effect of increased lipid concentration on the scattering.

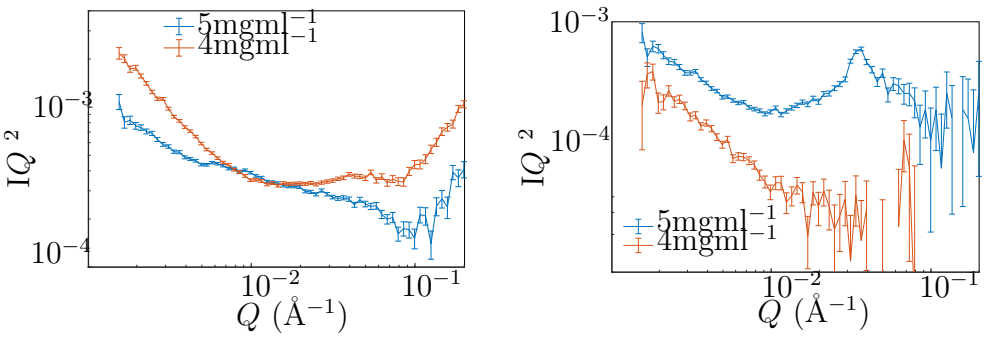

Figure 3.10 *Small angle neutron scattering measurement of* 4 mg ml^{-1} *MscL-proteoliposomes and* 5 mg ml^{-1} *MscL-proteoliposomes in different buffer contrasts plotted as an* IQ^2 *Kratky plots,* D_2O *on the left,* H_2O *buffer and d-31 lipids on the right.*

From the Kratky plots in Figure 3.10, the protein features are much more prominent in the higher protein concentration sample, independent of lipid concentration or protein to lipid ratio. From the SANS curves plotted as IQ^2 it is clear that the curves exhibit behaviour distinct from that of pure lipid liposomes. The pattern of the SANS curves is similar to that seen by Castorph for synaptic vesicles.[30]

3.3.7 Conclusion on Proteoliposome Scattering

Analysis of MscL containing proteoliposomes using small angle scattering has revealed that the proteoliposomes have very rough surfaces, given the proteoliposome interface Porod exponents of ~ 3, and our samples have been shown to

Table 3.7 *Comparison of MscL proteoliposome preperation between the method used in this thesis and the method used by Grage et al. in their SANS study.[75]*

	Our Method	Method used by Grage *et al.*[75]
Lipid	3:1 POPC:POPG	DOPC
Protein incorporation	CFPE	Bacterial overexpression and reconstitution
Protein H/D	Hydrogenated	Deuterated
Protein tag	His_6	His_6

contain single MscL channels.

Variation in proteoliposome roughness between the 4 mg ml^{-1} and 5 mg ml^{-1} proteoliposomes is seen, however the protein:lipid ratio is not directly correlated in our small sample size.

We have not carried out a systematic investigation into the role of lipid composition or concentration on clustering of MscL channels, or the absence of clustering in our case. Previous literature has suggested the possibility of lipid mediated clusters i.e. into more preferable lipid domains within a bacterium.[231] However other research using simulations have suggested that weak protein-protein interactions would cause the dynamic clustering of channels.[173] Therefore it would be an intrinsic property of the proteins rather than lipid environment.

It is important to directly compare our results with previous characterisation of MscL containing proteoliposomes carried out by Grage *et al.*.[75] They observed substantial clustering of MscL channels, a calculated 278 MscL channels per 120 nm liposome at a 1:10 protein:lipid ratio. Grage *et al.* speculate that *in-vivo* the formation of such large clusters would increase the dynamic range of the osmotic response afforded by MscL. In spite of the fact that many theoretical investigations [19, 115, 231] have further investigated the role of clustering, we have no evidence for it in our in vitro system and indeed, van de Berg **et al.** [231], find no evidence for it *in-vivo*.

There are several key differences in the preparation of proteoliposomes between our study and the study of Grage *et al.*, these are compared in Table 3.7.[75]

Any of the differences highlighted in Table 3.7 could be contributing to the observation of clustering in one *in-vitro* mimetic (Grage), but not the other (this work). Different lipids were used so the mimetic membranes have different elastic properties which in turn could affect protein folding but also protein diffusion across the membrane. Deuterating the protein could affect the protein stability, as not all proteins retain conformation when deuterated, a small change in the conformation could increase protein-protein interactions resulting in clustering. However the mostly likely cause of clustering is the different protein expression method used. Traditional protein expression and reconstitution as carried out by T. Forysth for the Grage et al. paper, uses bacteria to over express the protein of interest into the bacterial membrane before isolating the protein into detergent. The protein is then transferred into the lipid construct desired by detergent-lipid exchange. It may be that the overexpression in bacteria created clusters that are not separated in the extraction process. The reconstitution process could also influence clustering as a mixed detergent-lipid system could phase separate influencing clustering, this would require some detergent being left in the system.

Overall the MscL proteoliposome preperation method used in this thesis has more in common with the native production in a bacterial environment. The lipid construct 3:1 POPC:POPG is widely used as a close mimic to bacterial membranes in charge and fluidity.[38, 76, 78, 127] We have avoided the inclusion of detergent in our system by using CFPE and our protein is in its hydrogenous state (other than for exchangeable hydrogens). Our results suggest that the clusters observed by Grage *et al.* are an affect of the preparation method used rather than an intrinsic property of the MscL protein.[75] There is to date no evidence of untagged MscL clustering *in-vivo*.[231]

Our results should highlight the importance of choosing an appropriate expression and work up methodology if *in-vitro* mimetic-based studies are to provide meaningful insight into *in-vivo* biological systems. Studies employing mimetics that are unrepresentative of the native biological system, run the risk of being physical science curiosities rather than providing useful information to tackle biological questions. Our results can guide future research in choosing appropriate expression methodology to avoid clustering of MscL channels and is useful in understanding of bacterial survival and design of biosensors for which MscL channels are of great interest.[82, 106, 141]

3.4 Behaviour of Proteoliposomes in the Presence of Simple Antimicrobials

3.4.1 Effect of Lyso-PC on MscL Channels

The Mechanosensitive Ion Channel of Large Conductance (MscL) gates in response to an increase in membrane curvature and membrane tension, enabling it to act in bacteria to prevent osmotic shock.[22, 220]

By changing the lipid environment of *in-vitro* MscL in liposomes the channel functionality can be modified. A difference in lipid-chain lengths results in differences in the sensitivity of channel gating in conductance and patch clamp measurements.[57, 77] The addition of short-chained lysophosphatidylcholine (lyso-PC), an inverted cone-shaped lipid with a single tail, has been shown to gate a number of mechanosensitive channels including MscL.[143, 175]

A proposed mechanism by which lyso-PC gates MscL channels is that asymmetric insertion of the molecule into bilayers induces a curvature in the membrane and changes the bilayer lateral pressure profile.[77, 176] Other mechanisms have been proposed suggesting direct interaction with the N-terminus of the MscL channel,[166] the mechanism is still under considerable debate.[246] Lyso-PC is now commonly used to test the activity of MscL channels in *in-vitro* systems.[75, 194]

The potential changes in the radius of gyration (R_g) and shapes of the scattering objects in our system are illustrated in Figure 3.11. FRET measurements have revealed that the diameter of the MscL pore formed on gating is about 30 Å.[239] Gating may also involve a conformational change of the C-terminal region of the MscL channel that protrudes from the membrane; the literature disagrees on both the extent of conformational change of the C-terminal domain and what role this would have.[7, 16, 47]

A solution of 14:0 lyso-PC (5 µl, 400 µM) in D_2O buffer was added to a 500 µl proteoliposome sample from the sample protein expression of proteoliposomes previously measured. Figure 3.12 shows the change of the scattering profile of proteoliposomes before and after the addition of lyso-PC in D_2O contrast buffer.

By showing the two SANS intensity curves together we can see the subtle

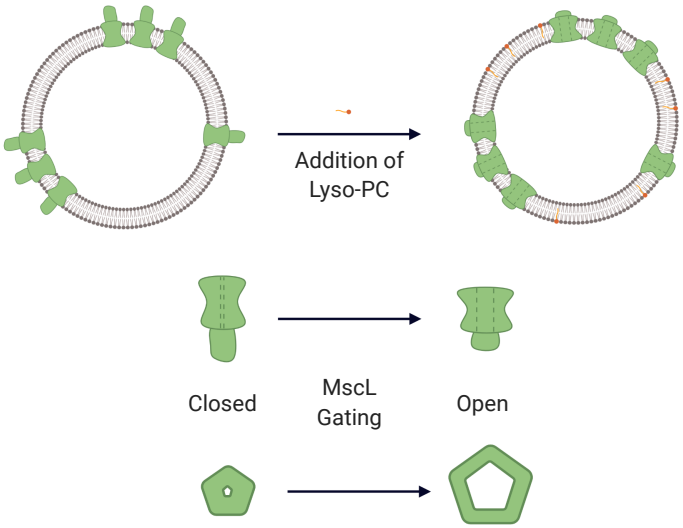

Figure 3.11 *Illustration of how insertion of lyso-PC into proteoliposomes may gate MscL channels and change their shape and radii of gyration.*

differences between the two samples. The Guinier-Porod fitting of this data and the fitted parameters are shown in Figure 3.13 and Table 3.8 respectively.

On addition of lyso-PC, a small increase in the fitted Radius of gyration of the $GP1$ region equating to the smaller cluster is seen from 26.1±2.6 Å to 29.5±1.2 Å.

MscL can be considered as a simplified shape of a uniform cylinder, see Figure 3.14.

The dimensions in Figure 3.14 are different to the literature lengths as there is much lower mass density in the c-terminal protrusion portion of the the protein, the dimensions chosen for the closed state result in a calculated R_g of 27.9 Å using the equation,

$$R_g^2 = (L^2/12) + (R^2/2), \tag{3.5}$$

where L is the length of the cylinder and R is the radius.

To estimate the change in R_g on gating, the dimensions of a simplified gated model of MscL were calculated, allowing for an increase in the protein diameter to 70 Å with a 30 Å pore based on current open channel models.[47] The model

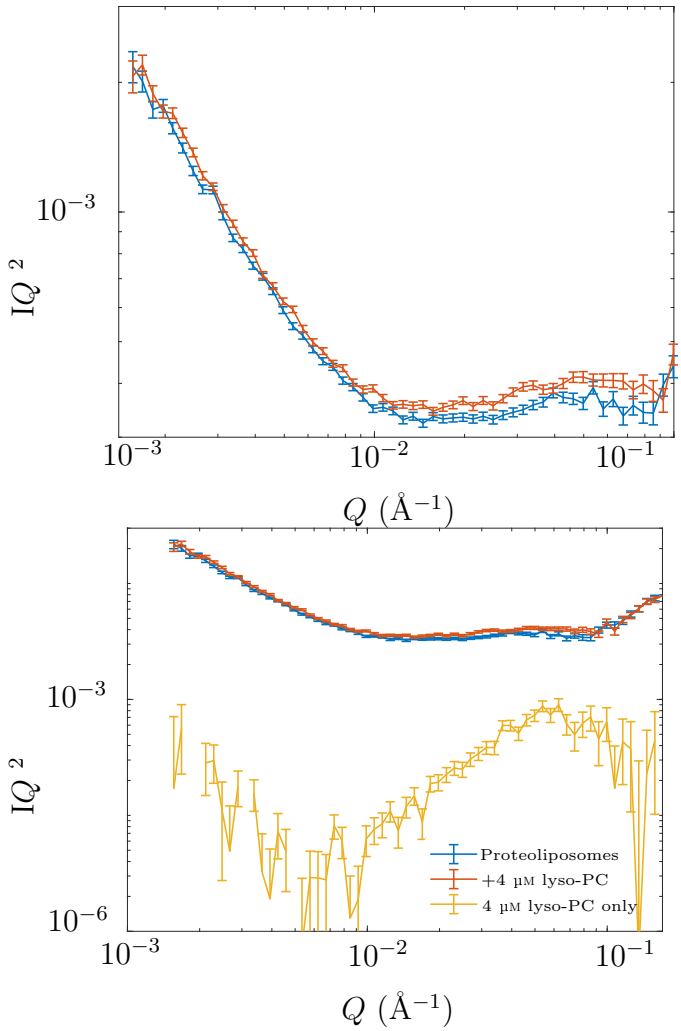

Figure 3.12 *Top:Small angle neutron scattering measurement of* 4 mg ml^{-1} *MscL-proteoliposomes in* D_2O *buffer before and after the addition of* 4 µM *lyso-PC, as a loglog plot of* IQ^2 *vs* Q*. Bottom: Same data as top panel with SANS of* 4 µM *lyso-PC in* D_2O *also plotted.*

assumes that a complete retraction of the protein protrusion (C-terminus) region occurs on gating, making the length of the protein 50 Å. Using these dimensions the radius of gyration on gating changes from 27.9 Å to 33.8 Å. It is worth noting that a larger change in radius of gyration would occur if the C-terminus regions stays mostly intact as some groups have suggested.[16, 245] Comparing the expected change in radius of gyration to the change we observe on addition of lyso-PC of an increase in 3 Å, suggests that not all of the channels in our proteoliposomes have gated.

The main difference in the fitted Guinier-Porod model of the proteoliposomes before and after the addition of lyso-PC is in the fitted s parameter, corresponding to the shape of MscL, more specifically the non-sphericity of MscL. Prior to

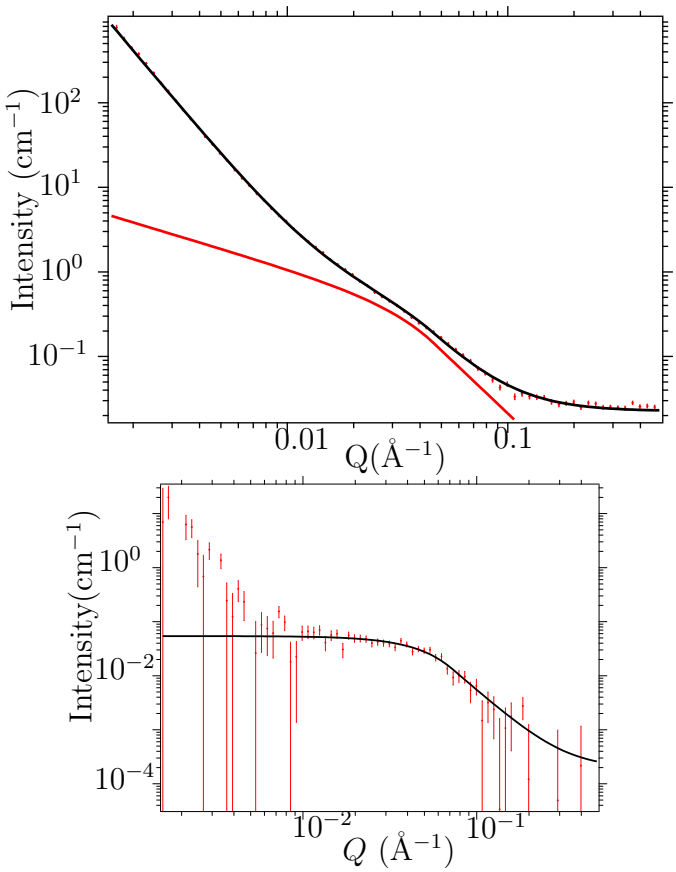

Figure 3.13 *TOP: Small angle neutron scattering measurement of* 4 mg ml^{-1} *MscL-proteoliposomes in* D_2O *buffer after the addition of* 4 µM *lyso-PC fitted to a 2-level Guinier-Porord model. Bottom:*4 µM *lyso-PC in* D_2O *buffer, fit to a single level Guinier-Porod model.*

lyso-PC addition $s = 0.96 \pm 0.03$, suggesting a rod shaped particle. After lyso-PC addition $s = 0.78 \pm 0.04$, somewhere between a spherical globular structure and a rod. This suggests that the differences between the radii of gyration projected onto the 3 Cartesian axes has decreased, which is consistent with the conformational change in gating.

The Porod exponent fitted to the second level of the fit does not change and viewing both SANS plots on the same graph shows little deviation at this low-Q region. This suggest little change to the overall surface of the proteoliposome with lyso-PC addition.

It's important to note that the deviation in the SANS curves is convoluted with the micellar phase of lyso-PC, as the micelles have a radius of gyration of 27.7(10) Å. The scattering curve from 4 µM lyso-PC micelles can be see in Figure 3.13 and overlaid in IQ^2 in Figure 3.12. Although the micellar phase is in the Q region of the protein scattering, the overlaid plots in IQ^2, in Figure 3.12 indicate that

Table 3.8 *Results of the two level Guinier-Porod fit to MscL-proteoliposomes before (Figure 3.6) and after addition of 4 μM lyso-PC (Figure 3.13) in D_2O buffer.*

Parameter	Before Lyso-PC		After Lyso-PC	
GP1				
s	0.963	±0.029	0.781	±0.035
G	1.33×10^{-2}	$\pm\ 1.70 \times 10^{-3}$	3.00×10^{-2}	$\pm\ 4.60 \times 10^{-3}$
R_g(Å)	26.1	±2.6	29.5	±1.2
d	3.24	±0.33	2.47	±0.05
GP2				
G	3.92×10^{12}	±0.10	3.52×10^{12}	±0.22
R_g(Å)	1×10^{6}		1×10^{6}	
d	3.14	±0.08	3.12	±0.06
χ^2	72.1		120	
Normalised χ^2	1.08		1.80	
Background	0.0281	±0.00174	0.0216	(fixed)

the scattering contribution from the micellar phase is low intensity and occurs at higher-Q to other observable changes in the scattering curve, i.e. the observation of increase in R_g is not due to contribution from a micellar phase, scattering from the micellar phase may result in an underestimation of the R_g of the protein since the micellar phase is not separately fitted in the model. A simple experiment to clarify this would be to use deuterated lyso-PC in D_2O buffer, unfortunately we do not have this data set for this thesis.

From the observations of the increase in radius of gyration and change in shape of the MscL in our proteoliposomes we can conclude that we have successfully expressed active protein channels. The magnitude of the change suggests that not all of the channels are gated at any one time.

3.4.2 Effect of the Antimicrobial Pexiganan on MscL Channels

Amphiphillic molecules other than lyso-PC molecules have been shown to gate MscL channels.[143] Pexiganan is an amphiphillic antimicrobial peptide known to insert into bacterial membranes.[73] Here we have tested Pexiganan (PXG) at a

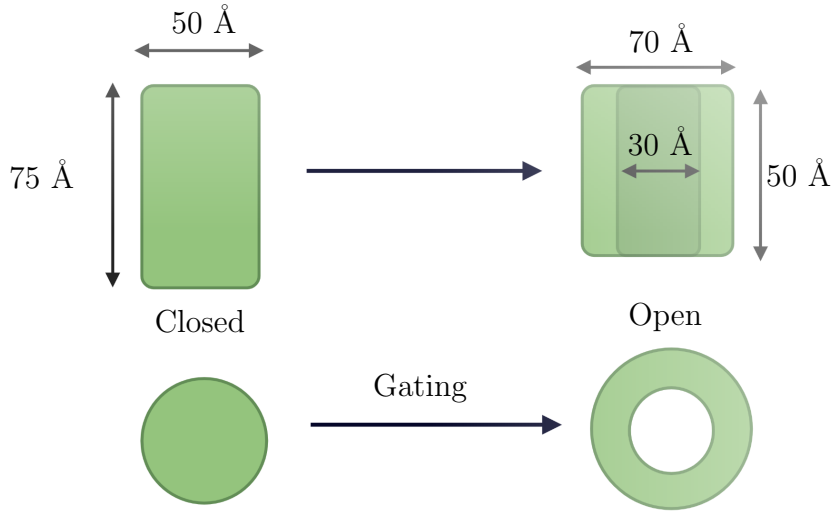

Figure 3.14 *Simplified dimensions of the protein MscL, before and after gating*

concentration close to its minimum inhibitory concentration of 4 µM to compare its effect on MscL clusters to the effect of lyso-PC.

5 µl of a 400 µM solution of pexiganan (PXG) in D_2O buffer was added to a 500 µl proteoliposome sample from the sample protein expression of proteoliposomes previously measured. Figure 3.15 shows the change in the scattering profile of proteoliposomes before and after the addition of pexiganan. Samples were measured as quickly as possible after the addition of pexiganan (measurement started with 30 minutes).

The difference in intensity of the scattering before and after the addition of pexiganan is largely due to the decrease in material in the pexiganan containing sample. This decrease in concentration occurs due to some of the proteoliposomes creaming out of the sample and therefore not being in the neutron beam path. It is clear it is an overall concentration decrease due to the decrease in intensity of the background at high-Q which is dependent on the amount of hydrogen in the sample and therefore the amount of incoherent scattering. Creaming may occur as the pexiganan interacts with the surface of the liposomes and may increase attraction between liposomes leading to some aggregation.

There are other observable changes in the features of the SANS curve which are better pinpointed with the Guinier-Porod analysis shown in Figure 3.16 and Table 3.9.

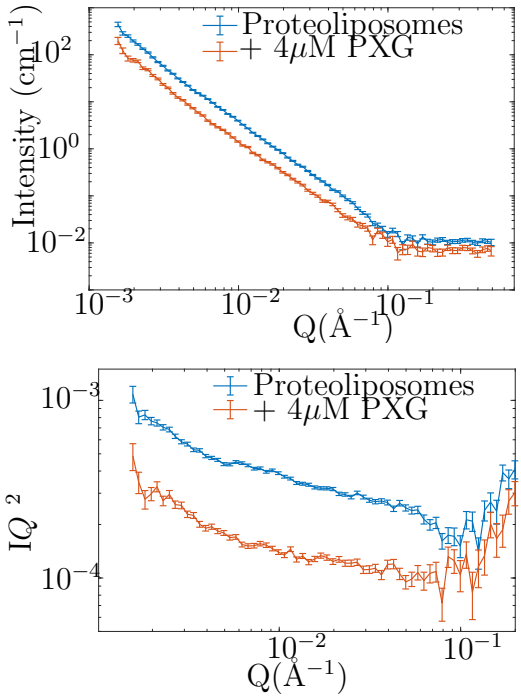

Figure 3.15 *Small angle neutron scattering curves of* 4 mg ml^{-1} *MscL-proteoliposomes in* D_2O *buffer before and after the addition of* 4 µM *pexiganan.*

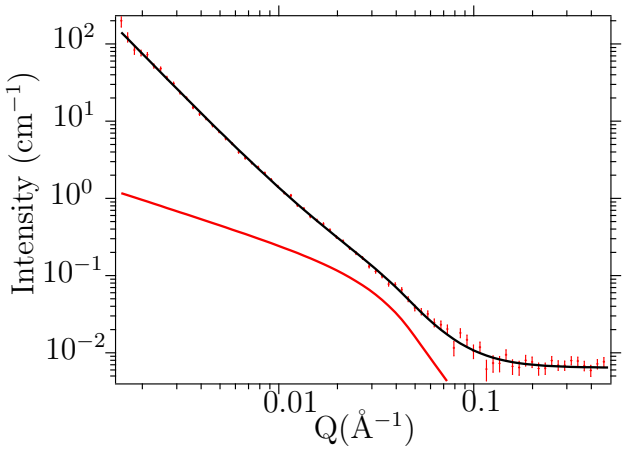

Figure 3.16 *Small angle neutron scattering measurement of* 5 mg ml^{-1} *MscL-proteoliposomes in* D_2O *buffer after the addition of* 4 µM *pexiganan fit to a 2-level Guinier Porod model.*

Comparing the fitted Guinier-Porod parameters determined for the sample before and after the addition of 4 µM pexiganan suggest that there are significant changes to the proteoliposomes. A large increase in the fitted radius of gyration for the GP1 region from the scattering from MscL is observed, much larger than seen when investigating lyso-PC. This could be due to a larger number of the channels being gated. Fitting of SANS measurements before and after the addition of

Table 3.9 *Results of the two level Guinier-Porod fit to* 5 mg ml^{-1} *MscL-proteoliposomes in* D_2O *buffer before (Figure 3.8) and after the addition of* 4 µM *pexiganan (Figure 3.16).*

Parameter	Pre-PXG addition		Post-PXG addition	
GP1				
$s1$	1.21	±0.03	0.816	±0.0943
G	2.7×10^{-3}	$\pm\ 2 \times 10^{-4}$	5.9×10^{-3}	$\pm\ 5.5 \times 10^{-3}$
R_g(Å)	29	±4.0	35.8	±3.3 (fixed)
d	3.5	(fixed)	3.5	(fixed)
GP2				
G	2.22×10^{10}	$\pm\ 2.91 \times 10^{9}$	1.68×10^{10}	$\pm\ 1.58 \times 10^{9}$
R_g(Å)	1×10^{6}		1×10^{6}	
d	2.51	±0.02	2.59	±0.01
χ^2	204.7		92.5	
Normalised Chi^2	1.35		1.14	
Background (cm^{-1})	0.009062		0.00598	

pexiganan in D_2O buffer contrast showed an increase in radius of gyration of the GP1 region, corresponding to single MscL channels from 29 ± 4 Å to 35 ± 3.3 Å. This is close to the change predicted from our simple model of gating presented in Section 3.4.1 from simple cylinder models, from 27.8 Å to 33.8 Å.

This experiment was repeated with a different contrast using proteoliposomes containing d31 lipids in H_2O buffer, see Figure 3.17.

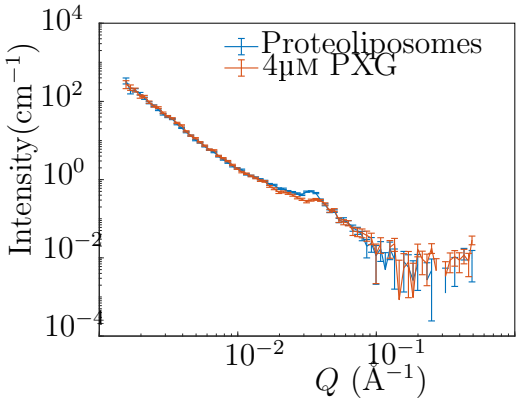

Figure 3.17 *Small angle neutron scattering measurement of* 4 mg ml^{-1} *MscL-proteoliposomes with partially deuterated lipids (d-31 POPC:POPG)in* H_2O *buffer before and after the addition of* 4 µM *pexiganan.*

The SANS curve has a prominent peak in these data sets, present both before

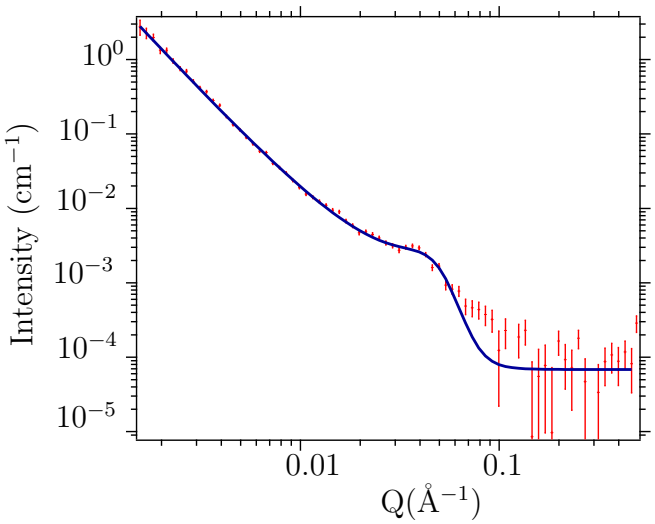

Figure 3.18 *Small angle neutron scattering measurement of* 5 mg ml^{-1} *MscL-proteoliposomes with partially deuterated lipids (d-31 POPC:POPG) in* H_2O *buffer after the addition of* 4 µM *pexiganan fitted to a Lorentz peak.*

and after the addition of pexiganan. As discussed in Section 3.3.6, the peak has been interpreted as a correlation peak between proteins embedded within a single bilayer as observed by Castorph *et al.*[30] The peak intensity decreases slightly as seen from the decrease in the magnitude of the peak pre-factor parameter in the Lorentzian peak fitting and also shifts to a higher Q value suggesting a decrease in the length scale of the scattering inhomogeneity. The peak width also increases suggesting a weaker correlation. The peak position changes from 0.0394 Å^{-1} to 0.0435 Å^{-1}, Assessing the peak position spacing a change from 159 Å for the proteoliposomes to 136 Å occurs after pexiganan addition.

Table 3.10 *Results of the Lorentz peak fitting to MscL-proteoliposomes in* H_2O *buffer.*

Fitting Parameters	Before PXG Addition	After PXG Addition
Porod exponent	2.91	2.91
B	1.15×10^{-7}	2.42×10^{-7}
R_g (Å)	1×10^{6} (fixed)	1×10^{6} (fixed)
Background (cm^{-1})	0.000628	0.0110
Peak Prefactor	74.0	104
Peak Position(Å^{-1})	0.0394	0.0469
Peak Width (Å^{-1})	0.0153	0.0201
Peak position spacing (Å)	159	136

If the protein channels are distributed evenly across the surface of the proteoliposomes, in the manner of the black pentagonal patches of a soccer ball, then a correlation feature would be present for the average distance between clusters. The decrease in this length after the addition of pexiganan suggests that the distance between clusters decreases as the channels gate. The decrease in the intensity of the peak and increase in peak width, would suggest some decrease in strength of the correlation which may occur if only some of the channels gate and a larger range of distances occur.

3.4.3 Conclusion on the Effect of Antimicrobials on MscL–Proteoliposomes

In this section, we used small angle neutron scattering to observe the gating of MscL channels in the presence of the amphiphillic molecules lyso-PC and pexiganan. In the presence of lyso-PC, the radius of gyration of the protein increased from 26.1±2.6 Å to 29.5±1.2 Å. In the presence of pexiganan, the increase was larger from 29.0 ±4Å to 35.8 ±3.3 Å. This suggests that whilst some channels gated in 4 µM lyso-PC, a greater proportion if not all of the channels gated in the presence of 4 µM pexiganan.

On both the addition of lyso-PC and pexiganan, the dimensionality parameter s decreased, suggesting a small change from a rod-shaped object towards a more globular shape. This is consistent with some re-arrangement of C-terminal protrusion as well as the in-plane expansion associated with gating of the MscL channel.

This is the first time the antimicrobial pexiganan has been shown to gate MscL and opens up the possibility of alternative antimicrobial mechanisms for the peptide other than a mechanism by which it assembles its own pore in the membrane. The 4 µM concentration shown here is consistent with the concentration pexiganan has been shown to cause cell death and membrane leakage but a lower concentration than the observations of a toroidal pore formation.[64] [185] [81]

Since the mechanosensitive ion channel of large conductance is found in many harmful bacterial strains and has a highly conserved structure and function it has been labelled as one of the top 20 suggested drug targets.[11] Other drugs have been shown to bind to MscL resulting in cell death [107], however an antimicrobial

that mechanism involves indirectly stimulating the MscL channel through the membrane may encounter fewer issues with resistance as it exploits the protein's function rather than structure. By showing that lyso-PC and pexiganan similarly force MscL to gate, and to remain gated over the period of an hour to be measured by SANS we opened a new possibility of antimicrobial drug development and targeting.

Chapter 4

Suspended Bilayers at the Air-Water Interface: observing MscL in planar lipid bilayers.

4.1 Introduction

The interest in bacterial membranes as drug targets for antimicrobial treatments has led to the development of several planar mimetic systems to facilitate investigation by surface sensitive techniques. [42, 46, 152] In this chapter we describe the development of a novel membrane mimetic combining advantages of floating bilayer systems [32] with the convenience of supported bilayers prepared by vesicle rupture. [56] The novel system has been used to gain an insight into the mechanism of the antimicrobial peptide (AMP) pexiganan. Our membrane mimetic incorporating the Mechanosensitive Ion Channel of Large Conductance (MscL) was used to test our hypothesis that pexiganan could gate the channel, in-line with previous studies that have observed gating of mechanosensitive channels in the presence of amphiphilic molecules. [143, 155, 176]

4.1.1 Background

Membrane protein conformation and function is traditionally determined from crystal structures using X-ray diffraction or at high concentrations of the proteins

stabilised in detergents using X-ray diffraction, NMR and EPR. Observing conformational changes of membrane proteins in lipid membranes, in an environment that more closely resembles their natural state in a bacterium is still a considerable challenge. By rupturing proteoliposomes into a planar bilayer suspended beneath a surfactant monolayer, we are able to use neutron reflectivity and FTIR to make inferences on the distribution of lipids and protein within a model bilayer. The model bilayer, by virtue of being suspended beneath the air-water interface, is free from constraints imposed on either solid supported or tethered bilayers. When investigating the mechanosensitive ion channel of large conductance (MscL), removal of constraints is crucial to observing its conformational changes, as it will allow greater change in lipid packing and bilayer curvature.

4.1.2 Suspended Bilayer Formation

In this chapter, a new platform is introduced to analyse bacterial lipids and proteins. The suspended bilayer is a membrane mimic composed of a bilayer suspended a few Angstroms under a surfactant monolayer at the air-water interface. A diagram depicting the model membrane structure is shown in Figure 4.1.

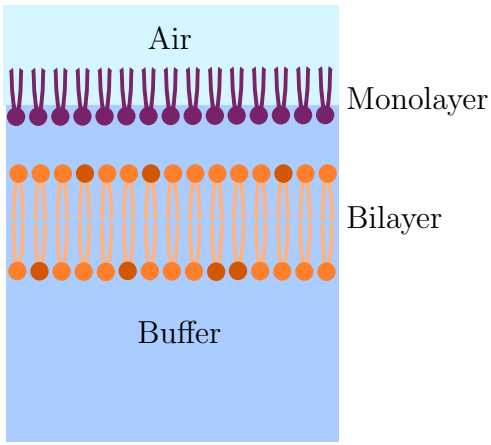

Figure 4.1 *Lipid bilayer membrane mimic graphic*

Forming a high coverage lipid bilayer requires optimisation of sub-phase conditions (in this case the solution phase) in order for vesicle rupture to occur. Vesicle rupture is dependent on the bending energy of the lipid bilayer, the vesicle to substrate contact energy and the energy associated with osmotic pressure.[109][248] Each of these is controlled through a combination of lipid

composition, vesicle diameter, ionic concentration, temperature, substrate and divalent cation concentration.[187]

Much of the literature on the effect of salt concentration on liposome rupture has been carried out as solid interfaces, commonly amorphous silicon oxide, SiO_2, for which the liposome to substrate contact energy dominates to a greater extent than in the system described herein. The effect of NaCl on liposome rupture is multi-fold, as it can give rise to differences in osmotic pressure between the inside and outside of the liposome and decrease the Debye-length, decreasing electrostatic repulsion between the lipid head groups and the substrate. Liposome rupture occurs in multiple stages: individual liposomes adsorb to the surface (surface-liposome interactions are dominant here) and at a critical coverage (aided by liposome-liposome interactions) the vesicles rupture to form a bilayer. The pathway of liposome rupture is shown in Figure 4.2. NaCl aids the adsorption of vesicles to surfaces, although at higher concentrations the rate of adsorption decreases as the liposomes are deformed in solution, increasing the hydrodynamic radius and hence reducing the rate of diffusion. [109] [221]

Calcium ions are also often used in bilayer formation. Calcium ions reduce the critical coverage of adsorbed vesicles needed before vesicle rupture at low concentration of 5mM for zwitterionic lipids.[201] Divalent ions reduce vibrational freedom of the lipid head groups, decreasing the hydrodynamic radius even at 1mM concentration of $CaCl_2$.[151] Calcium is also known to induce vesicle fusion in solution at 5mM concentration through bridging interactions. [168]

4.1.3 Gating of the Mechanosensitive Ion channel of Large Conductance

The role of the Mechanosensitive Ion Channel of Large Conductance (MscL) is to gate in response to a sudden change in osmotic pressure, increasing the probability of bacterial survival.[144] In bacteria, the gating of the MscL occurs when a bacterium moves to an environment of low osmolarity. In this low osmolarity environment the bacterium takes in water through diffusion and the cell expands increasing its membrane curvature and membrane tension. This causes the MscL to gate, opening its large 30 Å pore, releasing some of the contents of the cell.[49] This brief gating of the channel returns the cell to it's original size and reduces the pressure, preventing cell rupture.[129]

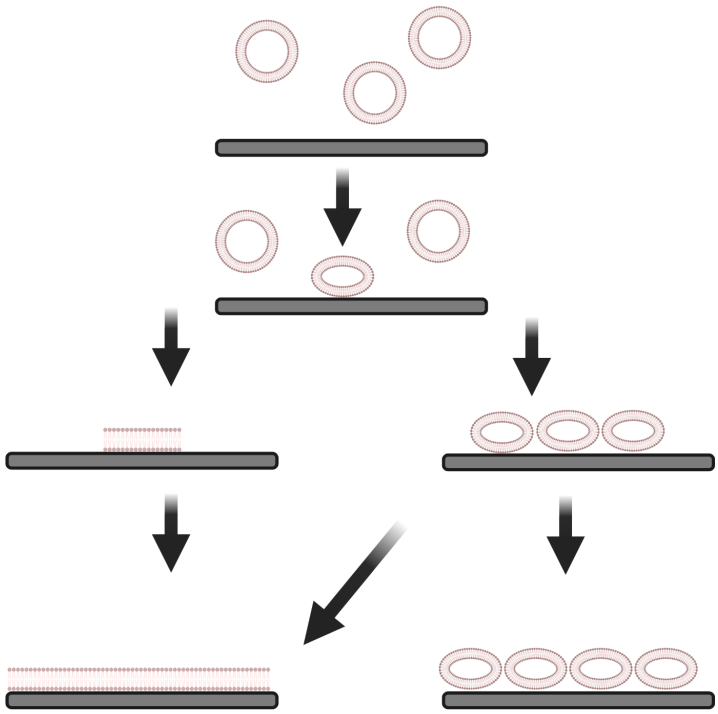

Figure 4.2 *Graphic depicting different pathways of vesicle deposition, (left) when surface-lipid interaction dominate and single vesicle rupture occurs and (right) when vesicle rupture occurs when liposome-liposome interactions dominate and a minimum coverage needs to occur before vesicle rupture.*

In addition to osmotic shock, MscL is known to gate in response to a change in potential across the membrane and in response to the insertion of amphiphilic molecules into the membrane.[143, 155, 175] The gating in response to amphiphilic molecule insertion is of particular interest to us, as it presents an alternative hypothesis as to how antimicrobial molecules cause membrane leakage; pores need not be formed, if instead native pores can be triggered to open. The mechanism by which amphiphilic molecules cause the gating of MscL is contentious.[157, 160, 176] It was originally thought that differential insertion of amphiphilic molecules increases membrane tension sufficiently to gate MscL channels.[143, 176] However, more recent studies point to membrane thinning effects as asymmetric insertion is not required.[52, 166] Other studies suggest amphiphilic molecules interfere with MscL-membrane coupling given that the effect of lyso-lipids is not directly correlated with an increase in membrane tension.[157]

On gating, the MscL forms a water-filled pore in the membrane of 30 Å, which has been confirmed through particle leakage, FRET and EPR measurements.[47,

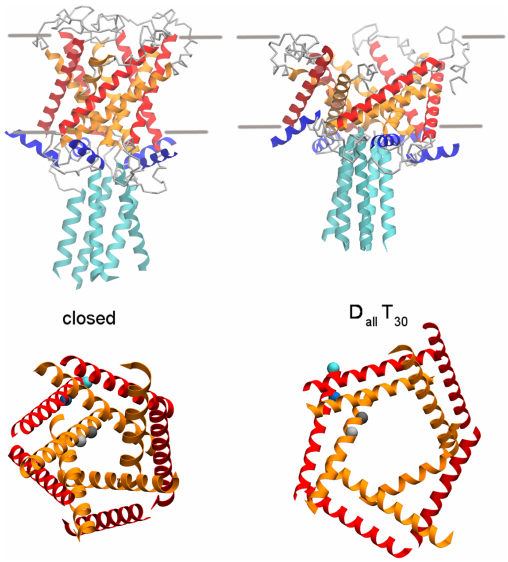

Figure 4.3 *Figure taken from Deplazes et al. [52]. Coarse grained molecular dynamics simulations restrained to FRET and EPR measurement of MscL in closed and open ($D_{all}\,T_{30}$) states.*

49, 239] This is a significant in-plane expansion of the channel. What is less agreed upon in literature is what happens to the c-terminus domain of the channel, coloured light blue in Figure 4.3. The c-terminus protrudes out from the membrane, with the crystal structure suggesting it protrudes about 35 Å from the bilayer in the closed state of MscL.[31] Studies using Electron Paramagnetic Resonance (EPR) and Molecular Dynamics (MD) simulations investigating the behaviour of the c-terminus during gating have resulted in different conclusions. One school of thought is that the c-terminus remains in the same position to act as a molecular sieve, to avoid loss of other macromolecules from the cytoplasm.[16, 245] Other groups suggest a complete or partial rearrangement of the c-terminus domains. [25, 47]

4.1.4 Aims

The principal goal was to develop a bilayer system incorporating MscL. By using neutron reflectivity to investigate conformational changes between the unperturbed state in the presence of the AMP pexiganan we had a secondary goal of gaining an insight into the mode of action of pexiganan. Our suspended bilayer construct is free from constraint other than that of the surrounding lipids, much like in its native bacterial environment.

Ellipsometry and Reflection Absorption Infrared Spectroscopy (RAIRS) experiments were used to find the ideal buffer, monolayer and liposome conditions for forming a single suspended bilayer underneath a monolayer at the air-water interface. Through careful design of the air-water trough used to contain the sub-phase for our neutron reflectivity measurements, we were able to form a single suspended bilayer, free from excess liposomes. By rupturing the protein containing liposomes (proteoliposomes), we were able to characterize MscL in the suspended bilayer.

4.2 Ellipsometry from suspended lipid bilayers.

4.2.1 Method

Ellipsometry measurements were carried out on a Beaglehole Picometer Light Ellipsometer at the Partnership for Soft Condensed Matter (PSCM) at the EPN campus (Grenoble, France). An explanation of Ellipsometry as a technique and a definition of the measurement parameters was given in the background chapter Section 2.5.9. A small laminar flow trough of 8 cm by 10 cm was used for all measurements and cleaned sequentially using Decon90 and ethanol before rinsing thoroughly with Milli-Q water. The measurements were made in 20 mM HEPES buffer containing 150 mM NaCl at pH 7.4.

Liposomes were prepared by dissolving the requisite amount of POPC:POPG in the minimum amount of chloroform. The chloroform was then evaporated under a stream of nitrogen and the lipid film rehydrated in HEPES buffer (20 mM,pH 7.4, 150 mM NaCl). The lipid solution was then sonicated at room temperature for 30 minutes before being extruded through 100 nm filters using the Avanti mini-extruder, a minimum of 11 times, after which the liposome solution is opalescent.

A measurement was first made of the clean air-water interface with agreement with the expected Brewster angle confirming that the interface is free from even molecular impurities.

A monolayer of the surfactant, Dimethyldioctadecylammonium bromide (DODAB), was prepared using a Hamilton syringe to spread 7.5 µl of a solution of 2 mg ml^{-1} DODAB in chloroform on the interface that is equivalent to an area per molecule of 55 $Å^2$ $molecule^{-1}$. After waiting 5 minutes for the chloroform to evaporate

completely a second ellipsometric measurement was made from the monolayer at angles from 30-70°. The laminar flow trough, detailed in the Appendix, enabled the subphase to be replaced underneath the monolayer by using two plastic syringes, pushing solution under the monolayer with one syringe whilst withdrawing the same volume out of the trough with the other syringe. Using this method a 0.1 mg ml^{-1} 3:1 POPC:POPG liposome solution was passed underneath the monolayer. The time taken to exchange was about 5 minutes. The start time of the time resolved measurement was five minutes after sub-phase replacement.

4.2.2 Results

Ellipsometry measurements were made of the clean interface, the surfactant monolayer and 1 hour after a 0.1 mg ml^{-1} liposome solution was passed under the DODAB monolayer, followed by 10 ml of buffer solution, see Figure 4.4.

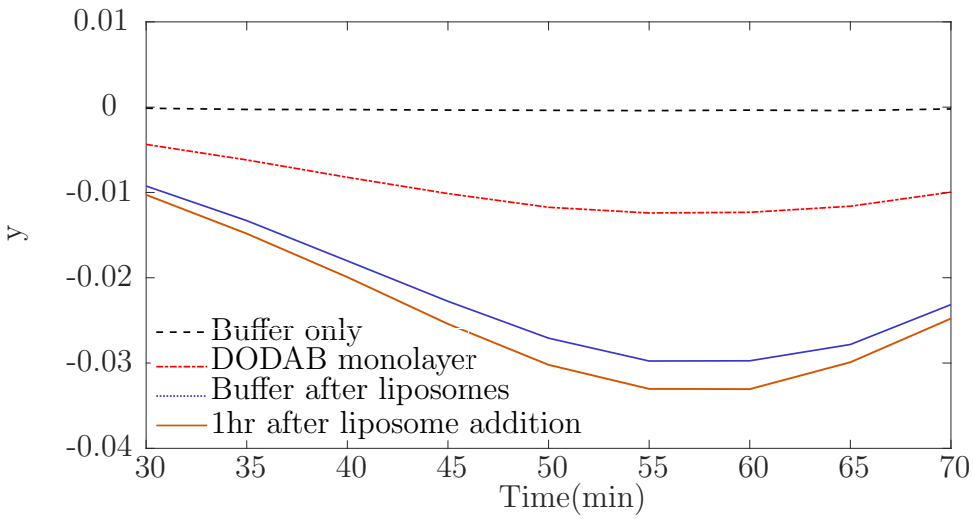

Figure 4.4 *Ellipsometry measurements taken at angles from* 30 *to* 70° *indicating the increase in refractive-index and thickness of material at the air-water interface.*

The parameter y is inversely proportional to the difference in refractive index of the materials and to the film thickness (analogous to the contrast in neutron scattering experiments). The decrease in y after spreading the monolayer and further decrease following the addition of liposomes show that both of these steps create a significant increase in material at the interface. Exchanging the subphase under the monolayer with 10 ml of 150 mM NaCl containing HEPES buffer (20 mM,pH 7.4) resulted in a small increase in y, suggesting some removal of material from the interface. From ellipsometry alone it is not possible to be

certain whether this lipid material is distributed as the desired bilayer, or instead a layer of vesicles, since the distal part of such a layer has a very high volume fraction of water, and thus a low contrast. Ellipsometry did however provide a first indication that lipid material will accumulate underneath a surfactant monolayer.

Measuring at a single angle (55°), the change in y with time after exchange under the monolayer of the subphase by a 0.05 mg ml^{-1} liposome solution is shown in 4.5.

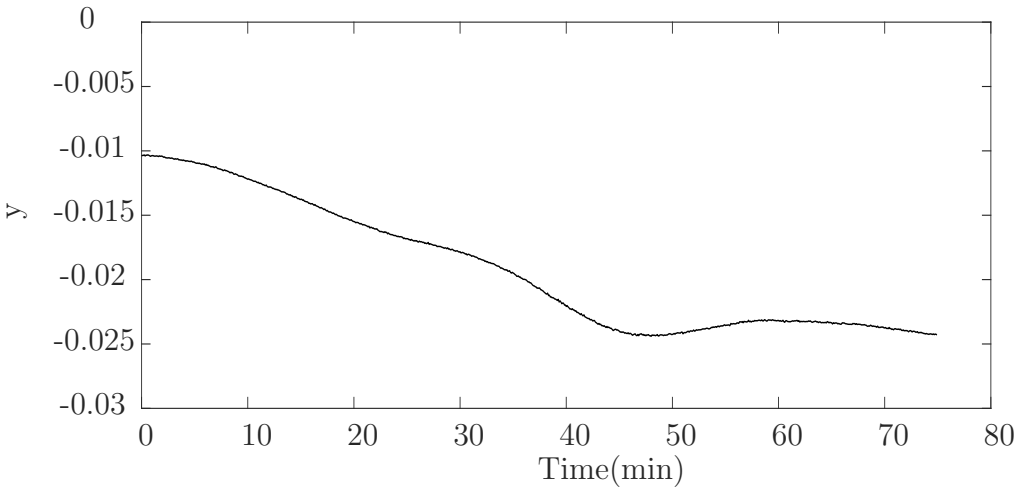

Figure 4.5 *Ellipsometry measurements taken at angle of* 55° *indicating the increase in refractive-index and thickness of material at the air-water interface.*

The minimum in y occurs after 45 minutes, after which we observe a small increase, followed by the start of a plateau. The decrease in y is proportional to the maximal surface excess but is also somewhat sensitive to the distribution of material at the interface. The gradient of the curve is not linear, which is not unusual with bilayer formation as you can expect multiple processes to be taking place. The curve suggests an initial absorption of liposomes at the interface occurred, with rupture of the liposomes occuring in multiple stages over time. This could suggest some initial rupture at low liposome coverage and a further liposome rupture process once a critical coverage has been reached.

4.2.3 Discussion

Ellipsometry measurements show that by replacing the subphase under a DODAB surfactant monolayer with a solution of 3:1 POPC:POPG liposomes we can

observe an increase in material present at the air-water interface. The increase in material is consistent with the formation of a bilayer, however ellipsometry alone cannot determine if we have a single uniform bilayer or a layer of vesicles or indeed a mixture of these two possibilities.

4.3 Reflection Absorption Infrared Spectroscopy of Suspended Bilayer Formation

4.3.1 Method

The Reflection Absorption Infrared Spectroscopy (RAIRS) spectra were collected at room temperature on a Thermo Scientific Nicolet iS50 FT-IR Spectrometer in the spectral range 900-4000 cm^{-1}, using a liquid-nitrogen cooled MCT (Mercury-Cadmium-Telluride) detector. The acquisition time of each measurement was 5 minutes (1024 co-added spectra). Before each measurement a series of background spectra was acquired from the air-water interface that had been cleaned by aspiration. These background spectra were used to normalise the sample spectra. The errors on the integrated band intensities were estimated by measuring a background-corrected spectrum of the clean buffer interface and integrating the area over the spectral region in which we observe the CH_2 asymmetric stretch band.

4.3.2 Results

Initially a small Langmuir-like trough (10 cm by 2.4 cm), designed by Luke Clifton (ISIS neutron and muon source), with a single barrier was used. A monolayer of DODAB was spread to the desired area per molecule (55 $Å^2 molecule^{-1}$) on an aspirated buffer interface and a solution of 5 mg ml^{-1} of 3:1 POPC:POPG liposomes was injected under the barrier to the desired concentration of 0.1 mg ml^{-1}. A range of NaCl and $CaCl_2$ concentrations were tested, over a range that previous studies had shown to be effective for bilayer formation. [109, 188]

In Figure 4.6, the results obtained using 75 mM and 150 mM NaCl buffer are compared, in the absence and presence of 2 mM $CaCl_2$. HEPES buffer in D_2O (20 mM, pD 7) was used as the base buffer, to avoid H_2O bands in the spectral

region of the CH_2 bands.

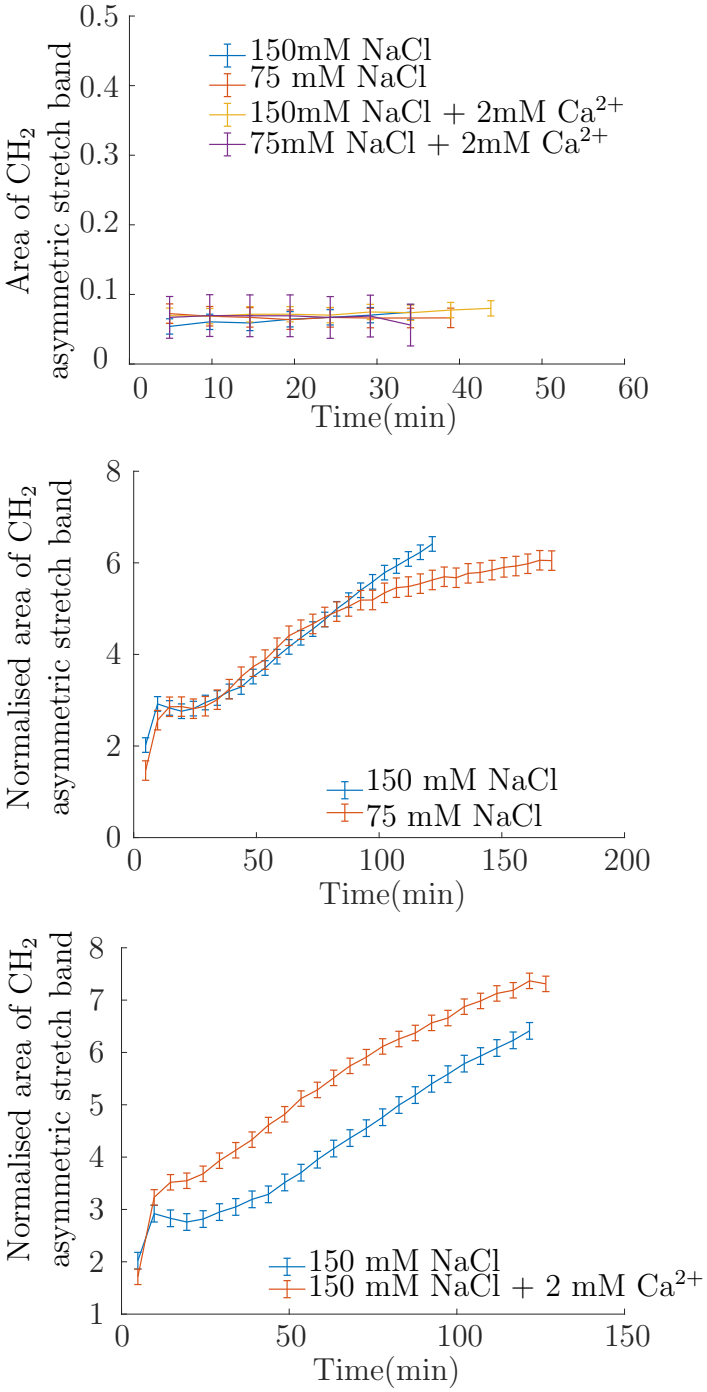

Figure 4.6 *Plots show the integration of the CH_2 asymmetric stretch bands over time after TOP: Spreading of a DODAB surfactant monolayer at the buffer-air interface, Middle: after the injection of 3:1 POPC:POPG liposomes to a concentration of* 0.2 mg ml^{-1} *in the trough in* 75 mM *and* 150 mM *NaCl. Bottom: after the injection of 3:1 POPC:POPG liposomes to a concentration of* 0.2 mg ml^{-1} *in the trough in* 150 mM *NaCl in both* 0 mM *$CaCl_2$ and* 2 mM *$CaCl_2$.*

The intergrated band intensity for the CH_2 bands of DODAB are equivalent in all measured buffers i.e. all measured values are within one error bar, see Figure 4.6 top figure. After the injection of liposomes, see middle and bottom figures of Figure 4.6, an immediate increase in the measured area of the CH_2 absorption bands is observed. This increase reaches a plateaus after about 10 minutes at a normalised area of around 3 and then continues to increase slowly. Given that the monolayer was spread to an area per molecule (APM) of 55 $Å^2$molecule^{-1} and estimating that the suspended bilayer has an APM of 60 $Å^2$molecule^{-1} (expected for a high-coverage POPC:POPG bilayer), then on forming the suspended bilayer one might expect the number of CH_2 groups to increase by a factor of 1.7 compared to the monolayer. This results in a normalised area of the CH_2 band of around 2.7.

It is worth noting that the RAIRS measurement is sensitive to a depth of about one micron from the interface and we are not able to distinguish between adsorbed vesicles/partially ruptured vesicles or bilayers. As shown in Figure 4.6, we observe little difference between the two NaCl concentrations but an increase in adsorbed material at the interface with increased calcium ion concentration.

Rupture of zwitterionic POPC only liposomes was also studied, to investigate the role of the negatively charged POPG in the deposition of lipid material at the interface. Partially deuterated lipids were used so that the accumulation of lipid could be observed by by examining the CD_2 stretching region of the spectrum. In Figure 4.7 we compare the increase in material underneath the surfactant monolayer after the addition of d-POPC liposomes and d:31 POPC:d-31 POPG liposomes. For POPC liposomes in calcium-free buffer no significant increase in the CH_2 stretch bands or CD_2 stretch bands is observed. With 2mM $CaCl_2$ present in the buffer, a small increase in area of the CD_2 stretch bands is present but to a much lower extent than when 3:1 POPC:POPG liposomes were used. From this we conclude that a difference in charge between the DODAB of the monolayer and the POPG in the liposome appears to play an important role in the accumulation of POPC:POPG lipid at the interface.

The measurements at 150 mM NaCl were repeated on a larger trough with dimensions 23.8 by 7 cm (surface area 166.6 cm^2 using a 60 ml volume of buffer. The method was repeated as described previously, spreading the DODAB at a volume and concentration that should equate to an area per molecule of 55 $Å^2$molecule^{-1} and injecting a high concentration of vesicles so that the concentration in the trough was 0.1 mg ml^{-1}. As the vesicles were injected

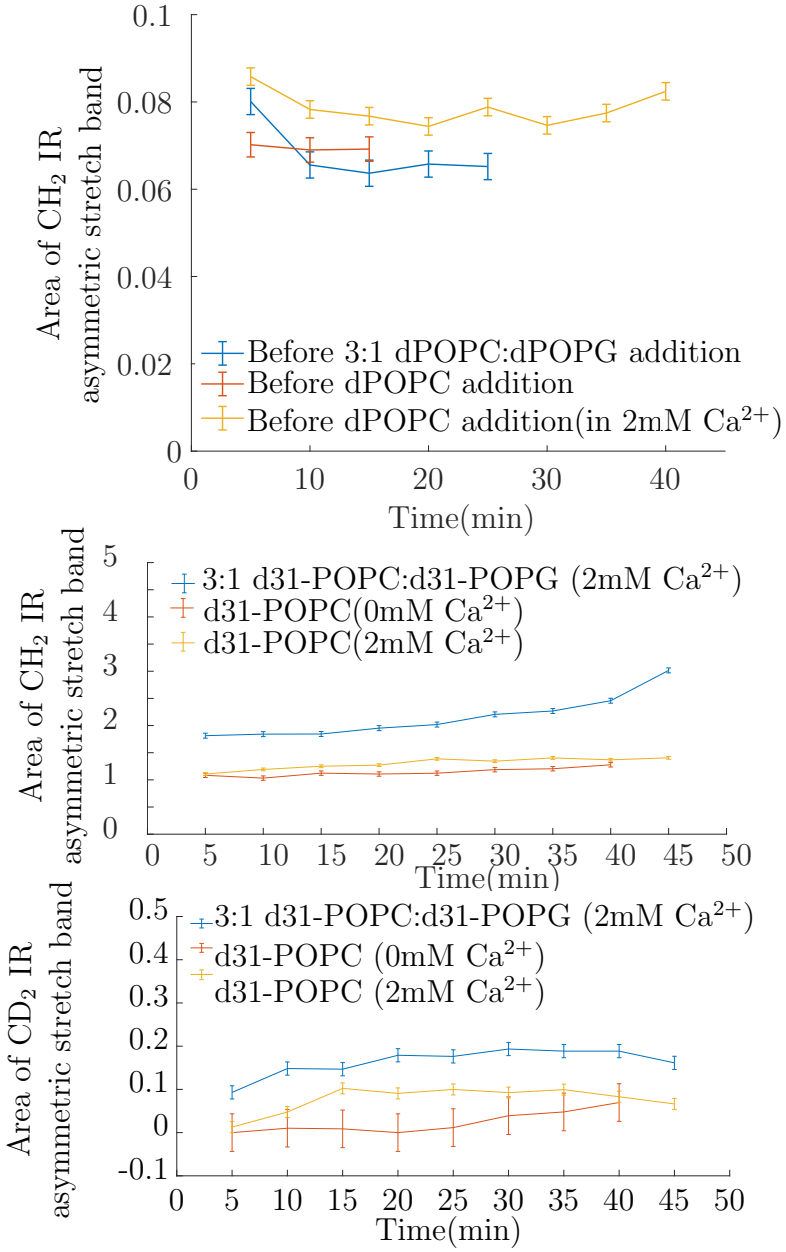

Figure 4.7 *Top and middle plots show the integration of the CH_2 asymmetric stretch bands over time after TOP: Spreading of a DODAB surfactant monolayer at the buffer-air interface, Middle: after the injection of 3:1 d-31 POPC:POPG liposomes or POPC only liposomes to a concentration of* 0.1 mg ml^{-1} *into the trough. Bottom plot shows the area of the CD_2 asymmetric stretch bands over time: after the injection of 3:1 d31-POPC:POPG liposomes or d31-POPC liposomes to a concentration of* 0.1 mg ml^{-1}.

another syringe was used to remove an equal volume of buffer so as to keep the height of the interface constant.

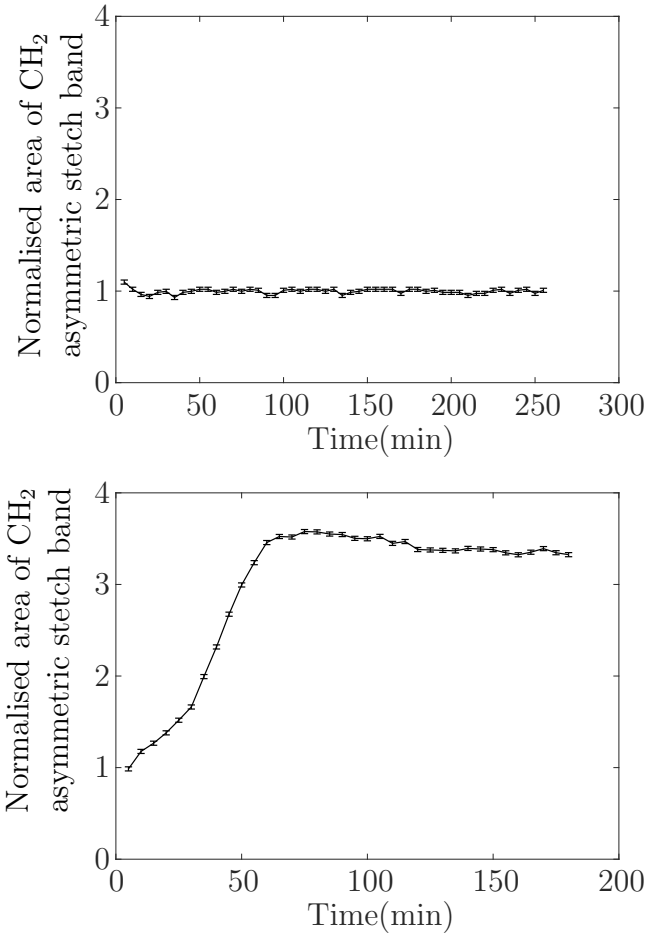

Figure 4.8 *Plots showing the area of the CH_2 asymmetric stretch bands over time after TOP: Spreading of a DODAB surfactant monolayer at the buffer-air interface and BOTTOM: after the injection of 3:1 POPC:POPG liposomes to a concentration of* 0.1 mg ml^{-1} *into a large trough containing* 20 mM *HEPES buffer,* 150 mM *NaCl at pD*7

Figure 4.8 shows that the time taken for adsorption of vesicles is longer in the larger trough showing that this method of injection is strongly diffusion-limited. For neutron reflectivity we used a laminar flow trough that replaces the buffer solution in the trough at a rate of 1 ml min^{-1} with a liposome solution, see the Appendix for details of the trough set-ups used.

4.3.3 Discussion

From the infrared experiments, it was determined that the optimum conditions for suspended bilayer formation were to inject 0.1 mg ml^{-1} liposomes in 150 mM NaCl 20 mM HEPES buffer underneath a monolayer of DODAB. Measurements

showed that the system is sensitive to NaCl concentration, Ca^{2+} concentration and the lipid composition. A higher amount of adsorbed material accumulated at the interface in the presence of calcium salt, higher than that we would expect for a bilayer. Other research has found that that calcium can facilitate multilayer formation.[168] Given these observations, we decided to progress our studies using only NaCl salt. Measurements using different troughs indicated that simply injecting liposomes into the sub-phase to reach the desired concentration would result in strongly diffusion limited bilayer formation, which motivated us to design the laminar flow trough we used in subsequent reflectivity measurements.

4.4 XRR Characterisation of DODAB Monolayer and Suspended Bilayers

X-ray reflectivity (XRR) measurements were performed with the aim of obtaining an additional contrast, that might help reveal some additional structural features, particularly relating to the distribution of the head groups in both the DODAB monolayer and within the suspended bilayer. As this was the final experiment on suspended bilayers, we also sought to make a final improvement to the methodology for forming the suspended bilayer. Motivated by the quicker measurement times in XRR compared to NR for this system, we wanted to reduce the overhead associated with the preparation of the DODAB monolayer. Through the two iterations of our NR trough, and accumulated experimenter skill, we had refined this process, but still the formation of a dense monolayer without rupture, by spreading alone had the potential to provide a bottleneck when two troughs were to be used; adding one too many drops of monolayer solution causes rupture, necessitating aspiration of the surface and the spreading to be recommenced. To decrease the probability of monolayer rupture, rather than spreading to a surface pressure of 30 mNm^{-1}, we instead designed a trough on which a monolayer to be spread to 10 mNm^{-1} and then compressed to 30 mNm^{-1} by means of a movable barrier that would form one wall of the trough parallel to the incident X-ray beam direction; the idea being inspired by the movable booms that are employed in swimming pools. Although the new flow trough seemed to work well, and definitely did greatly increase the ease of monolayer formation, being unable to analyse the XRR data in real-time meant that we were missing one crucial piece of feedback, that would have helped us to explain during the experiment why we were unable to form a complete suspended bilayer.

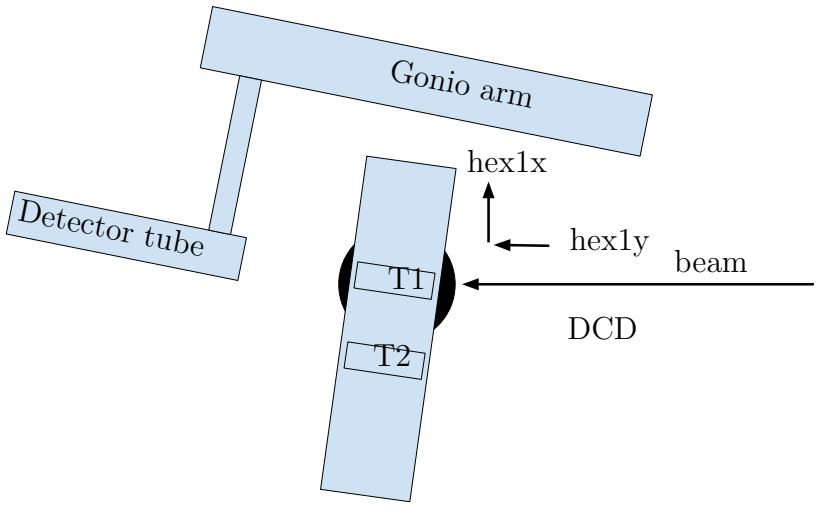

Figure 4.9 *Set up of X-ray reflectivity experiment on I07 at Diamond Light Source where T1 and T2 are the two troughs.*

Here I present the elements of the method that were specific to this synchrotron XRR experiment and the analysis of the data measured from the DODAB monolayer, since this provides a post-hoc rationalization of why suspended bilayer formation was not successful in this experiment, whereas it had become a robust procedure during the neutron reflectivity experiments.

4.4.1 Method

X-ray reflectivity measurements from the air-water interface were performed on I07 at Diamond, Oxfordshire, in standard double crystal deflector (DCD) set-up with an X-ray beam energy of 12.5 keV using two custom built laminar flow troughs. Data was collected over a Q_z range of $0.1 \leq Q_z \leq 0.6$ Å^{-1} and five levels of beam attenuation to compensate for the differing reflected intensities at the different Q_z, using the pilatus 1 detector. A diagram of the instrument set up is shown in Figure 4.9.

Two Generic Data Acquisition (GDA) software-controlled syringe pumps were used, with each pump being used in a push/pull mode to simultaneously inject and withdraw liquid from rows of inlet and outlet holes in the base of the trough to generate a laminar flow that exchanges the sub-phase underneath the monolayer,

see the Appendix section for greater detail.

Two identically machined laminar flow troughs were used: this was the final iteration of our trough design and included a barrier that ran parallel to the incident beam. The syringe pumps used were different models than used for neutron reflectivity experiments because of compatibility with the GDA and buffer solutions were injected in glass syringes at a rate of 6 $\mathrm{ml\,min^{-1}}$.

Our set-up allowed for surface pressure to be measured during preparation of the monolayer. The barriers allowed for the DODAB to be spread at 10 $\mathrm{mNm^{-1}}$ and then compressed to 30 $\mathrm{mNm^{-1}}$. This is preferable to spreading at a high surface pressure as this can result in the monolayer breaking. Spreading at a low surface pressure gives greater control and should result in higher reproducibility. Surface pressure measurements were made using a Wilhelmy plate,a thin piece of filter paper oriented perpendicular to the interface, and the force exerted on it was measured. The Wilhelmy plate was submerged in the experiment buffer for at least 30 minutes before assembling at the interface.

Data reduction was carried out by Andrew McCluskey, Diamond Light Source and analysed in RasCAL.

4.4.2 Results

The surfactant monolayers were prepared by spreading DODAB (0.25 mg $\mathrm{ml^{-1}}$ in chloroform) to a surface pressure of 10 $\mathrm{mNm^{-1}}$ and then compressed to 30 $\mathrm{mNm^{-1}}$ ($\sim$75% of the spread area) using a barrier that runs parallel to the incidence direction of the X-ray beam. Overall, four monolayers were prepared and measured in the experiment. The DODAB head group is small, so the surfactant monolayer was modelled as a single layer, as was the case in a previous study.[50] For all of the fits in this X-ray analysis, the sub-phase scattering length density was set to 9.43×10^{-6} $\mathrm{\AA^{-2}}$ and the scalefactor was set to 1.14. The Scattering Length Density (SLD) and reflectometry profiles of the fits to these measured monolayers are in Figure 4.10.

The monolayers were spread to 10 $\mathrm{mNm^{-1}}$ and compressed to a value of 30 $\mathrm{mNm^{-1}}$, which should equate to an area per molecule of 60 $\mathrm{\AA^2 molecule^{-1}}$. This was done by using barriers to compress the interface to three-quarters of the original surface area. The DODAB was spread to 10 $\mathrm{mNm^{-1}}$ surface pressure

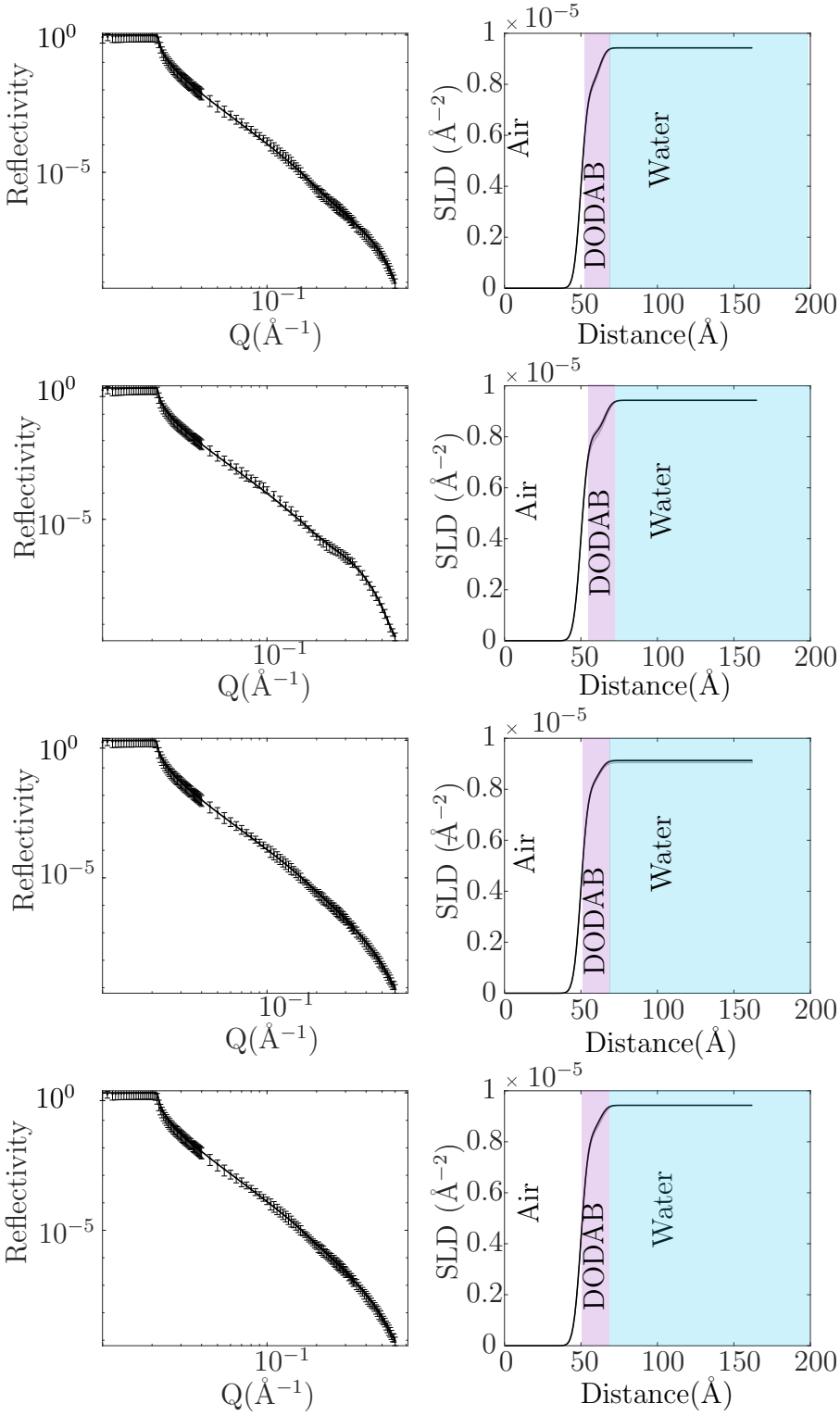

Figure 4.10 *X-ray reflectivity profiles and SLD profiles of DODAB surfactant monolayers*

Table 4.1 *Fitted model parameters of DODAB monolayer X-ray reflectivity profiles; 95% confidence intervals calculated with Bayesian analysis shown in the brackets.*

Monolayer	1	2	3	4
Surface Roughness(Å)	$3.84_{(3.7\ 3.89)}$	$3.58_{(3.54\ 3.62)}$	$3.84_{(3.78\ 3.90)}$	$3.82_{(3.77\ 3.86)}$
DODAB APM (Å^2)	$75.9_{(73.0\ 77.9)}$	$96.1_{(93.4\ 98.7)}$	$93.1_{(89.6\ 96.8)}$	$93.6_{(89.2\ 98.3)}$
Monolayer Hydration (%)	$3.63_{(2.33\ 5.00)}$	$5.55_{(4.58\ 6.56)}$	$5.36_{(4.33\ 6.41)}$	$0.74_{(0.05\ 1.64)}$

which should equate to 100 Å^2 molecule^{-1}. Fits to the measured data yielded APM values in our fitted models of 75.9 to 96.1 Å^2 molecule^{-1}, suggesting that something was wrong in the compression of the monolayers, resulting from the trough design. The Wilhelmy plates could have given a false recording on compression due to change in meniscus height, which in future could be avoided by using a clean Wilhelmy plate to measure the difference in surface pressure between the air and the interface once the monolayer is formed.

4.4.3 Discussion

Four surfactant monolayers were measured and fitted to a single layer model of DODAB. The variation between the spread monolayers was larger than expected, which provides a clue as to why we then struggled to form a complete suspended bilayer beneath this monolayer. In addition to the variability, the magnitude of the area per molecule is greater than we expected on the basis of the number of molecules spread and the compression ratio used. This higher area per molecule implies a concomitantly lower charge density within the monolayer, which in turn will decrease the adhesion energy between the POPG-containing liposomes or proteoliposomes and the monolayer. This means that there was insufficient free energy available per unit area to enable the flattening of the (proteo)-liposomes, which would be necessary for rupture into a complete bilayer. Further support for this balance between adhesion and curvature free energies, is provided by the observation that addition of proteoliposomes failed to add any material at all to the interface; the presence of the membrane spanning MscL in these vesicles stiffens them. All that remains, is to speculate on why the monolayer prepared in this manner had a larger and more variable area per molecule, when ostensibly the same final surface pressure was reached as in the case of the monolayers prepared by spreading alone during the NR experiments. The observed path-

dependence points towards this being a non-equilibrium effect, which in turn identifies a potential flaw in our design of the spread and compress methodology that we implemented for the XRR experiment.

DODAB has aqueous solubility, indeed DODAB liposomes can be prepared by the hot water method, in which the DODAB dissolves in water at 50 °C (which is above the chain melting transition temperature). In this experiment, we do not use a sub-phase above room temperature, but in the spread and compress methodology adopted for the XRR experiment, spreading to 10 mNm^{-1} means that the DODAB monolayer is initially in the expanded (fluid) phase, so as compression starts one might speculate that there is some dissolution into the subphase. By contrast in the monolayers prepared solely by spreading, it is the addition of the final drop of DODAB containing chloroform that drives the transition into the gel phase, in which the chains within the monolayer are constrained to be upright by their neighbours. From a physical chemistry point of view, it is interesting to speculate on why the surface pressure reading of 28 mNm^{-1} determined during the compression phase of the monolayer preparation did not, with the benefit of hindsight afforded by the post-experiment fitting of the data, correspond to the gel phase and the expected area per molecule of 55 $Å^2$. There are two broad explanations. Either this is associated with the mechanism of the hypothesized dissolution of some of the spread DODAB molecules from the fluid phase as it is compressed, or the experimental measurement of the surface pressure using the Wilhelmy plate. In the former case, one can imagine that on compression some of the gel phase DODAB molecules transition into micelles, which then remain either adsorbed at the interface or in the vicinity of the interface. In the case of the latter, it could be that moving the boom to compress the monolayer resulted in a subtle change in the height of the meniscus, affecting the buoyancy contribution to the net force on the Wilhelmy plate. Either way this effect would require further investigation if this spread and compress method is to be used to form stable high density monolayers, which in turn would allow for the formation of high coverage suspended bilayers.

With the benefit of hindsight, the solution to the problem may well have been contained within a Dabkowska *et al.* report [50] which found that addition of cholesterol to the DODAB monolayer forces the DODAB molecules to adopt a consistently upright configuration throughout the compression cycle, concomitant with a lower interfacial Gaussian width. Indeed for DODAB, their reported volume fraction profile shows a small peak with volume fraction above one, on

the sub-phase side of the monolayer; this could be explained in terms of adsorbed DODAB micelles, giving an apparent coverage of greater than one monolayer.

4.5 Neutron Reflectivity

4.5.1 Formation of Suspended Bilayer Kinetics

4.5.1.1 Experimental Design

Neutron reflectivity measurements were carried out using the INTER reflectometer at ISIS Neutron and Muon source, Rutherford Appleton Laboratory (Oxfordshire, UK). The reflected intensity was measured at glancing angles of 0.8° and 2.7°. The total illuminated area was 15 by 65 mm, measured at a resolution of 3% (DOI:10.5286/ISIS.E.RB1810674, May 2018) and 5% (DOI: 10.5286/ISIS.E.RB1910569, May 2019). The difference in resolution measured was due to different laminar flow troughs being used, the second trough had a narrower width and hence required narrower slits to be used, resulting in a lower resolution.

A specially designed laminar flow trough was used for the formation of suspended layers. The trough was cleaned with ethanol and Milli-Q water prior to the experiment. A solution of 2 mg ml^{-1} DODAB in chloroform was spread on an aspirated buffer surface to 27–28 mNm^{-1} whilst measuring the surface pressure using a Wilhelmy plate.

Reflectivity measurements of the monolayer were made after D_2O buffer solution had been passed through the laminar trough, underneath the monolayer. To form the suspended bilayer, 1 mg ml^{-1} liposome or proteoliposomes solutions were passed through the laminar trough at a flow rate of 1.5 $ml\,min^{-1}$ using a syringe pump in push pull mode. A volume of 20 ml was used, enough to replace the volume of the trough twice over. The liposome solution was left for 1 hour to diffuse across the stagnation layer. Then a D_2O solution of 300 mM NaCl in 20 mM HEPES buffer at pD 7 was passed through the trough followed by a solution of 150 mM NaCl, in order to remove any excess vesicles or multi-layers adsorbed to the suspended bilayer.

The reflectivity measured below the critical edge is slightly less than one due

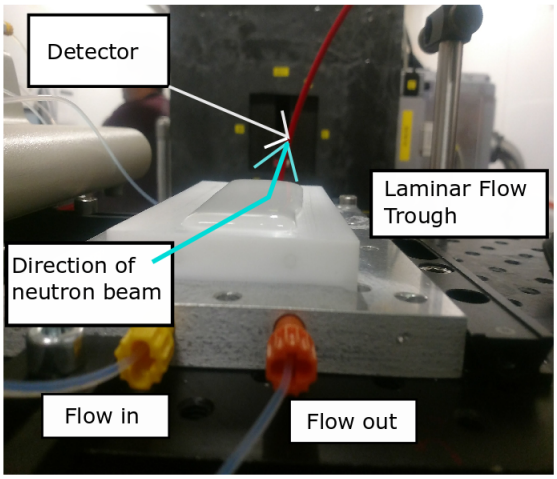

Figure 4.11 *Photos taken of the first experimental set-up on the INTER reflectometer at ISIS.*

to a small curvature of the DODAB-air interface caused by the comparatively narrow trough used in these measurements. This effect was characterized using the multi-detector, so we are confident that we are normalizing data correctly, but we choose to present it in this fashion rather than simply scaling the total reflection to unit reflectivity.

4.5.1.2 Model Description

Neutron reflectivity data measured from suspended lipid bilayers were fitted to the simplest possible model. The surfactant monolayer cannot be fitted conclusively using neutron reflectivity due to the tails being contrast matched to air and the lipid heads being sufficiently small and of sufficiently low contrast so as to make a negligible contribution to the measured neutron reflectivity. The monolayer does however have a small contribution to the reflectivity profile, most noticeable in the null-reflecting water (NRW) buffer contrast. For all of

Table 4.2 *Literature parameters for lipid volumes and scattering length densities.*

Material	Molecular Formula	Molecular Volume ($Å^3$)	Scattering Length (10^{-4}Å)	Scattering Length Density (10^{-6} $Å^{-2}$)
DODAB head	C_2H_6NBr	113 [50]	0.70	0.62
DODAB tail	$C_{36}H_{74}$	1061 [50]	-3.75	-0.35
POPC head	$C_{10}H_{18}NO_8P$	331 [9]	6.00	1.81
POPC tail	$C_{32}H_{64}$	932.5 [9]	-2.68	-0.29
POPG head	$C_8H_{12}O_{10}P$	291 [171]	7.14	2.45
POPG tail	$C_{32}H_{64}$	932.5 [9][171]	-2.68	-0.29

the neutron reflectivity fits in the following section, the monolayer had been constrained by prior probability distributions of the parameters defined by the posterior probability distributions determined from the XRR measurements. Specifically the prior for the area per molecule (APM) covered the range 70–100 $Å^2$ $molecule^{-1}$, and that for the DODAB hydration covered the range 0–15% volume fraction and the interface roughness was set to 3.75 Å. The reflectivity measured at an air-NRW interface is sensitive to the amount of material at the interface, as characterised by the product of the contrast of that inter-facial layer and the thickness of the layer, but rather insensitive to way in which that material is distributed. One might therefore expect there to be some correlation between the hydration parameter, which determines the SLD and hence the contrast of the layer and the APM, which determines the thickness of the layer. This means that there is no particular significance to the individual best fit parameters for the monolayer (with hindsight, it would probably have been best to fit a single surface excess parameter and keep the thickness of the layer fixed at some arbitrary but physically reasonable parameter, as we did with the interface roughness (fixed at capillary roughness of the air-water interface). This approach is explicitly employed by Campbell *et al.* and the appropriateness of the approach has been explicitly considered by a detailed investigation within a Bayesian evidence framework.[147] By comparing the results of fits to models that included a monolayer (with parameters constrained in the manner described) with a model that did not include the monolayer at all, we established that the main impact was on the thickness of the water gap between the interface and the suspended bilayer. This makes sense since at the null reflecting water (NRW)contrast buffer interface, this layer only becomes evident when there is a small perturbation of the SLD profile from zero caused by the explicit inclusion

of the DODAB monolayer; in the model that omits the DODAB layer, the first interface encountered by the neutrons is that formed between the head groups of the upper leaflet of the suspended bilayer and the water.

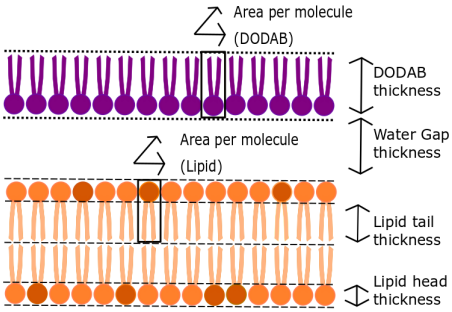

Figure 4.12 *Diagram of suspended lipid bilayer, indicating key structural parameters of the suspended bilayer system.*

The suspended bilayer model as depicted in Figure 4.12, consists of a single monolayer layer, a water layer gap and then four layers describing the inner and outer lipid head groups and tail groups of the bilayer. Two separate roughness parameters were fitted, corresponding to that of the surface and the bilayer. The bilayer structure was constrained to be symmetric (same parameters for inner and outer bilayer leaflets). The thickness and SLD profile of the bilayer was determined by fitting the area per molecule of the lipids and the number of water molecules per lipid head using literature values for molecular volumes and atomic scattering lengths.[9, 50, 171, 202] The free fitting parameters were the APM of the bilayer, water per lipid heads, the three roughness parameters and the thickness of the water gap between bilayer and the air-water interface. This represents the minimal complexity of model to closely reproduce the reflectivity measured in three buffer contrasts. After determining the parameters that minimized χ^2 using the DRAM global search strategy a MCMC analysis was carried out to determine the posterior probability distributions for each of the free parameters in the model. The MCMC analysis comprised 10 repeat runs of 10000 evaluations, following a burn in of 1000 evaluations. This analysis allows us to plot 95% confidence bands on the data and SLD profiles, as well as the posterior probability distributions for each parameter. The posterior probability distributions for 95% confidence intervals for the analysis of final lipid suspended bilayers are shown in the Appendix.

4.5.1.3 Results

Our initial experiment in May 2018 used liposomes at a concentration of 0.1 mg ml^{-1} passed through in a laminar flow under the monolayer in 150 mM NaCl buffer.

Figure 4.13 shows the results of fitting the data for our lipid only system to simple models of a) the bare D_2O interface b) after the spreading of a DODAB monolayer c) 1.5 hours after flowing the liposomes under the monolayer and d) again after 5.5 hours.

The final neutron reflectivity profile measured 5.5 hours after the passage of the liposomes, bottom of Figure 4.13, fits well to a model of a bilayer under a monolayer, however a large amount of diffuse material is still present. This diffuse layer is defined as a single layer underneath the bilayer, separated by a water gap. For the diffuse layer thickness, scattering length density (SLD) and hydration were allowed to vary freely. This diffuse layer is likely to be composed of partially ruptured liposomes as seen in other vesicle rupture studies.[121]

The fit to the final bilayer in Figure 4.13 corresponds to a full coverage bilayer with a 15 Å gap between the surface and bilayer but with a large diffuse layer. This initial experiment provided evidence that liposome rupture was occurring underneath the monolayer, and that adaptations were needed to the protocol to achieve an isolated suspended bilayer.

To decrease the time required for suspended bilayer formation, the liposome concentration was increased to 1 mg ml^{-1} and flushing the suspended bilayer construct using a laminar flow with salt solutions to remove any excess lipid or partially ruptured vesicles.

During the injection of liposomes, neutron reflectivity measurements were made over a narrower Q range ($0.1 \geq Q \geq 1.1$ $Å^{-1}$), continued for an hour after injection. This data was time sliced into 3 minute segments in Figure 4.14. After 36 minutes the reflectivity profile remains the same, suggesting that the maximum amount of material has reached the interface.

To remove any excess unruptured liposomes at the interface 40 ml of 300 mM NaCl in HEPES buffer was passed through the laminar trough. The neutron reflectivity profile was measured and then 40 ml of 150 mM NaCl was passed through the trough before the final measurement.

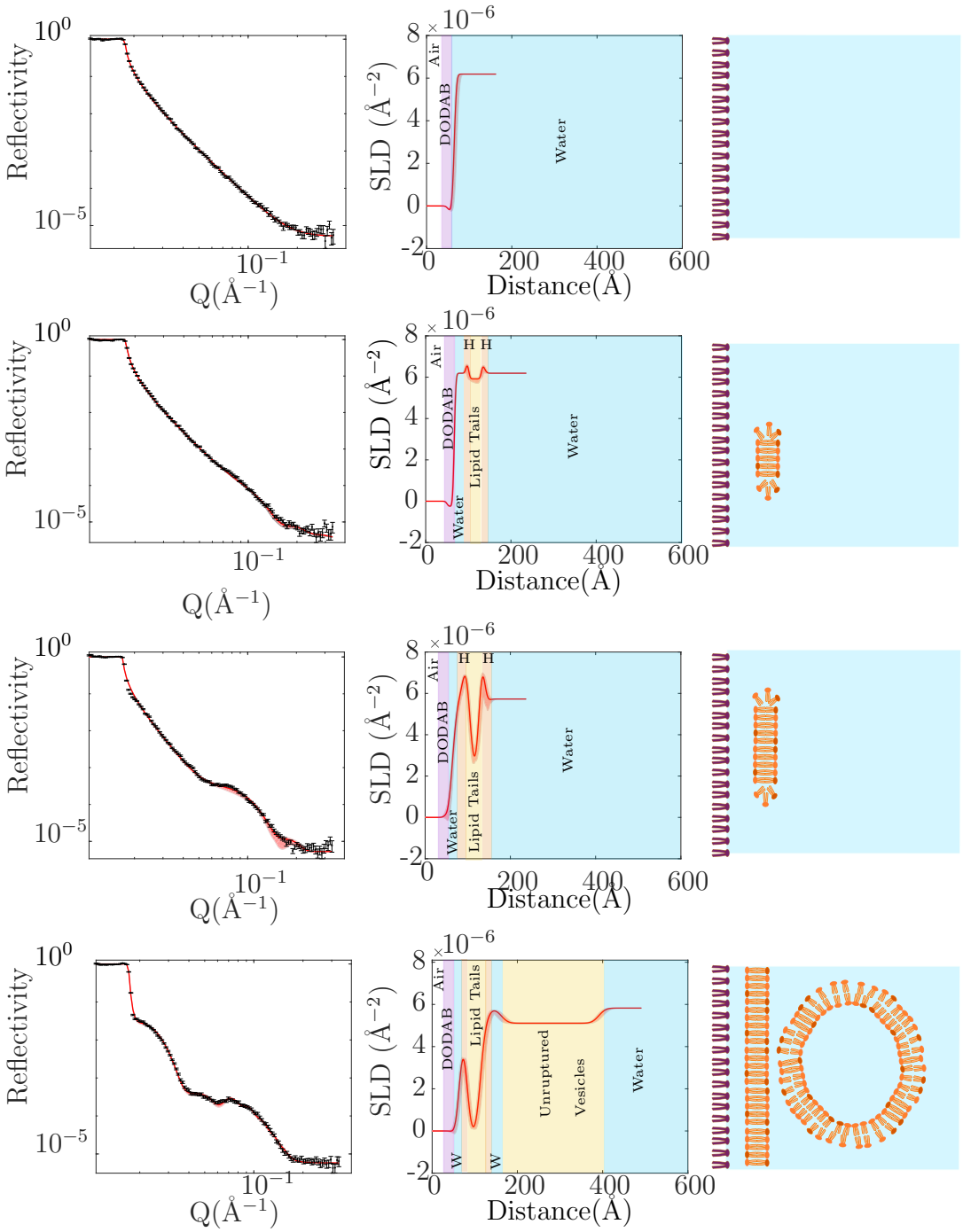

Figure 4.13 *Neutron reflectivity, corresponding SLD profiles and schematic representation of the interfacial structure for a clean D_2O interface(top), DODAB monolayer and suspended lipid bilayers when liposomes used at a* 0.1 mg ml^{-1} *concentration after* 1.5 *hours and after* 5.5 *hours(bottom). The reflectivity data points are depicted by the error bars (black) denoting the measurement uncertainty. The fits are shown as red lines with red shading denoting* 95% *confidence bands.*

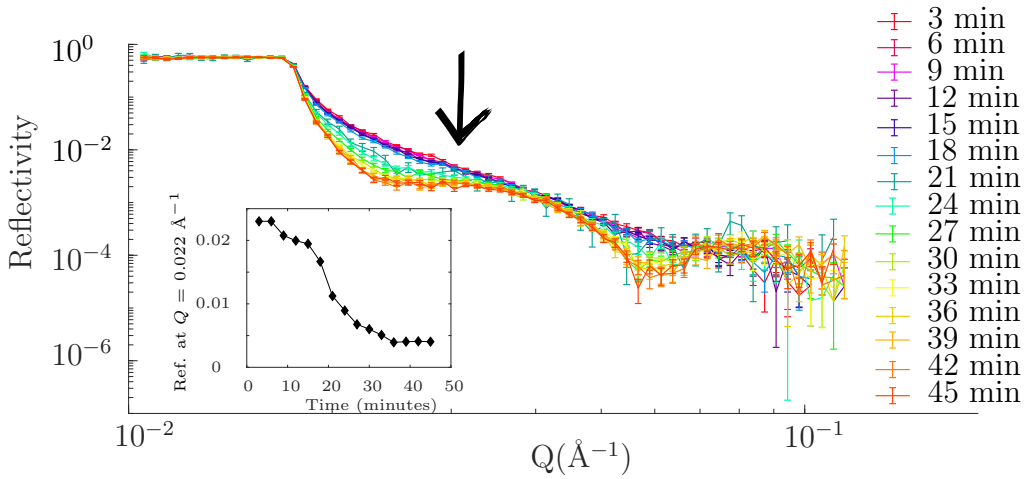

Figure 4.14 *Neutron reflectivity showing the formation of a suspended lipid bilayer; 0 minutes corresponds to the start of the injection of the liposomes.*

The resultant fits to reflectivity measured in D_2O are shown in Figure 4.15, which reveals the effect of these rinsing steps. Prior to passage of the 300 mM NaCl solution, some liposomes have already ruptured to form a double bilayer. The double bilayer model has another 5 layers, comprising: a second water gap, the thickness of which is allowed to vary in our model, and 4 layers making up the second bilayer, characterized by a fixed area per molecule and a hydration parameter that is allowed to vary. The 300 mM NaCl does not initially remove the double bilayer but does increase the water gaps between the monolayer and bilayer and between the two bilayers. This could be attributed to a screening of any favourable electrostatic interactions or to an increase in repulsive interactions associated with bilayer fluctuations. Addition of the 150 mM NaCl removes the second bilayer and the reflectivity profile fits well to a single uniform bilayer suspended under the monolayer.

MCMC analysis was carried out using the parameter values and uncertainties from the DRAM fitting to define the priors and co-fitting of the D_2O and the PMW contrasts. The laminar flow trough is useful in exchanging solvent contrasts without disturbing the monolayer and suspended bilayer. The fits and the 95% confidence interval bands from the MCMC analysis are shown in Figure 4.16.

4.5.1.4 Discussion of Lipid Bilayer Formation

Successful formation of a single bilayer suspended beneath a surfactant monolayer was achieved through optimisation of liposome concentration and subsequent

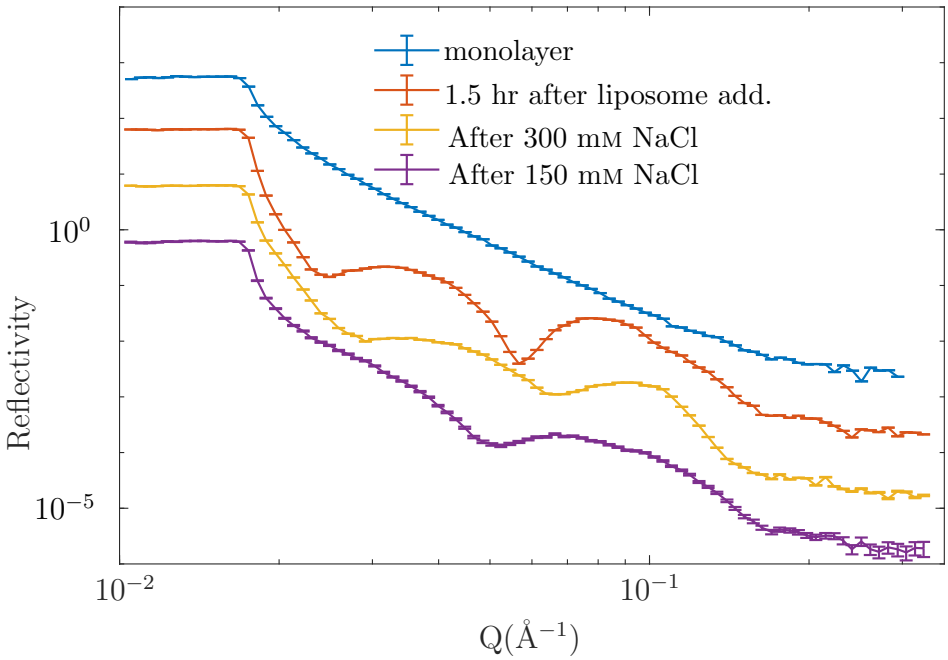

Figure 4.15 *Neutron reflectivity showing the formation of suspended lipid bilayers. The reflectivity profile of the DODAB monolayer is shown in blue. The reflectivity profile of the interface 1.5 hours after liposome passage in laminar flow under the monolayer is shown in red, with the reflectivity offset by a multiple of 10. The reflectivity profiles after rinsing with* 300 mM *NaCl and after rinsing with* 150 mM *NaCl are shown in yellow and purple respectively, each offset by a further multiple of 10 from the initial monolayer reflectivity profile.*

Table 4.3 *Best-fit model parameters of a suspended 3:1 POPC:POPG lipid bilayer underneath a surfactant monolayer, 95% confidence interval (CI) ranges determined from MCMC analysis. Hydration given as a percentage of the volume.*

Parameter	Fitted Value$_{95\%\ CI}$
Bottom of bilayer roughness(Å)	$8.9_{(8.0\ 9.8)}$
APM of bilayer(Å^2 molecule^{-1})	$58.3_{(56.5\ 60.4)}$
Water Gap between monolayer and bilayer(Å)	$11.5_{(6.8\ 14.9)}$
Water per lipid Head	$6.8_{(0.4\ 15.4)}$
Surface roughness(Å)	$5.3_{(4.1\ 6.7)}$
APM of monolayer(Å^{2}molecule^{-1})	$87_{(76\ 95)}$
Monolayer hydration (%)	$7.9_{(0.5\ 14.7)}$

rinsing steps with salt buffers. Since we were able to observe the kinetics of formation of our bilayer we can make some comments as to the mechanism of

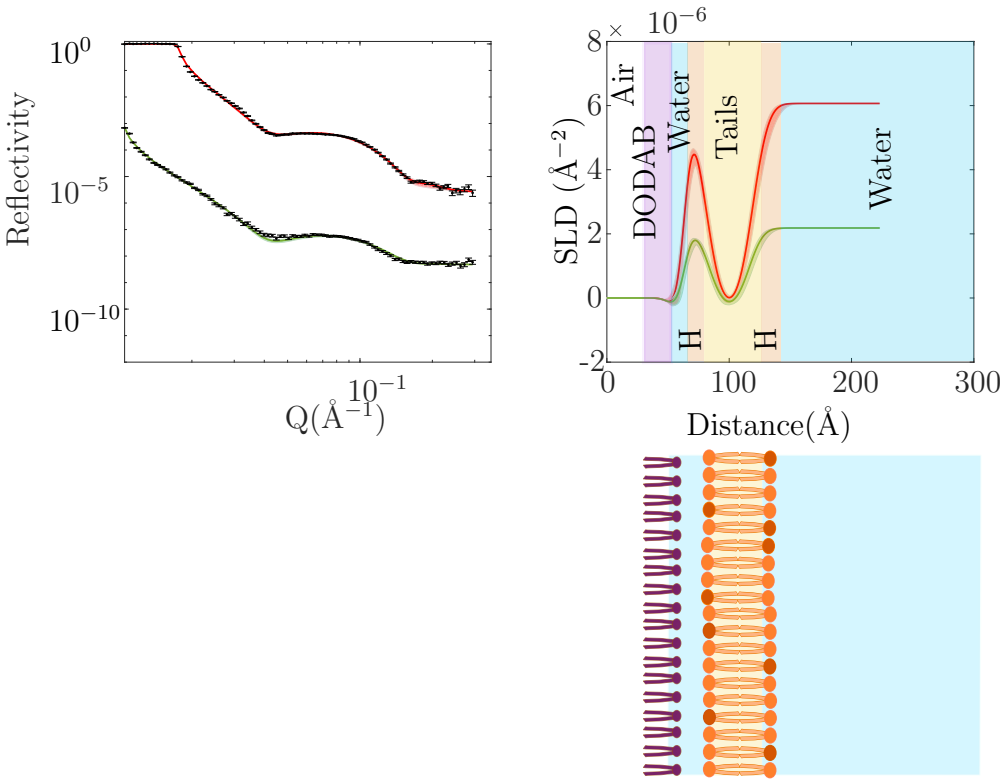

Figure 4.16 *Neutron reflectivity and SLD profiles for suspended lipid bilayers (LEFT) Data(error bars) and fits(solid line with lighter coloured 95% confidence interval) for the bilayer measured in D_2O (red) and protein matched water (green). (RIGHT) SLD profile of lipid bilayer corresponding to the fits in left panel.*

liposome rupture in our novel system.

At low concentrations we can model a single sparse bilayer. It is reasonable to assume that there is an adhesive/attractive interaction between the vesicle and the surfactant covered air-water interface to drive rupture of individual liposomes, prior to a critical coverage being reached. However this interaction appears to be weaker than that reported for silicon interfaces, often used for supported bilayer formation, as with time we observe the addition of diffuse material. This diffuse material is likely unruptured and partially ruptured vesicles.[79] With increased time or increased concentration, a critical coverage of lipid material, diffusely distributed as unruptured vesicles, is reached to enable bilayer formation to complete. Some diffuse material persists until the passage of first a 300 mM salt solution and then a 150 mM salt solution in laminar flow are completed. The observations of partially ruptured flattened vesicles agree with observations by *Koutsiobas et al.* that adsorbed vesicles form a flattened shape at the interface prior to a critical coverage being reached. [121]

The suspended lipid-only bilayer has a slightly higher roughness than solid-supported bilayers of 8 Å and an area per molecule of 58 ± 2.0 $Å^2$. Whilst there are many experimentally reported values for POPC area per molecule 65 $Å^2$, [125] 62.7 $Å^2$,[123] only one experimental POPG area per molecule is reported of 66 $Å^2$ at 30°C.[89] Many MD simulations of POPG bilayers suggest a lower APM value especially in the presence of salts, close to the concentration of NaCl we used at 154 mM a value as low as 51.4 $Å^2$ has been reported.[244] A separate MD simulation suggests that at 150 mM NaCl, that a POPG bilayer would have an APM of 54.8 $Å^2$ whilst a POPC bilayer would have an APM of 64.1 $Å^2$. [53] Other researchers have suggested that the average APM is linear with lipid composition so taking the values from the MD simulation conducted for a 150 mM NaCl buffer a 3 : 1 POPC:POPG bilayer would have an APM of 61.8 $Å^2$ in 150 mM NaCl. The thickness measurements are sufficiently consistent with a respectable range of literature estimates to enable us to conclude that we have a bilayer of mixed POPC:POPG composition.

Previously Wadsäter *et al.* observed the formation of DMPC, DMPG SMALP nanodiscs underneath the air-water interface, also observing that a difference in charge is needed between the nanodisc lipids and the monolayer.[234] Our continuous suspended bilayer mimic has the advantage of removing the need for any polymer in the bilayer region. Not only does this clean up the volume fraction and hence SLD profile, and as a consequence the observed reflectivity,

but it also removes the belt-like constraint that is present in the nanodisc system. This is important for the application for which the suspended bilayer system was designed to investigate: MscL. Since the gating of MscL is hypothesized to be actuated by a transmission of stress between the lipid and protein components of the bilayer, removing polymeric components that would not be present in a real bacterial membrane is important. Furthermore, as is explored in Chapter 3, it is thought that clustering of channels may play a role in the native behaviour of MscL in real bacteria, so having the MscL embedded in a continuous lipid bilayer, rather than isolated within nanodiscs is clearly important, if we are to have hope of observing the function in addition to the structure of the MscL in our suspended bilayer system.

4.5.2 Effect of Amphipathic Molecules on the Suspended Bilayer

Suspended bilayers provide a flexible membrane mimic to test the interaction of the membrane with biologically relevant antimicrobial molecules. We have investigated the effect of the antimicrobial peptide pexiganan (PXG) and the surfactant 16 : 0 lyso-PC.

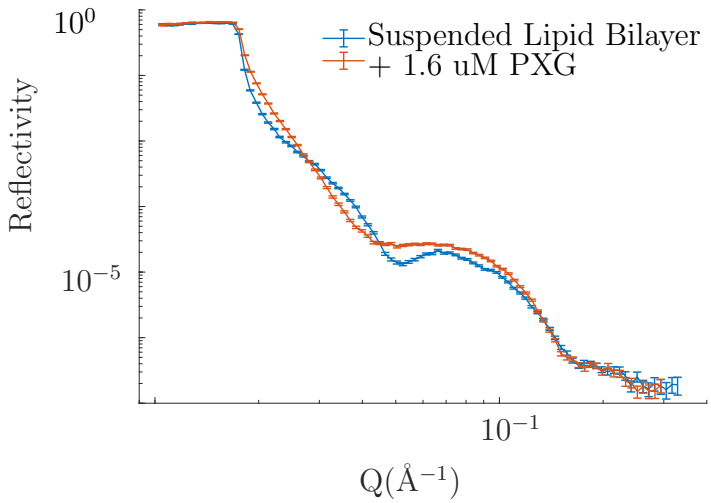

Figure 4.17 *Neutron reflectivity profiles of suspended lipid bilayers before and after the addition of* 1.6 µM *pexiganan.*

A 20 ml solution of 1.6 µM pexiganan (China Peptides, 98% purity) in 150 mM NaCl 20 mM HEPES in D_2O, pD 7 was passed through the laminar flow trough at a rate of 1.5 ml min^{-1} followed by 20 ml of the desired contrast buffer.

A comparison of the measured reflectivity profiles before and after pexiganan addition in D_2O buffer is shown in Figure 4.17.

Part of the change in the reflectivity curves is due to the removal facilitated by the passage of the laminar flow of the PXG solution under the suspended bilayer, of some residual diffusely distributed lipid material following the formation of this suspended bilayer (this is a different bilayer from the one previously described in Section 4.5.1.3). The diffuse layer fit to the reflectivity profile of the suspended bilayer in Figure 4.18 has the SLD of the lipid tails and is allowed to freely hydrate.

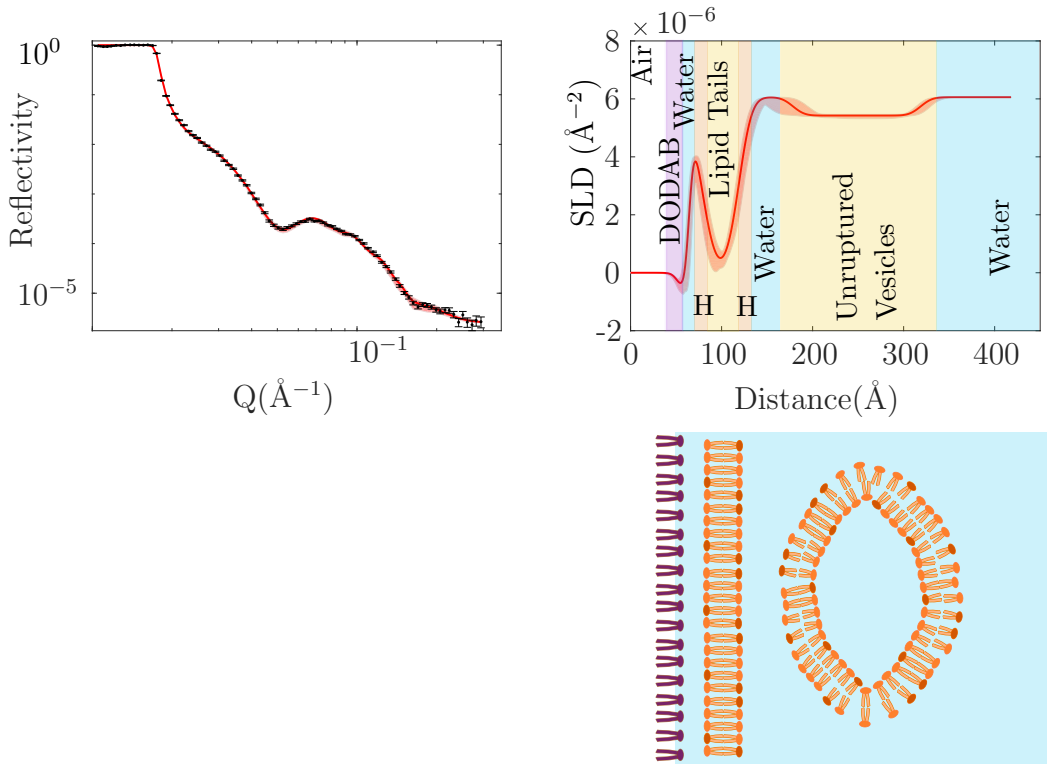

Figure 4.18 *Neutron reflectivity and SLD profiles for suspended lipid bilayers before exposure to* 1.6µM *pexiganan. (Top Left) Data(error bars) and fits(solid line with lighter coloured* 95% *confidence interval) for the bilayer measured in* D_2O *(red) and protein matched water (green). (Top Right) SLD profile of lipid bilayer corresponding to the fits. (Bottom) Cartoon diagram depicting the distribution of material in the SLD profile.*

There is a small modulation of the fringe at $Q = 0.1$ Å^{-1} for the data measured in D_2O seen in Figure 4.17. This can be associated with the slight thinning of

the head group layer, which can be inferred from the decrease in the hydration at constant area per molecule. Such a thinning implies a small reorientation of the lipid head group, which could be consistent with the small but finite coverage of PXG inferred from the model. This would be consistent with a low coverage carpet model for the interaction of PXG with the lipid leaflet. L. McKinley reports a surface coverage of PXG interacting with a monolayer model for a single 3:1 POPC:POPG bilayer of 0.05:1 PXG:lipid.[149] A further indication that this may be the relevant binding modality of PXG is provided by the increase in the roughness of the bilayer/sub-phase interface following exposure to PXG and the small increase in the thickness of the water gap between the bilayer and the monolayer. The latter observation is consistent with a decrease in the attraction between the bilayer and the monolayer. As PXG is cationic AMP, binding in this dilute carpet mode would compensate a greater number of the negative charges associated with the POPG head groups. This in turn would mean there were a smaller driving force for counterion release due to proximity with the DODAB monolayer, weakening the attractive component of the interaction potential. Binding of PXG could also soften the fluctuation modes of the bilayer, increasing both the interface roughness (as is observed) and the repulsive component of the interaction potential between the bilayer and the DODAB monolayer. The net result is an increase in the thickness of the water gap, as has also been observed by Clifton et al. from their studies of the interaction of salt concentrations with floating bilayers. [45]

Adsorbed PXG is explicitly included in the model, although the best fit parameter value of $0.6 \pm 0.4\%$ is not only low (lower than the concentrations at which toroidal pores have been observed) but also not particularly well-defined (broad confidence interval). The effect of the PXG is via the thinning effect described above, rather than its contribution to the SLD profile. The coverage could have been inferred more precisely by using deuterated PXG, but this was outwith the scope of these experiments.

We separately investigated the effect of another amphiphilic molecule, with known antimicrobial properties, the single-(saturated) tailed lipid lyso-PC, specifically 16 : 0 deuterated lyso-PC (dlyso-PC). A 20 ml solution of 4 µM dlysoPC was flowed through the laminar trough at a rate of 1.5 $\mathrm{ml\,min^{-1}}$.

In Figure 4.20 there is a comparison of the reflectivity profiles in protein-matched water (PMW) before and after addition of the dlyso-PC. Small changes in the reflectivity curves in Figure 4.20 are partly down to a small shift in the PMW

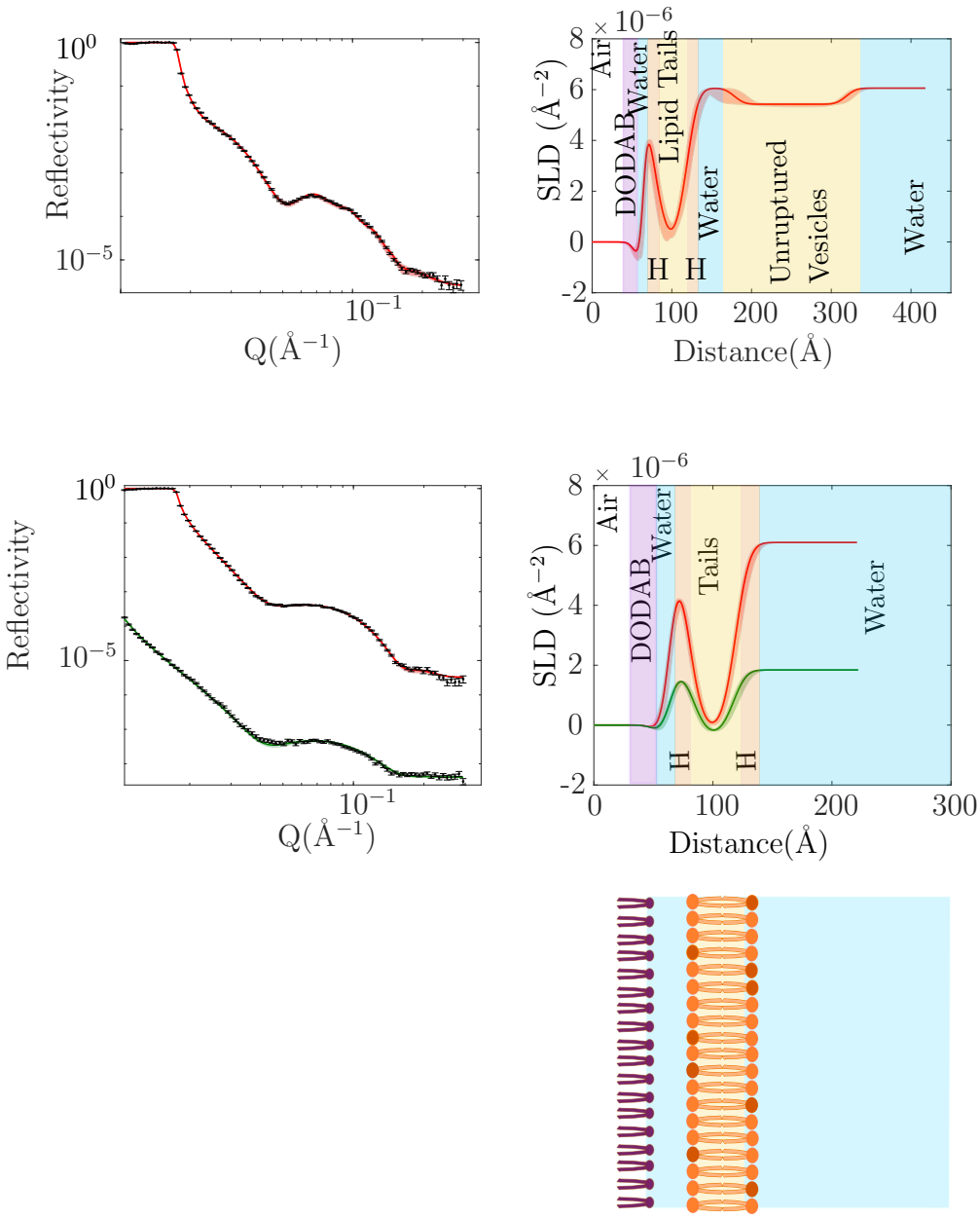

Figure 4.19 *Neutron reflectivity and SLD profiles for suspended lipid bilayers after exposure to* 1.6 µM *pexiganan. (Top Left) Data and fits for the bilayer (Middle Left) Data and fits for the bilayer and pexiganan measured in* D_2O *(red) and protein matched water (green).(Right) SLD profiles of models fitted to the reflectivity data. (Bottom) Cartoon diagram depiction of the distribution of material in the SLD profile. PXG is not explicitly shown in the diagram due to its low coverage.*

Table 4.4 *Fitted model parameters of a suspended 3:1 POPC:POPG lipid bilayer underneath a surfactant monolayer before and after passage of a solution of a solution of*1.6 µM *pexiganan by laminar flow under the suspended bilayer. Pexiganan coverage is expressed as a percentage volume of the bilayer layers.*

	Pre PXG	Post PXG
Parameter	Fitted Value	Fitted Value
APM of bilayer(Å^2 molecule^{-1})	$58_{(55\ 60)}$	$58_{(57\ 59)}$
APM of bilayer in PMW(Å^2 molecule^{-1})	N/A	$55.0_{(54\ 57)}$
Water Gap (Å)	$10.2_{(5.5\ 13.4)}$	$13.8_{(13.0\ 14.0)}$
Water per lipid Head	$3.7_{(0.1\ 11.3)}$	$0.4_{(0.0\ 1.5)}$
Bilayer roughness(Å)	$13_{(11\ 15)}$	$8.7_{(8.3\ 9.3)}$
Surface roughness(Å)	$4.3_{(3.3\ 5.0)}$	$6.5_{(5.7\ 7.3)}$
Pexiganan coverage(%)	$0.0_{(Fixed)}$	$0.62_{(0.17\ 0.96)}$
Second Water Gap (Å)	$57_{(41\ 75)}$	N/A
Diffuse layer hydration (%)	$90_{(89\ 91)}$	N/A
Diffuse layer thickness(Å)	$140_{(118\ 158)}$	N/A
Diffuse layer roughness (Å)	$10_{(7\ 13)}$	N/A

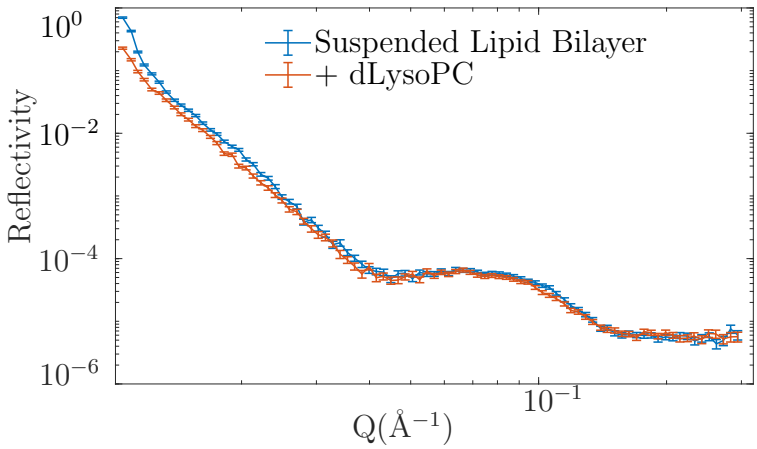

Figure 4.20 *Neutron reflectivity profiles of suspended lipid bilayers before and after the addition of* 4 µM *deuterated lyso-PC*

buffer contrast but there is some shift at $Q = 0.1$ Å^{-1}, which can be associated with the change in head group thickness. Fitting the curves to models in Rascal highlighted the changes in the bilayer that occurred.

Addition of dlyso-PC results in a significant decrease in the area per molecule of lipids in the bilayer. The observed decrease seems not unreasonable at first sight, suggesting significant insertion of lyso-PC. However this is in apparent

Table 4.5 *Fitted model parameters of a suspended 3:1 POPC:POPG lipid bilayer underneath a surfactant monolayer before and after flowing a solution of* 4 µM *dlysoPC. % Hydration is the volume of the layer that is water. Lyso-PC coverage is also expressed as a % of the volume.*

	Post dLysoPC	Pre dLysoPC
Parameter	Fitted Value	Fitted Value
Bilayer Roughness(Å)	$9.5_{(8.7\ 10.3)}$	$8.9_{(8.0\ 9.8)}$
APM of Bilayer(Å^2 molecule^{-1})	$47.1_{(45.8\ 48.9)}$	$58.3_{(56.5\ 60.4)}$
Water Gap (Å)	$3.0_{(0.7\ 6.0)}$	$11.1_{(6.8\ 14.9)}$
Water per Lipid Head	$14.0_{(9.03\ 17.8)}$	$6.8_{(0.4\ 15.4)}$
Surface Roughness(Å)	$4.4_{(2.4\ 6.6)}$	$5.3_{(4.1\ 6.7)}$
Monolayer APM (Å^2 molecule^{-1})	$75.2_{(70.1\ 90.0)}$	$86.5_{(76.0\ 94.6)}$
Monolayer Hydration (%)	$5.5_{(0.2\ 14.2)}$	$7.9_{(0.5\ 14.7)}$
dlysoPC Coverage(%)	$2.2_{(1.7\ 2.6)}$	NA

contradiction to the low value ($2.2_{(1.7\ 2.6)}$ %) determined for the best fit lyso-PC coverage parameter. The resolution to this apparent contradiction is rather similar to the effect observed with PXG, with the principle effect being a restructuring of the bilayer rather than due to an explicit change in SLD due to insertion of the deuterated molecule. Specifically lyso-PC has a lower packing parameter than either POPC or POPG. Insertion of such a conically shaped molecule will introduce regions of high spontaneous curvature. This will decrease the projected area per molecule but also increase the apparent level of hydration (as is observed) since the now rippled bilayer will include water in the the troughs in the undulating rippled layer. A significant decrease in the water gap is also apparent from 11.5 to 2.95 Å.

4.5.2.1 Discussion

Addition of pexiganan and lyso-PC both caused changes in the reflectivity profiles as highlighted by the changes in the fitted models. The results from pexiganan addition suggest a thinning of the lipid head groups. Thinning of lipid membranes has been suggested as a crucial part of the antimicrobial mechanism for similar helical peptides to pexiganan.[135] Atomic force microscopy measurements by Mecke *et al.* provided evidence that pexiganan causes thinning of supported DMPC bilayers of 11 Å (± 2 Å). [150] Our results do not show as strong a thinning effect as the *Mecke et al.* study which may be due to our suspended

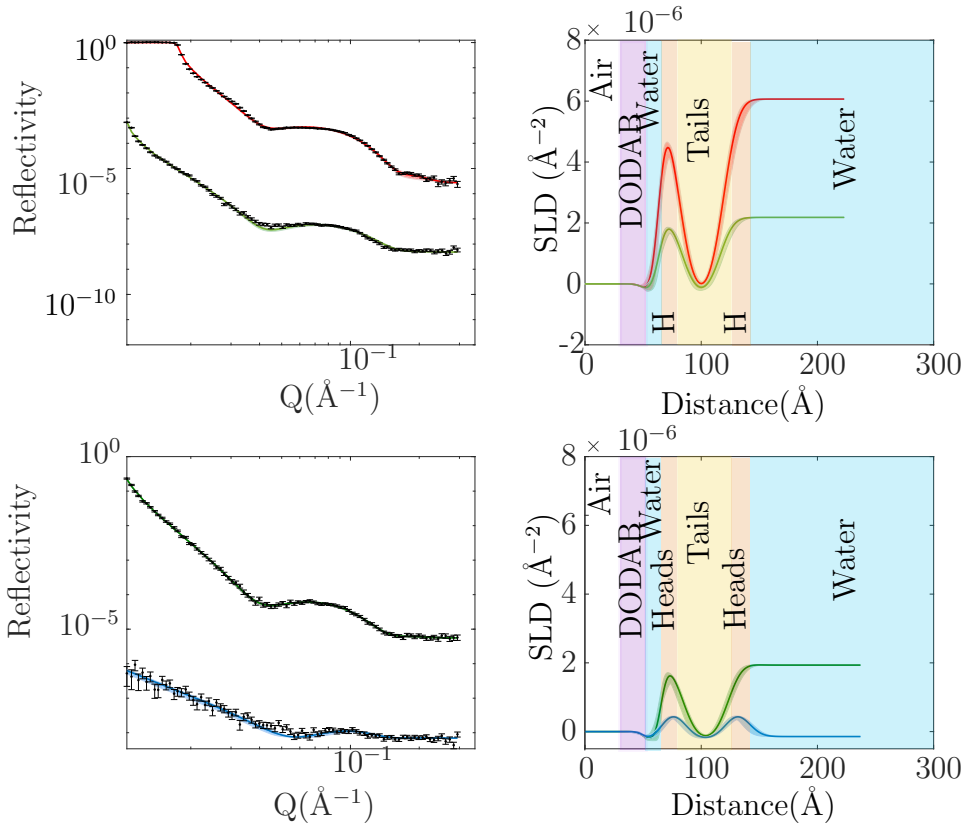

Figure 4.21 *Neutron reflectivity and SLD profiles for suspended lipid bilayers before and after exposure to* 4 μM *deuterated* 16 : 0 *lyso-PC. (Top Left) Data (error bars) and fits (solid line with lighter coloured* 95% *confidence interval) for the bilayer measured in* D_2O *(red) and protein matched water (green). (Mid Left) Data and fits for the bilayer and lyso-PC measured in protein matched water and NRW (blue) (Top Right) SLD profile of lipid bilayer corresponding to the fits in top left panel. (D) SLD profile of lipid bilayer corresponding to the fits in mid left panel. (Bottom) Cartoon depiction of the composition of material in the suspended bilayer after lyso-PC addition.*

bilayer mimic having a larger freedom of movement than a supported bilayer. [150]

It may be that if thinning and an increase in bilayer curvature occurred, we observed an undulating bilayer that appears thicker in our simple model. Both lyso-PC and pexiganan could also form adsorbed layers above or below the bilayer which hasn't been allowed in these models.

Our overall results on pexiganan addition are in agreement with existing antimicrobial literature given the observation of membrane thinning and increase

in disorder of the lipids. It is important to note that our models suggest we are at a very low coverage of pexiganan in our system (less than 1%). Much of the extensive literature on pexiganan focuses on pre-assembled pexiganan-lipid formulations, often at higher pexiganan compositions.[81, 92, 241] The observation of pexiganan forming toroidal pores was found between 1-5% pexiganan bilayer coverage.[145] Here we have demonstrated that using a planar bilayer mimetic and neutron reflectivity, the interaction of a lipid bilayer and a solution of pexiganan can be observed.

The effect of lyso-PC addition on the lipid bilayer differed from that of pexiganan as we observed a large decrease in APM, which would suggest that the lipid leaflet became thicker. However, the observed increase in bilayer thickness is likely to be a side-effect of increased undulations of the lipid bilayer caused by an increase in curvature from lyso-PC insertion.

4.5.3 Neutron Reflectivity of MscL Incorporated Suspended Bilayers

4.5.3.1 Experimental Set-up

Proteoliposome Preparation. The plasmid pDuet-1 wt MscL-6-His construct under T7 promoter was supplied by Paul Rohde (Boris Martinac Group, Cardiac Research Institute, Sydney). The cell free protein expression method was taken from Abdine *et al.*[3], with small modifications. More details are given in Section 3.1.4.

The MscL protein was expressed directly into 3 : 1 POPC:POPG liposomes at a ratio of 1:8 (w/w) protein to lipid. The yield was 0.5mg of protein per ml of reaction mixture. Protein expression was carried out less than a week before use in experiments. Proteoliposomes were separated from the reaction solution by centrifugation and the proteoliposomes pellet was rinsed with 150 mM KCl 20 mM HEPES buffer. The proteoliposomes were resuspended by sonication at room temperature for 10 minutes and finally extruded using a microextruder with 100 nm pore diameter filters. Proteoliposomes were stored in 150 mM KCL, 20 mM HEPES buffer, pH 7.2 at 4 °C until day of use. Before use, proteoliposomes were dialysed into the appropriate buffer, for neutron reflectivity measurements this was 150 mM NaCl, 20 mM HEPES buffer in D_2O at pD 7. This was the starting

buffer for the NR measurements, with subsequent contrast changes being made in-situ by laminar flow under the suspended bilayer.

Preparation of suspended bilayer containing MscL. The suspended bilayer formation was carried out using the same method as the lipid-only bilayer. The key difference being that the proteoliposomes are larger than the liposomes, 250 nm diameter compared to 100 nm. Despite repeated sonication and extrusion, the proteoliposomes remain at 250 nm (the mean diameter determined by DLS). Proteoliposomes were passed underneath the formed DODAB surfactant monolayer at a lipid concentration of 1 mg ml^{-1} in 150 mM NaCl 20 mM HEPES D_2O buffer at pD 7.

4.5.3.2 Model Description

A model comparable to the lipid bilayer model was used to calculate the reflectivity from the suspended bilayer containing MscL. Once again the surfactant monolayers were constrained to that of a DODAB monolayer measured by XRR and separate roughness parameters are included for the upper and lower bilayer leaflets. The protein channel MscL is a transmembrane protein so occupies a percentage of both of the lipid head layers and tails layers. It is also expected to protrude from the membrane by about 40 Å on the basis of the crystal structure listed as 2OAR on the protein structure database. [31]

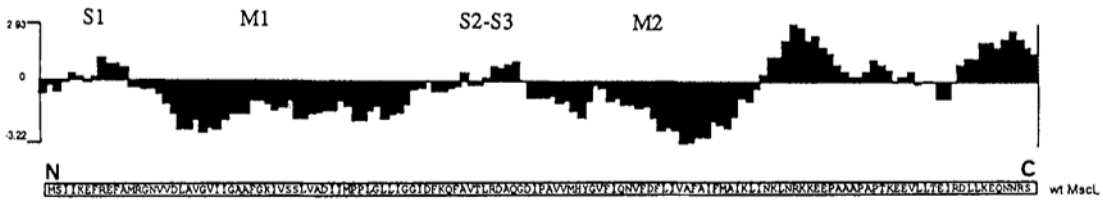

Figure 4.22 *Figure and Caption taken from [86]. The amino acid sequence of the MscL ORF and the corresponding Kyte-Doolittle hydropathy plot with the two predicted a-helical transmembrane domains (M1, M2) and a-helical amphipathic regions (S1,S2 to S3). The terminal ends of the protein are labeled N and C respectively*

When initially fitting the reflectivity data, protrusions with independent levels of hydration were included on both sides of the membrane to test whether there is preferential orientation. Reproducibly, the fits tended to have no protrusion above the upper bilayer leaflet and a significant protrusion below the bilayer

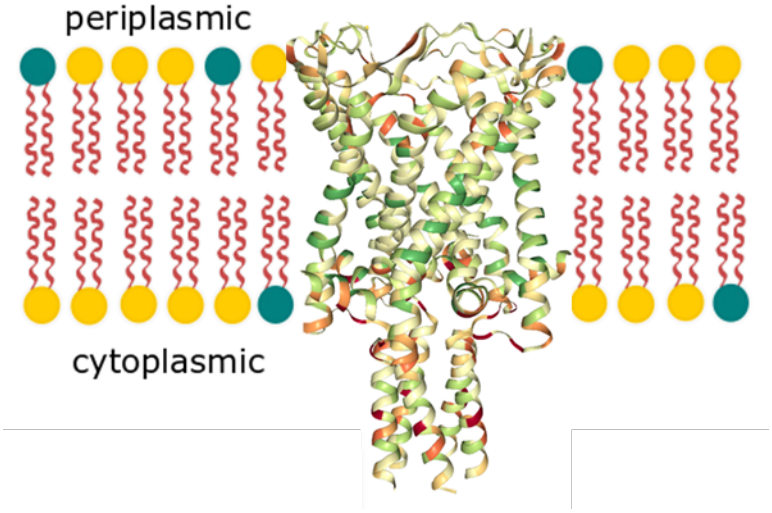

Figure 4.23 *Representation of how the MscL 2OAR crystal structure may sit in the lipid membrane. Hydrophobicity representation of MscL residues taken from the protein database.*

suggesting the MscL is preferentially oriented with the C-terminus facing the sub-phase rather than the DODAB monolayer. Since the crystal structure of MscL is well known, we used the volume of the transmembrane portion of the protein and C-terminal protrusion as constraints in our model. The protein in the model is thus described as two regions of constant protein volume fraction The thickness of the first is determined by the thickness of the lipid bilayer, fitted as the lipid APM, and the thickness of the second rectangle is allowed to vary freely. The ratio of protein to lipid is also a free parameter as we cannot be sure that our bilayer will have an identical composition to the proteoliposomes from which it is formed. The only bilayer hydration parameter is the water per lipid head (WPLH) parameter, and the C-terminal protrusion layer has explicit hydration in the model, as any volume not occupied by the protein has the same scattering length density as the buffer. The SLD of MscL was calculated by using the approximated volume from amino acid volumes in each section and assuming that H-D exchange was limited to 80% for the labile hydrogens for the transmembrane portion and 90% for membrane protruding parts of the protein. This means that the SLD of the protein changes slightly depending on the buffer contrast, as can be seen in Figure 4.24.

The model with the lowest χ^2 value and proper posteriors separates the protein into 2 sections, a transmembrane section and protrusion section, with the protrusion volume being constrained to be the difference between the total protein volume and the volume of the transmembrane region. The protrusion volume

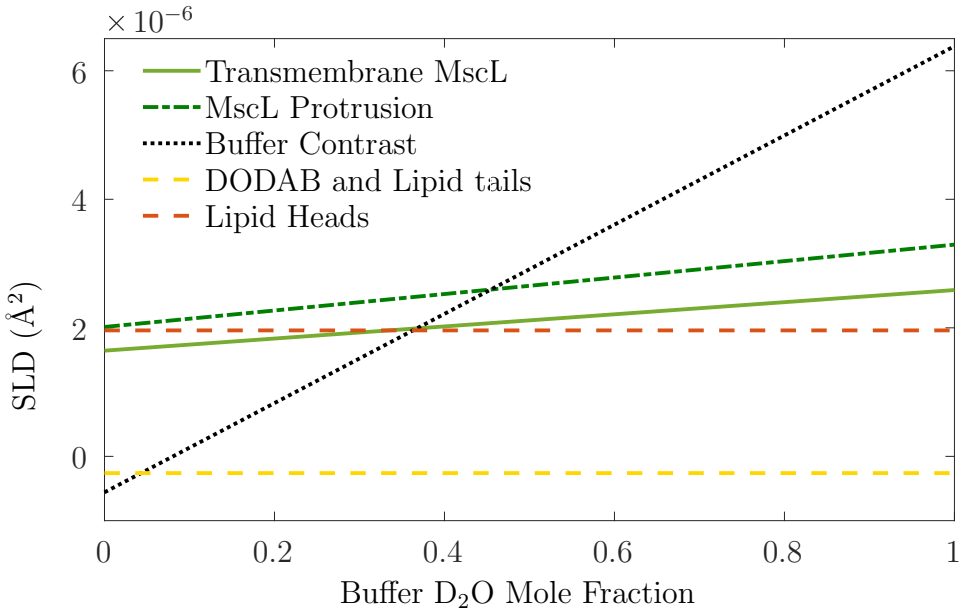

Figure 4.24 *Scattering length density of different suspended bilayer components with different amounts of D_2O in the buffer*

includes the C-terminus region, N-terminus region and the His-tag.

The complexity of the protein containing model was increased incrementally to ensure any additional complexity improved the quality of the fit and lead to proper parameter posteriors in the Bayesian analysis. The simplest model, contained only the transmembrane portion of the protein.

Figure 4.25 shows the effect of increasing complexity of the model on the best-fit reflectivity profiles. Both the top and second from top models have an unrealistic roughness at the air-water interface (less than 1 Å) and the bottom model did not form a proper posterior for the periplasmic loop section, suggesting that it does not have a significant protrusion from the lipid head group region. The 3rd model appears to provide the most appropriate description of the protein-containing bilayer. We further introduced an explicit surfactant monolayer with parameters constrained by the posterior probability distribution determined by XRR. This resulted in a better agreement between the measured and calculated reflectivities, particularly for the data set measured in NRW. The monolayer was constrained to a parameter range as determined by XRR and achieved the fit in Figure 4.26, which achieved a better fit to the reflectivity profiles, in particular for the NRW contrast. The small discrepancy that remains between the calculated and measured reflectivity for NRW at $Q \sim 0.035\text{A}^{-1}$ is almost certainly due to the overly simplistic description of the monolayer. Whilst a

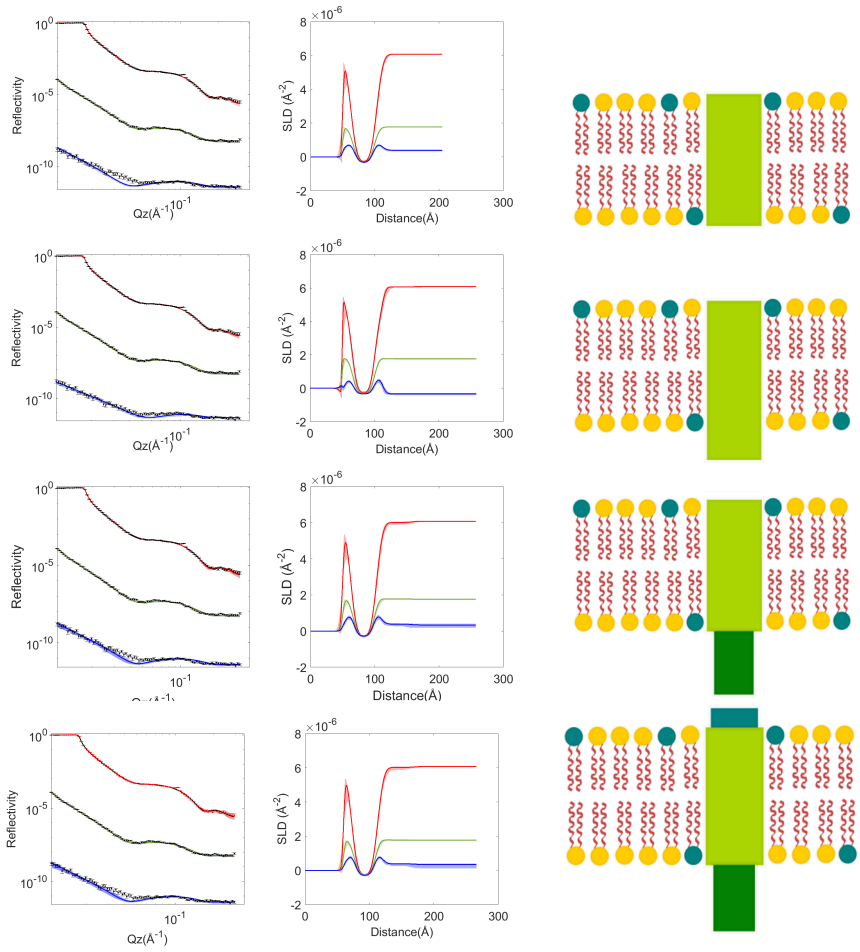

Figure 4.25 *Neutron reflectivity and fit to models of MscL-containing suspended bilayer models, not containing the monolayer structure.*

more complex representation could be used, as in Dabkowska *et al.*, this would come at the expense of greater model complexity, which in a formal Bayesian model comparison would be penalized by an unfavourable Occam factor.[50] The Occam factor is a statistical tool in model selection, to penalise models with a larger number of parameters to avoid over-fitting. Since it is the bilayer properties that are of interest in this study, we have not sought to increase the complexity of the representation of the monolayer.

The area per molecule fitted for the MscL containing bilayer is lower than expected for a 3:1 POPC:POPG bilayer. This could be a consequence of the presence of the protein increasing the thickness of the bilayer to match that of the transmembrane domain. It could also be consequence of the additional material in the low coverage multilayer stack, that can be inferred from the small Bragg peak present in the D_2O contrast. The best fit model contains 2.6±1.8% MscL protein within the bilayer, lower than the formulated composition

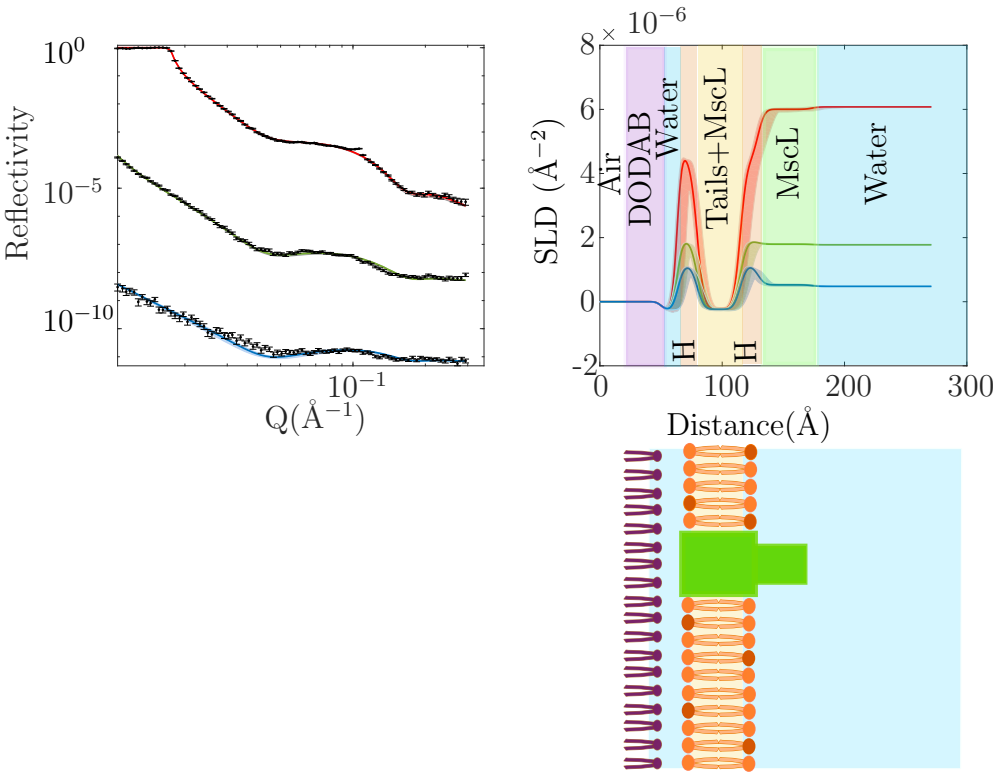

Figure 4.26 *Neutron reflectivity and fit to a MscL containing suspended bilayer model, containing the monolayer structure. A small Bragg peak is present in the reflectivity profile of the D_2O buffer contrast, that is not fit with the model. The Bragg peak suggest that there will be some bilayer stacking in the structure, though the intensity is so weak it is unlikely to be more that 1% of the bilayer that has multi-layers underneath.*

Table 4.6 *Fitted model parameters and 95% confidence intervals for neutron reflectivity measurements from an MscL containing suspended bilayer (shown in Figure 4.26.*

Parameter	Fitted Value
APM of Bilayer(Å^2 molecule^{-1})	$56.8_{(55.9\ 57.7)}$
Water per Lipid Head	$0.5_{(0.0\ 2.2)}$
Water Gap (Å)	$9.4_{(8.7\ 9.9)}$
Bilayer Roughness(Å)	$6.1_{(5.6\ 6.7)}$
Protein Coverage (%)	$2.6_{(0.8\ 4.2)}$
Protrusion Thickness (Å)	$60_{(38\ 82)}$
APM of DODAB (Å^2 molecule^{-1})	$65_{(55\ 88)}$
Surface Roughness (Å)	$3_{(0\ 7)}$
DODAB Hydration (%)	$7_{(0\ 14)}$

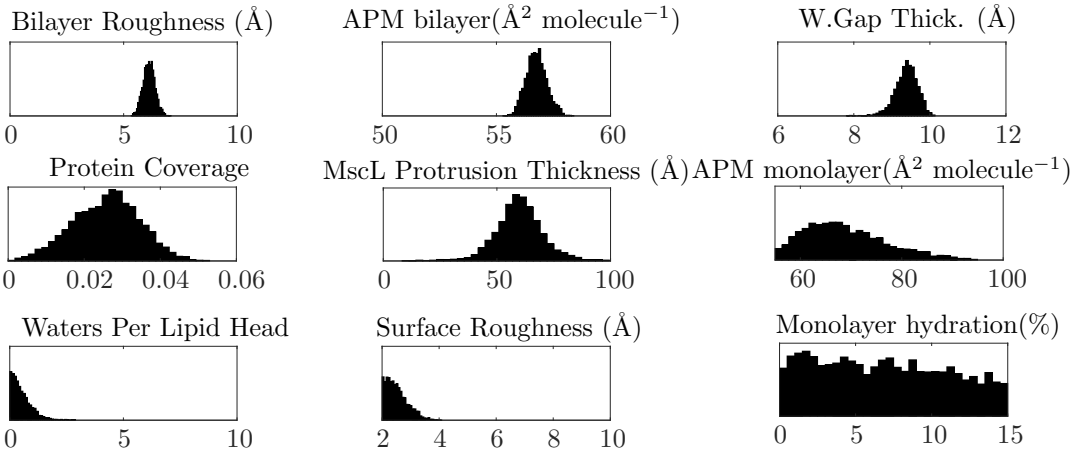

Figure 4.27 *Posteriors of Bayesian analysis parameters of fitting an MscL model a reflectivity measurements of our suspended bilayer.*

of the proteoliposomes. This suggests that the MscL is mobile within the proteoliposome, and it is the regions of the proteoliposome that have a lower coverage of MscL that interact with the DODAB monolayer during the rupture process, and that some protein is lost from the bilayer during rupture. The peak of the posterior for the MscL protrusion is at 60 Å, which is larger than the 40 Å predicted on the basis of the crystal structure. However Figure 4.27 shows that this parameter spans a relatively wide range, indicating a degree of conformational disorder in this protruding region. The flat posterior observed for the monolayer hydration, supports the assertion that the data is not particularly sensitive to the monolayer parameters; indicating that the data provides little information about the monolayer.

4.5.4 Formation Kinetics of MscL Containing Suspended Bilayers

The procedure used for the formation of suspended bilayers containing our protein of interest is the same as the method used for the formation of our lipid only construct, simply using proteoliposomes instead of using liposomes. The proteoliposomes are significantly larger with diameters of 270 nm compared to 100 nm as measured by dynamic light scattering. One might also expect the presence of the protein also changes the density of the proteoliposomes and the bending rigidity of the membrane compared to the liposomes. All of these factors:

size, density and bending rigidity are likely to affect liposome rupture kinetics. Our plan was that by having an optimised method for liposome rupture, working with high concentrations of liposomes (1 mg ml^{-1}) and an osmotic shock rupture step, this would also be sufficient to rupture our proteoliposomes.

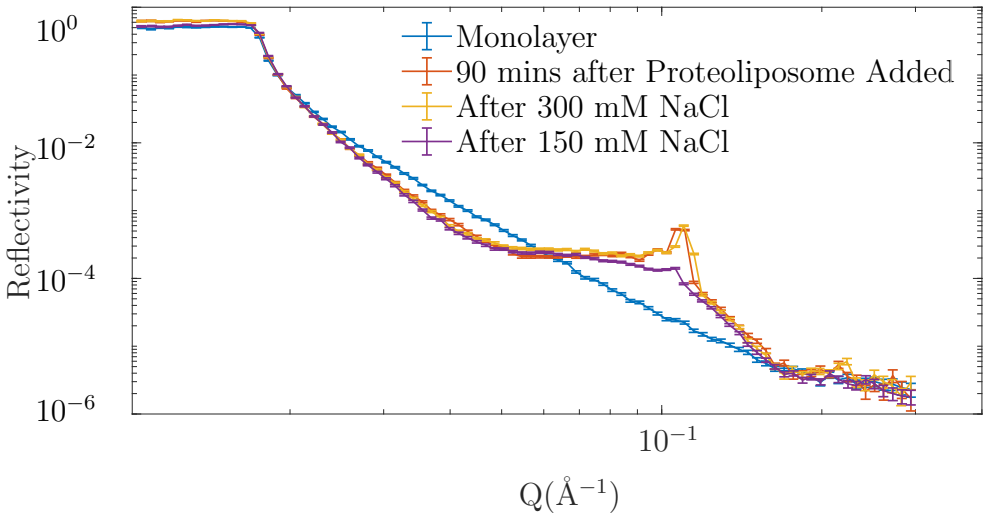

Figure 4.28 *Neutron reflectivity showing the formation of MscL-containing suspended lipid bilayers.*

Figure 4.28 displays the formation steps of the MscL-containing suspended bilayer. In comparison to the liposome only system, no large diffuse material can be inferred from the reflectivity profiles prior to salt addition. There is however a Bragg peak at $Q = 0.1$ Å^{-1}. This suggests that for proteoliposomes, the monolayer-vesicle interactions plays a more important role in bilayer formation than does reaching a critical coverage to induce rupture. The observed Bragg peak is likely due to patchy bilayer stacking that is mostly removed by the salt washes. The presence of the protein may make bilayer stacking more favourable as the protein could act as sticky sites.

Fitting of the Bragg feature was performed by M. Skoda, using a mixed area model in Refnx.[162] The scattering length density value for the lipids was constrained to values used in the Rascal models but the SLD of the DODAB monolayer and subphase were allowed to vary. Note that protein was not included in these models as that level of complexity is not required to make inferences about the coverage of the multi-layers. The lipid leaflet model allows for the combination of two models: that of our single suspended bilayer and that of a low-coverage bilayer stack. For the fits in Figure 4.29 and Figure 4.30 the bilayer stack model has 13 bilayers for which the thickness of the bilayer and spacing between bilayers

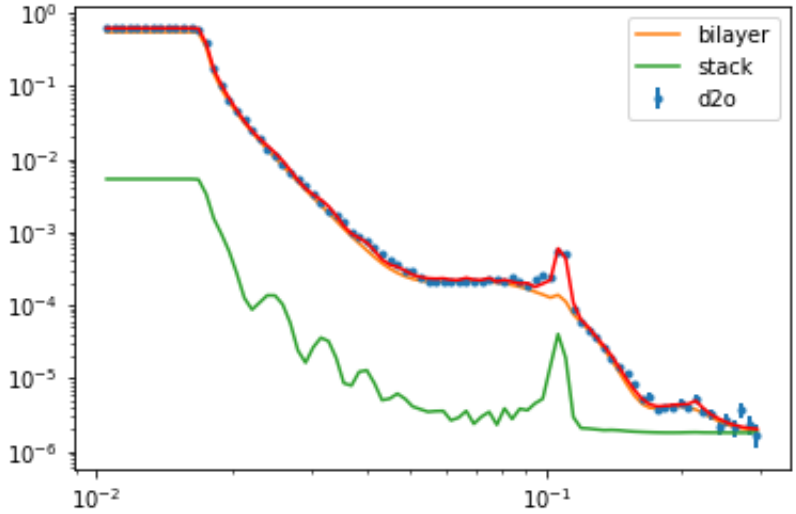

Figure 4.29 *Neutron reflectivity profiles of the layer formed* 90 *minutes after injection of proteoliposomes fit to a Refnx lipid leaflet model to fit the Bragg feature. Fitting performed by M.Skoda.*

was allowed to vary. In fitting the data it was noted that the fits are not sensitive to bilayer properties within the stack. This is due to the stack being low coverage and only contributing to a small portion of the reflectivity profile. The best fit parameter values and their uncertainties were determined from MCMC Bayesian Analysis and are listed in Table 4.7 and Table 4.8 . The calculated errors of the fit to the suspended bilayer before the 300 mM salt rinse, shown in Table 4.7, are unrealistically small for the resolution of the instrument, this is due to the large number of parameters in the model fitting a single reflectivity profile. The large number of parameters has resulted in over-fitting of the data, therefore the model over-determines the data. Whilst the fit can give some indication to the amount of material contributing to the multilayer stack (only about 1% of the total bilayer), detailed information on lipid packing or bilayer spacing should not be concluded from such an analysis.

Table 4.7 *Table showing the best fit parameters and uncertainties to the fitted reflectivity profile in Figure 4.29*

Parameter		Value		
Scalefactor of bilayer fit		0.542	±	0.00005
Scalefactor of multilayer fit		0.00533	±	0.0000005
Background	(E^{-6} $Å^{-2}$)	2.296	±	0.002
DODAB Thickness	(Å)	23.6	±	0.0003
DODAB SLD	($E^{-6}Å^{-2}$)	0.416	±	0.0004
DODAB Roughness	(Å)	3.15	±	2.18
Water Thickness	(Å)	8.9	±	0.0007
Water Roughness	(Å)	9.91	±	2.96
APM bilayer	($Å^{-2}$ molecule^{-1})	66.2	±	0.007
Inner Head Thickness	(Å)	4.75	±	0.0004
Tail Thickness	(Å)	14.5	±	0.02
D_2O SLD	($E^{-6}Å^{-2}$)	6.14	±	0.006
Bilayer/Solvent Roughness	(Å)	5.47	±	0.54
Bilayer Water Thickness	(Å)	19.1	±	0.02
Bilayer Water Roughness	(Å)	3.4	±	2.4
Bilayer Solvation	(%)	0.63	±	0.07
APM in the stack	($Å^{-2}$ molecule^{-1})	77	±	16
Inner Head Thickness	(Å)	4.0	±	2.4
Tail Thickness	(Å)	16.6	±	0.02

Table 4.8 *Table showing the best fit parameters and uncertainties to the fitted reflectivity profile in Figure 4.30*

Parameter		Value		
Scale of bilayer fit		0.5420	±	0.0004
Scale of Multilayer Fit		0.00533	±	0.00005
Background D_2O	(E^{-06}Å^{-2})	2.3	±	2.2
DODAB thickness	(Å)	23.6	±	0.03
DODAB SLD	(Å^{-2})	0.416	±	3.90×10^{-5}
DODAB roughness	(Å)	3	±	2
water thickness	(Å)	8.82	±	0.001
water roughness	(Å)	10	±	3
Area per Molecule	(Å^{-2} molecule^{-1})	66.2	±	0.007
inner head thickness	(Å)	4.75	±	0.000421
Tail Thickness	(Å)	14.5	±	0.2
D_2O Buffer SLD	(E^{-06}Å^{-2})	6.14	±	0.06
Bilayer Roughness	(Å)	5.47	±	0.01
Bilayer Water Thickness	(Å)	19.1	±	0.002
Bilayer Water Roughness	(Å)	3	±	2
Stack Area per Molecule	(Å^{2} molecule^{-1})	77	±	16
Inner Head thickness	(Å)	4	±	2
Tail Thickness	(Å)	16.6	±	0.002
Background NRW	(E^{-06}Å^{-2})	1.92	±	0.002
NRW Buffer SLD	(E^{-06} Å^{-2})	0.257	±	0.003
Background PMW	(E^{-06}Å^{-2})	3.03	±	0.0003
PMW Buffer SLD	(E^{-06}Å^{-2})	1.80	±	0.0002

The fitted parameters to the reflectivity profile in Figure 4.29 are shown in Table 4.7. Given the difference in scale between the suspended bilayer and the stack, we can conclude that the stack has $0.98 \pm 0.01\%$ coverage. Therefore the amount of material in the stack contributes little to the overall material observable by neutron reflectivity.

The bilayer stack present in the final MscL-containing bilayer was also fitted. This was achieved after rinsing with two different salt concentrations. Once again the bilayer stack has a low coverage of less than 1% of that of the bilayer.

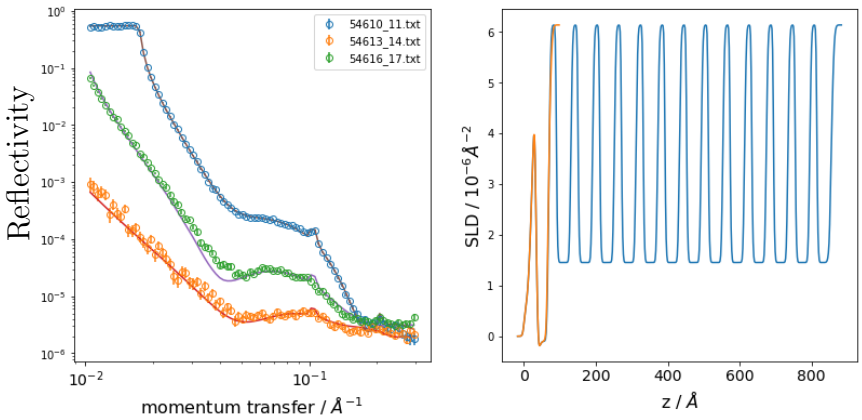

Figure 4.30 *Neutron reflectivity profiles of the layer after rinsing with* 300mM *NaCl and the standard* 150mM *NaCl buffer. Fit to a Refnx lipid leaflet model to fit the Bragg feature. Fitting performed by M. Skoda.*

4.5.5 Effect of Pexiganan on MscL Containing Bilayers

A solution of 1.6 µM pexiganan was passed through the laminar trough underneath our MscL-containing suspended bilayer, allowing the impact of the protein on the response of the bilayer to pexiganan to be investigated. The conditions matched those of our lipid suspended bilayer to enable us to compare the effect of the protein on the membrane's response to pexiganan. The protein coverage in the pexiganan model was constrained to the best fit parameter value of 2.6% determined for the MscL containing datasets. The available volume of the protein protrusion (C-terminal, His-tag and N-terminal regions) is constrained by the overall volume of the protein and the volume of the transmembrane portion of the protein. The volume fraction of the protein in the protein protrusion layer of the model is therefore dependent on the thickness of the membrane and the protrusion thickness. In the pexiganan model, the only protein parameter that is allowed to vary is the protrusion thickness. If a gating of the MscL channel were to occur we may expect a conformational change that involves a retraction or partial retraction of the c-terminal domains.

Figure 4.31 shows the difference in the reflectivity profile and scattering length density profiles before and after pexiganan addition to the MscL containing bilayer. Some difference can be seen by eye in the scattering length density profiles, notably the difference in thickness of the bilayer and of the protrusion. Bayesian analysis of this model and the comparison to the previous MscL model make these difference more apparent, see Figure 4.33 below for the posteriors

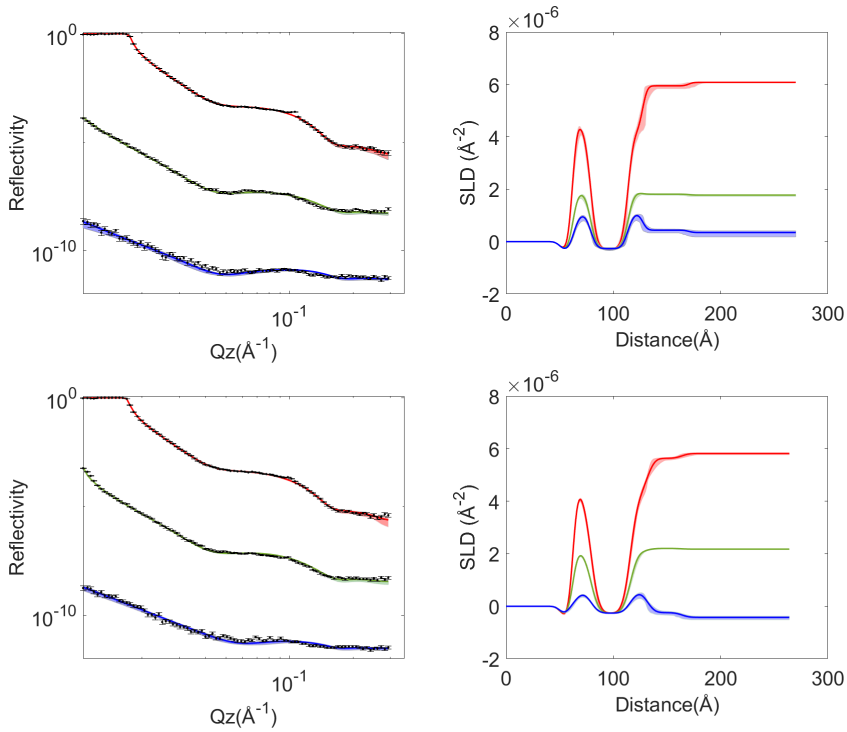

Figure 4.31 *Neutron reflectivity and SLD profiles for suspended lipid bilayers containing the MscL protein before and after exposure to* 1.6 µM *pexiganan. (Top left) Data (shown as error bars)and fits (solid lines with lighter coloured 95% confidence interval for the bilayer measured in* D_2O *(red), protein matched water (green) and* H_2O *(blue). (Bottom Left) Data and fits for the bilayer and pexiganan, the pexiganan is not explicitly in the model. (Top right) SLD profile of lipid bilayer corresponding to the fits in panel in top left. (Bottom right) SLD profile of lipid bilayer corresponding to the fits in panel bottom left.*

from the Bayesian analysis.

The addition of pexiganan results in a decrease in the area per molecule of lipids in the bilayer, as we previously observed in our lipid-only bilayer. We also observe a 30 Å decrease in the extent of the protrusion out from the bilayer. Comparing the posterior probability distributions shows this change to be statistically significant and we attribute this to the gating of MscL triggered by the interaction of PXG with the bilayer.

4.5.6 Discussion

Mechanosensitive ion channel of large conductance, MscL, has been successfully incorporated into our novel suspended bilayer mimic. The protein channel density

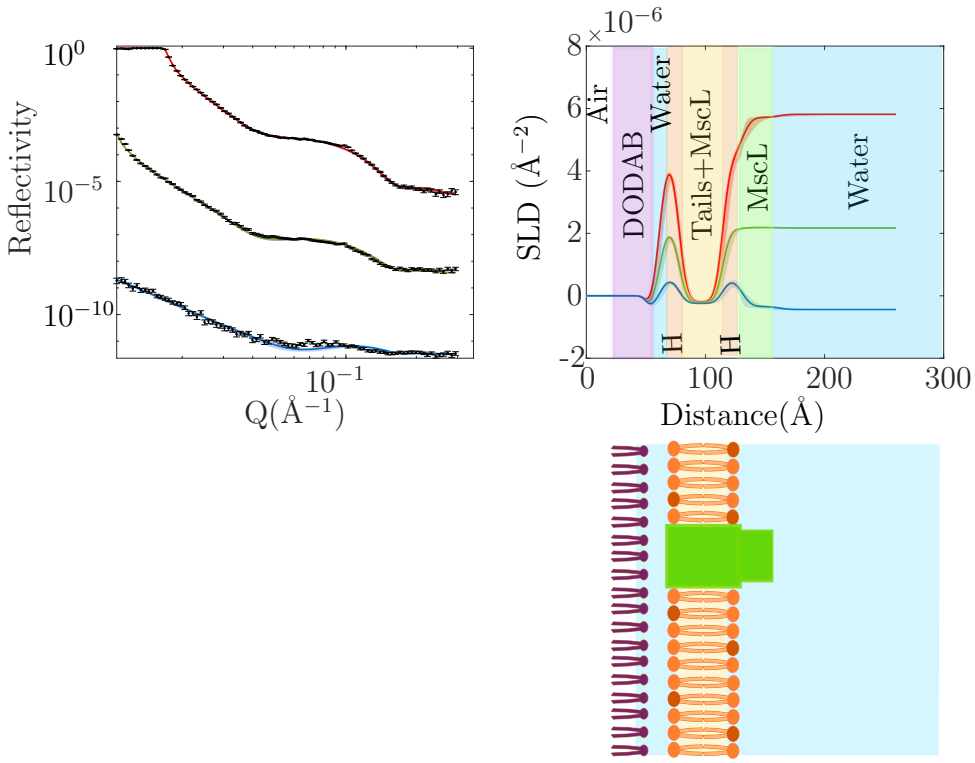

Figure 4.32 *Reflectivity profile of MscL-containg suspended bilayer after exposure to a solution of* 1.6µM *pexiganan and the corresponding fitted SLD profile with simple diagram.*

associated with the protein channel can be incorporated into a model to calculate the reflectivity as two blocks: transmembrane and protruding into the sub-phase; the latter indicating a preferential orientation of the channel in the bilayer. The incorporated channel undergoes a conformational change in the presence of pexiganan.

As far as the author is aware there are no reports of pexiganan being tested on any protein and lipid membrane mimetics. Previous literature has solely used lipid only mimetics, as is the case for many other antimicrobial peptide investigations which form the basis of the field current understanding antimicrobial peptide mechanisms.

Previous literature have argued whether gating of MscL arises from purely an increase in curvature (which would require asymmetric insertion)[176] or a change in membrane tension.[52] Our results suggest that an increase in membrane tension occurs (inferred from the decrease in APM of the lipids) on insertion of pexiganan, concurrent with a conformational change of the embedded protein, which we take to be a signature of the gating of the MscL. An increase in curvature cannot be inferred from our results since this might be expected to

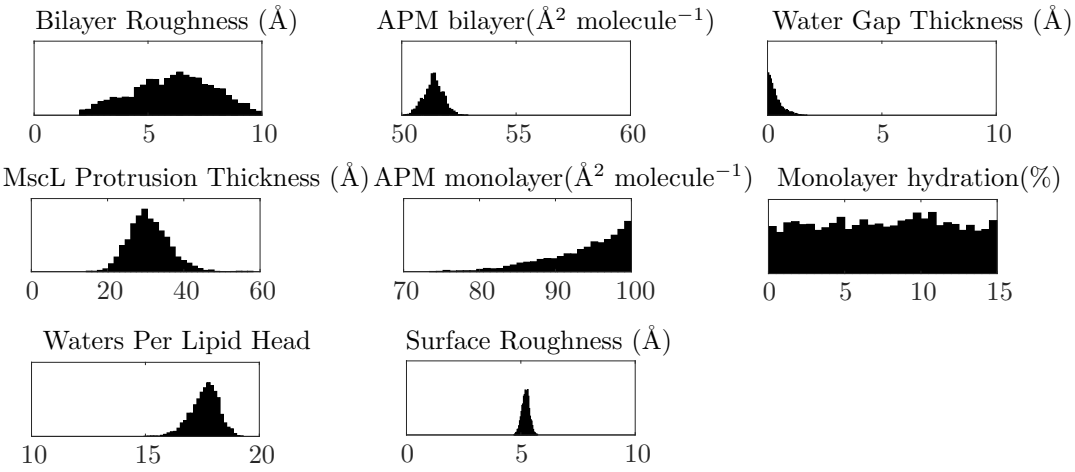

Figure 4.33 *Posteriors of analysis parameters of fitting an MscL model a reflectivity measurements of our MscL containing suspended bilayer in the presence of pexiganan.*

result in an increase in the bilayer roughness, which is not the case. Note that we are assuming gating has occurred with the conformational change of the MscL channel, and there is some literature to suggest that partially-gated forms of MscL can exist.[113] MscL held in a partially gated conformation is likely to reduce the ability of a bacterium to self-regulate osmotic pressure and decrease its likelihood of survival.

Overall we observe a partial retraction of the C-terminal region into the bilayer since the thickness of the protrusion decreases from 60 Å to 30 Å. Partial retraction of the C-terminal region is consistent with EPR measurements by *Bavi et al.* that observed dissociation of only the top C-terminal segments of the MscL channel on gating.[16]

4.6 Chapter Conclusion

We have developed a novel bacterial membrane model which has enabled us to gain an insight into the mechanism of the antimicrobial peptide pexiganan. The ease of incorporation of unhindered protein into our system through the rupture

Table 4.9 *Table of pest fit parameters for an MscL containing lipid bilayer before and after pushing a solution of* 1.6 µM *pexiganan using laminar flow underneath the formed bilayer.*

	Pre PXG addition	Post PXG addition
Parameter	Fitted Value	Fitted Value
APM of bilayer(Å^2 molecule^{-1})	$56.8_{(55.9\ 57.7)}$	$51.4_{(50.5\ 52.2)}$
Water Gap (Å)	$9.38_{(8.72\ 9.88)}$	$0.34_{(0.00\ 1.11)}$
Bilayer roughness(Å)	$6.1_{(5.6\ 6.7)}$	$6.1_{(2.7\ 9.3)}$
Protein Coverage (%)	$2.6_{(0.8\ 4.2)}$	$2.6_{(fixed)}$
Protrusion thickness (Å)	$60_{(38\ 82)}$	$31_{(22\ 42)}$
APM of DODAB (Å^2 molecule^{-1})	$69_{(57\ 88)}$	$94_{(81\ 100)}$
DODAB hydration (vol%)	$6.9_{(0.4\ 14.4)}$	$7.5_{(0.4\ 14.6)}$

of proteoliposomes makes it a valuable platform to explore other proteins and membranes.

Liposomes can be ruptured underneath a monolayer of surfactant to form a bilayer. The set-up and conditions to achieve the formation of this suspended bilayer were initially optimised using ellipsometry and RAIRS and then further optimised using neutron reflectivity. A charged surfactant was used and the liposome composition needs an overall opposite charge for successful bilayer formation. Similar lipid and surfactant compositions have been used by other groups to facilitate the formation of layers of nanodiscs at the air-water interface. The time required for bilayer formation was found to be dependent on liposome concentration (concentrations of 0.05 mg ml^{-1}, 0.1 mg ml^{-1} and 1 mg ml^{-1} were tested) and salt concentration. The salt concentrations used were similar to the optimum conditions found for bilayer formation on silicon interfaces.

The following method was optimised for the formation of good quality bilayers: A surfactant monolayer was spread to the desired surface pressure. Liposomes were then passed through at a concentration of 1 mg ml^{-1} under the surfactant monolayer using a laminar flow trough. After an hour a solution of higher salt concentration (300 mM) was passed through the trough, followed by the original 150 mM NaCl buffer solution.

The difference in kinetics observed between formation of the lipid bilayers and lipid-protein bilayers will largely have been driven by the size difference of the liposomes. However, given that a Bragg feature was only observed in the protein-containing system, it is likely that the kinetics are also dependent on

other liposome properties such as the bending rigidity of the liposomes and the possibility of the protein acting as a sticky site for other material to absorb underneath.

We can successfully report formation of our novel bacterial membrane mimic, which we refer to as a suspended bilayer. Our suspended lipid-only bilayer has a slightly high roughness of 8 Å and an area per molecule of 58 $Å^2$ ($\pm$ 2 Å) which is close to expected literature values for a mixed POPC:POPG bilayer. The bilayer has a significant 11 Å gap between itself and the surfactant monolayer, providing flexibility in the membrane and removal of constraint from the surface. We were also able to prepare high coverage suspended bilayers containing MscL protein from proteoliposomes. The final coverage of protein within the bilayer was fitted as 2.57% ($\pm$1.8%).

Both of these systems were then tested with the antimicrobial peptide pexiganan where changes in the reflectivity profiles were observed. In the lipid-only bilayer, the interaction with pexiganan slightly decreased the APM and a 0.6% coverage of pexiganan in the bilayer was fitted. The decrease in APM was greater for the MscL containing bilayer which when combined with the conformational change implied by the large change in the protein protrusion thickness suggests that we are observing the opening of a large pore as the MscL gates open.

The decrease in APM of our our suspended bilayer both in the presence of lyso-PC and pexiganan suggests that symmetric insertion has occurred i.e. lyso-PC/pexiganan are present in both bilayer leaflets. Our model fitting suggest that an increase in membrane tension occurs (observed through the decrease in APM of the lipids) on insertion of pexiganan which results in the gating of MscL in our bilayer.

The change observed in thickness of the c-terminal protrusion is the first experimental evidence of movement of the C-terminal protrusion domain of MscL although it has been proposed in multiple molecular dynamics simulations. Observation of the gating in the presence of pexiganan suggests that MscL could be the Achilles heel of bacteria in the presence of low concentrations of surfactant and antimicrobial peptides. Permanent gating of the MscL channel would result in depolarisation of the bacterial membrane, resulting in bacterial death. By investigating the effect of pexiganan on a lipid and protein bacterial membrane mimic we have highlighted a possible mechanism of antimicrobial action.

Further details of MscL gating could be eluded from selective deuteration of

components in our system such as pexiganan or the MscL protein. Of particular interest would be to investigate MscL with the protrusion section deuterated so that the redistribution of the C-terminus could be further defined.

Chapter 5

MscL in Tethered Bilayers

5.1 Introduction

In-vitro membrane mimetics have been developed to provide a controlled, membrane-like environment in which membrane proteins can be studied.[204, 227] A comparison of model membranes is given in Chapter 1 as well as in several thorough review articles.[6, 12, 62] Traditionally used membrane mimetics such as solid-supported bilayers leave little space between the membrane and the solid support, generally only a few Å. Many membrane proteins have sections of their structure that are cytoplasmic or extracellular i.e. that do not sit only within the membrane of the bacteria. The close proximity of the solid support and lipid membrane in some models may not leave space for the protein protrusions from the membrane.[29, 228] Close proximity of the membrane to the surface can also allow the protein to interact with the surface, affecting conformation and function. Another well used model membrane is that of the floating bilayer which suffers from complex assembly protocols and limited stability.[63, 100, 192]

To increase the stability of a model membrane separated from a solid support, several tethering strategies have been introduced. The tethers increase the stability of the bilayer whilst maintaining a separation between the bilayer and the solid support.[69, 184]

Tethered bilayers can be studied using a broader range of techniques compared to floating bilayers. Due to their attachment to the solid-surface they can be studied using Quartz-Crystal Microbalance with Dissipation (QCM-D), Surface Plasmon

Resonance (SPR), Electrochemical Impedance Spectroscopy (EIS) and current voltage (CV) studies. Tethered bilayers can also be studied using techniques well suited to studying planar membrane mimetics such as atomic force microscopy (AFM), neutron reflectivity (NR) and ellipsometry.

Tethering of bilayers can be achieved through the use of an anchor lipid or through the use of a protein tether. Successful tethering of the membrane through protein tethering is highly dependent on the availability of the tether from the membrane and is not possible for all membrane proteins. Protein tethering is best achieved with proteins stabilised in detergent rather than in liposomes, as the protein is not sterically hindered by the bulky liposomes. Since the expression system used in this thesis is detergent-free, protein tethering was not a viable method. Using anchor lipids as the membrane tether is less system selective, and can be used to prepare planar lipid bilayers from proteoliposomes.

Incorporation of polymer cushions between solid supports and the model membrane has been shown to increase membrane fluidity, increasing the mobility of transmembrane proteins and lipid diffusion rates. PolyEthylene Glycol (PEG) has been exploited as a polymer cushion layer as it has been shown to produce stable tethered bilayers.[5] PEG has been shown to prevent non-specific absorption of proteins to surfaces and does not adsorb to lipid bilayers. [10, 181] These properties have led to a wide range of research using PEG moieties in liposomes to provide liposome stability and resistance to biological interactions for applications in liposome drug delivery.[85, 172] The advantage of these properties for model membranes is that non-selective absorption of the protein onto the solid substrate needs to be avoided and any tether should not interact with the lipid membrane, as that may affect the membrane properties.

Covalently linking PEG to a lipid at one end and a surface active linker at the other end enables it to be used as an anchoring lipid tether that shares some of the desirable physiochemical properties of a polymer brush. The surface active linker needs to be appropriate for the substrate being used such as silane linkers for silicon and thiol linkers for gold substrates. One method of forming tethered bilayers is to incorporate the tether lipid into the bilayer-forming lipid formulation and then to use either use Langmuir-Blodgett deposition or vesicle rupture to form a bilayer on the solid substrate. Whilst this method is simple to prepare, the resulting bilayer can be of variable quality; if the PEG composition is too high (above 15 mol%) then only small bilayer domains form and if the PEG composition is too low (less than 10 mol%) then multi-level bilayers form on top

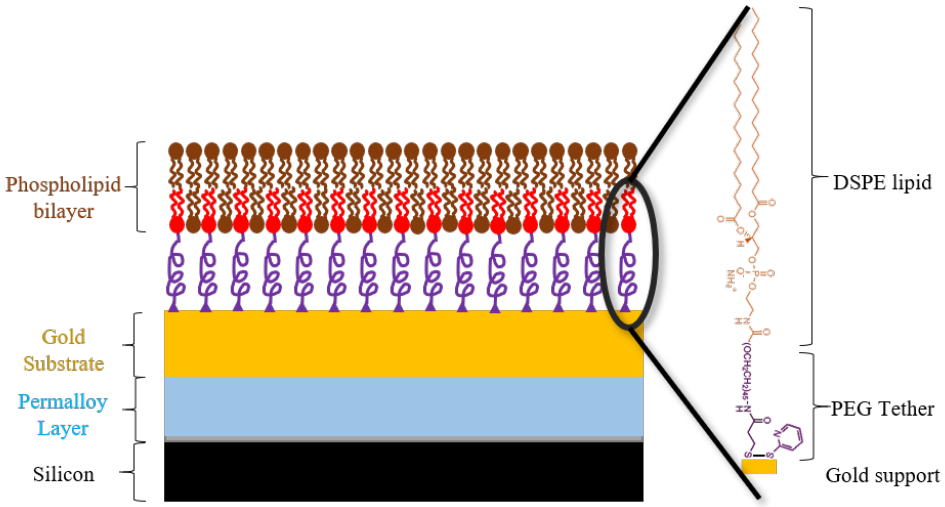

Figure 5.1 *Diagram of a tethered lipid bilayer, tethered using the PDP-PEG2000-DSPE tether investigated in this chapter.*

of and within the PEG cushion layer.[238, 240] An alternative formation strategy involves directly grafting the tethers to the surface and using them as an anchoring platform prior to liposome addition; tether density and spacer length can be tuned to control the membrane mimetic properties. Membrane properties that can be controlled include the mechanical properties of the membrane and the scattering length density profiles of the model. This anchoring platform approach has been successfully exploited for a number of tethers including amine-functionalised PEG DSPE (NH2-PEG-DSPE) on activated silicon.[235]

5.1.1 Aims

In this chapter, the aim was to achieve a tethered lipid bilayer membrane mimic that can be prepared by rupturing proteoliposomes onto a formed layer of lipid tethers. In the end the tether system was chosen to maximise the distance of the bilayer from the solid support. By testing MscL in multiple systems, we can compare the advantages and disadvantages of the membrane mimics. Furthermore, by testing the response of MscL in the presence of pexiganan in multiple systems, a conformational change can be confirmed as a true effect of pexiganan insertion rather than as artefacts of the membrane mimics themselves.

5.2 Optimisation of Tethered Bilayer Formation

The methodology for preparing tethered lipid bilayers was optimised using a quartz crystal micro-balance techniques capable of estimating the change in mass at a solid-interface. The theoretical background behind quartz crystal microbalance measurements was given in Section 2.5.10.

5.2.1 QCM Method and Materials

QCM-R measurements were performed on a Maxtek RQCM at the University of Edinburgh, Edinburgh, UK with 5 MHz Maxtek gold coated sensors. QCM-D measurements were performed on the Biolin Scientific E4 Q-Sense Instrument at ISIS, Oxford, UK. Gold-coated quartz sensors were prepared by RCA cleaning (submerging in a 1:1:50 mixture of NH_4OH: H_2O_2: H_2O, at 55°C for 10 minutes), rinsing with copious Milli-Q water, drying with nitrogen and ozone cleaning for 10 minutes. The sensors were then submerged in tether solution. The tether solution contained 0.1 mg ml^{-1} of N-(3P-(pyridyldithio)propionoyl)amino(polyethylene glycol)(2000) 1,2-distearoyl-sn-glycero-3-phosphoethanolamine(ammonium salt) (PDP-PEG2000-DSPE) in ethanol. The structure of the PDP-PEG2000-DSPE tether is shown in Figure 5.1. Sensors were submerged in the solution in a glass beaker, in the dark at 4°C for 12 hours prior to use. The sensors were rinsed with Milli-Q water before loading into the flow cells and the underside of the sensor dried with nitrogen before the cell was assembled. The QCM-D cells were cleaned prior to use as per manufacturer instruction and any tubing used was new and rinsed through with 20 ml of ethanol and 20 ml of Milli-Q water prior to use. Buffer and vesicle solutions were introduced to the sensor using a peristaltic pump flowing in the solution at 1 ml min^{-1}.

POPC and POPG lipids and PDP-PEG2000-PDP tethers were sourced from Avanti Lipids and purchased as solid powders. Components for buffer solution and ethanol were purchased from Sigma Aldrich. 3:1 POPC:POPG vesicles were prepared by dissolving a 3:1 mixture of POPC and POPG lipids in the minimum amount of chloroform, evaporating the chloroform under a steady stream on nitrogen and resuspending the lipid film in HEPES buffer (20 mM, pH 7.4,150 mM NaCl). To ensure unilamellar vesicles of diameter $\sim$ 100 nm, the vesicle solution was tip-sonicated using a Sonics Vibra Cell model VCX 500 with a CV33 converter

(5 seconds on, 5 seconds off at 20% power) for 30 minutes until opalescent.

A typical QCM protocol followed the following steps:

1. Buffer solution (10 ml) was passed through each of the flow cells and the measurement started with the sensors in HEPES buffer(20 mM, pH 7.4, 150 mM NaCl).

2. After testing that the frequency was stable for 30 minutes with only clean buffer in the cell i.e. there was no desorption of tether occurring, absorption of contaminants or bubbles in the system, then a solution of vesicles was passed through the cells at 1 $\mathrm{ml\,min^{-1}}$ using the peristaltic pump. 10 ml of vesicle solution is passed through each QCM cell.

3. After an hour, HEPES buffer (20 mM, pH 7.4, 300 mM NaCl) was passed through the cells to remove excess liposomes.

4. This was immediately followed by a salt rupture step, pushing 5 ml of lower salt concentration HEPES buffer (20 mM, pH 7.4, 150 mM NaCl) through the QCM cell.

This protocol was based on our previous optimisation in forming our suspended bilayers at the air-water interface in Chapter 4.

Since tethered bilayers are viscoelastic it was inappropriate to analyse the results quantitatively using the Sauerbrey equation. The system has high water content in the tether layer and also in any tethered liposomes. High water content increases elasticity such as when the liposomes remain intact on the tethers, which results in a high $-\Delta D/\Delta F$ value.[131] When the liposomes rupture, a more rigid layer is formed resulting in the $-\Delta D/\Delta F$ ratio decreasing. Using $-\Delta D/\Delta F$ to assess vesicle rupture has been employed by several groups.[119, 131] Though the added complication of a long tether layer has been shown to distort values. A study into the effect of using PEG2000-DSPE as a spacer molecule for membrane tethering on QCM results found $-\Delta D/\Delta F$ values between 1.8 and 5 for PEG tethered bilayers.[104] The value is dependent on the density of the tether as well as the bilayer structure. The QCM study by Inci *et al.* suggested that in their system, individual liposome rupture occurred and therefore only an increase in dissipation was observed with no subsequent decrease.[104]

5.2.2 Optimisation of Tethered Bilayer Formation

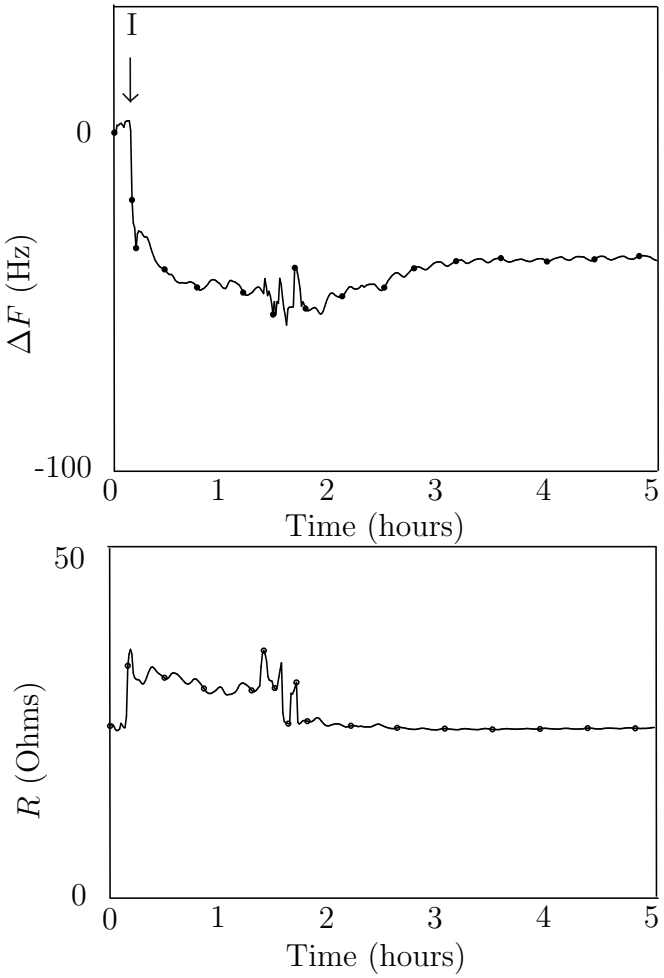

Figure 5.2 *QCM-R measurement of change in 3rd overtone frequency (Top) and resistance (Bottom) as a function of time following injection of* 0.5 mg ml^{-1} *liposomes over a DSPE-PEG2000-PDP tethered gold sensor (point of injection marked I). The 3rd overtone of the QCM trace is shown.*

After checking the stability of the tether, a solution of 100 nm diameter vesicles (3:1 POPC:POPG, 0.5 mg ml^{-1}, 10 ml) was passed over the QCM sensor using a peristaltic pump at 1 ml min^{-1}. The QCM-R measurement is shown in Figure 5.2.

As seen in Figure 5.2, the frequency decreased immediately after addition of vesicles (marked I) to -35 Hz and the rate of decrease in frequency slowed when the pump stopped. This decrease in frequency corresponds to the addition of mass at the sensor, in this case vesicles adsorbing to our tethered surface. The rate of decrease in frequency changes after the pump stops, this may be due to the

kinetics becoming diffusion limited when the solution is no longer being replaced. The frequency continued to decrease to a change of −55 Hz before increasing again to −35 Hz. This can be attributed to the critical coverage mechanism of vesicle rupture. In the critical coverage rupture mechanism, liposomes initially adsorb to the surface or in this case to the tethers until a high enough coverage is at the surface to support liposome rupture. When the liposomes rupture an increase in frequency occurs.

The conclusion that vesicle rupture is occurring is consistent with the resistance measurements. As resistance is proportional to dissipation, the initial increase in resistance can be associated with the adsorption of vesicles at the tether–solution interface; the subsequent decrease is consistent with the rupture of vesicles forming a compact, uniform layer at the tether interface.

Following the encouraging observations at liposome concentrations of 0.5 mg ml^{-1}, a higher concentration was tested at 1 mg ml^{-1} and salt-rinsing steps were added to ensure high coverage.

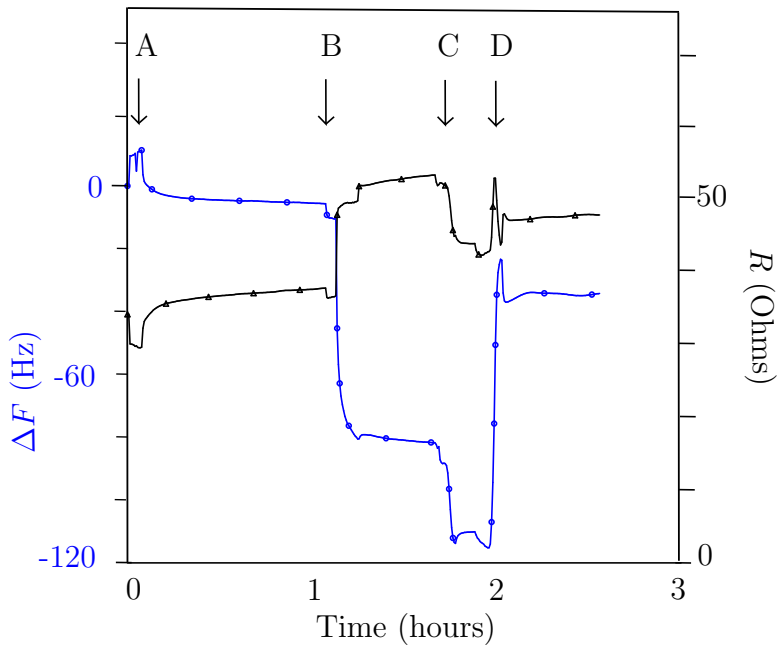

Figure 5.3 *QCM-R measurement of change in frequency and resistance of a PDP-PEG2000-DSPE tethered gold sensor after A) Flowing buffer through the cell, B) Flowing* 1 mg ml^{-1} *liposomes through the cell (marked as I in Figure 5.2, C) Flowing* 300 mM *NaCl and D) Flowing* 150 mM *NaCl. 3rd overtone from QCM measurement plotted.*

From Figure 5.3, a steep decrease in frequency occurs at point B when the liposomes are passed through the cell, accompanied by an increase in resistance

consistent with the absorption of intact vesicles. When 300 mM NaCl is passed through the cell at point C, both the frequency and resistance decrease, which is unusual. In the standard pattern of vesicle rupture, as highlighted in Figure 2.10 both a decrease in dissipation and an increase in frequency occur on vesicle rupture. When a further solution of 150 mM NaCl is passed through the cell at point D, a decrease in frequency is observed with no further decrease in resistance.

Measurements were repeated for liposome concentrations of 0.5 mg ml^{-1} liposomes and 1 mg ml^{-1} liposomes using QCM-D, but with the time between the first and second salt rinsing steps decreased from 1 hour to 10 minutes, see Figure 5.4.

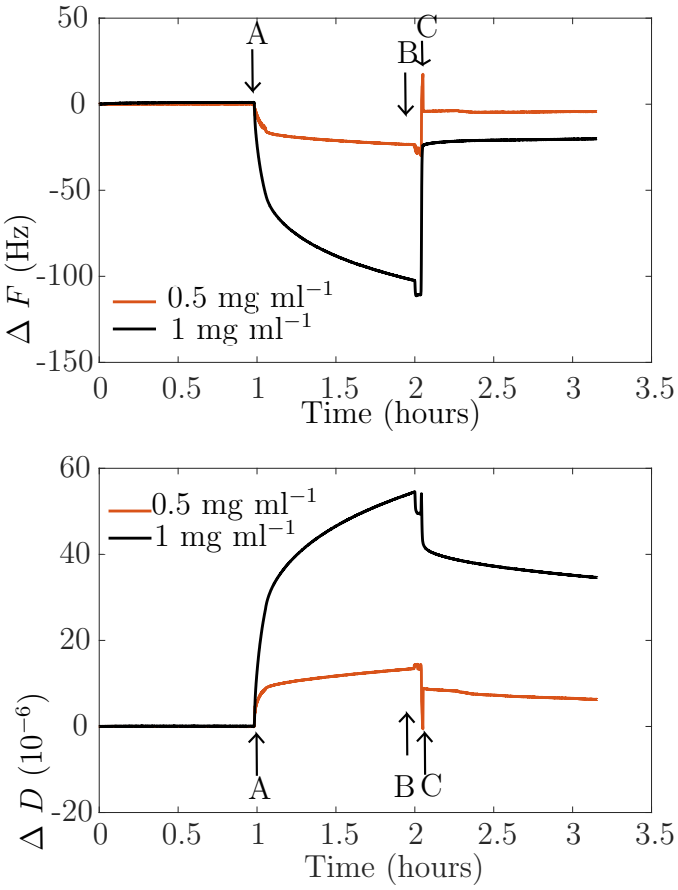

Figure 5.4 *QCM measurement of change in (3rd Overtone) Frequency (Top Figure) and change in Dissipation (Bottom Figure) of a DSPE-PEG2000-PDP tethered gold sensor after addition of liposomes (A) at* 0.5 mg ml^{-1} *(red line) and* 1 mg ml^{-1} *concentration (black line),* 300 mM *NaCl injected at point B followed by* 150 mM *NaCl at point C.*

The QCM-D results in Figure 5.4 follow the same pattern as the results obtained using QCM-R in Figure 5.2 and Figure 5.3. On the injection of liposomes into

the QCM cells, marked as point A in Figure 5.4, the frequency decreases and dissipation increases, consistent with intact liposome adsorption. Smaller changes are observed at the lower liposome concentration suggesting that fewer liposomes adsorb. Flushing the QCM cells with 300 mM, followed by 150 mM of NaCl results in the frequency increasing and dissipation decreasing. This observation is consistent with vesicle rupture rather than vesicle desorption as vesicle desorption would not result in a decrease in dissipation (unless all the liposomes were removed in which case the change in frequency would return to 0). The dissipation values measured are much larger than those observed for a bilayer on a solid substrate where $\Delta D < 1 \times 10^{-6}$. However, given that our bilayer is resting on a viscoelastic PEG tether cushion the larger dissipation is to be expected and is consistent with previous literature on PEG tethers.[104]

The QCM-D data measured for bilayer formation from 1 mg ml^{-1} POPC:POPG liposome solutions being deposited on a PEG tether layer can be compared to an alternative method of tethered bilayer preparation.[104] In this approach, liposomes containing a small molar percentage of lipids coupled to a reactive moiety by means of a PEG spacer are ruptured directly onto a clean surface. Inci *et al.* used this approach using DSPE-PEG2000 with an amine functional group on silicon, whereas we used a PDP, with a disulfide group on a gold surface. A comparison is shown in Figure 5.5.

On Figure 5.5, the blue data has been measured by QCM-D following the injection of 1 mg ml^{-1} liposomes incorporating 1 mol % DSPE-PEG2000-PDP. Injection of the 1 mol % DSPE-PEG2000-PDP liposomes results in a layer quickly forming on the QCM-D sensor and salt rinsing appears to have little impact on the change in frequency or dissipation. The final change in frequency measured when assembling the layer by this method is greater than that measured when assembling the layer using POPC:POPG liposomes and a pre-formed tether layer (shown in black).

In the literature, the $-\Delta D/\Delta F$ value has been used to understand liposomal behaviour in model membrane parameters.[97, 119] High water content such as when intact vesicles adsorb to the QCM sensor results in a high $-\Delta D/\Delta F$ value. When liposomes then rupture, a decrease in $-\Delta D/\Delta F$ value occurs. Our system is more complex as hydration of the PEG tether layer and of the adsorbed vesicles/ bilayer needs to be considered. Table 5.1 displays the calculated $-\Delta D/\Delta F$ values at different stages of the assembly of the tethered lipid bilayer, ΔF is normalised for the overtone as in a previous study.[104]

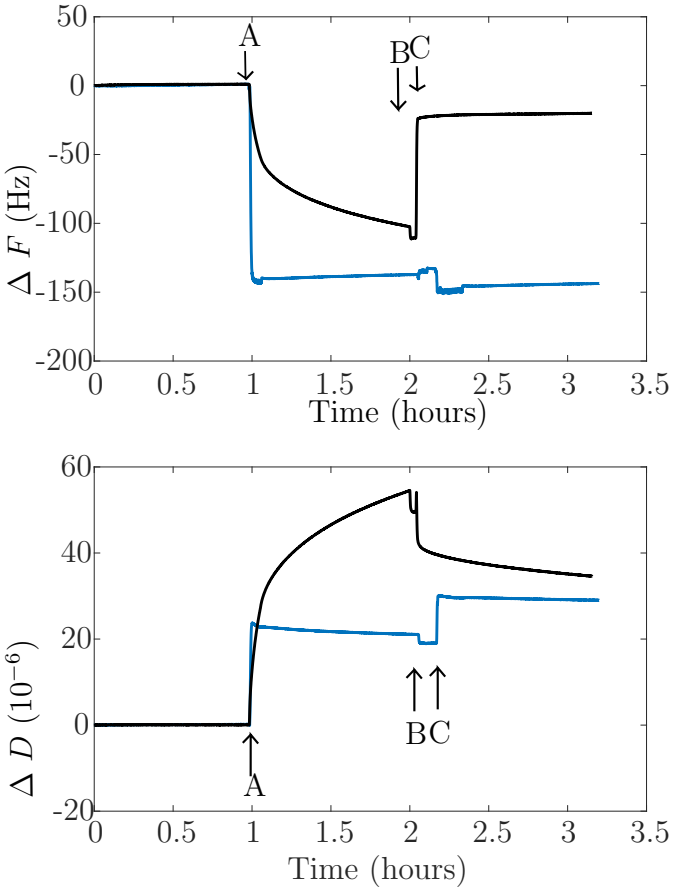

Figure 5.5 *QCM measurement of change in (3rd overtone) Frequency (Top Figure) and change in Dissipation (Bottom Figure) of a PEG2000-DSPE tethered gold sensor (black line) compared to a clean gold sensor (blue) after addition of liposomes (A) of* 1 mg ml^{-1} *1 mol% DSPE-PEG-PDP, POPC:POPG liposomes (blue line) or* 1 mg ml^{-1} *POPC:POPG liposomes (black line),* 300 mM *NaCl injected at point B followed by* 150 mM *NaCl at point C.*

The calculated $-\Delta D/\Delta F$ values of the assembled layers shown in Table 5.1 are of a similar magnitude to those observed in a separate study on PEG2000 tethered bilayers. [104] Previous studies on long-tethered bilayers have not commented on the change in $-\Delta D/\Delta F$ values during bilayer construction. An important observation is that our $-\Delta D/\Delta F$ values are greatest at the end of the assembly process. If individual vesicle rupture was occurring on contact with the tether layer then we would expect $-\Delta D/\Delta F$ to remain largely unchanged through the process. A standard vesicle rupture interpretation would expect $-\Delta D/\Delta F$ values to decrease on vesicle rupture, as the dissipation would tend to 0 when a rigid bilayer is formed at the interface. The hydrated PEG layer in the tether systems may complicate this picture. Given that presence of a viscoelastic layer increases

Table 5.1 *Calculated $-\Delta D/\Delta F$ of multiple QCM-D measurements from different liposome compositions, calculated from the 3rd overtone. The values given for 1* mg ml^{-1} *liposomes are the mean and range of three repeat measurements.*

Liposome Concentration (mg ml^{-1})	$-\Delta D/\Delta F_n$			
	10 min after liposomes added	1 hr after liposomes added	after 300 mM NaCl	after 150 mM NaCl
1.0	1.23(±0.35)	1.15(±0.45)	1.16(±0.44)	3.41(±1.70)
0.5	1.63	1.67	1.37	4.34
1.0 (1 mol% PEG)	0.48	0.46	0.42	0.6

$-\Delta D/\Delta F$ values, forming a high coverage bilayer on top of PEG tethers results in high ΔD and therefore $-\Delta D/\Delta F$ values. Given the viscoelastic nature of the tether layer used in these experiments, differentiating between vesicle removal and rupture is difficult on the basis of QCM-D alone.

The PEG spacer in our tethered bilayer provides a viscoelastic layer (a cushion) and holds a considerable amount of water. Trapped water contributes to the measured mass, found by other groups to cause a 1.5 to 10 times increase in estimated mass for viscoelastic spacer layers when calculated from the Sauerbrey equation. [41, 96] The Sauerbrey equation does not give a correct estimate of added mass for for viscoelastic layers, however using it for our system enables comparison with other literature values and between our different conditions. Table 5.2 shows the calculated mass load of the final formed layer for multiple repeats on to PEG-tethered layers of 1 mg ml^{-1} liposomes (3:1 POPC:POPG) and 0.5 mg ml^{-1} liposomes (3:1 POPC:POPG), as well as the rupture of 1 mg ml^{-1} 1% PDP-PEG-DSPE 3:1 POPC:POPG liposomes onto a clean gold sensor.

The mass load of fluid lipid bilayer on a solid substrate, with concominant low dissipation, has previously been measured to be 434 ng cm^{-2}.[189] The mass load of a bilayer attached to a solid substrate by means of a sparse PDP-PEG2000-DSPE spacer layer has been reported to be 770 for 0.5 mol% PDP-PEG-DSPE and 1500 ng cm^{-2} for 5 mol% PDP-PEG-DSPE when calculated from QCM-

Table 5.2 *Calculated Δm of multiple QCM-D measurements from different liposome compositions, calculated from the 1st overtone using the Sauerbrey equation.*

Liposome Concentration (mg ml^{-1})	Δm(ng cm^{-2})
1	2690
1	2113
1	1825
0.5	270
1 (1 mol% PEG)	3880

D. However, the mass calculated from SPR measurements on the same tethered bilayer after it had been dried was 152 for 0.5 mol% PDP-PEG-DSPE and 156 ng cm^{-2} for 5 mol% PDP-PEG-DSPE. The water content of the PEG-tethered bilayer increased the measured mass 10-fold for the 5 mol% tethers. The mass-load values calculated in Table 5.2 for our dense tethered bilayers produced from 1 mg ml^{-1} liposomes range from 1825–2690 ng cm^{-2} i.e. higher than observed by Coutable *et al.* for sparsely PEG-tethered bilayers.

The spacers used by Coutable *et al*, are in a mushroom conformation at 1 mol % and in a brush conformation at 5 mol%.[48] The mushroom to brush transition has been calculated to occur at 3.5 mol% in formed tethered bilayers.[165] In a denser packing of the PEG tethers, the PEG-molecules are more extended, increasing the thickness of the spacer but also increasing the overall amount of water bound in the layer. This increases the viscosity and the dissipation in the system. Denser packing of PEG tethers therefore results in a higher calculated mass load on bilayer formation. Our observation of a larger mass load on lipid bilayer formation suggests that we have denser packing of PEG tethers than the 5 mol% bilayer composition used by Coutable *et al.*.

When attempting bilayer formation at a lower liposome concentration, a lower mass load was recorded, suggesting that a lower fraction of the tether layer is covered in lipid bilayer. The similar $-\Delta D/\Delta F$ value suggests that the same type of structure is formed at both liposome concentrations.

The technique of using liposome rupture onto a tethered surface was compared to a method of incorporating the tethers into the liposomes prior to rupture.

Incorporating the tethers into the liposomes resulted in a lower $-\Delta D/\Delta F$ value and a much higher mass load of 3880 ng cm^{-2}. The lower $-\Delta D/\Delta F$ can be explained by the lower density of tethering resulting from testing 1 mol% PEG-tether liposomes. These tethers will have a thinner mushroom-like structure spacer that is ultimately less viscous and therefore will have a lower dissipation associated with it, hence the lower $\Delta D/\Delta F$ value. The higher mass load despite the lower tether density, indicates that liposome rupture did not occur when using tether-incorporated liposomes. Incorporating long tethers into liposomes can lower liposome-liposome interactions, reducing the likelihood of liposome rupture.[90, 169]

5.2.3 Summary

A method for preparing tethered lipid bilayers by rupturing liposomes onto a pre-tethered gold substrate was optimised using QCM. Comparison of the changes in frequency and dissipation to formation of similar lipid bilayers in literature suggest that we form a bilayer on a densely packed tether layer in brush conformation. [48]

In order to characterise the quality of the bilayer formed and determine whether we have a single planar bilayer or partially ruptured liposomes or multi-levels of bilayers such as seen by Watkins et al., the system required further investigation using different techniques. [240]

5.3 Polarised Neutron Reflectivity

5.3.1 Technique Background

Polarised Neutron Reflectivity (PNR) is determined by the spin dependent scattering arising from magnetisation of the sample, and is commonly used to provide information about magnetic thin films. The reflectivity profiles of neutrons polarised parallel or anti-parallel with respect to the sample's quantisation axis are measured. Standard PNR set up reduces the measured neutron intensity by at least a factor of two as one neutron spin state is measured at a time. A polarised supermirror is placed before the sample position and spin

flippers used to select the spin to be measured.

Our samples have a magnetic contrast layer under the gold surface. This magnetic contrast increases the information that can be obtained from the neutron reflectivity without having to introduce deuterium labelling of the membrane components or even change the sub-phase contrast; this can be advantageous for potentially delicate samples. [140]

5.3.2 Method

Polarised Neutron Reflectivity measurements were carried out on POLREF, ISIS, Didcot, UK over 4 days of awarded beamtime (RB1820534, 10.5286/ISIS.E.RB1820534).

Silicon blocks for neutron reflectivity measurements were sourced from PI-KEM, with thanks given to Frank Heinrich and Luke Clifton for organising. Silicon blocks were cleaned in piranha solution (3:1:5 sulphuric acid, 30% hydrogen peroxide and water), rinsed in a copious amount of Milli-Q water, dried under a stream of nitrogen and ozone-cleaned. The silicon blocks were determined to have less than 8 Å roughness prior to sending to the NIST nanofabrication facility. A 150 Å permalloy (80 % Nickel, 20% Iron) layer was deposited on the silicon oxide surface and this was subsequently capped by a 150 Å gold layer. Permalloy is a magnetically soft material, such that when the samples are coated in this way and placed in a magnetic field, the layer becomes fully magnetized. This results in a magnetic component of the SLD which is different for spin–up and spin–down neutrons. By measuring PNR, we obtain two reflectivity profiles (one for spin-up and one for spin-down neutrons) for each subphase contrast. This has previously been referred to as magnetic contrast.[36, 95] The means and extent to which the two magnetic contrasts provide additional experimental information relating to soft matter coatings, such as bilayer and polymer-spacer in our experimental system has recently been a subject of discussion.[102, 126] The presence of a permalloy layer for our system also acts as a spacer, increasing the reflectivity, which in turn decreases the noise over the Q range corresponding to the spatial frequencies of interest for the bilayer structure. This effect is independent of any magnetic contrast. However, the difference in spin-up and spin-down scattering length densities for the permalloy layer mean that neutrons encounter a different scattering potential. This will mean that the reflectivity profiles, measured in the two spin states, will be sensitive to different spatial

frequencies within the structure. It is certainly my experience that separate spin-up and spin-down reflectivity profiles help to constrain the fitting. Samples were measured in standard PNR mode at three angles of $\theta = 0.5, 1.2$ and 2.5. The set up used is shown in Figure 5.6.

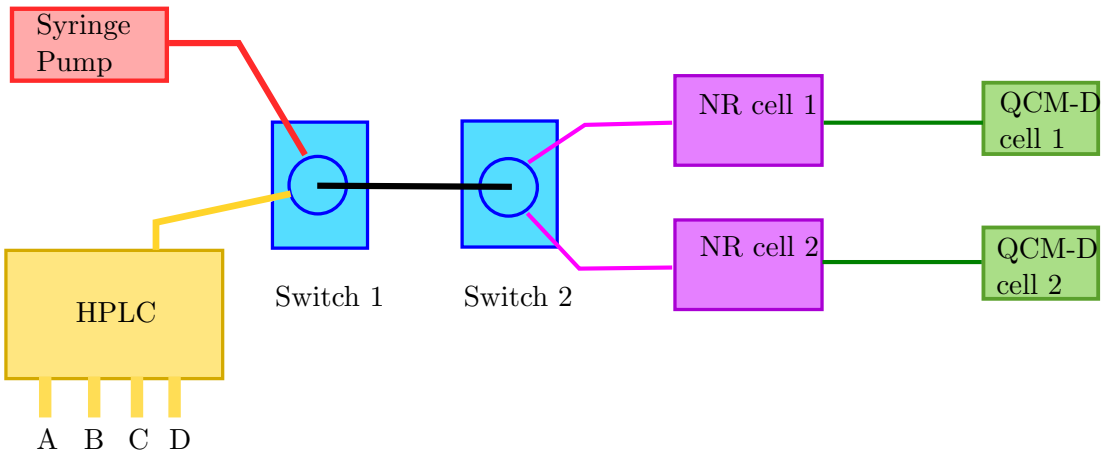

Figure 5.6 *Schematic of the liquid handling set-up used in the Polref PNR experiments. A HPLC pump and syringe pump were connected through two switch valves to two neutron reflectivity cells. This allowed for programmed switching of soution contrasts through the HPLC pump and for injection of liposomes or proteoliposomes through the syringe pump. The solution passes through the NR cells and then through QCM-D cells so that the formation of our tethered bilayer system can be followed by in-line QCM-D during the experiment.*

A HPLC pump was used to exchange buffer contrasts and salt concentrations and a syringe pump was used to push proteoliposomes into the cells. Note the standard solid-liquid neutron cells at ISIS were used with the magnets removed so as to not affect the polarisation across the sample. G-clamps were used to secure the neutron cells in place on the beamline.

The MscL-containing proteoliposomes used to prepare tethered bilayers in this section were prepared following the protocols outlined in Chapter 3 and Chapter 4. The protein MscL was expressed using the *E.coli* HY BiotechRabbit CFPE kit into liposomes of lipid composition 3:1 POPC:POPG, to a resulting weight-% of 15%. That is a 1:8 protein to lipid ratio by weight. Proteoliposomes were used within a week of protein expression. Before use the proteoliposomes were sonicated using a tip sonicator and extruded with 100 nm filters less than an hour before flowing into the neutron cells. Dynamic light scattering measurements using the Malvern zetasizer at ISIS Neutron and Muon Source determined the

size of the proteoliposomes to be 270 nm in diameter. Proteoliposome solutions (20 ml , 1 mg ml^{-1} were pushed through the neutron cells in deuterated HEPES buffer (20 mM, pD 7.0, 150 mM NaCl) at a flow rate of 2 $ml\,min^{-1}$. After an hour a solution of higher salt concentration buffer (20 ml, 20 mM HEPES, pD 7.0, 300 mM NaCl) is passed through the cell followed by a solution of the lower salt concentration buffer (20 ml, 20 mM HEPES, pD 7.0, 150 mM NaCl), after which the reflectivity measurements of the tethered bilayer are carried out. The flow rate of 2 $ml\,min^{-1}$ was used for all solution exchanges including into different solution contrasts.

5.3.3 Fitting and Model Parameters

The neutron reflectivity data from the tethered bilayer was fitted to parametrised simple slab layer models. The layers in our tether model are depicted in Figure 5.7. The solid layers making up the interfacial thin film have thickness and roughness parameters. The scattering length density (SLD) of the permalloy layer is initially fit for the different neutron spin contrasts as this is dependent on the set-up of the magnetic field, but were then fixed when fitting all subsequent measurements of the tethered bilayer formation. The tether was modelled by three layers, one for the PDP linker to the gold surface, one for the PEG spacer and one for the DSPE lipid. Since the tether is highly hydrated, the molecules will display a degree of conformational disorder, rather than being neatly aligned, so the different layers may have comparatively high interfacial width, with a broader distribution of where the sub-units in the tether layer such as the DSPE head groups reside. Given the high interfacial width, the DSPE head/tail groups are not modelled as distinct layers.

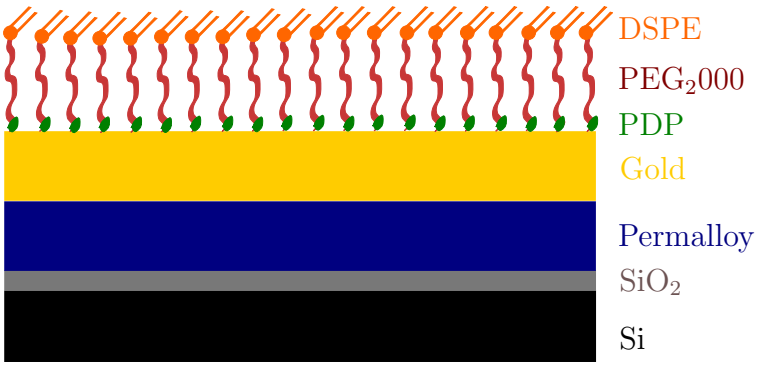

Figure 5.7 *Schematic of neutron reflectivity model layers for PDP-PEG2000-DSPE on a gold-permalloy coated neutron block*

Table 5.3 *Neutron Scattering Length Densities of the tethered lipid bilayer.*

Component	SLD ($\times 10^{-6}$ Å^{-2})
Silicon	2.07[124]
SiO_2 (amorphous)	3.41[124]
Gold	4.66
PDP	1.01
$(OCH_2CH_2)_n$	0.60[124]
DSPE head	2.20
DSPE tail	-0.36
DSPE	0.26
POPC head	1.81
POPG head	2.45
Ave. 3:1 POPC:POPG head	1.97
POPC/POPG tail	-0.29

In the literature, the DSPE lipids are often depicted as sitting apart from the PEG layer as depicted schematically in Figure 5.7.[104, 195] However the extent to which this is true will be a function of the grafting density and the degree of polymerisation of the PEG spacer. To the extent that the PEG spacer can be modelled as a polymer brush, the self-consistent field (SCF) theory of polymer brushes would predict that the chain ends are distributed through-out the brush.[153] The presence of the DSPE end group will add some further interaction terms into the SCF, so it is plausible that the lipids would segregate to the PEG-water interface. In a highly hydrated PEG tether, the lipids may be highly tilted to avoid the entropically unfavourable interaction of lipid tails with water. This tilting may increase the observed APM. Infrared measurements have suggested that the DSPE lipids sit out of the PEG layer, but that in low density tethering the lipids lie flat.[159] The area per molecule (APM) of the lipid will effectively be constrained by the grafting density of the PDP-PEG tethers.

The scattering length densities (SLDs) of the silicon, silicon oxide, and gold layers were fixed at literature values. As the SLD of the permalloy layer has a magnetic component, that is dependent on the strength of the applied static field and the exact composition of the film, this was fitted for the tether data and then fixed. The thicknesses and interfacial widths for gold, permalloy and silicon oxide layers were also fitted for the tether data and then fixed for the subsequent data sets.

The MscL-containing lipid bilayers were treated using a similar approach as in Section 4.5.3.2. The main deviation from that model is that the area per molecule

(APM) and water per lipid heads (WPLH) of the two bilayer leaflets were fitted separately. The composition of the the bilayer is assumed to be 3:1 POPC:POPG lipids despite the lower leaflet containing DSPE. The difference in the lipid tail and head volume between POPC, POPG and DSPE is sufficiently small that this will have negligible impact on the fitted parameters. The protein is incorporated into the model in the same way as in Section 4.5.3.2 with a protein coverage fitted along with a transmembrane thickness, with the coverage of the protrusion constrained to the fitted coverage of the transmembrane portion. The MscL protrusion was fitted to be only on the side of the bilayer that faces the subphase. When protrusions were allowed on both sides, the fits obtained were less favourable. However the PEG tethers may obscure any protrusion on that side on the membrane. A diagram of the tethered bilayer layers is shown in Figure 5.8.

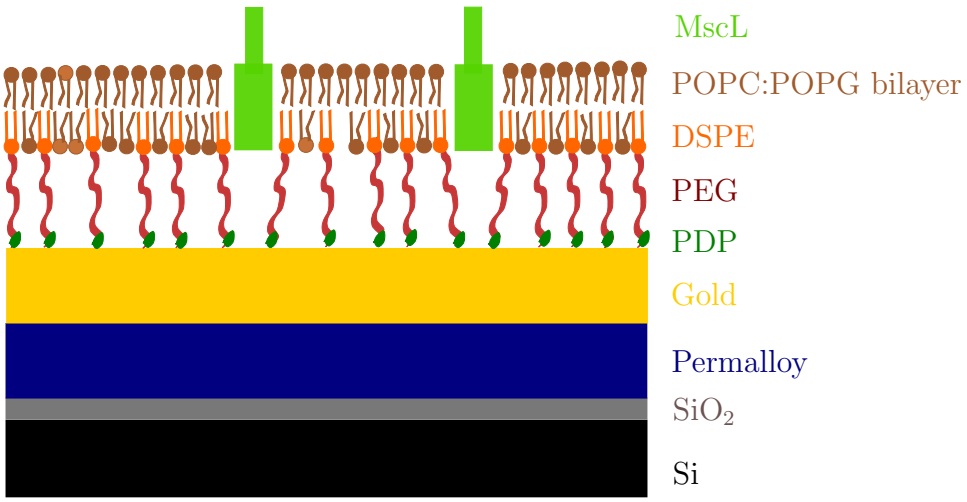

Figure 5.8 *Schematic of neutron reflectivity model layers for PDP-PEG2000-DSPE tethered bilayer incorporating MscL, on a gold-permalloy coated neutron block.*

5.3.4 Results

5.3.4.1 Analysis of Tether Layer

The tether functionalised surface was measured in three buffer contrasts: in D_2O, in gold matched water (GMW) and in H_2O. Unless otherwise stated, the buffer used is HEPES buffer (20 mM, pH 7.4/ PD 7, 150 mM NaCl). Two magnetic contrasts are shown for each of three buffer contrasts. Data is displayed in Q^4 to

best highlight differences between the contrasts and differences in the tether and bilayer layers.

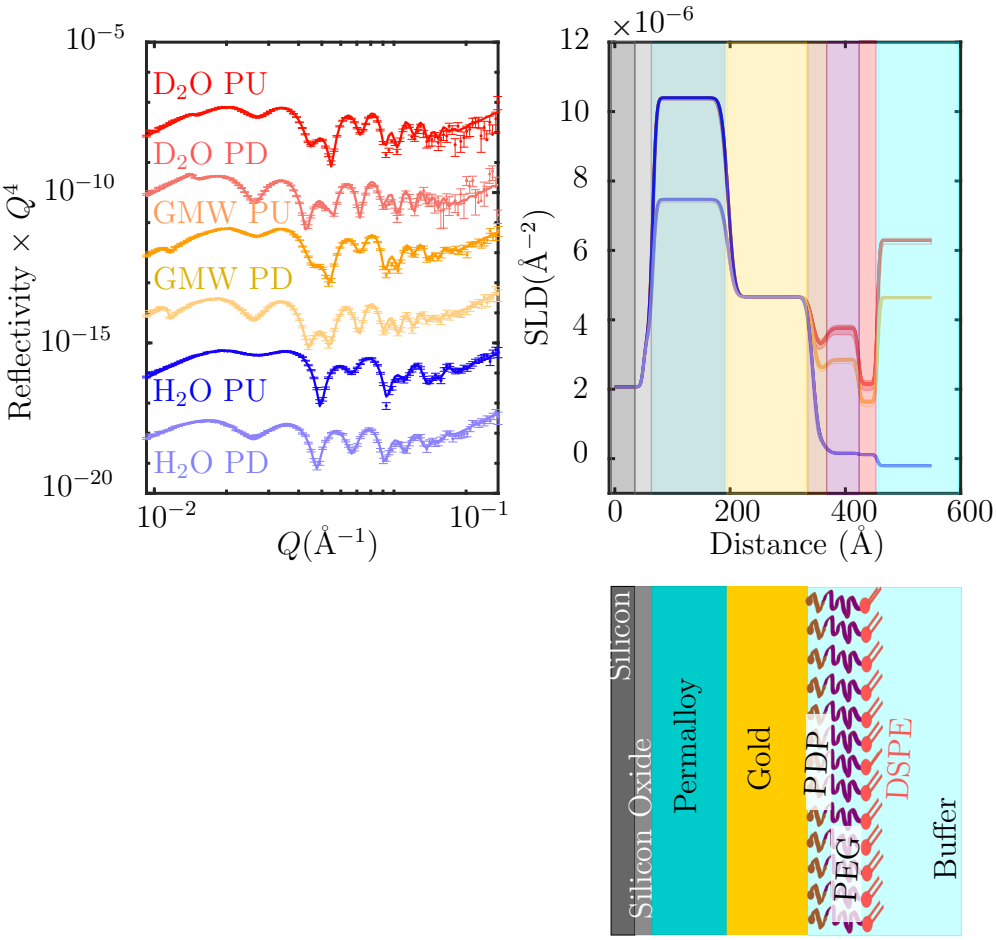

Figure 5.9 *Fitted neutron reflectivity of a PDP-PEG2000-DSPE tethered gold surface. Reflectivity profiles and fits for all solution and magnetic contrasts (PU= spin up, PD = spin down) shown plotted as Reflectivity × Q^4 vs Q. The scattering length density is plotted against the distance from the silicon interface and coloured lines link to the simple diagram below depicting the composition of layers in the structure.*

The fitted neutron reflectivity data for the tether layer is shown in Figure 5.9. The scattering length density profile in Figure 5.9 indicates a distinct DSPE lipid layer, seen very clearly in the "zoomed-in" scattering length density profile in Figure 5.10. The fitted values that contribute to the SLD profile are shown in Table 5.4 and the posterior distributions from the Bayesian analysis are displayed in Figure 5.11.

The MCMC analysis allows us to assess the quality of our fits to the reflectivity data and gives us a statistical interpretation of the uncertainty in our model. The Bayesian analysis of our tether model indicates that the thickness of the solid

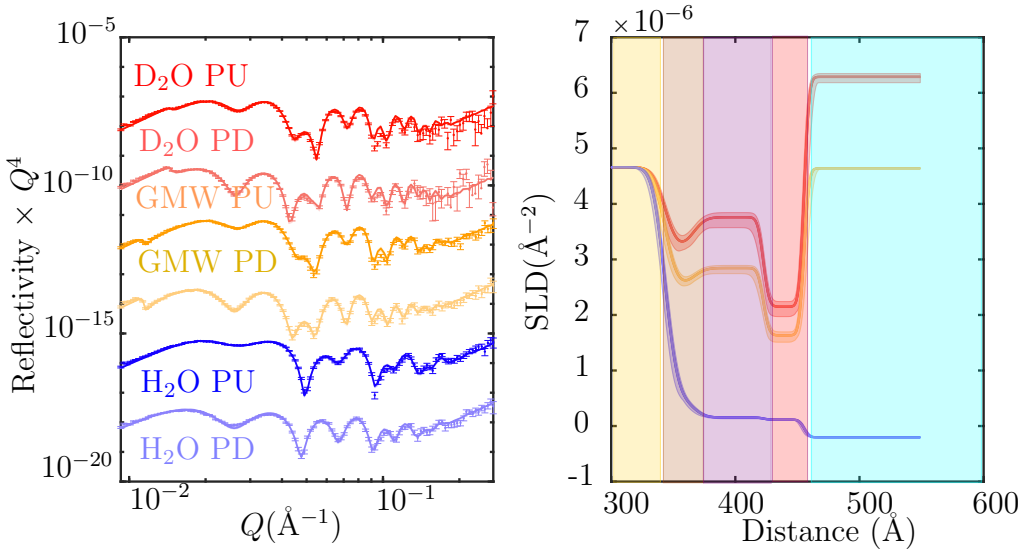

Figure 5.10 *Fitted neutron reflectivity of a PDP-PEG2000-DSPE tethered gold surface, the same data as depicted in Figure 5.9 with the SLD profile showing only the tether part of the model. Reflectivity profiles and fits for all solution and magnetic contrasts (PU= spin up, PD = spin down) shown plotted as Reflectivity × Q^4 vs Q. The scattering length density is plotted against the distance from the silicon interface with only the layers after the gold-interface shown.*

layers could be determined with a few Å error. The uncertainty in the tether layers is higher which is expected as the interfaces between the different segments will not be well defined. It is interesting that a distinct DSPE layer of low interfacial width appears in the best-fit model. This confirms the suggestion made in the Introduction to this chapter that contrary to a simple polymer brush (for which SCF theory predicts a parabolic density profile, with chain ends distributed throughout the layer), the DSPE-functional groups surface-segregate into a well-defined layer.

The best fit to the solid parameters of the solid layers (Silicon Oxide, permalloy and gold), derived from the fitting to the model for the reflectivity data measured from the tether layer, were used to constrain the fits for the subsequent bilayer analysis.

MscL containing liposomes (1 mg ml^{-1}, 15 ml) were injected into the laminar flow neutron reflectivity cells using a syringe pump at 2 ml min^{-1}. After 90 minutes a further 10 ml of MscL containing liposomes was injected to ensure that sufficient proteoliposomes interact with the DSPE moieties at the interface of the tether layer with the sub-phase. After an hour, 20 ml of 300 mM NaCl buffer was

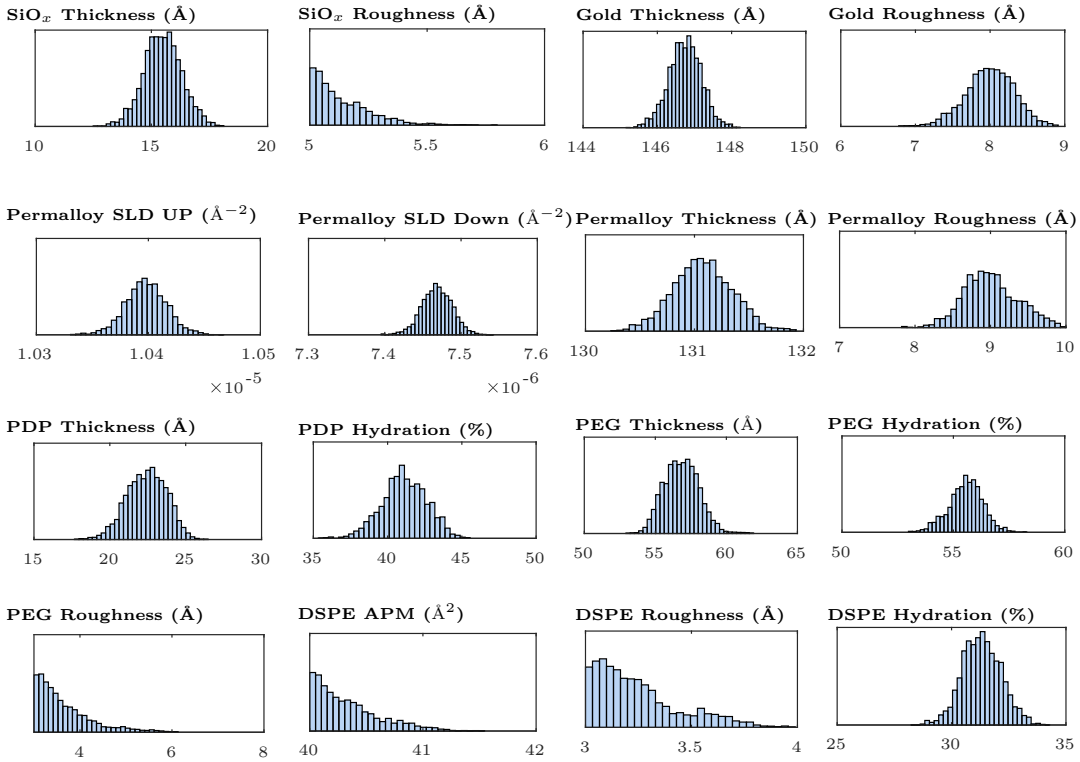

Figure 5.11 *Posteriors of Bayesian analysis of fitted model to neutron reflectivity of PDP-PEG2000-DSPE tethers on a Gold and permalloy coated silicon block.*

pushed through the cell, immediately followed by pushing through 20 ml of 150 mM NaCl buffer. The resulting layer was then measured in the three sub-phase contrasts, see Figure 5.12.

Separate area per molecule (APM) and water per lipid heads (WPLH) parameters were fitted for the two lipid leaflets of the lipid bilayer, indicated as upper leaflet (UL) and lower leaflet (LL) in Table 5.4. The water per lipid tail (WPLT) was constrained to be the same for both leaflets, as having two WPLT parameters did not improve the quality of the fits. The variation between leaflets was allowed due to the DSPE tether molecules being present in only the lower bilayer leaflet, making it more likely for that leaflet to be more densely packed. The best fit APM value of the lower lipid bilayer leaflet (LL) was 68 Å^{2}molecule^{-1} with 16 WPLH and the upper leaflet (UL) had a best fit APM of 113 Å^{2}molecule^{-1} and 9 WPLH. The WPLH values have a high uncertainty. This is due to the interfacial thickness (parametrised as roughness) on these thin layers being comparable to the layer thicknesses (11 Å).

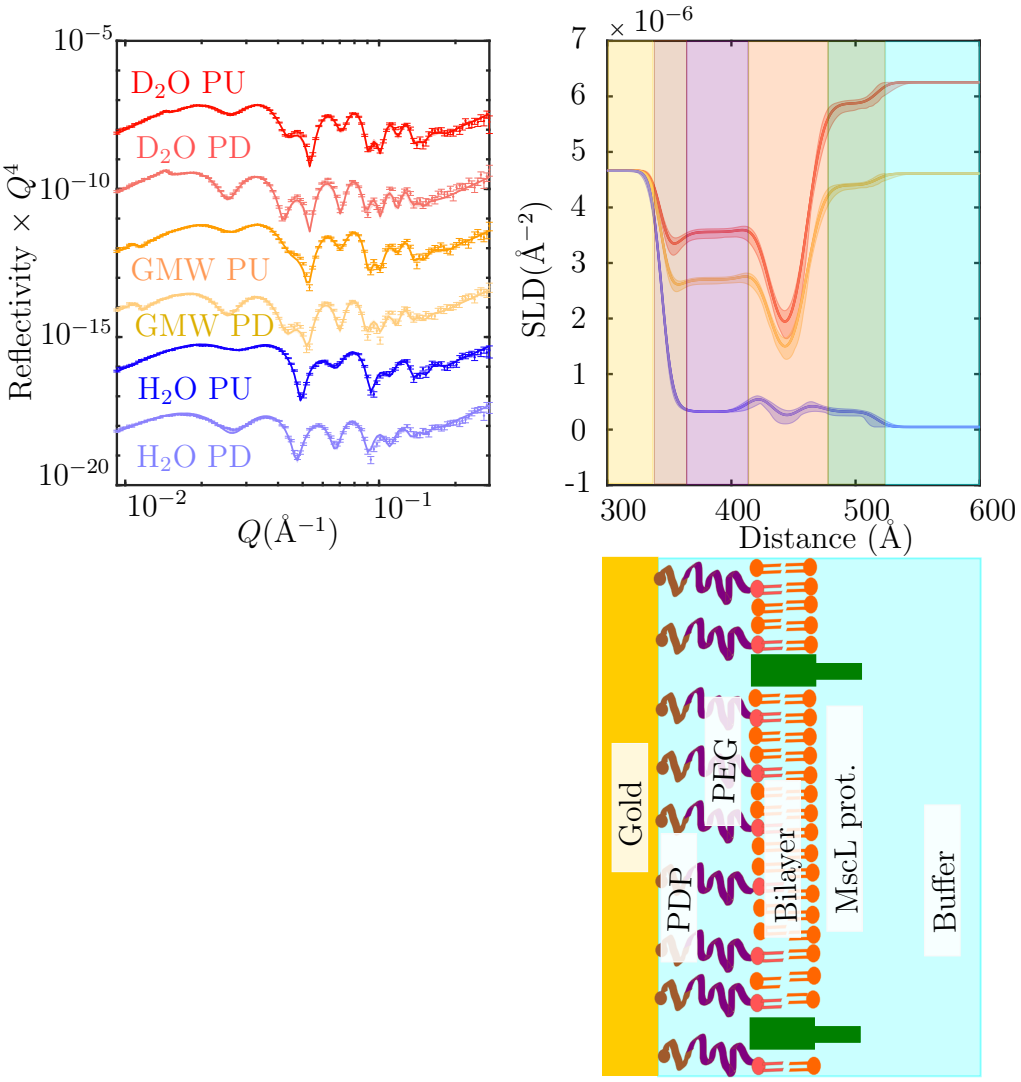

Figure 5.12 *Fitted neutron reflectivity of PDP-PEG2000-DSPE tethered 3:1 POPC:POPG bilayer containing MscL. Reflectivity profiles and fits for all solution and magnetic contrasts (PU= spin up, PD = spin down) shown plotted as Reflectivity × Q^4 vs Q. The scattering length density is plotted against the distance from the silicon interface and coloured layers link to the simple diagram below depicting the composition of layers in the structure. The confidence bands on the reflectivity profile fits and scattering length density plot are 95% confidence interval bands as calculated by Bayesian analysis, the corresponding posterior distribution plots are shown in Figure 5.13.*

Table 5.4 *Table of best-fit model parameters to neutron reflectivity data of a PDP-PEG-DSPE tethered gold-permalloy silicon block and of the formed tethered lipid bilayer containing MscL. UL= upper leaflet of the bilayer, LL= lower leaflet of the bilayer, WPLH= water per lipid head group, WPLT= water per lipid tail group.*

Model Parameter		Fitted value (95% confidence interval)			
		Tether		Tether + MscL Bil.	
Si Rough.	(Å)	4	(Fixed)	4	(Fixed)
SiO_2 Thick.	(Å)	15.5	(13.9 17.1)	15.5	(Fixed)
SiO_2 Rough.	(Å)	5.1	(5.0 5.4)	5.1	(Fixed)
Gold Thick.	(Å)	147	(146 148)	147	(Fixed)
Gold Rough.	(Å)	8.0	(7.3 8.6)	6.8	(6.1 7.5)
Permalloy-up SLD	($\times 10^{-6}$ Å^{-2})	10.4	(10.3 10.4)	10.4	(Fixed)
Permalloy-d. SLD	($\times 10^{-6}$ Å^{-2})	7.47	(7.43 7.51)	7.47	(Fixed)
Permalloy Rough.	(Å)	9.0	(8.3 9.7)	9.0	(Fixed)
Permalloy Thick.	(Å)	131	(130 132)	131	(Fixed)
PDP Thick.	(Å)	22.4	(19.8 24.8)	6.2	(5.0 8.9)
PDP hydration	(vol%)	41.1	(38.1 43.9)	29.1	(21.0 37.7)
PEG Thick.	(Å)	57	(55 59)	68	(63 73)
PEG hydration	(vol%)	55.6	(54.0 57.0)	53.1	(52.0 54.3)
PEG Rough.	(Å)	3.7	(3.0 5.2)	10.0	(8.9 11.0)
DSPE APM	(Å^2 molecule^{-1})	40.3	(40.0 41.0)	N/A	
DSPE Roughness	(Å)	3.2	(3.0 3.7)	N/A	
DSPE hydration	(vol%)	31.3	(29.7 33.0)	N/A	
Lipid APM (LL)	(Å^2 molecule^{-1})			68	(61 78)
WPLH (LL)				16.2	(9.3 19.8)
WPLT				9.1	(3.6 15.3)
Lipid Rough.	(Å)			11	(7 13)
MscL Coverage	(vol%)			18.2	(14.3 22.1)
ctMscL Thick.	(Å)			54	(48 59)
MscL Rough.	(Å)			7.7	(2.2 9.9)
Lipid APM (UL)	(Å^2 molecule^{-1})			113	(98 120)
WPLH (UL)				9.2	(0.3 23.3)

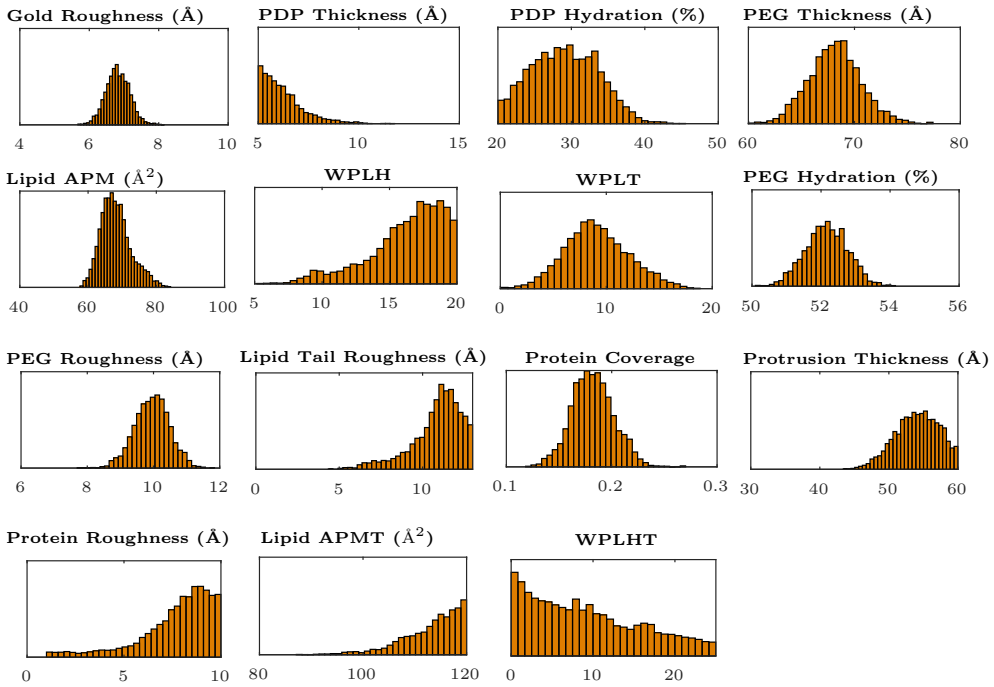

Figure 5.13 *Posteriors of Bayesian analysis of fitted model to neutron reflectivity of PDP-PEG2000-DSPE tethered bilayer containing MscL on a Gold and permalloy coated silicon block.*

The best fit WPLT parameter was determined to be 9 ±6. Since hydration of the lipid tails is not entropically favourable it is unlikely that water is evenly distributed across the the bilayer, but rather suggests that the bilayer coverage of the interface may be less than 100%. Water associated in the tail region is more likely in a system containing membrane protein pores, as some water may be lining the pore of the channel. The coverage of MscL within the lipid bilayer as a volume percentage of the lipid bilayer layers is $18 \pm 4\%$, equivalent to the weight composition of protein to lipid in the liposomes of 12.5% protein (w/w). The thickness of the MscL protrusion from the lipid bilayer (labelled as ctMscLThick in Table 5.4), has a best fit of 54±7 Å, close to the protrusion thickness calculated in the analysis of the data measured from the suspended bilayer.

Since the neutron reflectivity cells were connected to QCM-D cells, complementary QCM-D traces were analysed in real-time. The results are not directly comparable to the QCM-D traces analysed previously as the liposome-addition and rupture steps were carried out in D_2O. This is important for QCM-D which

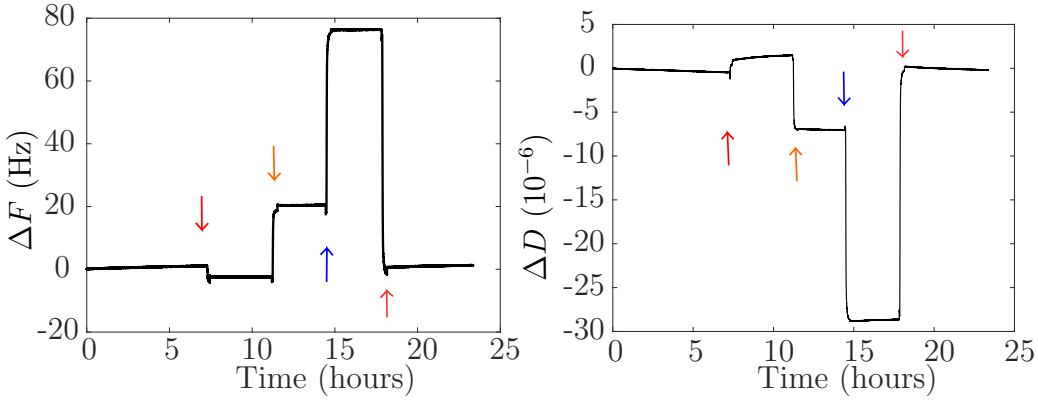

Figure 5.14 *QCM-D measurements taken in-line with neutron reflectivity showing the changes in frequency and dissipation when exchanging buffer contrast. The trace starts in D_2O though is incompletely exchanged so further D2O was pushed in to the neutron reflectivity cell and into the QCM cell (red arrow), exchanging to GMW (orange arrow), exchanging to H_2O and exchanging back to D_2O (red arrow). The incomplete exchange to D_2O was identified from the critical angle of the neutron reflectivity measurement.*

is sensitive to density and viscosity.[37] Vesicle rupture may be sensitive to the level of deuteration of the buffer (i.e. the D_2O vs H_2O content) as this will effect the buoyancy of the vesicles. Since the vesicles have a lower density that D_2O but a higher density than H_2O, it is an important consideration in design of neutron experiments. To illustrate the sensitivity of QCM to buffer density, Figure 5.14 shows the exchange of a tether functionalised layer with the sub-phase exchanging from D_2O to Gold-Matched Water (GMW) to H_2O.

Large changes in frequency and dissipation occur when exchanging the buffer contrast. On exchanging from from D_2O to H_2O an increase in frequency of ~80 Hz occurs and a decrease in dissipation of -28 $\times$ 10^{-6}. In our neutron reflectivity analysis of tethered bilayers, the formation steps of bilayer formation were carried out in D_2O.

The QCM-D curve collected during the formation of tethered bilayers for our neutron reflectivity measurement is shown in Figure 5.15. The QCM-D curves shown in Figure 5.15 show that a decrease in frequency and increase in dissipation occur on addition of the proteoliposomes as expected in our optimisation of the system. The change in frequency was lower than observed when optimising the system in H_2O buffer. The main differences are that the liposomes now have MscL incorporated into them and the formation step here was in deuterated buffer. The higher density of the buffer may have affected the formation mechanism of the lipid bilayer. The smaller decrease in frequency and smaller increase in

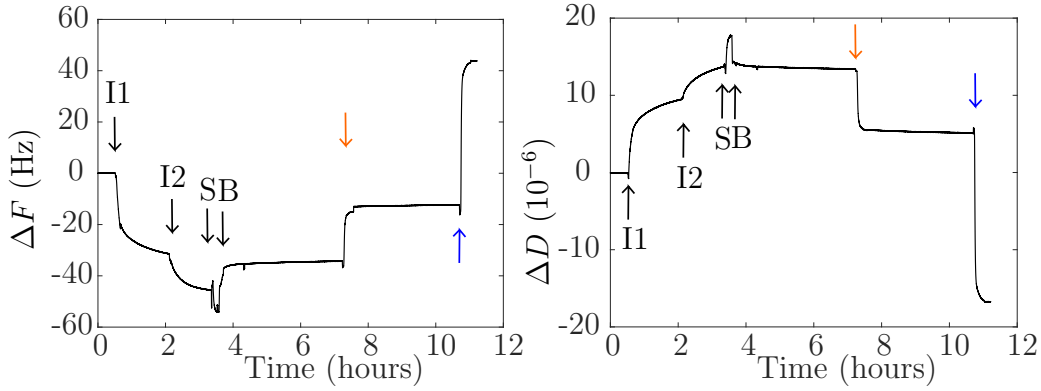

Figure 5.15 *QCM-D measurements taken in-line with neutron reflectivity showing the changes in frequency and dissipation during bilayer formation and after buffer contrast exchanges. The label I1 indicates the first injection of proteoliposomes (*15 ml*), I2 indicates the second injection of proteoliposomes (a further* 10 ml*). The label S indicates when* 20 ml *of* 300 mM *NaCl containing buffer is pushed through the cell and B marks when the standard* 150 mM *buffer (*20 ml*) is pushed through the cell. After tethered bilayer formation the neutron reflectivity measurement was made in D_2O and then the buffer was exchanged to GMW (orange arrow) and H_2O buffer (blue arrow).*

dissipation on addition of liposomes suggests that fewer liposomes are remaining adsorbed at the interface. However, the end point change in frequency of -35 Hz after the buffer rinsing steps is in agreement with the neutron reflectivity data that a high coverage bilayer has formed. It may be that in D_2O, rupture of individual proteoliposomes could be favoured, with the proteins acting as sticky patches, providing the necessary proteoliposome/tether layer adhesion energy to overcome the curvature energy of the proteoliposomes and drive their deformation and rupture. The QCM-D traces and fits to the neutron reflectivity both suggest bilayer formation was successful. The benefit of having the QCM-D in-line for the neutron reflectivity experiment was that we could quickly monitor changes on addition of the proteoliposomes but also check that the solution contrast had completely exchanged.

5.3.5 Discussion

In this chapter, it has been demonstrated that a lipid bilayer containing the bacterial membrane protein MscL, tethered to a gold substrate by PDP-PEG2000-DSPE molecules, can be formed by deposition and rupture of MscL-containing POPC:POPG proteoliposomes. The neutron reflectivity data measured from

the PDP-PEG2000-DSPE functionalised interface is best-fit by a model that comprises three layers of uniform scattering length density for the PDP linker, PEG and DSPE lipids respectively. The Flory radius (R_F) of PEG2000, MW of 2000 comprising 45 ethylene glycol units, is defined by $R_F = aN^{(3/5)}$ where N is the number of uncorrelated monomers and a is the Kuhn length. Taking literature estimates of the monomer persistence length of a = 3.4 Å, the Flory radius is estimated to be 33 Å for PEG2000.[117] The conformation of the tethered PEG chains will be determined by the distance between the PEG chains (D) compared to this Flory radius (R_F).

When $D > 2R_F$, the polymers retain the conformation that they would have in solution, forming a tethered layer that is described as a mushroom regime. When $D < R_F$ they are in a brush regime. The spacing between the grafting points can be determined from the PEG thickness as determined from the best fit to the measured neutron reflectivity data.

Between our fitting of the tethered surface and the tethered bilayer, the PDP thickness had large variation, highlighting an uncertainty in defining the interface between the PDP and PEG layers. I have therefore included the greater uncertainty of the PEG thickness in the following calculations. The thickness of the PDP-PEG2000 layer in the tether only measurement is 66 ±13 Å. Given the PEG thickness and that the molecular volume of PEG2000 is 2966.7 Å^3, the APM of the PEG tether can be calculated to be 47 Å^2 ± 10 Å^2. From the APM of a PEG chain, a distance between the tether sites can be estimated as $D = 2\sqrt{\frac{APM}{\pi}} = 7.7$ Å, significantly lower than the Flory radius of 33 Å. We can be confident that our system is in the brush regime.

On addition of the liposomes, the thickness of the tether is largely unchanged with a PDP-PEG thickness of 74 Å ± 7.7 Å. The best fit model for the bilayer formed on top of the tether has a large difference in packing of lipids between the upper and lower bilayer leaflets. It is somewhat difficult to robustly separate the APM in the upper and lower leaflets. What the neutron reflectivity measurement is most sensitive to is the overall thickness of the whole tail region. The APM of the upper leaflet will affect the thickness of the head group layer in this leaflet; this can be compensated for by incorporating water in the head group region. There is probably a bit less asymmetry than is suggested at first sight by the average APM$_L$ = 88 Å^2 and APM$_U$ =113 Å^2. Such asymmetry would certainly be expected to drive some curvature. However, the potential asymmetry shouldn't be dismissed, as the tethered bilayer contains a high coverage of protein, which

we know has a preferential orientation, and although we model it has having a cylindrical density profile through the bilayer, the interactions (effective APM) might be larger between the protruding C-terminal sections.

Furthermore, the tethering imposes some asymmetry on the bilayer, since the packing density in the lower leaflet is influenced by the tether density. The multi-component character of the bilayer means that there is scope for asymmetry in the tethered bilayer, although the experimental measurements conducted make it hard to be unequivocal in robustly assigning the extent of this asymmetry. To conclusively separate the APM of the two components requires one of the lipid components to be deuterated. This approach was not pursued in this work as it would make it more difficult to calculate the composition of the bilayer taken up by the protein and observe its conformational changes, which is our central aim.

Incorporation of the transmembrane MscL protein was successful, with a final protein coverage of 18% (±4 vol.%). The best fit roughnesses of the formed bilayer are high (11 Å) which is in-keeping with a bilayer formed on-top of a flexible polymer layer.

5.3.6 Interaction of Pexiganan with the Tethered Lipid Bilayer

The interactions of pexiganan with MscL using our new suspended lipid bilayer and liposome constructs are discussed in Chapters 3 and 4 respectively. The interaction of pexiganan with our tethered lipid bilayer is interesting in two respects: i) to test if the pexiganan causes gating of the MscL channel when the lipid bilayer has a different fluidity and ii) to test whether the tethered bilayer membrane mimic is suitable for observing protein conformation changes.

The response of the MscL containing bilayer to pexiganan was tested at two concentrations, by sequentially flowing 1.6 µM pexiganan in D_2O HEPES buffer and 3.2 µM pexiganan in the same buffer through the cell. Buffer rinses (20 ml were used between and after these steps to ensure that continuous deposition was not occurring during the NR experiments. The changes in the reflectivity profile are clearest in the H_2O buffer contrast due to the PEG layer being closest to contrast matched. The resulting reflectivity profiles and corresponding fits are shown in Figure 5.16 and Figure 5.17.

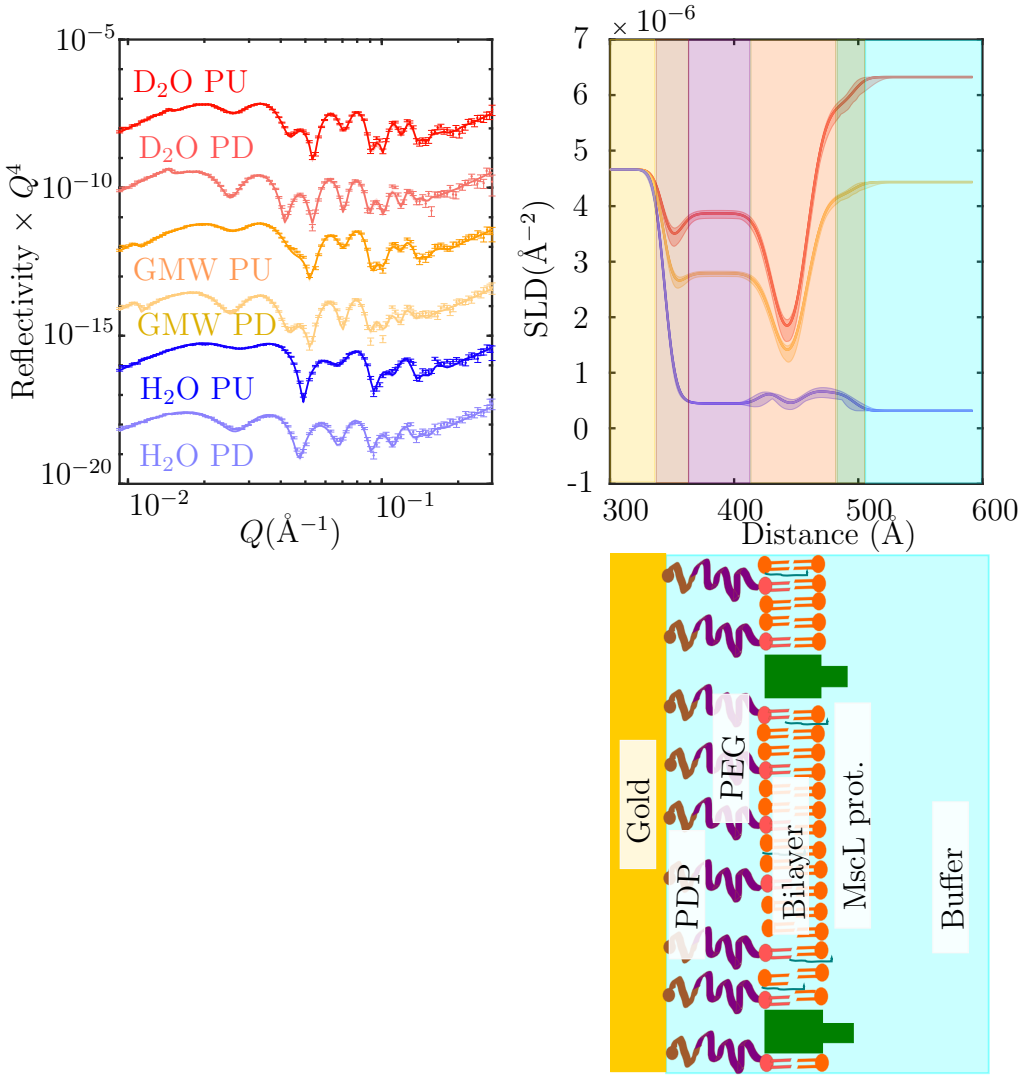

Figure 5.16 *Fitted Reflectivity Profiles of tethered bilayers containing MscL after the addition of pexiganan at* 1.6 µM. *Reflectivity profiles and fits for all solution and magnetic contrasts (PU= spin up, PD = spin down) shown plotted as Reflectivity* × Q^4 *vs* Q. *The scattering length density is plotted against the distance from the silicon interface and coloured lines link to the simple diagram below depicting the composition of layers in the structure.*

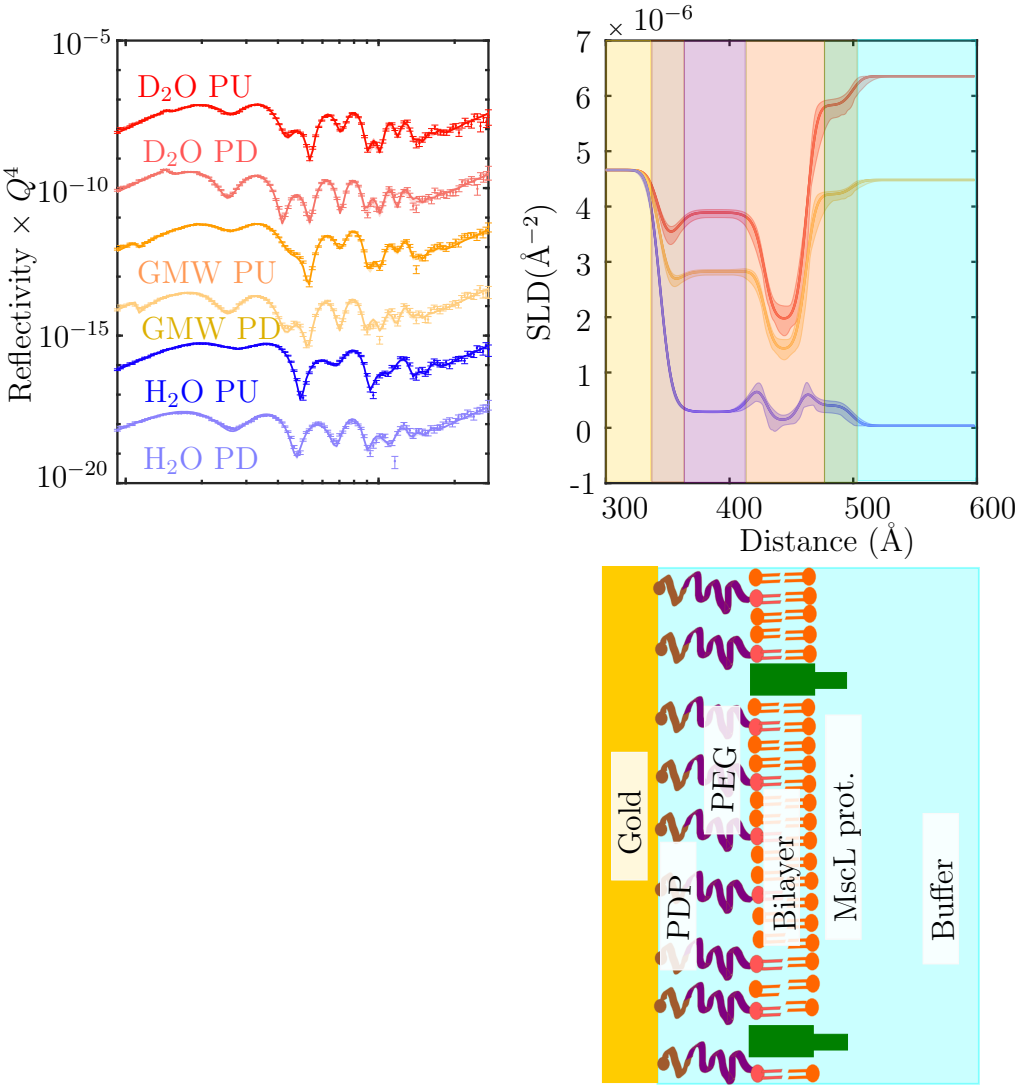

Figure 5.17 *Fitted Reflectivity Profiles of tethered bilayers containing MscL after the addition of pexiganan at* 3.2 µM.*Reflectivity profiles and fits for all solution and magnetic contrasts (PU= spin up, PD = spin down) shown plotted as Reflectivity* × Q^4 *vs* Q. *The scattering length density is plotted against the distance from the silicon interface and coloured lines link to the simple diagram below depicting the composition of layers in the structure.*

Table 5.5 *Fitted model parameters to PNR measurements of tethered lipid bilayer containing MscL before and after the addition of pexiganan solutions of* 1.6 µM *pexiganan and* 3.2 µM *pexiganan. The values are shown for the best fit including the* 95% *Confidence Interval (CI) range.UL= upper leaflet of the bilayer, LL= lower leaflet of the bilayer, WPLH= water per lipid head group, WPLT= water per lipid tail group.*

Model Parameter		Fitted value (95% CI)			
		1.6 µM pexiganan		3.2 µM pexiganan	
Gold rough	(Å)	6.8	(6.3 7.3)	7.3	(6.7 7.8)
PDP Thick.	(Å)	8.6	(8.0 10.1)	9.6	(9.0 11.1)
PDP hydration	(vol%)	33	(27 39)	35	(30 40)
PEG Thick.	(Å)	72	(67 78)	68	(63 73)
PEG hydration	(vol%)	57	(56 58)	58	(56 59)
PEG Rough.	(Å)	8.6	(7.7 11.0)	9.2	(8.4 10.1)
Lipid APM LL	($Å^2$ $molecule^{-1}$)	77	(69 97)	75	(67 93)
WPLH LL		12	(2 19)	8	(1 17)
WPLT		4	(0 9)	15	(9 19)
Lipid Rough.	(Å)	11	(10 12)	6	(3 10)
Protein Coverage	(vol%)	21	(17 24)	18	(15 22)
ctMscL Thickness	(Å)	37	(32 41)	36	(33 40)
MscL Rough.	(Å)	7.8	(4.3 9.8)	6.7	(3.1 9.6)
APM UL	($Å^2$ $molecule^{-1}$)	105	(82 119)	112	(92.4 120)
WPLH UL		5.2	(0.3 23.3)	5.5	(0.1 17.9)

By comparing Figure 5.16 and Figure 5.17 to Figure 5.12, differences can be seen between the reflectivity profiles of the tethered bilayer before and after pexiganan addition. These differences are most apparent in the GMW and H_2O contrasts. The initial difference between the bilayer and 1.6 µM pexiganan is larger than seen with subsequent addition of 3.2 µM pexiganan, though some differences are observed with the increased pexiganan concentration at high Q. The parameters that best-fit the data measured from the MscL-containing bilayer exposed to 1.6 and 3.2 µM pexiganan are shown in Table 5.5. The parameters corresponding to solid layers were constrained to the values corresponding to the best-fit to the tether data.

The relative width of the posterior to the prior provides a measure of the information that is learned about a particular parameter by performing the experiment. With this in mind, we can identify which aspects of the MscL-containing tethered bilayer we gain additional information about (beyond that embodied by our prior assumptions) by performing these experiments and which

aspects we gain less information about.

The most significant parameter in the former category is the ctMscL thickness, i.e. the thickness of the MscL C-terminus protrusion from the bilayer. The significant reduction of this value, and indeed the shift of the whole posterior probability distribution to lower values than in the absence of pexiganan, provides strong support that there has been a conformational change in the C-terminus region. This is consistent with the channel having been gated open and is very significant, it is to the author's knowledge the first example of protein function that has been able to be inferred from a NR measurement. More importantly it suggests that pexiganan may turn MscL into an Achilles heel for the bacterium.

From the bottom two rows of Table 5.5, it is clear that conducting the experiment has provided little additional information (beyond that embodied in our prior assumptions) about upper bilayer leaflet parameters; the WPLH (water per lipid tail) and APM (area per molecule). It is worthwhile to reflect on why that might be the case and if there is anything that can be done to increase the information gain for the top leaflet parameters. The models used to calculate the reflectivity, and hence determine the likelihood of any one of the measured data sets, are parametrized simple layer models. Such a model provides a good description of those parts of a structure comprising very well-defined layers; in the tethered bilayer system this means everything from the silicon substrate, up to the DSPE-containing lower leaflet (which also contains POPC/POPG/MscL). The interface between the top leaflet and the sub-phase is compositionally more complex. Although the coverage of pexiganan expected on the basis of monolayer studies [149] is sufficiently low for it to contribute little to the SLD profile, physically one might expect it to alter the structure of the upper leaflet/sub-phase interface. Indeed NR investigation of the interaction of PXG with a 3:1 POPC:POPG monolayer model for the sub-phase facing leaflet showed that exposure to 4 µM PXG increased the interfacial width (roughness) of this interface to 6 Å and increased the APM of the lipids (from 58 $Å^2$ to 77 $Å^2$) at a surface pressure of 30 mN m^{-1}, which is often regarded as the canonical leaflet pressure in a bilayer. This means that lipids of the bilayer are unlikely to be arranged like Guardsmen shoulder to shoulder, but instead adopt a more rippled arrangement. This means that at the sub-phase interface, there will be a mixture of water, lipid and the C-termini protrusions of the protein channels. Each of these components will be distributed over a finite range of z-values, perpendicular to the interface. For the case that the interaction potential of the bilayer with the underlying substrate can

Table 5.6 *Comparison of before and after the addition of the antimicrobial peptide pexiganan, in bilayer and MscL protrusion thickness of a tethered lipid bilayer. Lipid leaflet thicknesses calculated from the best fit values for area per molecule (APM) and water per lipid head (WPLH) and water per lipid tail (WPLT) parameters displayed in Table 5.5. The range in the brackets is an estimated error based on the 95% confidence interval of the APM parameters.*

Sample	MscL bilayer	+1.6 µM PXG	+ 3.2 µM PXG
Lower Bilayer leaflet Thick. (Å)	30 (26 33)	21 (17 23)	26 (21 29)
Top Bilayer leaflet Thick. (Å)	16 (15 18)	14 (12 18)	15 (14 18)
Total Bilayer Thick. (Å)	46 (41 51)	35 (29 41)	41 (35 47)
MscL Protrusion Thick. (Å)	54 (48 59)	37 (32 41)	36 (33 40)

be approximated by an harmonic potential, the probability distribution reflecting the fractional occupancy as a function of z will be Gaussian for each component. It is is possible to implement such a model representation of the interface by making use of the composition-space modelling approach used in [149] for the investigation of the effect of PXG on monolayer models for the outer leaflet. However, this comes at the expense of greater complexity of model, which via the Occam principle may actually decrease the information about the parameters in which we are truly interested, such as the conformation of the MscL C-terminus.

The changes in APM and water per lipid parameter were used to calculate the change in thickness of the bilayer leaflets on addition of pexiganan, shown in Table 5.5.

The change in thickness of the bilayer and in the protein protrusion are also apparent in the fitted SLD profiles shown in Figure 5.16 and Figure 5.17. The observable changes in the bilayer SLD with pexiganan include: i) the increase in SLD of the bilayer leaflets in the H_2O contrast, along with a thinning of the bilayer, along with a large change in thickness of the C-terminal protrusion.

The thinning of the bilayer leaflets is largest on the first addition of 1.6 µM pexiganan and a large difference in thickness occurs to the inner leaflet leaflet containing the lipid tethers. Bilayer thinning is a signature of a stretching of the bilayer (i.e it being placed under stress); the thinning is directly related to increase in APM, and thus an in-plane strain and accompanying stress. That the thinning decreases after further addition of pexiganan may suggest that insertion of pexiganan is less asymmetric in the bilayer leaflets with increased

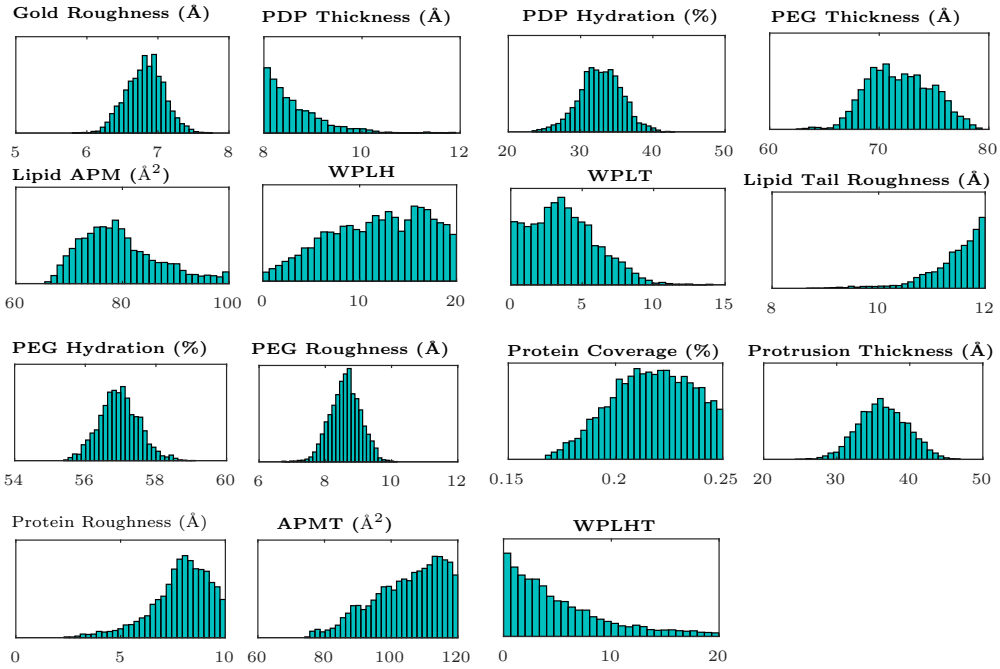

Figure 5.18 *Posteriors of Bayesian analysis of fitted model to neutron reflectivity of PDP-PEG2000-DSPE tethers on a Gold and permalloy coated silicon block.*

concentration, decreasing the stress of the bilayer. This would be consistent with the higher roughness observed at 1.6 µM pexiganan addition, than at 3.2 µM pexiganan addition.

The changes in scattering length density are supportive of a change in conformation of MscL, consistent with our findings in Chapter 4.

5.3.7 Discussion

It is interesting to compare the changes observed for the tethered system with those observed for the suspended bilayer. The membrane mimetics are different in multiple respects. The constraint on the bilayer from the monolayer support is likely to be different to that of a high density lipid tethered to a surface. Although the suspended bilayer mimetic was conceived to be unconstrained by a support, the lower roughness of the suspended bilayer compared to our tethered

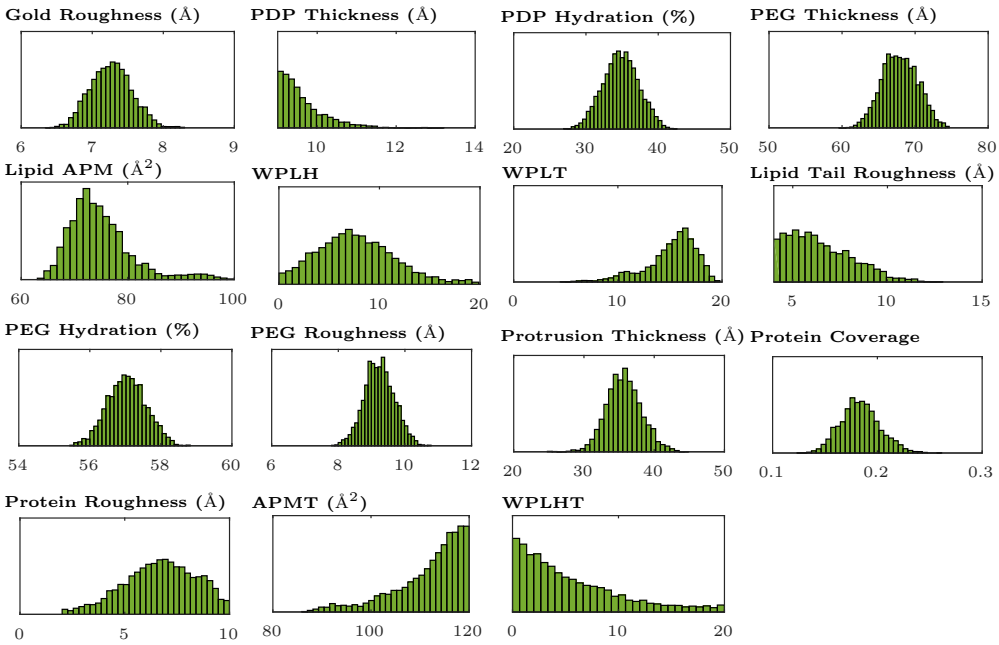

Figure 5.19 *Posteriors of Bayesian analysis of fitted model to neutron reflectivity of PDP-PEG2000-DSPE tethers on a Gold and permalloy coated silicon block.*

bilayer suggests that the interaction potential between the suspended bilayer and DODAB monolayer may be more constraining than that provided by the tether. One difference in the final prepared membrane mimetics is the packing of the lipids. In the tethered bilayer the APM of the outer lipid leaflet is high, 113 Å^{2}molecule^{-1}, despite high incorporation of protein into the bilayer, whereas in the suspended bilayer a low APM of about 68 Å^{2}molecule^{-1} was achieved in both leaflets. Despite these apparent differences in lipid packing, on addition of pexiganan to MscL-containing bilayers, a decrease in protrusion thickness of MscL was found to occur from 54 Å to 36 Å in the tethered bilayer, see Figure 5.20.

This observation combined with the change in radius of gyration observed in the SANS studies described in Chapter 3 give a strong indication that pexiganan is capable of causing gating of MscL channels over an extended time period. Note that more than 9 hours is needed in order to be observed in multiple solution contrasts by PNR.

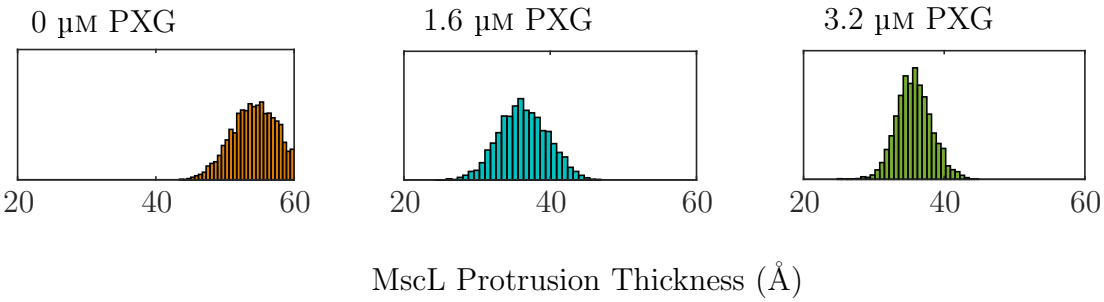

Figure 5.20 *Posterior distributions of the MscL protrusion thickness of the tethered MscL containing bilayer, before and after the addition of* 1.6 *and* 3.2 µM *pexiganan.*

We have demonstrated that pexiganan is able to induce a conformational change in MscL in multiple bacterial membrane mimics i.e. that of proteoliposomes, a suspended bilayer and a tethered lipid bilayer. The mimetics have different membrane curvatures, lipid packing and constraints on the lipid bilayers. That pexiganan at its minimum inhibitory concentration of 1.6 µM can inflict a conformational change in MscL consistent with gating across all constructs, suggests it is highly effective at creating this change. This observation provides a valuable insight into the mechanism of the antimicrobial activity of pexiganan.

5.3.8 Conclusion

A lipid bilayer containing the membrane protein MscL was tethered to a gold surface using long tethers of PDP-PEG2000-PDP. The tethered bilayer was characterised and tested at two concentrations of the antimicrobial peptide pexiganan using neutron reflectivity.

The reflectivity data from the tethered lipid bilayer was fitted to a model of a single planar bilayer composed of 3:1 POPC:POPG lipids and 20% volume composition of MscL. This is the first successful formation of long-tethered lipid bilayers using proteoliposome rupture onto a tethered surface. By first reacting a layer of PDP-PEG2000-DSPE molecules onto a gold surface an evenly distributed tether layer was formed. This is an improvement over other methods that rupture liposomes containing the PEG tethers, where often patches or domains of bilayers of different tether heights exist. Moreover we were able to achieve proteoliposome rupture into a planar bilayer containing high protein composition with a protein that reduces the likelihood of rupture. Therefore the system offers the opportunity to be used for a wide range of membrane proteins.

MscL is incorporated into the tethered bilayer to a high coverage of 17(±3)% ; the protrusion layer suggests that MscL is in its native conformation. The protrusion thickness of the protein was lower than observed in the suspended bilayer mimic, which might be expected to be accompanied by a weak curving of the bilayer, which could force the protein into a partially gated state. Existing literature suggests that an increase in curvature such as that caused by a difference in APM across leaflets, could cause gating of MscL.[17]

The tethered lipid bilayer was exposed to increasing concentrations of pexiganan; to 1.6 µM (close to the minimum inhibitory concentration of pexiganan for *E.coli*) and then to 3.2 µM. Addition of 1.6 µM pexiganan resulted in a thinning of the overall lipid bilayer, with the most significant thinning in the lower tethered leaflet. The thinning of the lipid bilayer was accompanied by a change in thickness of the fitted MscL protrusion thickness (54 Å ± 6 Å to 37 Å ± 5 Å). On the addition of further pexiganan the thickness of the protein protrusion remained constant but the thinning of the lipid bilayer appeared less apparent. A possible explanation is that at higher pexiganan concentration, the curvature of the bilayers decreases as pexiganan inserts into both layers. It is an interesting observation that even as bilayer curvature in the system decreased, the conformation of the MscL channel remained in a C-terminal retracted state, which we regard to be a signature of gating open.

Although we have been able to demonstrate changes in the lipid bilayer and protein from our reflectivity data it is important to note that a significant amount of the scattering occurs from the solid interfaces and from the PDP and PEG layers. A lower density of PEG tethers may make changes in the bilayer clearer in the reflectivity data and fitted SLD profiles. The danger with decreasing the tether density is reduced stability of the tethered bilayer and the presence of fewer tethered sites during proteoliposome rupture, required for the formation of the planar bilayer. Similarly, selective deuteration of POPC/POPG could be used to determine the composition of the lower leaflet.

Chapter 6

Conclusion

The work presented in this thesis is aimed investigating whether the membrane protein, the mechanosensitive ion channel of large conductance, can be exploited as an antimicrobial target. To achieve this required the optimisation of protein expression and the development of new membrane mimetics and analysis of the neutron and X-ray scattering from these systems. Each system investigated is summarised below along with any potential future work that could be conducted.

The Mechanosensitive Ion Channel of Large Conductance (MscL) was successfully expressed into liposomes using cell free protein expression. Analysing these proteoliposomes using small angle neutron scattering, it was determined that the proteoliposomes have a rough surface, consistent with proteins protruding out of the membrane across the surface. By fitting the scattering profiles to a Guinier-Porod model, the size and shape of the protein was extracted, along with the surface roughness. The radius of gyration of the protein was determined to be between 26-29 Å, the same size of individual MscL channels as previously determined from the crystal structure.[31]

Although no direct evidence of clustering was observed, we did observe a correlation peak in our partially deuterated lipids and H_2O buffer contrast, which suggests a regular arrangement of the channels across the membrane creating a correlation peak that could represent a repeated distance between the channels. The clustering seen in other work may be an artefact of their preparation protocol of their *in-vitro* MscL system, or due to their protein tag rather than clustering being an innate behaviour of the channel.[75, 167]

As part of future work it would be of interest to build a custom model that could fit both the scattering from the protein shape and the correlation feature. Such a model was developed by Castorph *et al.* for a similar system of synaptic vesicles.[30] Complex decorated models such as jscatter could also be modified to account for the correlation features seen. This type of patterned surface model could also have useful implications for modelling of viruses. The effect of the antimicrobial molecules lyso–pc and pexiganan on the proteoliposomes was investigated. An increase in radius of gyration of the protein was fitted on addition of lyso–pc (26 Å to 30 Å) and on addition of pexiganan (29 Å to 36 Å). A change in the dimensionality parameter was also fitted suggesting a change from a rod-shaped particle to a more spherical shaped particle. These changes in conformation are consistent with gating, as the in-plane portion of the protein expands creating a 30 Å pore (increasing the radius of gyration) and the section of the protein that protrudes from the membrane contracts (making the overall shape less rod-like and more globular). The smaller changes observed in the presence of lyso-pc suggest that it may be less effective at gating MscL than pexiganan, when testing at the same concentration. These SAS experiments provided an interesting initial observation of response of the channel to lyso-pc and pexiganan, although they were not extensive they indicated that we had successfully expressed active MscL channels into liposomes.

The second system investigated in this thesis was a novel planar membrane mimetic, a suspended bilayer. In essence it is a floating bilayer suspended beneath a surfactant monolayer at the air-water interface. The formation of the suspended bilayer was possible through the use of a laminar flow trough. A monolayer was spread at the air-water interface and the liposomes/proteoliposomes pushed through the sub–phase underneath the monolayer in laminar flow, to promote vesicle adsorption and rupture at the interface. Formation of a high coverage, good-quality bilayer at the air-water interface was achieved after optimisation of lipid and salt concentration through RAIRS and NR experiments. Formation of a bilayer containing MscL was achieved by rupturing MscL containing proteoliposomes underneath the monolayer. Successful incorporation of MscL into the flexible planar bilayer mimic enabled characterisation of the protein. The protein coverage of the bilayer was 2.6% by volume, and the C-terminal portion of the protein extended 60 Å. On addition of 1.6 µM pexiganan, the protrusion of the MscL decreases to 30 Å. This is the first experimental evidence of a contraction of the C-terminal domain during gating. An EPR study provided evidence that the symmetry of the C-terminal changed on gating, and contraction

of the C-terminal domain is suggested in molecular modelling.[25, 47, 52] The role of this protein domain is debated as it is not critical to the gating of the channel but is thought to provide some function as a molecular sieve, to prevent escape of large molecules through the open channel when it is gated.[16]

The suspended bilayer membrane mimetic provides an exciting platform to study other membrane proteins. The ease of preparation and relatively unconstrained bilayer in comparison to solid-supported mimetics should mean that it has a large advantage over other more commonly used approaches. Future work on development of suspended bilayers could involve working on another version of a laminar flow trough. Our trough development focussed initially on improving the pinning of the miniscus on the trough to ensure stability when exchanging the sub-phase. Our final trough version used in this thesis, used for XRR measurements, was developed to allow for compression of a spread monolayer, however this was not successful. The ideal trough for suspended bilayer formation would incorporate this feature to enable consistent monolayers and accurate measurement of surface tension. This development could be achieved with careful design of barriers.

The final system investigated in this thesis is a second planar membrane mimic, that of a tethered lipid bilayer. A bilayer was formed by rupture of proteoliposomes onto a dense brush of PDP-PEG2000-DSPE tethers on a gold surface. Analysis using QCM-D and polarised neutron reflectivity confirmed the formation of a high coverage bilayer on the tethers. Fitting of models to the PNR data revealed an asymmetric bilayer composition with a higher APM of the outer leaflet than the inner leaflet containing the lipid tethers. Despite this asymmetry, the MscL composition of the formed bilayer was close to the initial volume composition of the lipsomes at 20% and a protein protrusion 54 Å from the membrane was determined, close to the model from the suspended bilayer. Once again the MscL containing membrane mimic was tested in the presence of 1.6 µM pexiganan. This resulted in a decrease in the protrusion of Mscl (from 54 Å to 37 Å, as observed in our other planar membrane mimic. The addition of pexiganan also resulted in an increase in the area per molecule of the the lipid leaflets consistent with a thinning of the bilayer leaflets. This thinning effect has been observed by other groups for pexiganan but was not evident when testing our suspended bilayer mimic with pexiganan.[149, 150] This highlights an issue found by other groups that the lipid composition and model membrane mimic used can impact observations of insertion mechanisms. Despite the large differences in our

planar membrane mimics we observed a large change in conformation of MscL on addition of pexiganan in both systems of 20–30 Å.

The change in conformation of the MscL observed in our planar membrane mimics on addition of the antimicrobial pexiganan is strongly suggestive of MscL gating, especially combined with the conformational changes observed in our small angle scattering analysis. This is strong evidence that pexiganan, through insertion of the peptide into the membrane, forces the MscL to gate continuously (or at least over the time period of our observations of approximately 6 hours). Irreversible gating of the MscL channel would cause cell death through extended membrane leakage and hence present an alternative mechanism of pexiganan antimicrobial action. The wider implication of this result is that it can be used to understand the toxicity of pexiganan to different bacteria and be used to inform decisions on the drug formulation for anti-bacterial and anti-fungal treatments. Since we understand the pexiganan mechanism to be a result of its amphiphilic structure and ability to insert into bacterial membranes to induce stress on the protein, other antimicrobial peptides and surfactants are likely to be able to create the same response. An interesting further study would be to test a range of antimicrobial peptides on our MscL membrane mimics to determine the universality of this mechanism.

Preferential orientation of the MscL channel was found to have occurred in both our planar membrane mimetics. It is possible that the MscL channels are already preferentially oriented in the proteoliposomes used. This could be an effect of the nature of the CFPE, expressing the protein directly into the liposomes, however the subsequent extrusion and sonication steps make this unlikely. Preferential orientation within the liposome surface may occur due to membrane curvature, though this would be difficult to determine using SANS. Regardless, selective orientation within the liposomes would not guarantee selective orientation within our planar membrane mimetics, as the liposome rupture step itself would be disruptive. To address how preferential orientation was achieved, experiments using fluorescent tagging or selective deuteration could be performed. It may be that the rupture step in formation of our mimetics was sufficiently slow to allow for rearrangement of the protein, such that the protein protrusion could face away from unfavourable interactions with the air-water interface or tether layers.

.1 Appendix: Troughs Used to Analyse Suspended Bilayers in Chapter 4

Development of trough design occurred during the process of the project and hence results were gathered using different trough set-ups and design. Trough set-ups were also limited by the technique i.e. measurements made with elliposometry and RAIRS required the use of smaller troughs than those required for neutron reflectivity and X-ray reflectivity. Method of liposome injection/flow also discussed.

.1.1 Troughs used for Ellipsometry

Trough A. Teflon laminar flow trough with two barriers. Flow controlled by hand using plastic syringes. Silicon wafer placed at the bottom of the trough for ellipsometry measurements to reduce scattering from the bottom of the trough.

Trough diameter: 5.2 cm by 4 cm.

Trough volume: 10 ml

Injection Method: Laminar flow used to replace solution in trough, solution replaces using plastic syringes at either end of trough, one adding solution whilst the other removed.

Injection rate: As slowly and as controlled as possible by hand (roughly 2 $\mathrm{ml\,min^{-1}}$

.1.2 Troughs used for RAIRS

Trough B. Small trough (not laminar flow) with barrier, liposomes injected underneath barrier.

Trough diameter: 10 cm by 2.2 cm (barrier placed such that monolayer area is 7 cm by 2.2 cm)

Trough volume: 8 ml

Injection Method: Liposomes injected using a small plastic syringe and needle

underneath a barrier in the trough.

Injection rate: As slowly and as controlled as possible by hand, roughly 2 ml min^{-1}

Trough C. Large trough-Ben Thomas design aluminium trough coated with black Teflon. (Large trough was suited to existed set-up enabling measurements to be carried out under nitrogen, removing water vapour from air. Liposomes added through injection.

Trough diameters: 22.8 cm by 7 cm (166.6 cm^2)

Trough volume: 60 ml

Injection method: Syringe through monolayer, syringe used to add vesicle solution whilst another solution removed the same volume of buffer.

Injection rate: As slowly and as controlled as possible by hand.

.1.3 Troughs used for Neutron Reflectivity

Two troughs used of different design. **Trough D.**

Trough diameters: 3 cm by 10 cm

Trough volume: 20 ml

Injection method: Laminar Flow using a syringe pump with plastic syringes.

Injection rate: 1 ml min^{-1}

Surface tension not measured during spreading of the monolayer (although it would be possible on this trough).

Trough E. Second trough design altered to allow for improved pinning of the miniscus.

Trough diameters: 2.4 cm by 16 cm

Trough volume: 30 ml

Injection method: Laminar Flow using a syringe pump with plastic syringes.

Injection rate: 1 ml min^{-1}

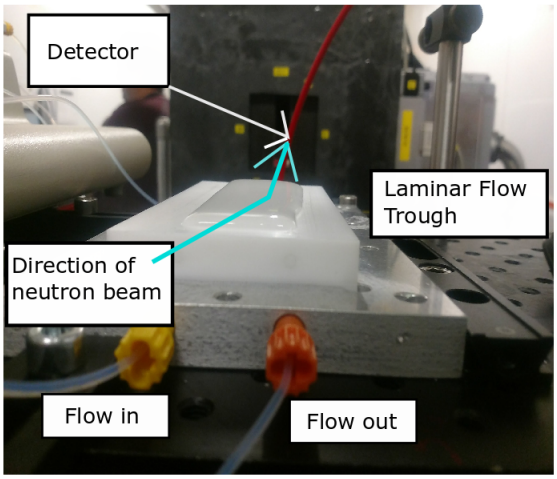

Figure 1 *Photos taken of the first inter experiment set up.*

Surface tension measured during spreading of the surfactant monolayer.

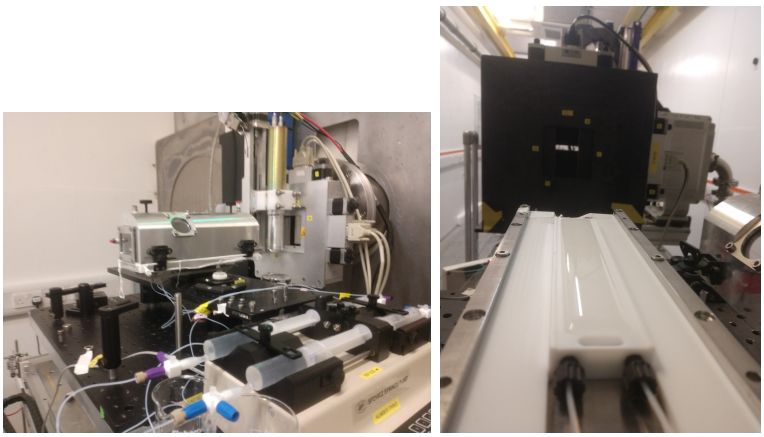

Figure 2 *Photos taken of the second inter experiment set up.*

.1.4 Troughs used for X-ray Reflectivity

Trough F1 and F2. Two troughs of same design used. Controlled rate injection of liposomes with glass syringes and syringe pump.

Trough diameters: 4 cm by 16 cm (compressed to 3 cm by 16 cm)

Trough volume: 30 ml

Injection method: Laminar Flow using a syringe pump with glass Hamilton syringes.

Injection rate: 6 ml min^{-1}

Surface pressure of monolayer was measured when spreading and then during compression.

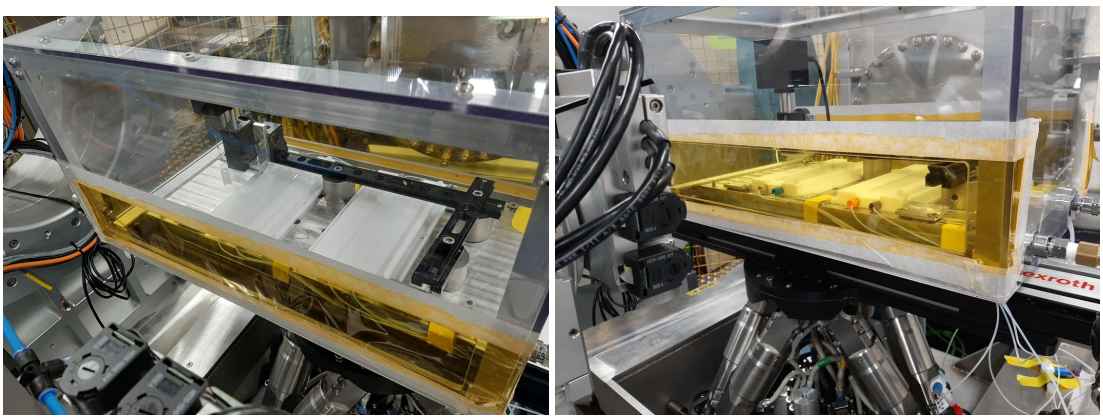

Figure 3 *Photos taken of the IO7 trough set up.*

.2 Appendix:Bayesian Analysis Posterior Probability distributions

Within this appendix are the posterior probability distribution results from Bayesian analysis (MCMC analysis) using Rascal software. These results are complimentary figures to the data fitted discussed in Chapter 4 on suspended bilayers.

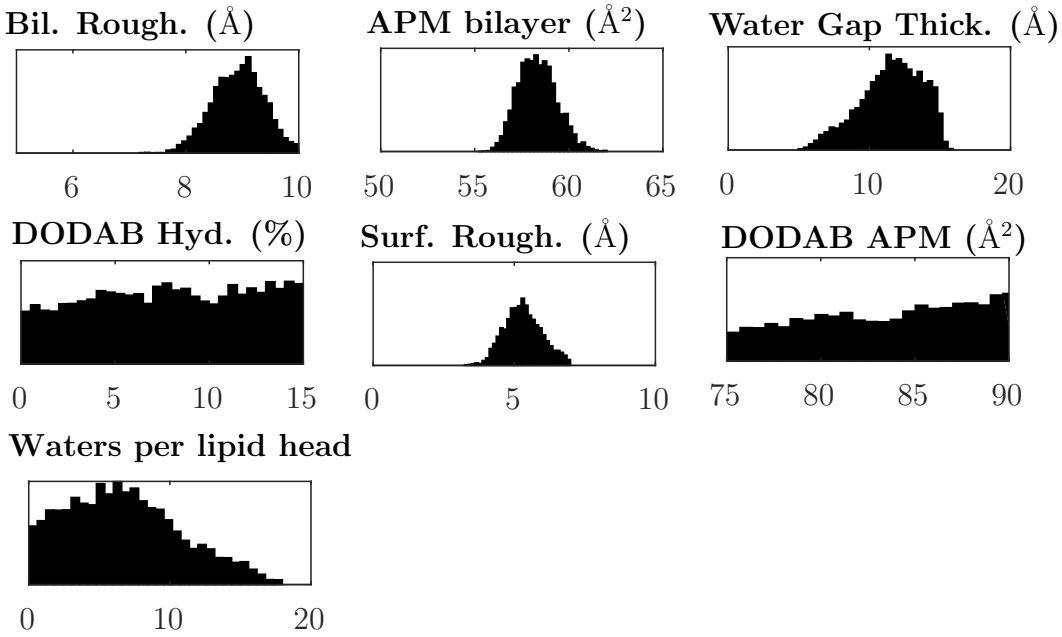

Figure 4 *Posteriors of analysis parameters of fitting a suspended bilayer model to reflectivity measurements of a 3:1 POPC:POPG bilayer suspended beneath a DODAB monolayer. The corresponding reflectivity profile and fit are shown in Figure 4.16.*

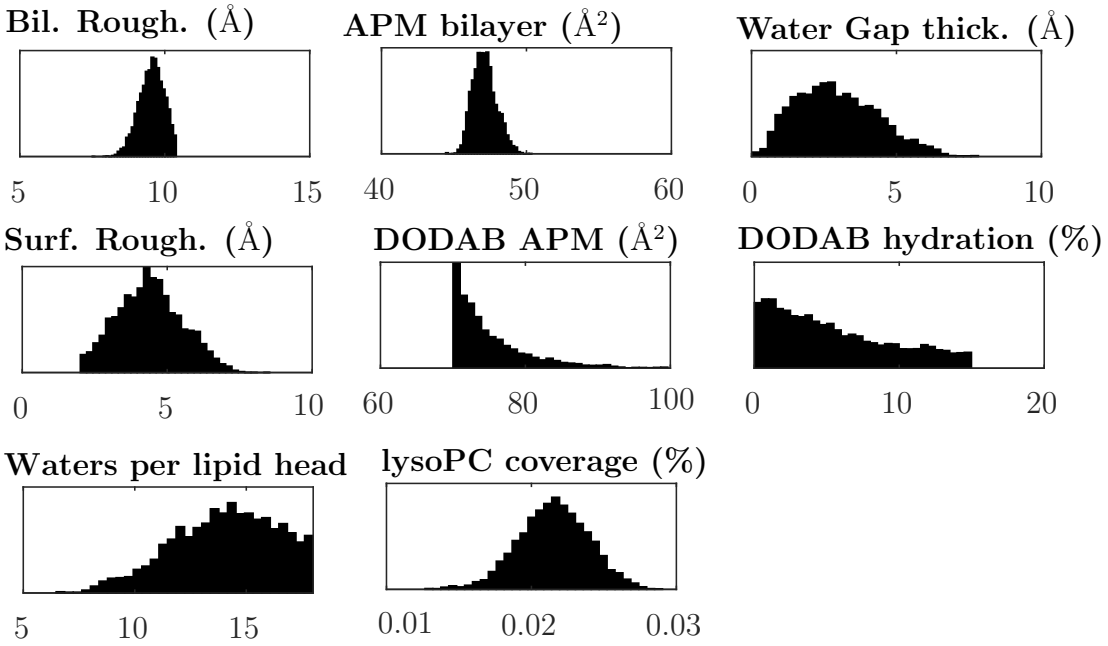

Figure 5 *Posteriors of analysis parameters of fitting a suspended bilayer model to reflectivity measurements of a 3:1 POPC:POPG bilayer suspended beneath a DODAB monolayer in the presence of* 4 µM *lyso-PC. The corresponding reflectivity profile and fit are shown in Figure 4.20.*

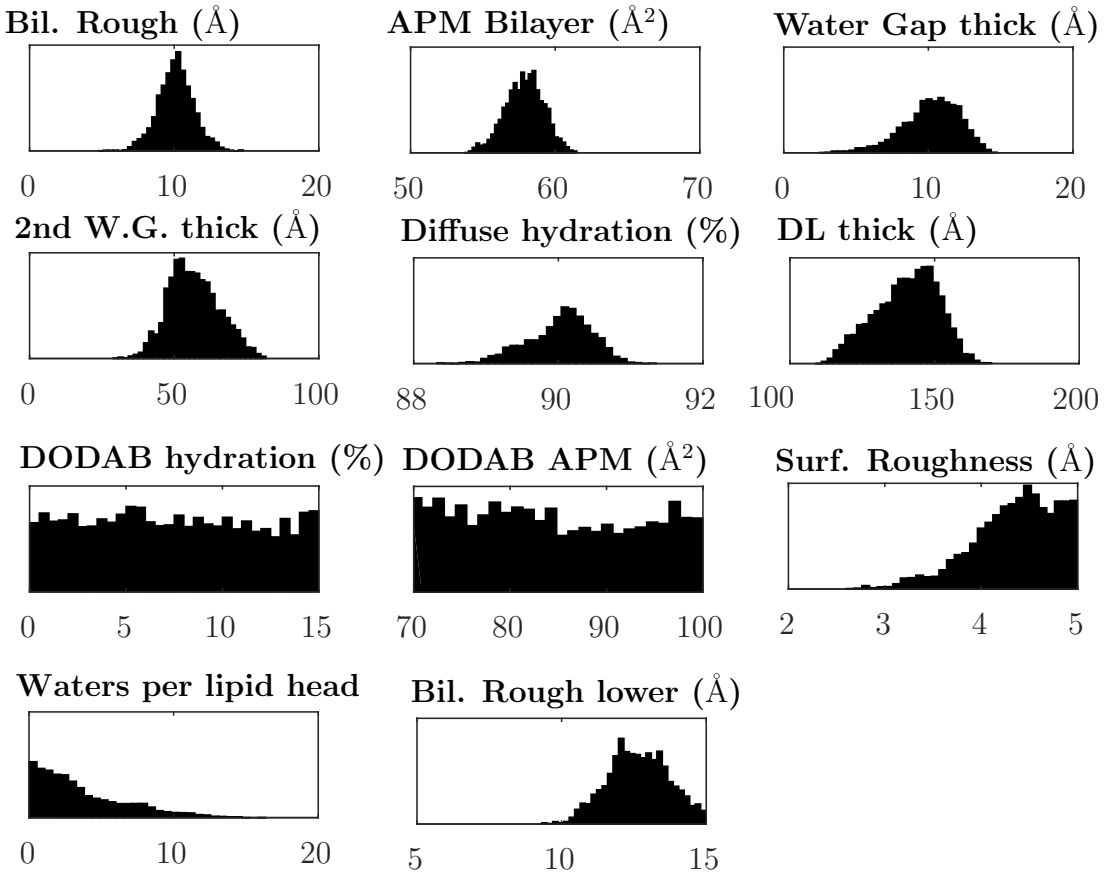

Figure 6 *Posteriors of analysis parameters of fitting a suspended bilayer model to reflectivity measurements of a 3:1 POPC:POPG bilayer suspended beneath a DODAB monolayer prior to the addition of pexiganan. The fitted model includes a diffuse layer underneath the bilayer.The corresponding reflectivity profile and fit are shown in Figure 4.18.*

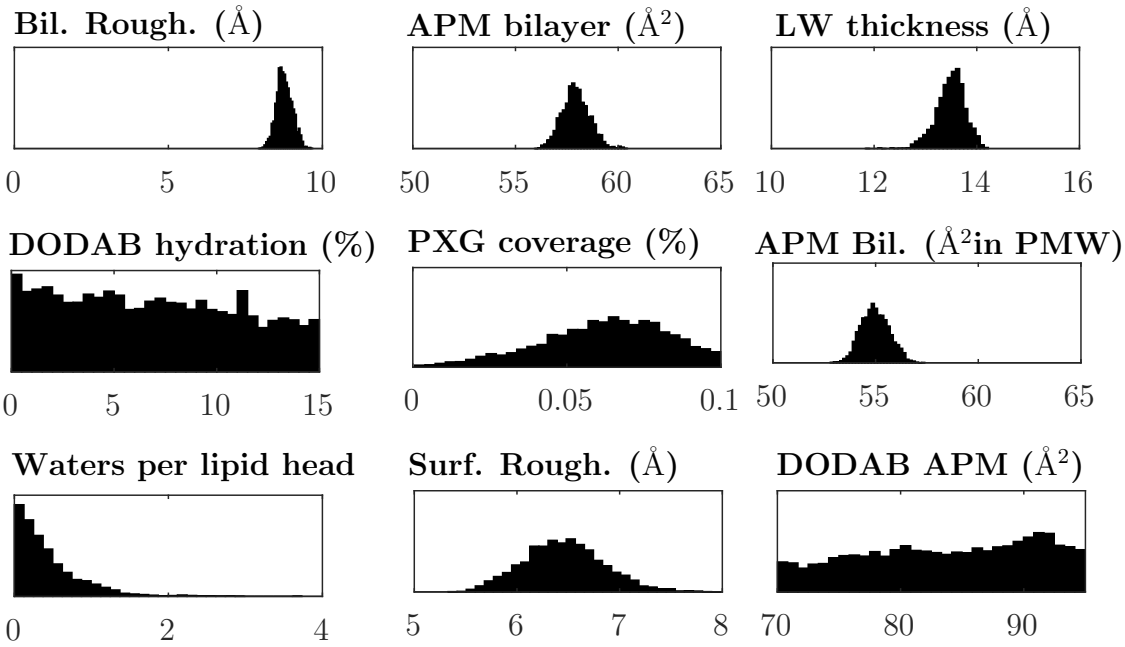

Figure 7 *Posteriors of analysis parameters of fitting a suspended bilayer model to reflectivity measurements of a 3:1 POPC:POPG bilayer suspended beneath a DODAB monolayer in the presense of* 4 µM *pexiganan. The corresponding reflectivity profile and fit are shown in Figure 4.19.*

Bibliography

[1] Abdelrasoul, M. A., A. R. Eid, and M. E. Badawy. "Preparation, characterizations and antibacterial activity of different nanoemulsions incorporating monoterpenes: in vitro and in vivo studies." *Archives of Phytopathology and Plant Protection* 53, 7-8: (2020) 310–334.

[2] Abdine, A., K.-H. Park, and D. E. Warschawski. "Cell-free membrane protein expression for solid-state NMR." In *Protein NMR Techniques*, Springer, 2012, 85–109.

[3] Abdine, A., M. A. Verhoeven, K.-H. Park, A. Ghazi, E. Guittet, C. Berrier, C. Van Heijenoort, and D. E. Warschawski. "Structural study of the membrane protein MscL using cell-free expression and solid-state NMR." *Journal of magnetic resonance* 204, 1: (2010) 155–159.

[4] Acosta, S., L. Quintanilla, M. Alonso, C. Aparicio, and J. C. Rodriguez-Cabello. "Recombinant AMP/Polypeptide Self-Assembled Monolayers with Synergistic Antimicrobial Properties for Bacterial Strains of Medical Relevance." *ACS Biomaterials Science & Engineering* 5, 9: (2019) 4708–4716.

[5] Albertorio, F., A. J. Diaz, T. Yang, V. A. Chapa, S. Kataoka, E. T. Castellana, and P. S. Cremer. "Fluid and air-stable lipopolymer membranes for biosensor applications." *Langmuir* 21, 16: (2005) 7476–7482.

[6] Andersson, J., I. Köper, and W. Knoll. "Tethered membrane architectures—design and applications." *Frontiers in Materials* 5: (2018) 55.

[7] Anishkin, A., V. Gendel, N. A. Sharifi, C.-S. Chiang, L. Shirinian, H. R. Guy, and S. Sukharev. "On the conformation of the COOH-terminal domain of the large mechanosensitive channel MscL." *The Journal of general physiology* 121, 3: (2003) 227–244.

[8] Apel-Paz, M., G. F. Doncel, and T. K. Vanderlick. "Membrane perturbation by surfactant candidates for STD prevention." *Langmuir* 19, 3: (2003) 591–597.

[9] Armen, R. S., O. D. Uitto, and S. E. Feller. "Phospholipid component volumes: determination and application to bilayer structure calculations." *Biophysical journal* 75, 2: (1998) 734–744.

[10] Arnold, K., O. Zschoernig, D. Barthel, and W. Herold. "Exclusion of poly (ethylene glycol) from liposome surfaces." *Biochimica et Biophysica Acta (BBA)-Biomembranes* 1022, 3: (1990) 303–310.

[11] Barh, D., N. Jain, S. Tiwari, B. P. Parida, V. D'Afonseca, L. Li, A. Ali, A. R. Santos, L. C. Guimarães, S. de Castro Soares, et al. "A novel comparative genomics analysis for common drug and vaccine targets in Corynebacterium pseudotuberculosis and other CMN group of human pathogens." *Chemical biology & drug design* 78, 1: (2011) 73–84.

[12] Barker, R. D., L. E. McKinley, and S. Titmuss. "Neutron Reflectivity as a Tool for Physics-Based Studies of Model Bacterial Membranes." In *Biophysics of Infection*, Springer, 2016, 261–282.

[13] Bass, R. B., P. Strop, M. Barclay, and D. C. Rees. "Crystal structure of Escherichia coli MscS, a voltage-modulated and mechanosensitive channel." *Science* 298, 5598: (2002) 1582–1587.

[14] Bassereau, P., R. Phillips, and P. Schwille. "Focus on the physics of the cell membrane." *New Journal of Physics* 14, 5: (2012) 055,021.

[15] Bavi, N., D. M. Cortes, C. D. Cox, P. R. Rohde, W. Liu, J. W. Deitmer, O. Bavi, P. Strop, A. P. Hill, D. Rees, et al. "The role of MscL amphipathic N terminus indicates a blueprint for bilayer-mediated gating of mechanosensitive channels." *Nature communications* 7, 1: (2016) 1–13.

[16] Bavi, N., A. D. Martinac, D. M. Cortes, O. Bavi, P. Ridone, T. Nomura, A. P. Hill, B. Martinac, and E. Perozo. "Structural dynamics of the MscL C-terminal domain." *Scientific reports* 7, 1: (2017) 1–11.

[17] Bavi, O., M. Vossoughi, R. Naghdabadi, and Y. Jamali. "The effect of local bending on gating of MscL using a representative volume element and finite element simulation." *Channels* 8, 4: (2014) 344–349.

[18] Bayerl, T. M., and M. Bloom. "Physical properties of single phospholipid bilayers adsorbed to micro glass beads. A new vesicular model system studied by 2H-nuclear magnetic resonance." *Biophysical journal* 58, 2: (1990) 357–362.

[19] Bialecka-Fornal, M., H. J. Lee, H. A. DeBerg, C. S. Gandhi, and R. Phillips. "Single-cell census of mechanosensitive channels in living bacteria." *PloS one* 7, 3: (2012) e33,077.

[20] BiotechRabbit. "RTS 500 ProteoMaster E. coli HY Kit BiotechRabbit." `https://www.biotechrabbit.com/rts-500-proteomaster-e-coli-hy-kit-405.html`, . Accessed: 2020-09-14.

[21] Blodgett, K. B., and I. Langmuir. "Built-up films of barium stearate and their optical properties." *Physical Review* 51, 11: (1937) 964.

[22] Blount, P., M. J. Schroeder, and C. Kung. "Mutations in a bacterial mechanosensitive channel change the cellular response to osmotic stress." *Journal of Biological Chemistry* 272, 51: (1997) 32,150–32,157.

[23] Blount, P., S. I. Sukharev, P. C. Moe, B. Martinac, and C. Kung. "[24] Mechanosensitive channels of bacteria." In *Methods in enzymology*, Elsevier, 1999, volume 294, 458–482.

[24] Boal, D., and D. H. Boal. *Mechanics of the Cell*. Cambridge University Press, 2012.

[25] Booth, I. R., and P. Blount. "The MscS and MscL families of mechanosensitive channels act as microbial emergency release valves." *Journal of bacteriology* 194, 18: (2012) 4802–4809.

[26] Booth, I. R., and P. Louis. "Managing hypoosmotic stress: aquaporins and medianosensitive channels in Escherichia coli." *Current opinion in microbiology* 2, 2: (1999) 166–169.

[27] Bruni, R., H. W. Taeusch, and A. J. Waring. "Surfactant protein B: lipid interactions of synthetic peptides representing the amino-terminal amphipathic domain." *Proceedings of the National Academy of Sciences* 88, 16: (1991) 7451–7455.

[28] Buda, R., Y. Liu, J. Yang, S. Hegde, K. Stevenson, F. Bai, and T. Pilizota. "Dynamics of Escherichia coli's passive response to a sudden decrease in external osmolarity." *Proceedings of the National Academy of Sciences* 113, 40: (2016) E5838–E5846.

[29] Castellana, E. T., and P. S. Cremer. "Solid supported lipid bilayers: From biophysical studies to sensor design." *Surface Science Reports* 61, 10: (2006) 429–444.

[30] Castorph, S., D. Riedel, L. Arleth, M. Sztucki, R. Jahn, M. Holt, and T. Salditt. "Structure parameters of synaptic vesicles quantified by small-angle x-ray scattering." *Biophysical journal* 98, 7: (2010) 1200–1208.

[31] Chang, G., R. H. Spencer, A. T. Lee, M. T. Barclay, and D. C. Rees. "Structure of the MscL homolog from Mycobacterium tuberculosis: a gated mechanosensitive ion channel." *Science* 282, 5397: (1998) 2220–2226.

[32] Charitat, T., E. Bellet-Amalric, G. Fragneto, and F. Graner. "Adsorbed and free lipid bilayers at the solid-liquid interface." *The European Physical Journal B-Condensed Matter and Complex Systems* 8, 4: (1999) 583–593.

[33] Chaudhary, N. K., N. Chaudhary, M. Dahal, B. Guragain, S. Rai, R. Chaudhary, K. Sachin, R. Lamichhane-Khadka, and A. Bhattarai.

"Fighting the SARS CoV-2 (COVID-19) pandemic with soap." *Preprints* 0, 0: (2020) 0.

[34] Chemspider. "Chemspider Pexiganan.", . `http://www.chemspider.com/Chemical-Structure.16742313.html`.

[35] Chen, H.-C., J. H. Brown, J. L. Morell, and C. Huang. "Synthetic magainin analogues with improved antimicrobial activity." *Febs Letters* 236, 2: (1988) 462–466.

[36] Chen, W., T. R. Gentile, K. V. O'Donovan, J. A. Borchers, and C. F. Majkrzak. "Polarized neutron reflectometry of a patterned magnetic film with a 3 He analyzer and a position-sensitive detector." *Review of scientific instruments* 75, 10: (2004) 3256–3263.

[37] Cheng, G., Z. Liu, J. K. Murton, M. Jablin, M. Dubey, J. Majewski, C. Halbert, J. Browning, J. Ankner, B. Akgun, et al. "Neutron reflectometry and QCM-D study of the interaction of cellulases with films of amorphous cellulose." *Biomacromolecules* 12, 6: (2011) 2216–2224.

[38] Cheng, J. T., J. D. Hale, M. Elliot, R. E. Hancock, and S. K. Straus. "Effect of membrane composition on antimicrobial peptides aurein 2.2 and 2.3 from Australian southern bell frogs." *Biophysical Journal* 96, 2: (2009) 552–565.

[39] Chi, E. Y., C. Ege, A. Winans, J. Majewski, G. Wu, K. Kjaer, and K. Y. C. Lee. "Lipid membrane templates the ordering and induces the fibrillogenesis of Alzheimer's disease amyloid-β peptide." *Proteins: Structure, Function, and Bioinformatics* 72, 1: (2008) 1–24.

[40] Cho, N.-J., C. W. Frank, B. Kasemo, and F. Hook. "Quartz crystal microbalance with dissipation monitoring of supported lipid bilayers on various substrates." *Nature protocols* 5, 6: (2010) 1096–1106.

[41] Cho, N.-J., K. K. Kanazawa, J. S. Glenn, and C. W. Frank. "Employing two different quartz crystal microbalance models to study changes in viscoelastic behavior upon transformation of lipid vesicles to a bilayer on a gold surface." *Analytical chemistry* 79, 18: (2007) 7027–7035.

[42] Chongsiriwatana, N. P., and A. E. Barron. "Comparing bacterial membrane interactions of antimicrobial peptides and their mimics." In *Antimicrobial Peptides*, Springer, 2010, 171–182.

[43] Claesson, M., N.-J. Cho, C. W. Frank, and M. Andersson. "Vesicle adsorption on mesoporous silica and titania." *Langmuir* 26, 22: (2010) 16,630–16,633.

[44] Clifton, L. A., S. C. Hall, N. Mahmoudi, T. J. Knowles, F. Heinrich, and J. H. Lakey. "Structural Investigations of Protein–Lipid Complexes Using Neutron Scattering." In *Lipid-Protein Interactions*, Springer, 2019, 201–251.

[45] Clifton, L. A., N. Paracini, A. V. Hughes, J. H. Lakey, N.-J. Steinke, J. F. Cooper, M. Gavutis, and M. W. Skoda. "Self-Assembled Fluid Phase Floating Membranes with Tunable Water Interlayers." *Langmuir* 35, 42: (2019) 13,735–13,744.

[46] Clifton, L. A., M. W. Skoda, E. L. Daulton, A. V. Hughes, A. P. Le Brun, J. H. Lakey, and S. A. Holt. "Asymmetric phospholipid: lipopolysaccharide bilayers; a Gram-negative bacterial outer membrane mimic." *Journal of The Royal Society Interface* 10, 89: (2013) 20130,810.

[47] Corry, B., A. C. Hurst, P. Pal, T. Nomura, P. Rigby, and B. Martinac. "An improved open-channel structure of MscL determined from FRET confocal microscopy and simulation." *Journal of General Physiology* 136, 4: (2010) 483–494.

[48] Coutable, A., C. Thibault, J. Chalmeau, J. M. Fran¸cois, C. Vieu, V. Noireaux, and E. Trévisiol. "Preparation of tethered-lipid bilayers on gold surfaces for the incorporation of integral membrane proteins synthesized by cell-free expression." *Langmuir* 30, 11: (2014) 3132–3141.

[49] Cruickshank, C. C., R. F. Minchin, A. Le Dain, and B. Martinac. "Estimation of the pore size of the large-conductance mechanosensitive ion channel of Escherichia coli." *Biophysical journal* 73, 4: (1997) 1925–1931.

[50] Dabkowska, A., D. Barlow, A. Hughes, R. Campbell, P. Quinn, and M. Lawrence. "The effect of neutral helper lipids on the structure of cationic lipid monolayers." *Journal of The Royal Society Interface* 9, 68: (2012) 548–561.

[51] Delhi, I. "Radius of Gyration." `http://www.scfbio-iitd.res.in/software/proteomics/rg.jsp`, . Accessed: 2020-10-14.

[52] Deplazes, E., M. Louhivuori, D. Jayatilaka, S. J. Marrink, and B. Corry. "Structural investigation of MscL gating using experimental data and coarse grained MD simulations." *PLoS Comput Biol* 8, 9: (2012) e1002,683.

[53] Dickey, A., and R. Faller. "Examining the contributions of lipid shape and headgroup charge on bilayer behavior." *Biophysical journal* 95, 6: (2008) 2636–2646.

[54] Dorwart, M. R., R. Wray, C. A. Brautigam, Y. Jiang, and P. Blount. "S. aureus MscL is a pentamer in vivo but of variable stoichiometries in vitro: implications for detergent-solubilized membrane proteins." *PLoS biology* 8, 12.

[55] Dupuy, A. D., and D. M. Engelman. "Protein area occupancy at the center of the red blood cell membrane." *Proceedings of the National Academy of Sciences* 105, 8: (2008) 2848–2852.

[56] Eeman, M., and M. Deleu. "From biological membranes to biomimetic model membranes." *Biotechnologie, Agronomie, Société et Environnement* 14, 4: (2010) 719–736.

[57] Elmore, D. E., and D. A. Dougherty. "Investigating lipid composition effects on the mechanosensitive channel of large conductance (MscL) using molecular dynamics simulations." *Biophysical journal* 85, 3: (2003) 1512–1524.

[58] Elsharkasy, O. M., J. Z. Nordin, D. W. Hagey, O. G. de Jong, R. M. Schiffelers, S. E. Andaloussi, and P. Vader. "Extracellular vesicles as drug delivery systems: Why and how?" *Advanced drug delivery reviews* 159: (2020) 332–343.

[59] Engelman, D. M. "Membranes are more mosaic than fluid.", 2005.

[60] Epand, R. F., J. E. Pollard, J. O. Wright, P. B. Savage, and R. M. Epand. "Depolarization, bacterial membrane composition, and the antimicrobial action of ceragenins." *Antimicrobial agents and chemotherapy* 54, 9: (2010) 3708–3713.

[61] Fernandez, D. I., A. P. Le Brun, T. C. Whitwell, M.-A. Sani, M. James, and F. Separovic. "The antimicrobial peptide aurein 1.2 disrupts model membranes via the carpet mechanism." *Physical Chemistry Chemical Physics* 14, 45: (2012) 15,739–15,751.

[62] Fragneto, G. "Neutrons and model membranes." *The European Physical Journal Special Topics* 213, 1: (2012) 327–342.

[63] Fragneto, G., T. Charitat, E. Bellet-Amalric, R. Cubitt, and F. Graner. "Swelling of phospholipid floating bilayers: the effect of chain length." *Langmuir* 19, 19: (2003) 7695–7702.

[64] Fuchs, P. C., A. L. Barry, and S. D. Brown. "In vitro antimicrobial activity of MSI-78, a magainin analog." *Antimicrobial agents and chemotherapy* 42, 5: (1998) 1213–1216.

[65] Gandhi, C. S., T. A. Walton, and D. C. Rees. "OCAM: a new tool for studying the oligomeric diversity of MscL channels." *Protein Science* 20, 2: (2011) 313–326.

[66] García-Añoveros, J., and D. P. Corey. "The molecules of mechanosensation." *Annual review of neuroscience* 20, 1: (1997) 567–594.

[67] Gerelli, Y. "Phase Transitions in a Single Supported Phospholipid Bilayer: Real-Time Determination by Neutron Reflectometry." *Physical review letters* 122, 24: (2019) 248,101.

[68] Gidalevitz, D., Y. Ishitsuka, A. S. Muresan, O. Konovalov, A. J. Waring, R. I. Lehrer, and K. Y. C. Lee. "Interaction of antimicrobial peptide

protegrin with biomembranes." *Proceedings of the National Academy of Sciences* 100, 11: (2003) 6302–6307.

[69] Giess, F., M. G. Friedrich, J. Heberle, R. L. Naumann, and W. Knoll. "The protein-tethered lipid bilayer: A novel mimic of the biological membrane." *Biophysical journal* 87, 5: (2004) 3213–3220.

[70] Glatter, O., and O. Kratky. *Small angle X-ray scattering*. Academic press, 1982.

[71] Gomes, D., R. Santos, R. S Soares, S. Reis, S. Carvalho, P. Rego, M. C Peleteiro, L. Tavares, and M. Oliveira. "Pexiganan in combination with nisin to control polymicrobial diabetic foot infections." *Antibiotics* 9, 3: (2020) 128.

[72] Goodsell, D. S. "Putting proteins in context: scientific illustrations bring together information from diverse sources to provide an integrative view of the molecular biology of cells." *Bioessays* 34, 9: (2012) 718–720.

[73] Gottler, L. M., and A. Ramamoorthy. "Structure, membrane orientation, mechanism, and function of pexiganan—a highly potent antimicrobial peptide designed from magainin." *Biochimica et Biophysica Acta (BBA)-Biomembranes* 1788, 8: (2009) 1680–1686.

[74] Goyal, R. K., and A. K. Mattoo. "Plant antimicrobial peptides." In *Host defense peptides and their potential as therapeutic agents*, Springer, 2016, 111–136.

[75] Grage, S. L., A. M. Keleshian, T. Turdzeladze, A. R. Battle, W. C. Tay, R. P. May, S. A. Holt, S. A. Contera, M. Haertlein, M. Moulin, et al. "Bilayer-mediated clustering and functional interaction of MscL channels." *Biophysical journal* 100, 5: (2011) 1252–1260.

[76] Gregory, S. M., A. Pokorny, and P. F. Almeida. "Magainin 2 revisited: a test of the quantitative model for the all-or-none permeabilization of phospholipid vesicles." *Biophysical journal* 96, 1: (2009) 116–131.

[77] Gullingsrud, J., and K. Schulten. "Lipid bilayer pressure profiles and mechanosensitive channel gating." *Biophysical journal* 86, 6: (2004) 3496–3509.

[78] Gupta, S. M., C. C. Aranha, J. R. Bellare, and K. Reddy. "Interaction of contraceptive antimicrobial peptide nisin with target cell membranes: implications for use as vaginal microbicide." *Contraception* 80, 3: (2009) 299–307.

[79] Gutberlet, T., R. Steitz, G. Fragneto, and B. Klösgen. "Phospholipid bilayer formation at a bare Si surface: a time-resolved neutron reflectivity study." *Journal of Physics: Condensed Matter* 16, 26: (2004) S2469.

[80] Haario, H., M. Laine, A. Mira, and E. Saksman. "DRAM: efficient adaptive MCMC." *Statistics and computing* 16, 4: (2006) 339–354.

[81] Hallock, K. J., D.-K. Lee, and A. Ramamoorthy. "MSI-78, an analogue of the magainin antimicrobial peptides, disrupts lipid bilayer structure via positive curvature strain." *Biophysical journal* 84, 5: (2003) 3052–3060.

[82] Halza, E., T. H. Bro, B. Bilenberg, and A. Kocer. "Well-defined microapertures for ion channel biosensors." *Analytical chemistry* 85, 2: (2013) 811–815.

[83] Hammouda, B. "A new Guinier–Porod model." *Journal of Applied Crystallography* 43, 4: (2010) 716–719.

[84] Hamouda, T., and J. Baker Jr. "Antimicrobial mechanism of action of surfactant lipid preparations in enteric Gram-negative bacilli." *Journal of applied microbiology* 89, 3: (2000) 397–403.

[85] Harris, J. M., and R. B. Chess. "Effect of pegylation on pharmaceuticals." *Nature reviews Drug discovery* 2, 3: (2003) 214–221.

[86] Häse, C., A. Le Dain, and B. Martinac. "Molecular dissection of the large mechanosensitive ion channel (MscL) of E. coli: mutants with altered channel gating and pressure sensitivity." *The Journal of membrane biology* 157, 1: (1997) 17–25.

[87] Haswell, E. S., R. Peyronnet, H. Barbier-Brygoo, E. M. Meyerowitz, and J.-M. Frachisse. "Two MscS homologs provide mechanosensitive channel activities in the Arabidopsis root." *Current Biology* 18, 10: (2008) 730–734.

[88] He, K., S. J. Ludtke, D. L. Worcester, and H. W. Huang. "Neutron scattering in the plane of membranes: structure of alamethicin pores." *Biophysical journal* 70, 6: (1996) 2659–2666.

[89] Hénin, J., W. Shinoda, and M. L. Klein. "Models for phosphatidylglycerol lipids put to a structural test." *The Journal of Physical Chemistry B* 113, 19: (2009) 6958–6963.

[90] Heyes, J., K. Hall, V. Tailor, R. Lenz, and I. MacLachlan. "Synthesis and characterization of novel poly (ethylene glycol)-lipid conjugates suitable for use in drug delivery." *Journal of Controlled Release* 112, 2: (2006) 280–290.

[91] Higgins, J. S., and H. C. Benoit. *Polymers and neutron scattering*. Oxford University Press, 1994.

[92] Hirsh, D. J., J. Hammer, W. L. Maloy, J. Blazyk, and J. Schaefer. "Secondary structure and location of a magainin analogue in synthetic phospholipid bilayers." *Biochemistry* 35, 39: (1996) 12,733–12,741.

[93] Hjelm Jr, R. P., P. Thiyagarajan, and H. Alkan-Onyuksel. "Organization of phosphatidylcholine and bile salt in rodlike mixed micelles." *The Journal of Physical Chemistry* 96, 21: (1992) 8653–8661.

[94] Hodgman, C. E., and M. C. Jewett. "Cell-free synthetic biology: thinking outside the cell." *Metabolic engineering* 14, 3: (2012) 261–269.

[95] Holt, S. A., A. P. Le Brun, C. F. Majkrzak, D. J. McGillivray, F. Heinrich, M. Lösche, and J. H. Lakey. "An ion-channel-containing model membrane: structural determination by magnetic contrast neutron reflectometry." *Soft Matter* 5, 13: (2009) 2576–2586.

[96] Hook, F., B. Kasemo, T. Nylander, C. Fant, K. Sott, and H. Elwing. "Variations in coupled water, viscoelastic properties, and film thickness of a Mefp-1 protein film during adsorption and cross-linking: a quartz crystal microbalance with dissipation monitoring, ellipsometry, and surface plasmon resonance study." *Analytical chemistry* 73, 24: (2001) 5796–5804.

[97] Hopfner, M., U. Rothe, and G. Bendas. "Biosensor-based evaluation of liposomal behavior in the target binding process." *Journal of Liposome research* 18, 1: (2008) 71–82.

[98] Huang, H. W. "Action of antimicrobial peptides: two-state model." *Biochemistry* 39, 29: (2000) 8347–8352.

[99] Hughes, A. "RasCAL MatLab Application for analysis of neutron and x-ray reflectivity.", . `https://sourceforge.net/projects/rscl/`.

[100] Hughes, A. V., S. A. Holt, E. Daulton, A. Soliakov, T. R. Charlton, S. J. Roser, and J. H. Lakey. "High coverage fluid-phase floating lipid bilayers supported by ω-thiolipid self-assembled monolayers." *Journal of The Royal Society Interface* 11, 98: (2014) 20140,447.

[101] Hughes, A. V., J. R. Howse, A. Dabkowska, R. A. Jones, M. J. Lawrence, and S. J. Roser. "Floating lipid bilayers deposited on chemically grafted phosphatidylcholine surfaces." *Langmuir* 24, 5: (2008) 1989–1999.

[102] Hughes, A. V., D. S. Patel, G. Widmalm, J. B. Klauda, L. A. Clifton, and W. Im. "Physical properties of bacterial outer membrane models: neutron reflectometry & molecular simulation." *Biophysical journal* 116, 6: (2019) 1095–1104.

[103] Ilavsky, J. "Small Angle Diffraction Tool Irena and Nika Manuals 1.5.1 documentation." https://saxs-igorcodedocs.readthedocs.io/en/stable/Irena/SmallAngleDiffraction.html, .

[104] Inci, F., U. Celik, B. Turken, H. O. Ozer, and F. N. Kok. "Construction of P-glycoprotein incorporated tethered lipid bilayer membranes." *Biochemistry and biophysics reports* 2: (2015) 115–122.

[105] Irena, and nika Manuals 1.5.1. "Guinier Porod Irena and nika Manuals 1.5.1 Documentation." `https://saxs-igorcodedocs.readthedocs.io/en/stable/Irena/GuinierPorod.html`, . Accessed: 2020-09-14.

[106] Iscla, I., C. Eaton, J. Parker, R. Wray, Z. Kovács, and P. Blount. "Improving the design of a MscL-based triggered nanovalve." *Biosensors* 3, 1: (2013) 171–184.

[107] Iscla, I., R. Wray, P. Blount, J. Larkins-Ford, A. L. Conery, F. M. Ausubel, S. Ramu, A. Kavanagh, J. X. Huang, M. A. Blaskovich, et al. "A new antibiotic with potent activity targets MscL." *The Journal of antibiotics* 68, 7: (2015) 453–462.

[108] Israelachvili, J. N., D. J. Mitchell, and B. W. Ninham. "Theory of self-assembly of hydrocarbon amphiphiles into micelles and bilayers." *Journal of the Chemical Society, Faraday Transactions 2: Molecular and Chemical Physics* 72: (1976) 1525–1568.

[109] Jackman, J. A., J.-H. Choi, V. P. Zhdanov, and N.-J. Cho. "Influence of osmotic pressure on adhesion of lipid vesicles to solid supports." *Langmuir* 29, 36: (2013) 11,375–11,384.

[110] Jacobs, M. L., M. A. Boyd, and N. P. Kamat. "Diblock copolymers enhance folding of a mechanosensitive membrane protein during cell-free expression." *Proceedings of the National Academy of Sciences* 116, 10: (2019) 4031–4036.

[111] Jagalski, V., R. D. Barker, M. B. Thygesen, K. Gotfryd, M. B. Kruger, L. Shi, S. Maric, N. Bovet, M. Moulin, M. Haertlein, et al. "Grafted biomembranes containing membrane proteins–the case of the leucine transporter." *Soft Matter* 11, 39: (2015) 7707–7711.

[112] Janosi, L., and A. A. Gorfe. "Simulating POPC and POPC/POPG bilayers: conserved packing and altered surface reactivity." *Journal of chemical theory and computation* 6, 10: (2010) 3267–3273.

[113] Jeon, J., and G. A. Voth. "Gating of the mechanosensitive channel protein MscL: the interplay of membrane and protein." *Biophysical journal* 94, 9: (2008) 3497–3511.

[114] Jepson, A. *E. coli motility and growth; a biophysical study.* Ph.D. thesis, University of Edinburgh, 2014.

[115] Kahraman, O., P. D. Koch, W. S. Klug, and C. A. Haselwandter. "Architecture and function of mechanosensitive membrane protein lattices." *Scientific reports* 6: (2016) 19,214.

[116] Kanazawa, K. K. "Steady state and transient QCM solutions at the metal solution interface." *Journal of Electroanalytical Chemistry* 524: (2002) 103–109.

[117] Kenworthy, A. K., K. Hristova, D. Needham, and T. J. McIntosh. "Range and magnitude of the steric pressure between bilayers containing phospholipids with covalently attached poly (ethylene glycol)." *Biophysical journal* 68, 5: (1995) 1921–1936.

[118] Khan, M. H., and K. Ramalingam. "Synthesis of antimicrobial nanoemulsions and its effectuality for the treatment of multi-drug resistant ESKAPE pathogens." *Biocatalysis and Agricultural Biotechnology* 18: (2019) 101,025.

[119] Khan, T. R., H. M. Grandin, A. Mashaghi, M. Textor, E. Reimhult, and I. Reviakine. "Lipid redistribution in phosphatidylserine-containing vesicles adsorbing on titania." *Biointerphases* 3, 2: (2008) FA90–FA95.

[120] Kloda, A., and B. Martinac. "Molecular identification of a mechanosensitive channel in archaea." *Biophysical journal* 80, 1: (2001) 229–240.

[121] Koutsioubas, A., M.-S. Appavou, and D. Lairez. "Time-resolved neutron reflectivity during supported membrane formation by vesicle fusion." *Langmuir* 33, 40: (2017) 10,598–10,605.

[122] Kratky, O. "X-ray small angle scattering with substances of biological interest in diluted solutions." *Progress in biophysics and molecular biology* 13: (1963) 105–IN1.

[123] Kučerka, N., M.-P. Nieh, and J. Katsaras. "Fluid phase lipid areas and bilayer thicknesses of commonly used phosphatidylcholines as a function of temperature." *Biochimica et Biophysica Acta (BBA)-Biomembranes* 1808, 11: (2011) 2761–2771.

[124] Kuhl, T. L., J. Majewski, J. Y. Wong, S. Steinberg, D. E. Leckband, J. N. Israelachvili, and G. S. Smith. "A neutron reflectivity study of polymer-modified phospholipid monolayers at the solid-solution interface: polyethylene glycol-lipids on silane-modified substrates." *Biophysical journal* 75, 5: (1998) 2352–2362.

[125] Lantzsch, G., H. Binder, and H. Heerklotz. "Surface area per molecule in lipid/C 12 E n membranes as seen by fluorescence resonance energy transfer." *Journal of fluorescence* 4, 4: (1994) 339–343.

[126] Le Brun, A. P., S. A. Holt, D. S. Shah, C. F. Majkrzak, and J. H. Lakey. "Monitoring the assembly of antibody-binding membrane protein arrays using polarised neutron reflection." *European Biophysics Journal* 37, 5: (2008) 639–645.

[127] Lee, J., C. Park, S.-C. Park, E.-R. Woo, Y. Park, K.-S. Hahm, and D. G. Lee. "Cell selectivity-membrane phospholipids relationship of the antimicrobial effects shown by pleurocidin enantiomeric peptides." *Journal of peptide science: an official publication of the European Peptide Society* 15, 9: (2009) 601–606.

[128] Lee, M.-T., W.-C. Hung, F.-Y. Chen, and H. W. Huang. "Many-body effect of antimicrobial peptides: on the correlation between lipid's spontaneous curvature and pore formation." *Biophysical journal* 89, 6: (2005) 4006–4016.

[129] Levina, N., S. Tötemeyer, N. R. Stokes, P. Louis, M. A. Jones, and I. R. Booth. "Protection of Escherichia coli cells against extreme turgor by activation of MscS and MscL mechanosensitive channels: identification of genes required for MscS activity." *The EMBO journal* 18, 7: (1999) 1730–1737.

[130] Lillemeier, B. F., J. R. Pfeiffer, Z. Surviladze, B. S. Wilson, and M. M. Davis. "Plasma membrane-associated proteins are clustered into islands attached to the cytoskeleton." *Proceedings of the National Academy of Sciences* 103, 50: (2006) 18,992–18,997.

[131] Lin, J., J. Szymanski, P. C. Searson, and K. Hristova. "Effect of a polymer cushion on the electrical properties and stability of surface-supported lipid bilayers." *Langmuir* 26, 5: (2010) 3544–3548.

[132] Lind, T. K., M. W. Skoda, and M. Cardenas. "Formation and characterization of supported lipid bilayers composed of phosphatidylethanolamine and phosphatidylglycerol by vesicle fusion, a simple but relevant model for bacterial membranes." *ACS omega* 4, 6: (2019) 10,687–10,694.

[133] Liu, Z., C. S. Gandhi, and D. C. Rees. "Structure of a tetrameric MscL in an expanded intermediate state." *Nature* 461, 7260: (2009) 120–124.

[134] Lovell, M., and R. Richardson. "Analysis methods in neutron and X-ray reflectometry." *Current opinion in colloid & interface science* 4, 3: (1999) 197–204.

[135] Ludtke, S., K. He, and H. Huang. "Membrane thinning caused by magainin 2." *Biochemistry* 34, 51: (1995) 16,764–16,769.

[136] Ludtke, S. J., K. He, W. T. Heller, T. A. Harroun, L. Yang, and H. W. Huang. "Membrane pores induced by magainin." *Biochemistry* 35, 43: (1996) 13,723–13,728.

[137] Lundbæk, J. A., P. Birn, A. J. Hansen, R. Søgaard, C. Nielsen, J. Girshman, M. J. Bruno, S. E. Tape, J. Egebjerg, D. V. Greathouse, et al. "Regulation of Sodium Channel Function by Bilayer Elasticity The Importance of Hydrophobic Coupling. Effects of Micelle-forming Amphiphiles and Cholesterol." *Journal of General Physiology* 123, 5: (2004) 599–621.

[138] Luzzati, V. "Interpr 'e tation of absolute measurements of central X-ray scattering in point or linear collimation: Solutions of globular particles and rods." *Acta Crystallographica* 13, 11: (1960) 939–945.

[139] Magnussen, O., B. Ocko, M. Regan, K. Penanen, P. S. Pershan, and M. Deutsch. "X-ray reflectivity measurements of surface layering in liquid mercury." *Physical review letters* 74, 22: (1995) 4444.

[140] Majkrzak, C., and N. Berk. "Inverting neutron reflectivity from layered film structures using polarized beams." *Physica B: Condensed Matter* 267: (1999) 168–174.

[141] Majumder, S., J. Garamella, Y.-L. Wang, M. DeNies, V. Noireaux, and A. P. Liu. "Cell-sized mechanosensitive and biosensing compartment programmed with DNA." *Chemical Communications* 53, 53: (2017) 7349–7352.

[142] Martinac, B. "Mechanosensitive ion channels: molecules of mechanotransduction." *Journal of cell science* 117, 12: (2004) 2449–2460.

[143] Martinac, B., J. Adler, and C. Kung. "Mechanosensitive ion channels of E. coli activated by amphipaths." *Nature* 348, 6298: (1990) 261–263.

[144] Martinac, B., M. Buechner, A. H. Delcour, J. Adler, and C. Kung. "Pressure-sensitive ion channel in Escherichia coli." *Proceedings of the National Academy of Sciences* 84, 8: (1987) 2297–2301.

[145] Matsuzaki, K. "Magainins as paradigm for the mode of action of pore forming polypeptides." *Biochimica et Biophysica Acta (BBA)-Reviews on Biomembranes* 1376, 3: (1998) 391–400.

[146] Matsuzaki, K., O. Murase, H. Tokuda, S. Funakoshi, N. Fujii, and K. Miyajima. "Orientational and aggregational states of magainin 2 in phospholipid bilayers." *Biochemistry* 33, 11: (1994) 3342–3349.

[147] McCluskey, A. R., A. Sanchez-Fernandez, K. J. Edler, S. C. Parker, A. J. Jackson, R. A. Campbell, and T. Arnold. "Bayesian determination of the effect of a deep eutectic solvent on the structure of lipid monolayers." *Physical Chemistry Chemical Physics* 21, 11: (2019) 6133–6141.

[148] McCluskey, A. R., J. Cooper, T. Arnold, and T. Snow. "A general approach to maximise information density in neutron reflectometry analysis." *Machine Learning: Science and Technology* 1, 3: (2020) 035,002.

[149] McKinley, L. *Neutron Reflectivity studies of Bacterial Membranes, Peptides and Proteins.* Ph.D. thesis, University of Edinburgh, 2017.

[150] Mecke, A., D.-K. Lee, A. Ramamoorthy, B. G. Orr, and M. M. B. Holl. "Membrane thinning due to antimicrobial peptide binding: an atomic force microscopy study of MSI-78 in lipid bilayers." *Biophysical journal* 89, 6: (2005) 4043–4050.

[151] Melcrová, A., S. Pokorna, S. Pullanchery, M. Kohagen, P. Jurkiewicz, M. Hof, P. Jungwirth, P. S. Cremer, and L. Cwiklik. "The complex nature

of calcium cation interactions with phospholipid bilayers." *Scientific reports* 6: (2016) 38,035.

[152] Merz, C., W. Knoll, M. Textor, and E. Reimhult. "Formation of supported bacterial lipid membrane mimics." *Biointerphases* 3, 2: (2008) FA41–FA50.

[153] Milner, S. T., T. A. Witten, and M. E. Cates. "Theory of the grafted polymer brush." *Macromolecules* 21, 8: (1988) 2610–2619.

[154] Miyazaki, H., N. Midorikawa, S. Fujimoto, N. Miyoshi, H. Yoshida, and T. Matsumoto. "Antimicrobial effects of lysophosphatidylcholine on methicillin-resistant Staphylococcus aureus." *Therapeutic advances in infectious disease* 4, 4: (2017) 89–94.

[155] Moe, P., and P. Blount. "Assessment of potential stimuli for mechano-dependent gating of MscL: effects of pressure, tension, and lipid headgroups." *Biochemistry* 44, 36: (2005) 12,239–12,244.

[156] Moe, P. C., P. Blount, and C. Kung. "Functional and structural conservation in the mechanosensitive channel MscL implicates elements crucial for mechanosensation." *Molecular microbiology* 28, 3: (1998) 583–592.

[157] Mukherjee, N., M. D. Jose, J. P. Birkner, M. Walko, H. I. Ingolfsson, A. Dimitrova, C. Arnarez, S. J. Marrink, and A. Koçer. "The activation mode of the mechanosensitive ion channel, MscL, by lysophosphatidylcholine differs from tension-induced gating." *The FASEB Journal* 28, 10: (2014) 4292–4302.

[158] Mukherjee, S., R. K. Kar, R. P. R. Nanga, K. H. Mroue, A. Ramamoorthy, and A. Bhunia. "Accelerated molecular dynamics simulation analysis of MSI-594 in a lipid bilayer." *Physical chemistry chemical physics* 19, 29: (2017) 19,289–19,299.

[159] Munro, J. C., and C. W. Frank. "Adsorption of lipid-functionalized poly (ethylene glycol) to gold surfaces as a cushion for polymer-supported lipid bilayers." *Langmuir* 20, 8: (2004) 3339–3349.

[160] Najem, J. S., M. D. Dunlap, I. D. Rowe, E. C. Freeman, J. W. Grant, S. Sukharev, and D. J. Leo. "Activation of bacterial channel MscL in mechanically stimulated droplet interface bilayers." *Scientific reports* 5: (2015) 13,726.

[161] Nele, V., M. N. Holme, U. Kauscher, M. R. Thomas, J. J. Doutch, and M. M. Stevens. "Effect of formulation method, lipid composition, and PEGylation on vesicle lamellarity: a small-angle neutron scattering study." *Langmuir* 35, 18: (2019) 6064–6074.

[162] Nelson, A. R., and S. W. Prescott. "refnx: neutron and X-ray reflectometry analysis in Python." *Journal of applied crystallography* 52, 1: (2019) 193–200.

[163] Neu, H. C. "The crisis in antibiotic resistance." *Science* 257, 5073: (1992) 1064–1073.

[164] Nevot, L., and P. Croce. "Characterization of surfaces by grazing X-ray reflection application to the study of polishing of some silicate glasses." *Revue de Physique Applique* 15, 3: (1980) 761–80.

[165] Nicholas, A. R., M. J. Scott, N. I. Kennedy, and M. N. Jones. "Effect of grafted polyethylene glycol (PEG) on the size, encapsulation efficiency and permeability of vesicles." *Biochimica et Biophysica Acta (BBA)-Biomembranes* 1463, 1: (2000) 167–178.

[166] Nomura, T., C. G. Cranfield, E. Deplazes, D. M. Owen, A. Macmillan, A. R. Battle, M. Constantine, M. Sokabe, and B. Martinac. "Differential effects of lipids and lyso-lipids on the mechanosensitivity of the mechanosensitive channels MscL and MscS." *Proceedings of the National Academy of Sciences* 109, 22: (2012) 8770–8775.

[167] Norman, C., Z.-W. Liu, P. Rigby, A. Raso, Y. Petrov, and B. Martinac. "Visualisation of the mechanosensitive channel of large conductance in bacteria using confocal microscopy." *European Biophysics Journal* 34, 5: (2005) 396–402.

[168] Ohki, S., and O. Zschörnig. "Ion-induced fusion of phosphatidic acid vesicles and correlation between surface hydrophobicity and membrane fusion." *Chemistry and physics of lipids* 65, 3: (1993) 193–204.

[169] Oku, N., and Y. Namba. "Long-circulating liposomes." *Critical reviews in therapeutic drug carrier systems* 11, 4: (1994) 231–270.

[170] Organization, W. H. "Antimicrobial resistance global report on surveillance: 2014 summary." Technical report, World Health Organization, 2014.

[171] Pan, J., F. A. Heberle, S. Tristram-Nagle, M. Szymanski, M. Koepfinger, J. Katsaras, and N. Kučerka. "Molecular structures of fluid phase phosphatidylglycerol bilayers as determined by small angle neutron and X-ray scattering." *Biochimica et Biophysica Acta (BBA)-Biomembranes* 1818, 9: (2012) 2135–2148.

[172] Papahadjopoulos, D., T. Allen, A. Gabizon, E. Mayhew, K. Matthay, S. Huang, K. Lee, M. Woodle, D. Lasic, and C. Redemann. "Sterically stabilized liposomes: improvements in pharmacokinetics and antitumor therapeutic efficacy." *Proceedings of the National Academy of Sciences* 88, 24: (1991) 11,460–11,464.

[173] Paraschiv, A., S. Hegde, R. Ganti, T. Pilizota, and A. Šarić. "Dynamic clustering regulates activity of mechanosensitive membrane channels." *Physical Review Letters* 124, 4: (2020) 048,102.

[174] Parratt, L. G. "Surface studies of solids by total reflection of X-rays." *Physical review* 95, 2: (1954) 359.

[175] Perozo, E., D. M. Cortes, P. Sompornpisut, A. Kloda, and B. Martinac. "Open channel structure of MscL and the gating mechanism of mechanosensitive channels." *Nature* 418, 6901: (2002) 942–948.

[176] Perozo, E., A. Kloda, D. M. Cortes, and B. Martinac. "Physical principles underlying the transduction of bilayer deformation forces during mechanosensitive channel gating." *Nature structural biology* 9, 9: (2002) 696–703.

[177] Perron, G. G., M. Zasloff, and G. Bell. "Experimental evolution of resistance to an antimicrobial peptide." *Proceedings of the Royal Society of London B: Biological Sciences* 273, 1583: (2006) 251–256.

[178] Phillips, R., J. Kondev, J. Theriot, and H. Garcia. *Physical biology of the cell*. Garland Science, 2012.

[179] Plant, A. L. "Self-assembled phospholipid/alkanethiol biomimetic bilayers on gold." *Langmuir* 9, 11: (1993) 2764–2767.

[180] Poon, W. C., A. T. Brown, S. O. Direito, D. J. Hodgson, L. Le Nagard, A. Lips, C. E. MacPhee, D. Marenduzzo, J. R. Royer, A. F. Silva, et al. "Soft matter science and the COVID-19 pandemic." *Soft matter* 16, 36: (2020) 8310–8324.

[181] Prime, K. L., and G. M. Whitesides. "Self-assembled organic monolayers: model systems for studying adsorption of proteins at surfaces." *Science* 24: (1991) 1164–1167.

[182] Purrucker, O., A. Förtig, R. Jordan, and M. Tanaka. "Supported membranes with well-defined polymer tethers—incorporation of cell receptors." *ChemPhysChem* 5, 3: (2004) 327–335.

[183] Puu, G., and I. Gustafson. "Planar lipid bilayers on solid supports from liposomes–factors of importance for kinetics and stability." *Biochimica et Biophysica Acta (BBA)-Biomembranes* 1327, 2: (1997) 149–161.

[184] Raguse, B., V. Braach-Maksvytis, B. A. Cornell, L. G. King, P. D. Osman, R. J. Pace, and L. Wieczorek. "Tethered lipid bilayer membranes: formation and ionic reservoir characterization." *Langmuir* 14, 3: (1998) 648–659.

[185] Ramamoorthy, A., S. Thennarasu, D.-K. Lee, A. Tan, and L. Maloy. "Solid-state NMR investigation of the membrane-disrupting mechanism of antimicrobial peptides MSI-78 and MSI-594 derived from magainin 2 and melittin." *Biophysical journal* 91, 1: (2006) 206–216.

[186] Reardon, S. "Antibiotic resistance sweeping developing world: bacteria are increasingly dodging extermination as drug availability outpaces regulation." *Nature* 509, 7499: (2014) 141–143.

[187] Reimhult, E., F. Höök, and B. Kasemo. "Vesicle adsorption on SiO 2 and TiO 2: dependence on vesicle size." *The Journal of chemical physics* 117, 16: (2002) 7401–7404.

[188] Reviakine, I., and A. Brisson. "Formation of supported phospholipid bilayers from unilamellar vesicles investigated by atomic force microscopy." *Langmuir* 16, 4: (2000) 1806–1815.

[189] Richter, R., A. Mukhopadhyay, and A. Brisson. "Pathways of lipid vesicle deposition on solid surfaces: a combined QCM-D and AFM study." *Biophysical journal* 85, 5: (2003) 3035–3047.

[190] Riessberger-Gallé, U., J. Hernández-López, G. Rechberger, K. Crailsheim, and W. Schuehly. "Lysophosphatidylcholine acts in the constitutive immune defence against American foulbrood in adult honeybees." *Scientific reports* 6, 1: (2016) 1–10.

[191] Rigaud, J.-L., and D. Lévy. "Reconstitution of membrane proteins into liposomes." In *Methods in enzymology*, Elsevier, 2003, volume 372, 65–86.

[192] Rondelli, V., G. Fragneto, S. Motta, E. Del Favero, and L. Cantù. "Reflectivity from floating bilayers: can we keep the structural asymmetry?" In *Journal of Physics: Conference Series*. IOP Publishing, 2012, volume 340, 012083.

[193] Rose, P. W., B. Beran, C. Bi, W. F. Bluhm, D. Dimitropoulos, D. S. Goodsell, A. Prlić, M. Quesada, G. B. Quinn, J. D. Westbrook, et al. "The RCSB Protein Data Bank: redesigned web site and web services." *Nucleic acids research* 39, suppl_1: (2010) D392–D401.

[194] Rosholm, K. R., M. A. Baker, P. Ridone, Y. Nakayama, P. R. Rohde, L. G. Cuello, L. K. Lee, and B. Martinac. "Activation of the mechanosensitive ion channel MscL by mechanical stimulation of supported Droplet-Hydrogel bilayers." *Scientific reports* 7: (2017) 45,180.

[195] Rossi, C., and J. Chopineau. "Biomimetic tethered lipid membranes designed for membrane-protein interaction studies." *European Biophysics Journal* 36, 8: (2007) 955–965.

[196] Russell, T. "X-ray and neutron reflectivity for the investigation of polymers." *Materials science reports* 5, 4: (1990) 171–271.

[197] Sackmann, E. "Supported membranes: scientific and practical applications." *Science* 271, 5245: (1996) 43–48.

[198] Sauerbrey, G. "Verwendung von Schwingquarzen zur Wagung dunner Schichten und zur Mikrowagung." *Zeitschrift fur physik* 155, 2: (1959) 206–222.

[199] Schiessel, H., R. Metzler, A. Blumen, and T. Nonnenmacher. "Generalized viscoelastic models: their fractional equations with solutions." *Journal of physics A: Mathematical and General* 28, 23: (1995) 6567.

[200] Schmiedel, H., L. Almásy, and G. Klose. "Multilamellarity, structure and hydration of extruded POPC vesicles by SANS." *European Biophysics Journal* 35, 3: (2006) 181–189.

[201] Seantier, B., and B. Kasemo. "Influence of mono-and divalent ions on the formation of supported phospholipid bilayers via vesicle adsorption." *Langmuir* 25, 10: (2009) 5767–5772.

[202] Sears, V. F. "Neutron scattering lengths and cross sections." *Neutron news* 3, 3: (1992) 26–37.

[203] Sehnal, D., A. Rose, J. Kovca, S. Burley, and S. Velankar. "Mol*: Towards a common library and tools for web molecular graphics MolVA." *EuroVis Proceedings* 10.

[204] Shen, H.-H., T. Lithgow, and L. Martin. "Reconstitution of membrane proteins into model membranes: seeking better ways to retain protein activities." *International journal of molecular sciences* 14, 1: (2013) 1589–1607.

[205] Shenoy, S., R. Moldovan, J. Fitzpatrick, D. J. Vanderah, M. Deserno, and M. Lösche. "In-plane homogeneity and lipid dynamics in tethered bilayer lipid membranes (tBLMs)." *Soft matter* 6, 6: (2010) 1263–1274.

[206] Silverman, A. D., A. S. Karim, and M. C. Jewett. "Cell-free gene expression: an expanded repertoire of applications." *Nature Reviews Genetics* 21, 3: (2019) 1–20.

[207] Singer, S. J., and G. L. Nicolson. "The fluid mosaic model of the structure of cell membranes." *Science* 175, 4023: (1972) 720–731.

[208] Sivia, D. S. *Elementary scattering theory: for X-ray and neutron users.* Oxford University Press, 2011.

[209] Sivia, D., and J. Webster. "The Bayesian approach to reflectivity data." *Physica B: Condensed Matter* 248, 1-4: (1998) 327–337.

[210] Smani, Y., J. Domínguez-Herrera, J. Ibáñez-Martínez, and J. Pachón. "Therapeutic efficacy of lysophosphatidylcholine in severe infections caused by Acinetobacter baumannii." *Antimicrobial agents and chemotherapy* 59, 7: (2015) 3920–3924.

[211] Sprong, R. C., M. F. Hulstein, and R. Van der Meer. "Bactericidal activities of milk lipids." *Antimicrobial Agents and Chemotherapy* 45, 4: (2001) 1298–1301.

[212] Steinbacher, S., R. Bass, P. Strop, and D. C. Rees. "Structures of the prokaryotic mechanosensitive channels MscL and MscS." *Current topics in membranes* 58: (2007) 1–24.

[213] Steinem, C., A. Janshoff, W.-P. Ulrich, M. Sieber, and H.-J. Galla. "Impedance analysis of supported lipid bilayer membranes: a scrutiny of different preparation techniques." *Biochimica et Biophysica Acta (BBA)-Biomembranes* 1279, 2: (1996) 169–180.

[214] Stokes, N. R., H. D. Murray, C. Subramaniam, R. L. Gourse, P. Louis, W. Bartlett, S. Miller, and I. R. Booth. "A role for mechanosensitive channels in survival of stationary phase: regulation of channel expression by RpoS." *Proceedings of the National Academy of Sciences* 100, 26: (2003) 15,959–15,964.

[215] Sukharev, S. "Mechanosensitive channels in bacteria as membrane tension reporters." *The FASEB journal* 13, 9001: (1999) S55–S61.

[216] ———. "Purification of the small mechanosensitive channel of escherichia coli (mscS): the subunit structure, conduction, and gating characteristicsin liposomes." *Biophysical journal* 83, 1: (2002) 290–298.

[217] Sukharev, S., M. Betanzos, C.-S. Chiang, and H. R. Guy. "The gating mechanism of the large mechanosensitive channel MscL." *Nature* 409, 6821: (2001) 720–724.

[218] Sukharev, S., and D. P. Corey. "Mechanosensitive channels: multiplicity of families and gating paradigms." *sci. sTKE* 2004, 219: (2004) re4–re4.

[219] Sukharev, S. I., P. Blount, B. Martinac, F. R. Blattner, and C. Kung. "A large-conductance mechanosensitive channel in E. coli encoded by mscL alone." *Nature* 368, 6468: (1994) 265–268.

[220] Sukharev, S. I., W. J. Sigurdson, C. Kung, and F. Sachs. "Energetic and spatial parameters for gating of the bacterial large conductance mechanosensitive channel, MscL." *The Journal of general physiology* 113, 4: (1999) 525–540.

[221] Sut, T. N., J. A. Jackman, and N.-J. Cho. "Understanding How Membrane Surface Charge Influences Lipid Bicelle Adsorption onto Oxide Surfaces." *Langmuir* 35, 25: (2019) 8436–8444.

[222] Takeda, M., and M. Kainosho. "Cell-free protein production for NMR studies." In *Protein NMR techniques*, Springer, 2012, 71–84.

[223] Tanaka, M., and E. Sackmann. "Polymer-supported membranes as models of the cell surface." *Nature* 437, 7059: (2005) 656–663.

[224] Te Winkel, J. D., D. A. Gray, K. H. Seistrup, L. W. Hamoen, and H. Strahl. "Analysis of antimicrobial-triggered membrane depolarization using voltage sensitive dyes." *Frontiers in cell and developmental biology* 4: (2016) 29.

[225] Teppner, R., S. Bae, K. Haage, and H. Motschmann. "On the Analysis of Ellipsometric Measurements of Adsorption Layers at Fluid Interfaces." *Langmuir* 15, 20: (1999) 7002–7007.

[226] ThermoFisher. "SimplyBlue SafeStain ThermoFisher." `https://www.thermofisher.com/order/catalog/product/LC6065#/LC6065`, . Accessed: 2020-09-14.

[227] Tiede, D. M. "Incorporation of membrane proteins into interfacial films: model membranes for electrical and structural characterization." *Biochimica et Biophysica Acta (BBA)-Reviews on Bioenergetics* 811, 4: (1985) 357–379.

[228] Tien, H. T., and Z. Salamon. "Formation of self-assembled lipid bilayers on solid substrates." *Journal of electroanalytical chemistry and interfacial electrochemistry* 276, 3: (1989) 211–218.

[229] Todd, E. C., B. S. Michaels, J. Holah, D. Smith, J. D. Greig, and C. A. Bartleson. "Outbreaks where food workers have been implicated in the spread of foodborne disease. Part 10. Alcohol-based antiseptics for hand disinfection and a comparison of their effectiveness with soaps." *Journal of Food Protection* 73, 11: (2010) 2128–2140.

[230] Ulman, A. *An Introduction to Ultrathin Organic Films: From Langmuir–Blodgett to Self–Assembly*. Academic press, 2013.

[231] Van Den Berg, J., H. Galbiati, A. Rasmussen, S. Miller, and B. Poolman. "On the mobility, membrane location and functionality of mechanosensitive channels in Escherichia coli." *Scientific reports* 6: (2016) 32,709.

[232] Van Der Spoel, D., E. Lindahl, B. Hess, G. Groenhof, A. E. Mark, and H. J. Berendsen. "GROMACS: fast, flexible, and free." *Journal of computational chemistry* 26, 16: (2005) 1701–1718.

[233] Volinsky, R., S. Kolusheva, A. Berman, and R. Jelinek. "Investigations of antimicrobial peptides in planar film systems." *Biochimica et Biophysica Acta (BBA)-Biomembranes* 1758, 9: (2006) 1393–1407.

[234] Wädsater, M., J. B. Simonsen, T. Lauridsen, E. G. Tveten, P. Naur, T. Bjornholm, H. Wacklin, K. Mortensen, L. Arleth, R. Feidenhans, et al. "Aligning nanodiscs at the air–water interface, a neutron reflectivity study." *Langmuir* 27, 24: (2011) 15,065–15,073.

[235] Wagner, M. L., and L. K. Tamm. "Tethered polymer-supported planar lipid bilayers for reconstitution of integral membrane proteins: silane-polyethyleneglycol-lipid as a cushion and covalent linker." *Biophysical journal* 79, 3: (2000) 1400–1414.

[236] Wallin, M., J.-H. Choi, S. O. Kim, N.-J. Cho, and M. Andersson. "Peptide-induced formation of a tethered lipid bilayer membrane on mesoporous silica." *European Biophysics Journal* 44, 1-2: (2015) 27–36.

[237] Walton, T. A., and D. C. Rees. "Structure and stability of the C-terminal helical bundle of the E. coli mechanosensitive channel of large conductance." *Protein Science* 22, 11: (2013) 1592–1601.

[238] Wang, X., R. N. Sanderson, and R. Ragan. "Evaluation of young's modulus of tethered 1-palmitoyl-2-oleoyl-sn-glycero-3-phosphocholine membranes using atomic force spectroscopy." *The Journal of Physical Chemistry C* 118, 50: (2014) 29,301–29,309.

[239] Wang, Y., Y. Liu, H. A. DeBerg, T. Nomura, M. T. Hoffman, P. R. Rohde, K. Schulten, B. Martinac, and P. R. Selvin. "Single molecule FRET reveals pore size and opening mechanism of a mechano-sensitive ion channel." *Elife* 3: (2014) e01,834.

[240] Watkins, E. B., R. J. El-khouri, C. E. Miller, B. G. Seaby, J. Majewski, C. M. Marques, and T. L. Kuhl. "Structure and thermodynamics of lipid bilayers on polyethylene glycol cushions: Fact and fiction of PEG cushioned membranes." *Langmuir* 27, 22: (2011) 13,618–13,628.

[241] Williams, R. W., R. Starman, K. M. Taylor, K. Gable, T. Beeler, M. Zasloff, and D. Covell. "Raman spectroscopy of synthetic antimicrobial frog peptides magainin 2a and PGLa." *Biochemistry* 29, 18: (1990) 4490–4496.

[242] Wong, J. Y., J. Majewski, M. Seitz, C. K. Park, J. N. Israelachvili, and G. S. Smith. "Polymer-cushioned bilayers. I. A structural study of various preparation methods using neutron reflectometry." *Biophysical Journal* 77, 3: (1999) 1445–1457.

[243] Xie, J.-Y., and G.-H. Ding. "Studies on sensitivity to tension and gating pathway of MscL by molecular dynamic simulation." *Acta Mechanica Sinica* 29, 2: (2013) 256–266.

[244] Yang, H., Y. Xu, Z. Gao, Y. Mao, Y. Du, and H. Jiang. "Effects of Na+, K+, and Ca2+ on the structures of anionic lipid bilayers and biological implication." *The Journal of Physical Chemistry B* 114, 50: (2010) 16,978–16,988.

[245] Yang, L.-M., R. Wray, J. Parker, D. Wilson, R. S. Duran, and P. Blount. "Three routes to modulate the pore size of the MscL channel/nanovalve." *ACS nano* 6, 2: (2012) 1134–1141.

[246] Yoshimura, K., and M. Sokabe. "Mechanosensitivity of ion channels based on protein–lipid interactions." *Journal of The Royal Society Interface* 7, suppl_3: (2010) S307–S320.

[247] Zasloff, M., B. Martin, and H.-C. Chen. "Antimicrobial activity of synthetic magainin peptides and several analogues." *Proceedings of the national academy of sciences* 85, 3: (1988) 910–913.

[248] Zhu, T., Z. Jiang, E. M. R. Nurlybaeva, J. Sheng, and Y. Ma. "Effect of osmotic stress on membrane fusion on solid substrate." *Langmuir* 29, 21: (2013) 6377–6385.